Investigation of the Yttria-Zirconia-Titania-Ceria system for potential SOFC materials

A thesis presented for examination for the title of PhD

By

Richard Buchanan

University of St. Andrews

November 2003

DECLARATION

I, Richard Buchanan, hereby certify that this thesis, which is approximately 41,500 words in length has been written by me, that it is the record of work carried out by me and that it has not been submitted in any previous application for a higher degree.

Date: 5/1/2004 Signature of Candidate:

I was admitted as a research student in September 2000 and as a candidate for the degree of Doctor of Philosophy in September 2001, the higher study for which this is a record was carried out in the University of St. Andrews between 2000 and 2003.

Date: 5/1/2004. Signature of Candidate:

I hereby certify that the candidate has fulfilled the conditions of the Resolution and Regulations appropriate for the degree of Doctor of Philosophy in the University of St. Andrews and that the candidate is qualified to submit this thesis in application for that degree

Date: 5/1/2004 Signature of Supervisor:

In submitting this thesis to the University of St. Andrews I understand that I am giving permission for it to be made available for use in accordance with the regulations of the University for the time being in force, subject to any copyright vested in the work not being affected thereby. I also understand that the title and abstract will be published, and that a copy of the work may be made and supplied by any bona fide library or research worker.

Date: 5/1/2004 Signature of Candidate:

Acknowledgments

I would like to thank the following people for their assistance over the past three years

My research supervisor, Professor John Irvine for help and suggestions.

Mrs Sylvia Williamson for help and assistance with thermal analysis measurements

Members of Professor Irvine's research group for putting up with me and occasional help/ assistance.

Dr John Bradley for assistance in carrying out conductivity measurements (AC Impedance and Four-terminal DC conductivity studies).

Dr Shanwen Tao for assistance in the fuel cell test measurements, as well as some assistance with Four-terminal DC conductivity measurements.

Dr Juan-Carlos Ruiz-Morales for electrochemical studies on $Y_{0.15}Zr_{0.57}Ti_{0.13}Ce_{0.15}O_{1.925}$ as a SOFC electrode.

Funding was provided by EPSRC

Abstract

This work comprised an investigation of the Y_2O_3-ZrO_2-TiO_2-CeO_2 (YZTC) system, with compositions of formula $Y_{0.20-x}Zr_{0.62-y}Ti_{0.18-z}Ce_{x+y+z}O_{1.9+x/2}$. When fired in air at 1,400-1,500°C, most investigated YZTC compositions had cubic fluorite structures. Limiting compositions were at x=0.075 and either y=0.15, z=0.10 or y=0.10, z=0.05. Unit cell sizes were 5.111-5.228 Å, increasing with increasing CeO_2 content and decreasing TiO_2 content. Increasing TiO_2 content hindered the formation of single-phase cubic structures. Cubic phase formation was favoured with high Y content, intermediate to high Ce content and lower Ti content. All compositions containing 3 mol% TiO_2 were single-phase cubic, helped by the size effect of Ce^{4+} ions. With increasing TiO_2 content, the minimum amount of Y_2O_3 required for stabilisation was 6.67 mol% with 8 mol% TiO_2, 8 mol% with 13 mol% TiO_2 and 11 mol% with 18 mol% TiO_2. Cubic structures became the exception with high TiO_2 content.

Reduction studies indicated that at 900-1,000°C, almost all Ce^{4+} is reduced in 5% H_2/ Argon. This reduction caused a colour change to dark brown/ black. The unit cell expanded by up to 0.053Å as well, increasing with increasing CeO_2 content. Firing in air at 1,400-1,500°C caused more reduction of Ce than in argon at 900-1,000°C. For thermal expansion, α was 10.25-11.68*10^{-6} K^{-1} in O_2 and argon, up to 0.98*10^{-6} K^{-1} higher than α in 5% H_2/ argon. Sintering experiments with Fe_2O_3 indicated that sintering is accelerated with up to 1.59 mol% Fe_2O_3 addition.

Ionic conductivities in air were in the range 2.61-9.95*10^{-3} Scm^{-1} at 900°C, increasing with increasing ZrO_2 and decreasing TiO_2 content. E_{act} was in the range 1.12-1.24 eV. In 5% H_2/ argon, conductivity was increased and E_{act} was decreased, due to the presence of an electronic contribution to conductivity.

In DC conductivity measurements at ~900°C, the ionic domain is present down to 10^{-16} atm pO_2 for 10 mol% CeO_2, rising to 10^{-11} atm for 25 mol% CeO_2. The electronic conductivity region below these pO_2 levels changes in nature with increasing Ce content. For 10 mol% CeO_2, it is n-type on reduction and oxidation. This changes with 15 mol% CeO_2, as on reduction, σ reaches a maximum at a particular pO_2, and then decreases with decreasing pO_2 below this level. n-type conductivity is seen on oxidation. For 25 mol% CeO_2, the same behaviour is observed on reduction but on oxidation, there is only σ increasing with increasing pO_2.

The behaviour at low pO_2 of σ decreasing with decreasing pO_2 is due to a combination of decreasing electronic conductivity, due to most of the Ce^{4+} being reduced to Ce^{3+} below the conductivity maximum, as well as ionic conductivity decreasing due to clustering of oxygen vacancies, leading to less 'free' oxygen vacancies. There also appeared to be a hysteresis in this process between reduction and oxidation which is suggested to be due to defect ordering.

Table of Contents

Chapter 1: Introduction

Contents

1: Introduction

1.1: What is a Solid Oxide Fuel Cell (SOFC)?

Essentially, the SOFC is an energy conversion device that electrochemically combines fuel and oxidant to produce heat and electricity. It consists of two porous electrodes (anode and cathode) with a dense, ion-conducting electrolyte between them. A typical diagram of how a fuel cell operates is shown as Figure 1.1. The electrical circuit involves fuel fed into the anode side of the system, where it is oxidised, releasing electrons that go to the external circuit. At the same time, the oxidant is fed into the cathode side of the system, where electrons are taken from the external circuit and are used to reduce the oxidant. The resultant flow of electrons leads to the production of DC electricity.

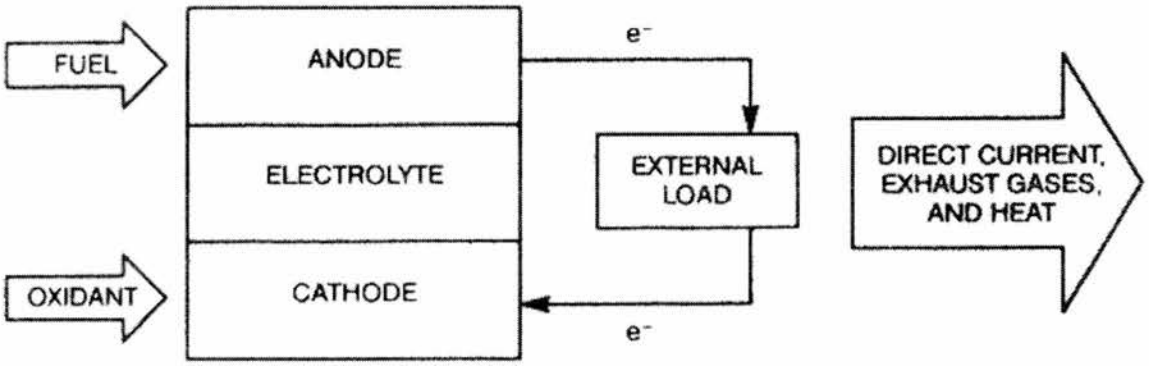

Figure 1.1: Simple schematic of SOFC operation [1]

In practice, however, SOFC systems are not operated as just one single cell, but tend to be arranged in the form of systems that comprise of several cells linked together to form a single stack.

One of the main features of the SOFC is its high energy conversion efficiency. This is due to the fuel cell converting the fuel's chemical energy directly into electrical energy rather than conversion into thermal energy, followed by subsequent conversion of thermal into electrical energy. Thus, the fuel cell's energy conversion efficiency is not subject to the Carnot limitation.

Compared to other means of power generation, the SOFC offers certain advantages. Principally, the SOFC should yield higher energy conversion efficiency; it is modular in construction, has high efficiency at part load, minimal site restrictions, it can be used as a combined heat & power system and less production of pollutants due to using less fuel per kilowatt of power produced.

The beginning of the fuel cell was in 1839 with the first fuel cell developed by William Grove. This fuel cell operated at room temperature and used dilute sulphuric acid as an electrolyte, a hydrogen anode and an oxygen cathode [2]. This was probably the first ever type of electric power supply, as conventional batteries like the lead-acid battery or Lechlance-type cells did not exist and a set of four cells in series were used for electrolysis of water. Essentially, research and development of solid oxide electrolyte-based fuel cells started in 1899, with Nernst's discovery of solid oxide electrolytes. This discovery happened when Nernst discovered ionic conductivity in 9 mol% Y_2O_3/ ZrO_2 [3]. The first ever fully operational solid oxide fuel cell was operated in 1937 at 1,000°C by Baur and Preis [4].

1.2: Fuel cell types

Currently, there are several different types of fuel cell in operation and they tend to be characterised or named after the type of electrolyte used in each system, as the electrolyte governs the operating temperature. The main types of fuel cells are listed below [5, 6]

Alkaline Fuel Cell (AFC)

The AFC uses KOH soaked in a matrix as the electrolyte, operating at 150 - 200°C and uses either pure H_2 or hydrazine for fuel. It is important that the hydrogen used as fuel is very pure, as impurities could lead to the formation of a solid carbonate that can reduce the cell performance. Power generation efficiencies of up to 70% have been obtained for the AFCs and these cells have been used in space missions to provide electricity and drinking water.

Direct methanol fuel cell (DMFC)

The DMFC uses a polymer electrolyte, normally operates at 50 - 90°C and uses liquid methanol as fuel but tends to draw hydrogen from the methanol without the need for reforming. General efficiency is ~40% from a DMFC and usually a higher temperature leads to higher efficiency. One of the main problems, however, with a DMFC is that fuel can cross over from the anode to the cathode without producing any energy.

Phosphoric acid fuel cell (PAFC)

The PAFC uses phosphoric acid soaked in a matrix as the electrolyte. The PAFC operates at 150 - 200°C and uses either hydrogen reformed from hydrocarbons and alcohol.

The efficiency of power generation is ~40%, although up to 85% of the steam that is produced by this cell can be reclaimed for cogeneration purposes.

One particular problem that is faced by the PAFC is at low temperatures. This is potentially due to carbon monoxide, which can poison the Pt electro catalyst in the anode. That said, however, the PAFC can tolerate a CO concentration of up to 1.5%. Another potential poison is sulphur or sulphur compounds that must be removed from gasoline if it is to be used as a fuel. There is also the sulphuric acid fuel cell (SAFC) that operates at 80 - 90°C and can use alcohol or impure H_2 as fuel. SAFC uses sulphuric acid as its electrolyte

Proton-exchange membrane fuel cell (PEMFC)

The PEMFC uses a polymer proton exchange membrane electrolyte and operates at 50 - 80°C. It tends to use lower purity hydrogen reformed from hydrocarbons or methanol but it very sensitive to impurities, however. The electrolyte is a poly-(perfluorosulphonic) acid polymer and the membrane is usually coated on both sides with particles of highly dispersed metal alloys (usually containing Pt) that act as active catalysts.

One primary advantage that the PEM fuel cell has over other low temperature fuel cells is that the electrolyte is solid and does not lead to corrosion or electrolyte management problems.

One factor that seems to be common for these lower temperature fuel cells is that hydrocarbons cannot be used directly as fuel and they have to be reformed, so that the hydrogen content is used as the fuel, instead. In the higher temperature region, the fuel cells tend to be the molten carbonate fuel cell (MCFC) and the SOFC.

Molten carbonate fuel cell (MCFC)

The MCFC electrolyte is normally a solution of carbonates of lithium, sodium and potassium soaked in a matrix. The operating temperature is ~650°C, which is required for the electrolyte to achieve a suitable level of conductivity. This also has an advantage in that the high temperatures remove the need for noble metal catalysts to assist in electrochemical processes of oxidation and reduction.

Also, the MCFC can use a variety of different fuel types such as H_2, CO and hydrocarbons such as natural gas, propane or marine diesel. It is also possible to carry out internal reforming of hydrocarbons to utilise the resultant hydrogen as fuel. The oxidant is oxygen, air or carbon dioxide.

Solid Oxide Fuel Cell (SOFC/ PCFC)

The SOFC normally uses the ceramic oxide-ion conducting material YSZ as electrolyte and currently deployed SOFCs operate at ~1,000°C, in order to obtain suitable electrochemical reaction kinetics. H_2, CO and hydrocarbons can be used as fuel; although hydrocarbons may need steam reforming that can be carried out internally, to avoid carbon deposition on the anode.

A second type of SOFC is the protonic ceramic fuel cell (PCFC). The electrolyte material used is a thin barium cerate membrane, which is a proton-conducting electrolyte material, in contrast to the conventional YSZ SOFC electrolyte, which is an oxide ion-conducting material. The PCFC operates at 600-700°C and hydrogen is the most common fuel. The mechanisms by which the PCFC operate are similar to those of the SOFC, although one contrast is that in the SOFC, water is produced at the anode but in the PCFC, water is produced at the cathode.

Eminently, the higher temperature fuel cells such as the SOFC and the MCFC tend to have advantages in that they can utilise hydrocarbons directly (within reason) and tend to generate energy more efficiently at up to 60% or up to 90% if the exhaust heat is recovered and used in a combined heat/ power plant.

Results of Current Fuel Cell Research

Most recent fuel cell research interest has been in the PEM and SOFC systems. The PEM fuel cells tend to be most suitable for cars and mass transportation. Whilst the SOFC tends to be the most demanding of the systems in terms of materials and suitability requirements, there is interest in SOFC development due to inherent advantages that outweigh the apparent disadvantages.

The principal advantages of the SOFC over other systems are that in fuel input to electricity output terms, the SOFC is the most efficient type of fuel cell. There is also flexibility in the types of fuel that can be used in a SOFC, which can use hydrocarbons as well as hydrogen. The SOFC has a modular and solid-state construction, which contains no moving parts and this means that the system is quiet and can be used indoors (in the case of a domestic fuel cell). The operating temperature of up to 1,000°C can also be used to generate high quality exhaust heat that can be used in co-generation or combined heat/power systems.

Other advantages that the SOFC has are that it generally does not use any noble metals, which have the problem of resource availability and expense when used in manufacturing vast quantities of SOFCs. The SOFC does not have to worry about electrolyte management systems, as opposed to other fuel cells that can have molten or potentially corrosive electrolyte materials that are difficult to handle or may need to be circulated around the cell. This is due to the SOFC electrolyte being a solid refractory oxide that is heated up to temperatures well below its melting point.

There is also no production of CO in the exhaust gases in the SOFC, as its high operating temperature would allow the oxidation of any CO produced to CO_2. The final advantage of the SOFC is a potentially long lifetime of up to 80,000 hours of usage [5].

1.3: General SOFC Operation. [7]

Most SOFC systems operate at temperatures ranging from 900 – 1,000°C and can use either hydrogen or carbon monoxide as fuel. Given appropriate internal or external reforming conditions, however, a wide range of hydrocarbons, especially natural gas could also be used as a source of hydrogen. Some fuel cells, however, cannot use hydrocarbons directly as a fuel and would require them to be reformed to release hydrogen, which would be used as the fuel. An example of this problem is that if dry natural gas is used as a fuel and a Ni-YSZ cermet was used as the anode, the reactions involved would lead to carbon deposition on the anode, which would cause it to lose its electrocatalytic activity.

Operating at up to 1,000°C allows for reforming hydrocarbons internally, reducing some potential costs by removing the need for an expensive external reformer. The reactions involved in steam reforming using methane as an example are shown below in equations (1)-(4).

Formation of 'syngas' (CO/ H_2 mixture) from steam reforming

$$CH_4 + H_2O \leftrightarrow CO + 3H_2 \quad (1)$$

The resultant CO and H_2 can then be electrochemically oxidised, as per reactions (2) and (3)

$$H_2 + O^{2-} \leftrightarrow H_2O + 2e^- \quad (2)$$

$$CO + O^{2-} \leftrightarrow CO_2 + 2e^- \quad (3)$$

Steam reforming is also associated with the gas shift reaction, shown as equation (4)

$$CO + H_2O \leftrightarrow CO_2 + H_2 \quad (4)$$

One problem with steam reforming is that there must be an adequate amount of steam present to cause reaction (1). If this is not the case, however, then this could lead to carbon deposition that can be caused by either the cracking of methane or by the Boudouard reaction. These processes are shown as equations (5) and (6). [8]

$$CH_4 \leftrightarrow C + 2H_2 \quad (5)$$

$$2CO \leftrightarrow C + CO_2 \quad (6)$$

Nickel is a good catalyst for both steam reforming and electrochemical oxidation of hydrogen. The most commonly used SOFC anode material is the Ni/YSZ cermet (ceramic/ metal composite). While Ni is a very good catalyst, its very high activity can damage the SOFC when running with methane as a fuel due to carbon deposition. While the operating temperature of up to 1,000°C allows favourable kinetics for internal steam reforming, such reforming does have one main disadvantage, however. Internal steam reforming is a highly endothermic process, which would cause temperature gradients within the fuel cell, leading to cooler zones within the cell and reduced performance.

On the other hand, the high operating temperatures lead to the production of high quality exhaust heat that can be used in co-generation/ combined heat/power plants, increasing the effective efficiency of the system. In terms of efficiency levels, the SOFC can yield up to 60% in normal cycle operation. In a combined cycle pressurised SOFC-turbine system, the efficiency can rise to 70%. Finally, if the SOFC is used as a combined heat and power plant by re-circulating the exhaust heat for other uses, the efficiency can rise to almost 90% [9].

Currently, research is going on to develop SOFC systems that can operate at 700 - 800°C or even lower. The advantages of a lower operating temperature are that a wider range of materials that can be used, as well as less demanding conditions on the seals and 'balance of plant' components. It also means that the start-up and cool-down times for the SOFC system will be reduced, as the system does not have to go to as high a temperature. Another advantage of lower SOFC temperatures would be that the interconnects could be made from metals, as opposed to doped lanthanum chromite, for which fabrication is difficult and expensive due to it having poor sinterability.

1.4: SOFC components [1, 7]

There are four principal component types in the SOFC system. These are the electrolyte, anode, cathode and interconnect. The most commonly used materials are YSZ for

the electrolyte, $LaMnO_3$ doped with Sr or Ca for the cathode, Ni/YSZ for the anode and $LaCrO_3$ doped with Sr or Ca for the interconnection. Each of these components serves certain functions and there are certain requirements to be met for materials that are suitable for use as that type of SOFC component.

Examples of the requirements for SOFC components are that each component must be stable in chemical, phase, morphological and dimensional terms in oxidising or reducing environments that it will be exposed to. All components must be chemically compatible with each other and must have levels and types of conductivity (electronic or ionic) that are suitable for their intended roles.

Other general requirements for SOFC components are that they must have similar levels of thermal expansion coefficient, in order to avoid excessive mismatches that can cause cracks in the cell or detachment of components from each other during the processes of fabrication and general operation. There are also density requirements that have to be met by the components. These are that the interconnect and electrolyte must be either fully dense or at least 95% of full density, in order to avoid gas mixing that would lead to fuel/ oxidant reaction occurring in regions of the fuel cell where they are not supposed to happen. For the anode and cathode, however, they must be porous, in order to allow the fuel and oxidant gases to be transported to the reaction sites, as well as allowing the reaction products to diffuse away.

1.4.1: SOFC electrolyte materials

The most commonly used SOFC electrolyte material is YSZ, which has adequate oxide-ion conductivity and is stable in oxidising and reducing atmospheres. This is in contrast to pure ZrO_2, which has many problems that would make it unsuitable as a potential electrolyte material [1].

Firstly, pure ZrO_2 is unsuitable, as its ionic conductivity is very low. Also, there are two main phase transitions, which have associated volume changes. The structure of ZrO_2 is monoclinic at room temperature and at 1,170+°C, the structure changes from monoclinic to tetragonal. The tetragonal structure, however, is metastable and can easily revert back to monoclinic and this transition causes a significant volume change of 3-5%. The second phase transition is at 2,370°C, where the tetragonal structure changes to the cubic fluorite structure, which is stable up to the melting point of ZrO_2 (2,700°C).

If ZrO_2 is doped with certain divalent or trivalent cations, they can have the effect of stabilising the cubic structure to lower temperatures than 2,370°C. If ZrO_2 is doped with enough of an aliovalent cation, the cubic structure can be made stable down to room temperature, which would effectively remove the phase transition phenomena that could cause problems. These cations also have a further effect in that they increase the concentration of oxygen vacancies in the structure, which increases the oxide-ion conductivity of the material and extends the pO_2 range over which this ionic conductivity occurs. The most commonly used stabilising dopants are CaO, MgO, Y_2O_3 and Sc_2O_3.

The mechanism for stabilisation of ZrO_2 is by the substitution of Zr^{4+} cations for divalent or trivalent cations that are usually larger than the Zr^{4+} cations but are large enough to be suitable cations for the 8-coordinate environment of the cubic M_4O_8 structure. Also, the stabilisation effect creates oxygen vacancies by charge compensation, according to the following Kroger-Vink notations:

$$Y_2O_3 \xrightarrow{ZrO_2} 2Y'_{Zr} + V_O^{\cdot\cdot} + 3O_O^x$$

$$CaO \xrightarrow{ZrO_2} Ca''_{Zr} + V_O^{\cdot\cdot} + O_O^x$$

Thus, fully stabilised ZrO_2 is preferred to pure or partially stabilised ZrO_2, as there are no phase transitions that could occur during cell operation. Also, the conductivity of fully stabilised ZrO_2 follows typical Arrhenius behaviour. A final note on stabilised ZrO_2 is that the use of Y_2O_3 as the most common stabiliser is not purely an issue of conductivity, but of stability as well. Despite YSZ not having the highest oxide-ion conductivity of the stabilised ZrO_2 systems, it offers the highest performance stability and is also widely available and fairly inexpensive.

One alternative type of electrolyte material that has been tried is Bi_2O_3, which like ZrO_2, requires to be doped in order to stabilise its cubic structure down from 735°C to room temperature. At temperatures comparable to those used for stabilised ZrO_2, doped Bi_2O_3 shows the highest levels of ionic conductivity. At 700°C, the conductivity was ~0.1 Scm^{-1} and at 500°C, the ionic conductivity was ~0.01 Scm^{-1}. Thus, the conductivity of doped Bi_2O_3 can be 10 to 100 times that of stabilised ZrO_2 [10-12].

One would think that this would make doped Bi_2O_3 a suitable candidate as a SOFC electrolyte material for operating temperatures of <1,000°C. There are drawbacks that make this type of material less suitable. Firstly, the ionic conductivity of doped Bi_2O_3 occurs over a considerably narrower pO_2 range than stabilised ZrO_2. Secondly, the doped Bi_2O_3 reduces easily at low pO_2 and can be reduced to Bi metal at 600°C at a pO_2 of $\leq 10^{-13}$ atm. Thus, this

would make doped Bi_2O_3 not very suitable as a potential electrolyte material, as it has to be stable in both oxidising and reducing environments.

Possible alternatives to the YSZ electrolyte materials are Scandia-zirconia, doped ceria and doped lanthanum gallate perovskites. In terms of the doped lanthanum gallate perovskites, one material that was of interest was $La_{0.8}Sr_{0.1}Ga_{0.8}Mg_{0.2}O_3$, which was reported to have an ionic conductivity of 0.17 Scm^{-1} at 800°C, which is much higher than that of YSZ at a comparable temperature. One problem, however, with the LSGM is that it is susceptible to the formation of impurity phases if there are slight deviations from intended stoichiometry, as well as the evaporation of Ga or Ga oxides at high temperatures. Impurity phases are also a problem, as they can cause considerable changes to the material properties and also, one of the preferred requirements of a SOFC component material is a guarantee of stability of the properties of the material, especially during fabrication [13].

1.4.2: SOFC cathode materials

In the SOFC, the cathode works as the 'air electrode', which is subjected to oxidising environments of oxidant. The main reaction that occurs at the cathode is the reduction of oxygen atoms or molecules to oxide ions using electrons released from the anode side of the system, as follows:

$$O_2 + 4e^- \rightarrow 2O^{2-}$$

At 1,000°C, the only materials that are potentially suitable for use as SOFC cathode materials appear to be noble metals or metal oxides with high electronic conductivity. Noble metals, however, appear to be unsuitable due to their relatively high cost. So, cathode material research has been based on metal oxides. The most commonly used cathode material is doped $LaMnO_3$ [1].

$LaMnO_3$ itself is a perovskite oxide that has p-type electronic conductivity. The formula can vary with pO_2, leading to a material that can have oxygen excess, deficiency, or it can be stoichiometric. The p-type conductivity is due to cation vacancies and doping with a lower valency cation on either the A or B site. The most commonly used cathode material; however, is Sr-doped $LaMnO_3$ (LSM). The way in which doping increases conductivity is that replacing La^{3+} with Sr^{2+} causes a charge-compensation mechanism that leads to some of the Mn^{3+} cations becoming Mn^{4+}, as can be shown below [14].

$$LaMnO_3 \xrightarrow{SrO} La^{3+}_{1-x}Sr^{2+}_{x}Mn^{3+}_{1-x}Mn^{4+}_{x}O_3$$

Thus, electronic conductivity happens via the small polaron hopping mechanism.

Doping $LaMnO_3$ with Sr has another effect in that the thermal expansion coefficient (α) of the material increases with increasing Sr content. α ranges from $11.2*10^{-6}$ K^{-1} for $La_{0.99}MnO_3$ to $12.8*10^{-6}$ K^{-1} for $La_{0.69}Sr_{0.30}MnO_3$ [15]. This means that α for the cathode material is higher than for YSZ, although this difference has not appeared to cause any significant mismatch-related problems.

While LSM has been the most commonly used SOFC cathode material, it does have one problem when used along with a YSZ electrolyte, however. This is that at temperatures of 1,200+°C, LSM can react with YSZ to form $La_2Zr_2O_7$ and $SrZrO_3$ phases that have low conductivity and reduce overall fuel cell performance [16, 17]. Another problem with LSM is that it suffers from low oxide ion mobility, which is an important property for a good cathode material, especially for SOFCs operating at low temperatures.

Other materials that have been investigated as potential SOFC cathodes have been cobaltate perovskite materials, such as $La_{1-x}Sr_xCoO_{3-\delta}$ (LSC). The interest in these materials was due to them having high oxide ion conductivities comparable to or higher than YSZ and high electronic conductivities in the range 100 – 1,000 Scm^{-1}. Thus, they are potentially interesting mixed ionic-electronic conductors [18].

LSC and related materials cannot be utilised as cathodes when YSZ is used as the electrolyte. This is because LSC-related materials $Dy_{1-x}Sr_xCoO_3$ and $Sm_{1-x}Sr_xCoO_3$ reacted with YSZ to form $SrZrO_3$ after 96 hours at 900°C, as well as forming CoO at 1,000°C [19]. $La_{0.84}Sr_{0.16}CoO_3$ tends to react with YSZ to form $La_2Zr_2O_7$ and $SrZrO_3$ [20]. $Gd_{1-x}Sr_xCoO_3$ also reacts with YSZ, although there was no reaction observed for $GdCoO_3$ [21]. This implies that LSC-based materials are much more reactive towards YSZ than LSM, as LSM tends to form these reaction products at a higher temperature of 1,200+°C.

When using ceria-based electrolytes, however, LSC-based materials were found to be cathode of choice, as there was no sign of electrolyte-cathode reaction and this type of cathode showed better electrochemical performance than LSM with this type of electrolyte [20].

In addition to the LSC materials, there has also been research carried out on LSCF (Fe-doped LSC) as $Ln_{1-x}Sr_xCo_{1-y}Fe_yO_{3-\delta}$, where Ln represents a lanthanide (usually La, but research has been done using other lanthanides in its place). Like LSC, it does offer high conductivity, as $La_{1-x}Sr_xCo_{1-y}Fe_yO_{3-\delta}$ at 900°C had an electronic conductivity of 230 Scm^{-1} and ionic conductivity of 0.2 Scm^{-1}, along with a high oxygen diffusion coefficient [22, 23].

Another study indicated that $La_{1-x}Sr_xCo_{1-y}Fe_yO_3$ (with the ranges x= 0.2 – 0.4, y<0.8) has an electronic conductivity of 200 – 300 Scm^{-1} between 600 and 800°C [24]. It is possible to get even higher conductivity in LSCF, as $La_{0.84}Sr_{0.16}Co_{0.7}Fe_{0.3}O_3$ attained 643 Scm^{-1} at 800°C, as opposed to 115 Scm^{-1} from $La_{0.84}Sr_{0.16}Co_{0.3}Fe_{0.7}O_3$. This showed that increased Fe doping leads to reduced conductivity [25].

Further investigations involved a study of $La_{0.6-z}Sr_{0.4}Co_{0.2}Fe_{0.8}O_{3-\delta}$, $La_{0.6}Sr_{0.4-z}Co_{0.2}Fe_{0.8}O_{3-\delta}$, $(La_{0.6}Sr_{0.4})_{1-z}Co_{0.2}Fe_{0.8}O_{3-\delta}$, looking into the effect of A-site deficiency. It was found that conductivity increased with temperature up to 600°C, then dropped sharply at temperatures above 600°C, which was suspected to be due to lattice oxygen loss at those temperatures.

Also, when z (extent of A-site deficiency) increased, conductivity decreased and these factors led to the conclusion that the behaviour above 600°C was due to an alternative charge compensation mechanism. Usually, for a perovskite, the charge compensation mechanism for A-site deficiency is for the B-site cations to change from B^{3+} to B^{4+}, whereas for these systems, the mechanism involved is oxygen vacancy formation. Conductivity ranged from 166-417 Scm^{-1} at 700°C.

In studies on the $Ln_{1-x}Sr_xCo_{1-y}Fe_yO_{3-\delta}$ system, where Ln was Gd, Pr or Nd (x=0.2, 0.3), it also showed high electronic conductivity with increasing Fe content leading to reduced conductivity. The choice of lanthanide influenced conductivity as well. At 800°C, the conductivity of $Ln_{1-x}Sr_xCoO_{3-\delta}$ ranged from 825 – 2,154 Scm^{-1} (Ln = Pr or Nd, x=0.2, 0.3). For $Ln_{1-x}Sr_xFeO_{3-d}$, conductivity was ~68 Scm^{-1}. When Gd was used as the lanthanide, the conductivity was lower at 800°C. For $Gd_{0.8}Sr_{0.2}CoO_{3-\delta}$, conductivity was only 464 Scm^{-1} and ~10 Scm^{-1} for $Gd_{0.8}Sr_{0.2}FeO_{3-\delta}$. Despite this, the conductivities were higher than could be obtained for LSM [26].

Another important property that was investigated for $Ln_{1-x}Sr_xCo_{1-y}Fe_yO_{3-\delta}$ was the thermal expansion behaviour. One particular concern is that the thermal expansion coefficient (α) is very high for Co-rich compositions, especially at T>700°C. For the compositions containing no Fe, α is in the range 18-20*10^{-6} K^{-1} up to 1,000°C, although it is in the range 14-15.5*10^{-6} K^{-1} at 700°C [22, 26]. Thus, α is very high when compared to the electrolyte materials YSZ (10.5*10^{-6} K^{-1}) and $Gd_xCe_{1-x}O_{2-x/2}$ (12.5*10^{-6} K^{-1}). At high temperatures, the reason for the high α is that when Sr is present, Co is present as Co^{4+}, which is unstable at higher temperatures and may become Co^{3+}, leading to a lattice expansion and high α [26]. α

decreases with increasing Fe content to ~$14*10^{-6}$ K^{-1} for $La_{1-x}Sr_xCo_{0.2}Fe_{0.8}O_{3-\delta}$ at 700°C [22] and down to $12\pm0.5*10^{-6}$ K^{-1} for $Ln_{1-x}Sr_xFeO_{3-\delta}$ [26]. This brings α down much closer to the level of α for $Gd_xCe_{1-x}O_{2-x/2}$.

To conclude on LSC and LSCF, they appear to be very suitable as SOFC cathode materials for operating temperatures below 1,000°C (maybe even down to 600-700°C), due to their high ionic and electronic conductivity. YSZ cannot be used as an electrolyte, however, as LSC and LSCF can react with YSZ to form $La_2Zr_2O_7$ and $SrZrO_3$ at 900 – 1,000°C, in contrast to the less reactive LSM, that only reacts with YSZ at 1,200+°C. Doped ceria electrolytes tend to be used with LSC and LSCF, as they do not react.

Finally, while doping LSC with Fe reduces conductivity, LSCF still has sufficient conductivity to be suitable as a SOFC cathode, although LSCF also has an advantage of having a thermal expansion coefficient closer to that of the electrolyte.

There has been an attempt at using a non-perovskite material as a SOFC cathode, however. One system that has been investigated is $La_xSr_{2-x}FeO_{4+\delta}$, which has the K_2NiF_4-type structure [27]. The motivation behind this was to consider the suitability of materials that contain excess oxygen as interstitial oxide ions for SOFC systems.

Current investigations were centred on thermal stability and conductivity and it was found that the K_2NiF_4-type phase was stable up to 1,100°C in air or vacuum. Electronic conductivity was also found to increase with increasing oxygen content, where the conductivity was higher in air than for argon and higher in oxygen than for air. Ultimately, it was found that the materials warranted further investigation, as they were stable at temperatures higher than normal SOFC operating temperatures. That said, electronic and ionic conductivity are present in these materials but were not as high as would be desired for a cathode material. Further work on compositions could remedy this by tailoring the conductivity.

1.4.3: SOFC anode materials

The SOFC anode is the 'fuel electrode' and is involved in the oxidation of the fuel to its reaction products. The environment on this side of the fuel cell tends to be strongly reducing due to the nature of the fuel, which can be hydrocarbons, hydrogen or even carbon monoxide.

The main reactions at the anode tend to be as follows, depending on the fuel:

$H_2 + O^{2-} \rightarrow H_2O + 2e^-, CO + O^{2-} \rightarrow CO_2 + 2e^-$ or

$CH_4 + 4O^{2-} \rightarrow 2H_2O + CO_2 + 8e^-$

For suitable anode materials, it has been thought that the reducing conditions on the anode side of the SOFC should allow for the use of metals. The range of metals that could be suitable, however, is restricted to nickel, cobalt and noble metals, due to the typical SOFC operating temperature of 1,000°C and the required catalytic properties. The most commonly used metal used in anode materials is nickel, as it is fairly inexpensive, in relation to metals such as platinum and palladium [1].

There are some problems with using nickel on its own as an anode, however. One problem is that over long periods of time at 1,000°C, nickel would not remain porous. In order to alleviate this and other problems, the nickel is mixed with YSZ to form a ceramic/ metal composite or 'cermet'. YSZ has the effect of preventing the sintering of the nickel particles at 1,000°C and it also has the effect of reducing the thermal expansion coefficient of the resultant material to a level that is closer to that of the other cell components. Another advantage of YSZ is its oxide ion conductivity that assists in the electrochemical oxidation processes.

1.4.4: SOFC interconnect materials

The main purpose of the interconnect material is to separate the oxidant and fuel gases in the SOFC. The most common interconnect materials have tended to be Ca or Sr-doped Y or La chromites, as they tend to meet the majority of the stringent requirements placed on interconnect materials.

Usually the interconnect is in the form of a strip that runs along the length of the fuel cell, acting as an electric contact to the cathode, as well as protecting the cathode from the reducing environment on the fuel side of the SOFC [28, 29].

Principal requirements are that the interconnect must be stable in both reducing and oxidising environments, reasonable electronic conductivity (at least 1 Scm^{-1} at 1,000°C [30]), no ionic conductivity and a thermal expansion coefficient that matches other cell components. [28]

Ceramic Interconnect Materials

Doped lanthanum chromites tend to have p-type electronic conductivity due to small polaron hopping that has been observed at temperatures ranging from ambient to 1,400°C and

pO_2 levels down to 10^{-18} atm [29], as well as Cr^{4+} ion formation at high pO_2. Any ionic conductivity present is due to the formation of oxygen vacancies at low pO_2 [30]. Other oxides such as $YCrO_3$ have been tried as possible interconnection materials but they have not been as successful in deployment as lanthanum chromites.

There are some serious problems with doped lanthanum chromites that are incompatible with some of the general requirements for a SOFC component. Firstly, there is a thermal expansion mismatch with YSZ. YSZ has a thermal expansion coefficient of $10.3*10^{-6}$ K^{-1} between 350 and 1,000°C. In the case of $La_{0.99}Cr_{1-x}Mg_xO_3$, the thermal expansion coefficients of these materials were $9.4 - 9.5*10^{-6} K^{-1}$ ($x \leq 0.15$), which is lower than that of YSZ. In the case of $La_{0.99-x}Sr_xCrO_3$ (x=0.02 to 0.20), however, the thermal expansion coefficient increased with increasing Sr content from 10.2 to $11.1*10^{-6}$ K^{-1} [30]. Thus, it expands more than YSZ does.

Secondly, doped lanthanum chromites have difficulty sintering in oxidising environments. $LaCrO_3$ generally requires sintering conditions such as firing temperatures of up to 1,775°C at an oxygen activity level of 10^{-12} to 10^{-9}. These conditions are too extreme for co-sintering other components alongside, as there would be detrimental effects. Also, it would be rather expensive to co-sinter everything else under those conditions.

There has been considerable research in the field of using metals or metal alloys as SOFC interconnect materials, particularly for use at intermediate operating temperatures up to 800°C. One reason for using alternative interconnects at these temperatures is that the conductivity of doped $LaCrO_3$ is only enough at temperatures of >800°C [31]. Below 800°C, it is unsuitable as an interconnect, as the conductivity decreases substantially at lower temperatures [32]. Thus, doped $LaCrO_3$ would be unsuitable as an interconnect for an ITSOFC operating at 600-800°C.

Metallic Interconnect Materials

The use of metallic interconnects would get around some of the difficulties encountered in the design of planar SOFCs and the advent of the anode-supported planar SOFC allows an operating temperature of <800°C, a temperature at which metals or alloys could be used as interconnects [33].

In principle, metallic interconnects should offer many advantages over the ceramics. Firstly, metallic interconnects can easily fulfil the requirement of gas-impermeability, as it is much easier to fabricate a fully dense metal than it is for a ceramic. They also tend to have

bulk electrical conductivities that can be several orders of magnitude higher than those of ceramics, thus minimising internal resistance [34].

Other potential advantages are that metallic interconnects can have higher thermal conductivity, removing thermal gradients that can run along the plane of the interconnect and across the other SOFC components. Metals are also more able to withstand thermal stresses than ceramics, meaning that the requirement for matching thermal expansion coefficients between those of the interconnect and other cell components is not as strict in this case. [34]

With these metallic interconnects, one concern is resistance to corrosion reactions such as oxidation, sulphidation and carburisation. For oxidation, the formation of oxide scales on the surface is inevitable, as this is thermodynamically favourable [35]. The ideal situation is for a metallic interconnect to have sufficient oxidation resistance to last over the planned lifetime of the SOFC (~40,000 hours). Also, it is desirable that any oxide scale formed should have a high electronic conductivity, good chemical stability, slow growth rate and be well adhered to the substrate. Sulphidation can be less critical, as the sulphur-containing species can be scrubbed out by desulphurisation. This means that carburisation is the only other reaction of concern [33].

The reason why carburisation is of concern for metallic interconnects is that in reformed fuel gas containing CO or CO_2, these could react with the steel and form carbides, where large carbide particles forming along ferrite grain boundaries tends to make steel brittle and reduce the amount of Cr present. This is because Cr tends to be consumed in carbide formation, leading to less oxidation resistance, as there is less Cr available to form the oxidation-resistant Cr_2O_3 layer.

The carburisation of Fe-based steel was compared to Fe-based steel clad in Ni (to provide oxidation resistance) and this was tested by annealing the steels at 750°C for 1,000 hours in a reformed fuel environment containing CO and CO_2. The findings were contrary to what was predicted, as all of the steel was expected to have carburised. In reality, the Fe-based steel showed no signs of carburisation but the Ni-clad steel did. The reason for this was that the normal Fe-based steel was protected from carburisation by the Cr_2O_3 layer, which was not present on the Ni-clad steel and the layer acted as a barrier to carbon diffusion. [36]

Cr-rich alloys

One of the primary types of metallic interconnect is the Cr-based alloy. This type is favoured, as these alloys have a moderate level of oxidation resistance and good corrosion resistance. This is due to formation of thin oxide scales of Cr_2O_3, which has a low resistivity

at high temperatures (1,300 Ωcm at 25°C, 100 Ωcm at 800°C). Unfortunately, Cr_2O_3 has a growth rate of ~10,000 times that of Al_2O_3. So, one improvement in Cr-based alloys would be to obtain an acceptable compromise between enhanced electronic conductivity and low growth rate of oxide scale [33].

Cr-based alloys show similar thermal expansion to that of electrolyte material YSZ containing 8 mol% Y_2O_3, although with slightly higher thermal expansion coefficients, as found for the alloys named Cr-0.4La_2O_3 and Cr-5Fe-1Y_2O_3. It was also found that these alloys showed much less thermal expansion than stainless steels (α was up to $16*10^{-6}$ K^{-1} at 800°C for stainless steels) [37].

Addition of reactive metals such as Y, La, Ce or Zr (or their oxides) to Cr-based alloys improves resistance to oxidation by retarding the kinetics of the oxide scale formation process. In tests where the alloys were exposed to SOFC fuel and oxidant atmospheres, Y_2O_3-containing alloys showed very little mass gain. The corrosion studies also found that oxide scale forms faster in a H_2O/H_2 atmosphere than in air and that CO makes corrosion worse [33].

Despite the research that has gone into Cr-based alloys, they are not totally suitable for SOFC application above 700°C. It is suspected that there is a problem with long-term stability, in that these materials do not have sufficient oxidation resistance at 800°C or higher, even with the addition of reactive metals to increase oxidation resistance. Estimates on the growth of oxide scale on Cr-based alloys were based on oxidation studies on Ducrolloy (Cr-5Fe-1Y_2O_3) at 900°C. These studies estimated that the thickness of the scale would be 10 μm after 1 year and 23 μm after 5 years of operation at this temperature [38]. This is believed to be too much oxide scale growth for reliable operation as a SOFC interconnect. In terms of contact resistance, after oxidation at 1,000°C for 75 hours, there was such a thick layer of Cr_2O_3 scale that formed that it caused the ASR to be ~4 Ωcm^2 (considerably greater than the required level of 0.1 Ωcm^2) [39]. Thus, without a coating to reduce contact resistance, Ducrolloy was deemed to be unsuitable as an interconnect material.

There is another disadvantage with the Cr-based alloys, which is the potential for the formation of volatile Cr^{6+} species. The Cr_2O_3 protective scale tends to be formed in equilibrium with reactions that can form the volatile Cr^{6+} species when the Cr-based alloys are oxidised at high temperatures. This causes a particular problem in that the volatile Cr species tend to reduce the performance of the SOFC [38,40,41]. This is due to the volatile species reducing and depositing as Cr_2O_3 at the interface between the cathode and electrolyte.

This reduces performance by increasing concentration and activation polarisations. The reactions involved in Cr volatilisation and Cr_2O_3 deposition that reduces SOFC performance tend to involve the formation of the volatile $CrO_2(OH)_2$ from Cr_2O_3 and H_2O, followed by reduction at low pO_2 to reform Cr_2O_3 [42].

To overcome the Cr volatilisation problem, one suggested remedy is to coat a thin layer of doped $LaCrO_3$ onto the Cr-based alloy. This has the effect of reducing oxide scale thickness, as well as improving chemical compatibility with other cell components, provided the interfacial resistance does not go up too much. It was found that the volatilisation rate of Cr was reduced by a factor of 100 at 950°C for a Cr-5Fe-1Y_2O_3 alloy when a 30μm protective layer of Sr-doped $LaCrO_3$ was coated onto the surface [40].

Fe-rich alloys

Fe-based alloys are the other main type of potential metallic SOFC interconnect, as they are supposed to offer advantages over the Cr-based alloys by having higher ductility, better workability and being cheaper as well [33]. The main types of Fe-based alloys are Fe-Cr-Mn [43] and Fe-Cr-W [44] alloys, which have low thermal expansion coefficients. For protection against corrosion and oxidation, these alloys tend to contain 17% Cr by mass, so that it forms Cr_2O_3 scale. Unfortunately, this does confer the disadvantages that plague the Cr-based alloys, especially with Cr volatilisation [33].

The addition of other elements also affects the oxidation behaviour of the Fe-based alloys. When Ni was added, no Cr_2O_3 scale formed on the Fe-17Cr-0.4Y-2Ni alloy and at 800 °C there was a large mass gain after oxidation. When Ti was added, a large mass gain was observed for the Fe-25Cr-0.1Y-2.5Ti alloy, although Ti is supposed to assist in the formation of oxide scale. Due to these large mass gains observed for the Ti and Ni-containing alloys, Ti and Ni were deemed to be unsuitable as additives.

The addition of Mn promotes the oxidation process, as the Fe-25Cr-0.2Y-1.6Mn and Fe-17Cr-0.2Y-1Mn alloys showed greater mass gains than equivalent Mn-free alloys. It also has the effect of forming surface scales of Cr_2MnO_4 or other spinels on top of the Cr_2O_3 layer. Thus, the addition of Mn leads to increased thickness of surface scales, although the resistance of the scales is lowered, as the Cr/Mn spinels have lower resistance than Cr_2O_3. Y tends to retard the oxidation kinetics of Fe-based alloys, as Fe-25Cr-0.2Y and Fe-17Cr-0.2Y alloys showed very little mass gains even after 1,000 hours at 800°C. This means that the addition of reactive elements suppresses the growth of oxide scale. [33]

The addition of Zr or Al to the alloy was also found to improve oxidation resistance. The cause of the enhanced oxidation resistance for Al additions was found to be due to the formation of Al_2O_3 scales, although it has been suggested that no more than 1% Al by mass be added, in order to prevent the formation of a continuous Al_2O_3 layer, which is an insulator. For the Fe-based alloys, the thermal expansion can be close to that of YSZ, as the alloy Fe18Cr9W showed promise, in having a thermal expansion coefficient of $11*10^{-6}$ K^{-1}, close to that of YSZ (8 mol% Y_2O_3) [43,44]. Generally, Fe-Cr alloys tend to show thermal expansion coefficients of $9\text{-}12*10^{-6}$ K^{-1} [31].

Another curiosity of the Fe18Cr9W alloy is that at 1,000°C, a duplex layer of $CrMnO_2$ spinel and Cr_2O_3 forms at the alloy/ cathode interface with LSM as the cathode. This could imply that the alloy could react with LSM at 1,000°C [44].

Finally, the resistance of the Fe-Cr alloy was compared to that of the doped $LaSrCrO_3$ ceramic interconnect. In this case, a Fe-16Cr alloy was used and it was found that in addition to the normal Cr_2O_3 scales, there was also a very thin, discontinuous layer due to $MnCr_2O_4$ [45]. One important consideration for a metallic interconnect is that it has low electrical resistivity across its protective oxide layer. In the determination of the alloy resistivity, it was unaffected by the presence of the $MnCr_2O_4$, which has a lower resistivity than Cr_2O_3 and the contribution of any Al_2O_3 was also ignored, as it was judged that the Al concentration was too low for external oxidation or formation of Al_2O_3 precipitates to have any effect. So, the resistivity of the alloy was assumed to be that of Cr_2O_3.

The resistivity of the Fe-Cr alloy (Cr_2O_3) was higher in air than in H_2/ H_2O at 800°C, although it was higher than that of a 0.5cm thick $La_{0.85}Sr_{0.15}CrO_3$ ceramic (38 $m\Omega cm^2$ in air, 60 $m\Omega cm^2$ in H_2/H_2O) after 100 hours in H_2/ H_2O and after 1,000 hours in air at 800°C, rising with increasing annealing time. This implies that the Fe-16Cr alloy would be unsuitable as a SOFC interconnect by itself unless there was surface modification.

For an oxidised metallic interconnect, the contact resistance is expressed in terms of ASR (area specific resistance/ Ωcm^2), defined as the resistivity and thickness of the layer of interest multiplied by each other. The acceptable level of ASR for an interconnect is usually <0.1 Ωcm^2 [34].

This was remedied when the alloy had a layer of $La_{0.6}Sr_{0.4}CoO_3$ applied by spray pyrolysis coating. The resistivity of the coated Fe-Cr alloy did not increase with increasing annealing time and it was measured as 20 $m\Omega cm^2$ in air and 45 $m\Omega cm^2$ in H_2/H_2O at 800°C. This is less than that of the $La_{0.85}Sr_{0.15}CrO_3$ ceramic but it is still higher than that of a Ni-20Cr

alloy coated with (La, Sr)CoO_3, which had a resistivity of <5 mΩcm^2 even after heating in air at 1,000°C for 1,200 hours [46]. Thus, metal alloys could be used as potential SOFC interconnect materials at temperatures below 800°C, in the place of doped $LaCrO_3$.

1.5: Types of SOFC design

1.5.1: Tubular design

Figure 1.2 illustrates a schematic of the tubular SOFC design, by Siemens Westinghouse [5, 47]. In this type of cell, the main support is the cathode tube made from doped lanthanum manganite, made by extrusion and sintering. Then, the other components are deposited as thin layers onto the cathode tube, which can account for most of the mass of the cell. For example, the electrolyte (YSZ) is deposited by electrochemical vapour deposition as a dense layer that is ~40μm thick [48].

The anode (Ni/YSZ) can be applied in one of two ways. The first way is the application of nickel slurry, followed by EVD of YSZ. The second way is to sinter Ni/YSZ slurry onto the tube. The interconnection is produced as a strip of doped lanthanum chromite that is deposited along the length of the cell by plasma spraying [49].

Extensive testing of tubular SOFC systems has found that they can perform satisfactorily running for long periods of time (25,000+ hours [47]) under various types of operating conditions and have shown levels of performance degradation of <0.1% per 1,000 hours of continuous use. The power density of a typical tubular cell has been measured at 1,000°C to be in the region of 250-300 mWcm^{-2}. This power density is fairly low, however, and it is most likely that the tubular SOFC system is only suitable for stationary power generators and not for transport.

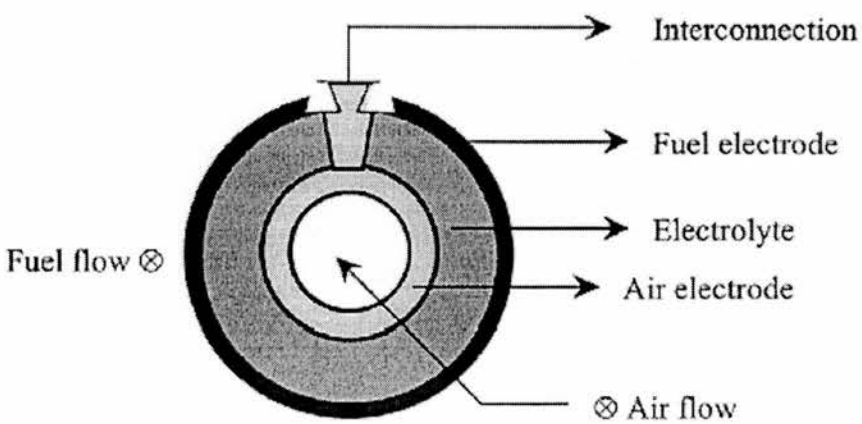

Figure 1.2: Design of a tubular SOFC [5]

1.5.2: Planar SOFC systems

The planar design is the other most commonly used SOFC design. In contrast to the tubular systems, planar SOFCs claim to be able to offer greater power densities in the order of ~2 W cm^{-2} [50, 51]. In the most general version of the planar SOFC, the cell components are thin, flat plates. The interconnection tends to be ribbed on both sides, which forms gas flow channels and can also be used as a bipolar gas separator that makes a contact between the anode of one cell and the cathode of the next cell. Fabrication involves fairly inexpensive techniques such as tape casting, slurry sintering, screen-printing or plasma spraying. A typical planar SOFC design is illustrated in Figure 1.3 [5]

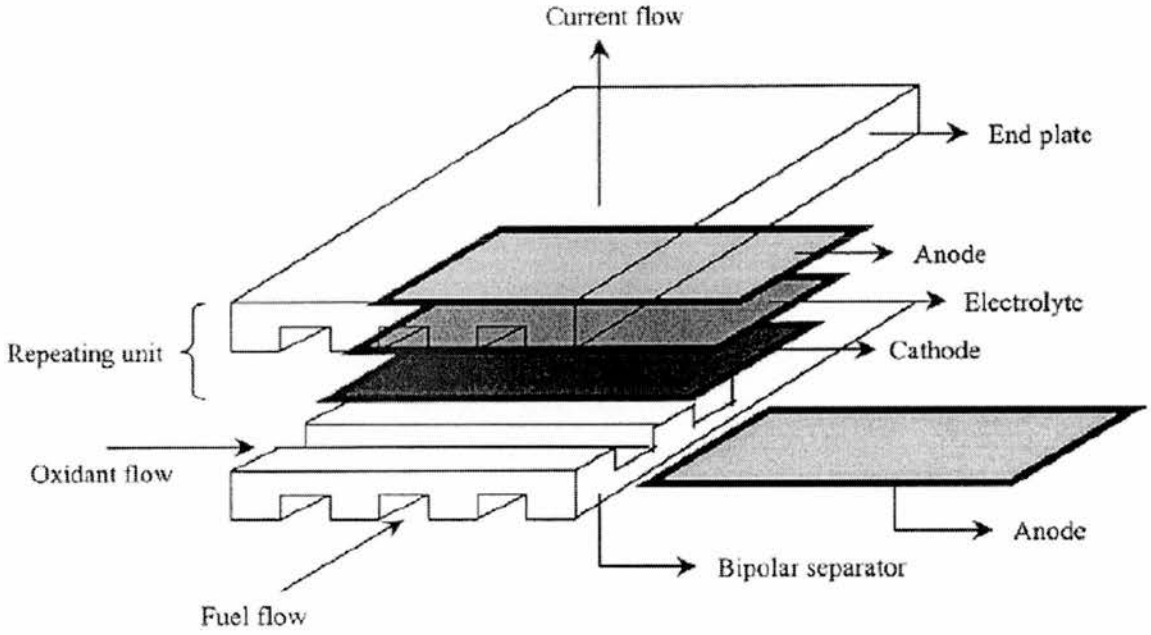

Figure 1.3: Typical planar SOFC design [5]

While the most common types of planar cells tend to be electrolyte-supported, this has one main disadvantage. The electrolyte in the electrolyte-supported cell tends to be a ~150μm thick YSZ layer. This leads to a large ohmic resistance and restricts the operating temperature to ~1,000°C.

Electrode-supported planar SOFC cells are under development. The main reason for trying to develop an electrode-supported cell is that the electrolyte layer can be made much thinner (down to 5-20μm). This should reduce the ohmic resistance of the electrolyte, allowing the cell to operate at a lower of ~800°C.

The preferred type of electrode-supported planar SOFC is anode-supported. The typical anode in this system is Ni/YSZ. The benefits of using the anode as the support are as

follows: It should lead to better thermal and electrical conductivity, improved mechanical strength and minimises support-electrolyte chemical interactions. In testing, planar anode-supported SOFCs have yielded power densities up to 1.8 Wcm^{-2} at 800°C [50]. Another development in this type of system is a cell where the anode and electrolyte are tape cast, laminated together and co-fired at 1,350°C [52]. In this case, the electrolyte layer is ~10μm thick and the anode layer is ~600μm thick.

The cathode used can be made of LSM, LSM / YSZ composite or LSF (lanthanum strontium ferrite), screen printed onto the electrolyte, then sintered. In a cell that used a LSF cathode with a $Sm_{0.2}Ce_{0.8}O_{1.9}$ layer between cathode and electrolyte, it yielded a power density of ~1 Wcm^{-2} at 800°C. The oxidant used was air and the fuel was a 97% H_2/ 3% H_2O mixture [53].

The final consideration on the performance of planar SOFCs is that the microstructure of the cathode and cathode/ electrolyte interface has a considerable effect on performance. It is believed that optimisation of microstructures would lead to higher levels of performance and stability.

Finally, there is another type of planar SOFC design called 'radial planar', as shown in Figure 1.4 [5]. In this design, the appearance of the cell is like a CD, where the oxidant and fuel do not flow along the electrode surfaces but tend to diffuse through the porous electrodes from the centre of the disk out towards the periphery.

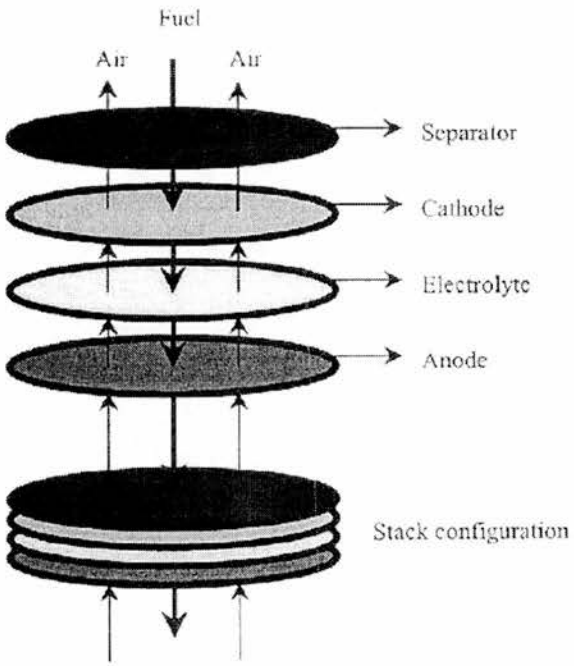

Figure 1.4: Typical radial planar SOFC design [5].

1.6: Effect of impurities on SOFC performance

Studies have been carried out on the effect of gaseous impurities that may be present in the fuel or oxidant gases, such as SO_2, moisture, NH_3 and H_2S. In the long term, SOFCs can tolerate small levels of these impurities without significant problems. [29]
The effect of moisture in the oxidant gas was just a slight decrease in voltage, caused by a drop in pO_2. Deliberately adding water into the fuel gas can enhance the performance of a SOFC anode considerably. This will significantly decrease voltage due to an increase in pO_2. Sulphur dioxide did not appear to cause any problems either.

Ammonia acts as a fuel. The presence of H_2S, however, in the fuel gas can hinder performance [54]. At a H_2S concentration of 1 ppm, after 24 hours of testing, the cell voltage fell 10% and fell further over time. When the H_2S was removed from the fuel, the detrimental effects caused by the H_2S also disappeared. This indicates that the effect of H_2S on performance is either totally or partially reversible [29, 54].

The characteristics of sulphur poisoning on SOFCs are that polarization impedance and DC over-voltage increased with H_2S concentrations exceeding 0.05 ppm at 750°C, 0.5 ppm at 900°C and 2 ppm at 1,000°C.

The amount of time taken for the effect of the sulphur impurity to fully saturate was independent of sulphide concentration. Also, the poisoning effect appears to be temperature dependent, as the amount of time for poisoning to saturate decreased from 200 minutes at 750°C to 67 minutes at 1,000°C. In addition, when the sulphide impurity was removed from the fuel gas, the amount of time taken for the system to recover from the performance losses due to the sulphur poisoning was also temperature dependent, ranging from 67 minutes at 1,000°C to 100 hours at 750°C. [54]

Thus, if SOFC developers come up with new systems that can operate at lower temperatures using natural gas as fuel, then they may need to employ a high-grade desulphurization unit to remove sulphur compounds in the fuel, before it is admitted into the fuel cell. This is important, as sulphur-containing compounds are added deliberately to natural gas supplies used by domestic customers, to give the gas an odour to assist in identifying whether or not there is a gas leak [54].

1.7: Interest in YZT

The 'state of the art' SOFC anode, Ni-YSZ, cannot utilise hydrocarbon fuels directly and requires that the hydrocarbons be steam reformed releasing hydrogen that can be utilised.

An alternative would be to develop an anode material that can use dry methane as a fuel directly, eliminating the need for steam reforming. Such anodes could be made of materials called MIEC (mixed ionic-electronic conducting) oxides. It is believed that lattice oxygen is active in the oxidation of hydrocarbons and that the mixture of ionic and electronic conductivity widens the electro-active region by allowing oxide ions to reach throughout the entire anode/gas interface.

One category of MIEC material is doped stabilised zirconia, where electronic conductivity is due to a multivalent dopant. Thus, this is where the interest in YZT (TiO_2-doped YSZ) lies. YZT materials are stable at high temperatures, compatible with YSZ in chemical and thermomechanical terms and have a high electro catalytic activity [55]. The presence of TiO_2 exhibits electronic conduction that can be imparted upon addition to YSZ. Thus, YZT would yield mixed conduction. Also, it would not suffer from some of the problems associated with other materials such as LSM that can react with YSZ to form $La_2Zr_2O_7$ and $SrZrO_3$, causing deterioration of the electrolyte [7].

Investigations on YZT have shown that it is possible to achieve good electrochemical performance with these materials, even though these cubic fluorite materials have poor electronic conductivity. Low electrochemical resistances from these materials show the benefit of having good oxide ion availability. [56]

The following defect model explains the electronic conductivity of YZT [57].

At low pO_2, oxygen is released from YZT, as shown below, generating oxygen vacancies.

$$O_O^x \leftrightarrow [V_O^{\cdot\cdot}] + 2e^- + \tfrac{1}{2} O_2(g)$$

The electrons released by this process are trapped by Ti^{4+} ions that change their valence state from 4+ to 3+ and the overall process can be expressed as:

$$2[Ti_{Zr}^x] + O_O^x \leftrightarrow 2[Ti_{Zr}^{'}] + [V_O^{\cdot\cdot}] + \tfrac{1}{2} O_2$$

The condition for electroneutrality for this situation is $[Ti_{Zr}^{'}] = 2[V_O^{\cdot\cdot}]$ and generally, electronic conduction of YZT is due to a small polaron hopping mechanism where trapped electrons hop between Ti^{4+} and Ti^{3+} ions.

Also, at temperatures above 1,000°C, pO_2-dependence studies show that total conductivity increases with decreasing pO_2 and the effect is more pronounced with increasing TiO_2 content. In addition, this effect starts to develop at higher pO_2 levels when the temperature is increased. At temperatures below 1,000°C, electronic conductivity is lower. Thus, at low pO_2, YZT shows n-type electronic conductivity.

Mixed ionic-electronic conductivity [58]

It appears that mixed conductivity is important in SOFC cathodes, as the reduction of oxygen occurs over the entire electrode surface, where ions and electrons are mobile, as opposed to the case of solely electronic conductors, where this reaction is restricted to the gas-electrode-electrolyte interface. As the entire electrode surface area can be used for the charge transfer reaction, this would lead to a significant reduction in polarization losses at the electrode/electrolyte interface.

One mixed conductivity system is the YZT system, where the presence of TiO_2 increases the amount of electronic conductivity in YSZ, an oxide ion conductor. Other transition metal/lanthanide dopants have included ceria, terbia, iron and nickel and they can impart either p-type or n-type electronic conductivity into YSZ [59].

Doping one material with another is one way of altering the extent of ionic and electronic conductivity. It is thought that another could be through dispersal of oxide particles instead. It is believed that the optimum SOFC performance could be obtained through using the same oxide material in both electrode and electrolyte. This can only work through appropriate doping to control the ionic and electronic contributions to conductivity. While there may be some work in this direction, the general case for SOFCs is to use YSZ as the electrolyte and $LaMnO_3$ as the cathode. As has been said, there appears to be promise in the use of YZT as an anode component. [60]

1.8: Doping with ceria

Interest in ceria is that it has been used as a catalyst for partial or complete oxidation of hydrocarbons. This is because its lattice can contain a lot of oxygen vacancies, acting as an oxygen sink for reactions occurring at its surface or at the surface of a ceria-supported catalyst. In particular, there is interest in ceria-based SOFC anodes for using fuels such as methanol, methane or 'syngas' because it resists carbon deposition and can be used as a catalyst for carbon combustion. In terms of internal reforming, ceria is a less active catalyst than nickel. Thus, a ceria-based catalyst/ anode has advantages over a conventional nickel catalyst.

Firstly, carbon deposition does not reduce the catalytic activity of ceria, as is the case for nickel, when hydrocarbons are used as fuel. Secondly, the fact that ceria is a less active catalyst for internal steam reforming than nickel is actually an advantage. This is because nickel is too active for reforming, in that it can cause problems in the SOFC because

temperature gradients can form within the system, due to reforming being a strongly endothermic process. These internal temperature gradients cause damage to ceramics by thermal shock fractures.

One of the most investigated types of ceria-based SOFC materials has been gadolinia-doped ceria ($Gd_xCe_{1-x}O_{2-x/2}$) [61]. The structure of ceria is cubic fluorite, just like the cubic phase of ZrO_2, as attained through stabilisation or at very high temperature without stabilisation [62]. The fluorite structure is very tolerant to considerable doping and reduction without changing phase. Also, ceria does not experience any phase transitions between room temperature and its melting point (2,477°C). It is pale yellow in colour, due to a Ce^{4+}-O^{2-} electronic transition. When reduced, $CeO_{2-\delta}$ can change to a blue or black colour when deviating from normal stoichiometry. Pure CeO_2 has a unit cell parameter of 5.411 Å. Also, α, the linear thermal expansion coefficient has been measured as $11*10^{-6}$ K^{-1} at room temperature, rising to $12*10^{-6}$ K^{-1} at 1,000°C. [63]

Unlike zirconia, ceria is classed as a mixed conductor. At high temperatures and low pO_2 levels, there is reduction equilibrium between Ce^{3+} and Ce^{4+} that controls the amount of oxygen vacancies present and makes a significant number of charge carriers available. At temperatures above 700°C, non-stoichiometric ceria ($CeO_{2-\delta}$) is an oxygen-deficient n-type semiconductor between 200 and 1,300°C. Overall, the conductivity of ceria is a mix of n-type electronic and oxide ion conduction. The presence of impurities would affect the concentration of electronic carriers and thus, affect the absolute conductivity. The charge carriers present in $CeO_{2-\delta}$ are small polarons. [63]

1.9: Ceria-zirconia system

There have been some studies carried out on the CeO_2-ZrO_2 [62] and the Y_2O_3-ZrO_2-CeO_2 systems [59]. It is well known that the tetragonal and cubic phases of zirconia can be stabilised to room temperature by doping with either alkaline earth or lanthanide oxides. (This means that these phases can be attained without going to the high temperatures required for them to be attained by undoped zirconia) [59]. In the CeO_2-ZrO_2 system, the structure of the resultant solid solution depends on the CeO_2 concentration [62].

Solid solutions containing up to 50 mol% CeO_2 have tetragonal structures. This can be subdivided further, as those containing 24-48 mol% CeO_2 comprise of two tetragonal phases, called T° and T', whereas those containing at least 16 mol% CeO_2 only have one tetragonal phase, T°. Those containing at least 50 mol% CeO_2 have the cubic fluorite structure.

The resultant solid solutions have mechanical properties comparable to those of the Y_2O_3-ZrO_2 system. While the mechanisms for the stabilisation of ZrO_2 by lanthanide or alkaline earth oxides are known, the same cannot be said for the CeO_2-ZrO_2 system, where it is most likely due to the fact that the Ce^{4+} cation is much larger than the Zr^{4+} cation. One reason for this is that the dopant has the same valence as the cation it replaces, meaning that the electroneutrality of the material is not affected. The number of oxygen vacancies in ZrO_2 (anti-Frenkel defects) is not affected either [62].

In terms of conductivity, the CeO_2-ZrO_2 materials exhibit significant electronic conductivity, whereas conventional stabilised zirconias tend to be ionic conductors only. Conductivity studies on the ZrO_2-CeO_2 system containing 16- 90 mol% CeO_2 indicated that ionic conductivity was independent of both CeO_2 concentration and structure type (cubic or tetragonal). It was actually predicted that the number of electronic and ionic defects present in the materials would be constant between 500-1,000°C over a pO_2 range of $1\text{-}10^{-6}$ atm. Arrhenius plots of bulk conductivities are shown in Figure 1.5 (tetragonal) and 1.6 (cubic), with Arrhenius parameters shown in Table 1.1.

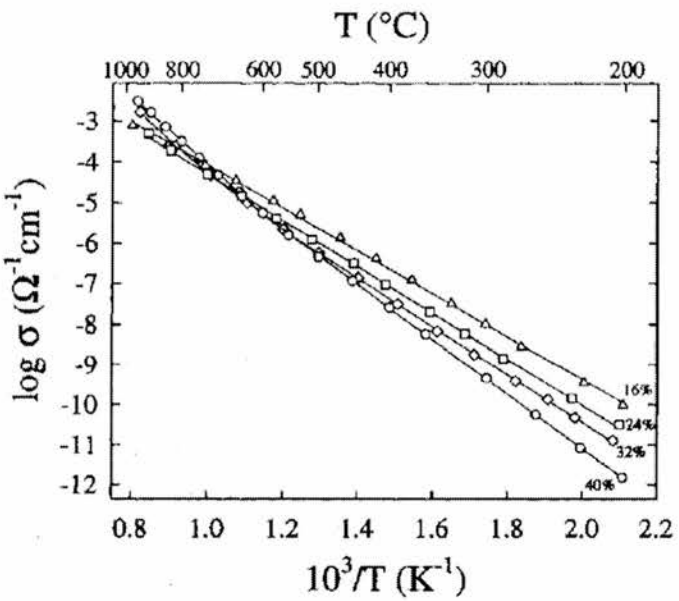

Figure 1.5: Arrhenius plots of tetragonal CeO_2-ZrO_2 solid solutions [62]. Numbers in this diagram refer to CeO_2 concentration in mol%.

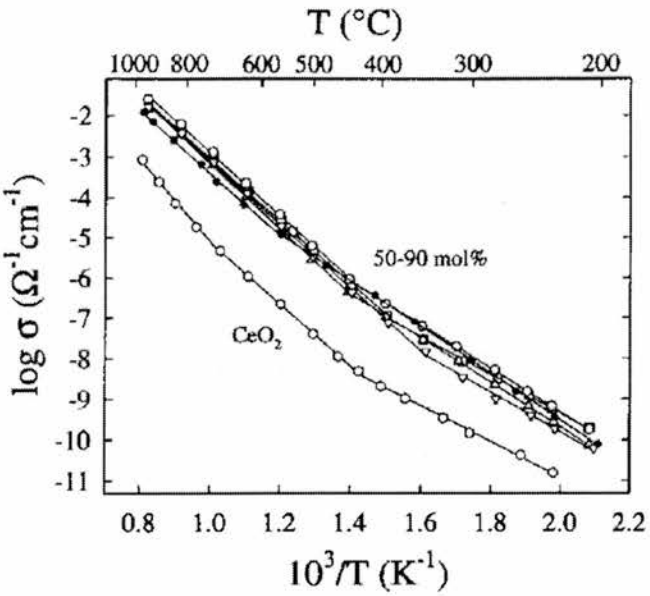

Figure 1.6: Arrhenius plots of cubic CeO_2-ZrO_2 solid solutions [62]

Table 1.1: Arrhenius parameters for CeO_2-ZrO_2 system [62]

CeO_2 content/ mol%	Low Temp E_{act}/ eV	A/ Scm^{-1}	High Temp E_{act}/ eV	A/ Scm^{-1}
16	1.042	14.4	-	-
24	1.140	27.6	-	-
32	1.200	45.0	1.700	$2.0*10^4$
40	1.340	260.0	1.670	$2.1*10^4$
50	1.140	90.1	1.560	$2.5*10^4$
60	1.080	15.0	1.606	$8.0*10^4$
70	1.052	19.2	1.550	$7.9*10^4$
80	0.910	0.60	1.530	$4.3*10^4$
90	0.910	0.30	1.580	$6.9*10^4$
100	0.860	0.01	2.010	$1.1*10^5$

Bulk conductivities of tetragonal CeO_2-ZrO_2 at 1,000°C were in the range $10^{-3} - 10^{-2}$ Scm^{-1}. The activation energy increased with increasing CeO_2 content from 1.04 to 1.34 eV in the 16-40 mol% CeO_2 range. The ionic conductivity range of the cubic solid solutions at 1,000°C (50-90 mol% CeO_2) was $10^{-2} - 0.1$ Scm^{-1}. The activation energy at low temperature decreased with increasing CeO_2 content from 1.140 to 0.91 eV. At high temperatures, the activation energy was 1.60 ± 0.1 eV.

For these CeO_2-ZrO_2 solid solutions, the bulk conductivity is a combination of electronic and ionic contributions [64]. The nature of the electronic contribution changes with temperature. Between 400-750°C, it is p-type, due to electron holes introduced by impurities of lower valency like Ca^{2+}. At above 750°C, there is a transition from p-type to n-type conductivity, with electrons being the charge carriers, localised in the Ce ions, whose concentration increases with increasing temperature, due to increasing deviation from oxygen

stoichiometry [62, 65]. Thus, this transition in electronic conductivity causes the change in activation energy at high temperatures.

Compared to pure CeO_2, the conductivities of the cubic solid solutions were between 1 and 2 orders of magnitude higher. CeO_2 also had the lowest activation energy (0.86 eV) at low temperature and the highest activation energy (2.01 eV) at high temperature.

Electronic conductivities changed in pO_2 dependence with temperature, as measured from 650-1,000°C, where log σ vs. log pO_2 exhibited a slope of -1/4 at 650°C, decreasing with increasing temperature to -1/5 at 950°C. This was in line with what has been reported about the behaviour of non-stoichiometric $CeO_{2-\delta}$ and can be explained in a similar fashion. The assumption taken is that as temperature increases, more electrons become localised on the cerium ions, due to changing oxygen stoichiometry. [62]

In the case of the CeO_2-Y_2O_3-ZrO_2 or CeO_2-YSZ system, studies have been carried out on CeO_2-doped 8 mol% YSZ, $Ce_xZr_{1-x}Y_{0.16}O_{2.24}$ or $(CeO_2)_x (ZrO_2)_{1-x} (Y_2O_3)_{0.08}$, where x ranged from 0 to 0.3 [59]. The conductivity of the 8 mol% YSZ was compared to the CeO_2-doped samples over a pO_2 range from 1 to 10^{-17} atm. Compared to YSZ, the composition where x=0.1 showed a lower ionic conductivity at 1,000°C ($8.6*10^{-2}$ Scm^{-1} compared to 0.14 Scm^{-1} for YSZ). Then, at lower pO_2 ($<10^{-10}$ atm at 1,000°C), the conductivity falls dramatically below the plateau.

With higher Ce content, where x=0.2 and 0.3, there is a change in the σ/pO_2 behaviour. The ionic conductivity at 1,000°C falls further ($5.6*10^{-2}$ Scm^{-1} for x=0.2 and $4*10^{-3}$ Scm^{-1} for x=0.3). Then, this pO_2-independent ionic conductivity was replaced by electronic conductivity in reducing atmospheres at x=0.2 and 0.3, although there is a pO_2 level where the conductivity reaches a maximum, then it falls sharply below that pO_2 level. The pO_2 range for ionic conductivity narrows with increasing CeO_2 content. This is illustrated in Figures 1.7-1.9, representing plots of σ with pO_2 for $(CeO_2)_x (ZrO_2)_{1-x} (Y_2O_3)_{0.08}$ for x=0.1 (1.7), 0.2 (1.8) and 0.3 (1.8), respectively.

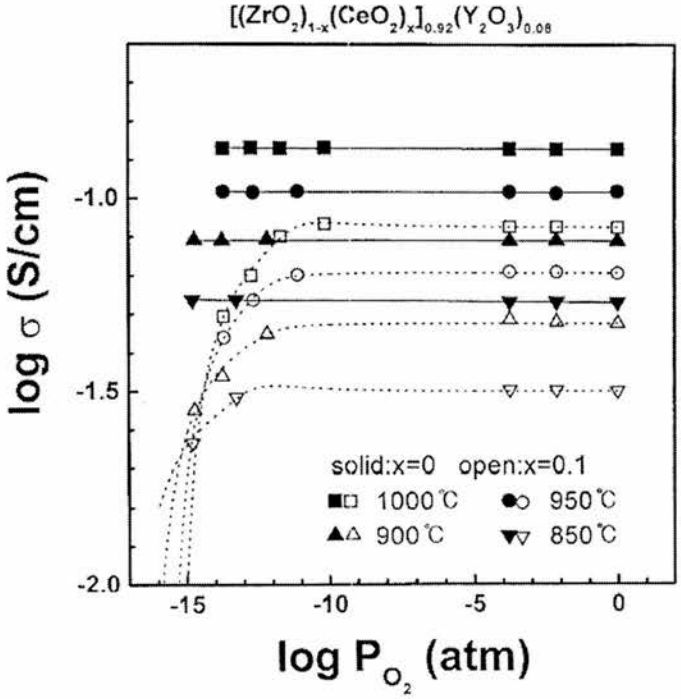

Figure 1.7: Conductivity of $(CeO_2)_x (ZrO_2)_{1-x} (Y_2O_3)_{0.08}$ (x=0, 0.1) vs. pO_2 [59].

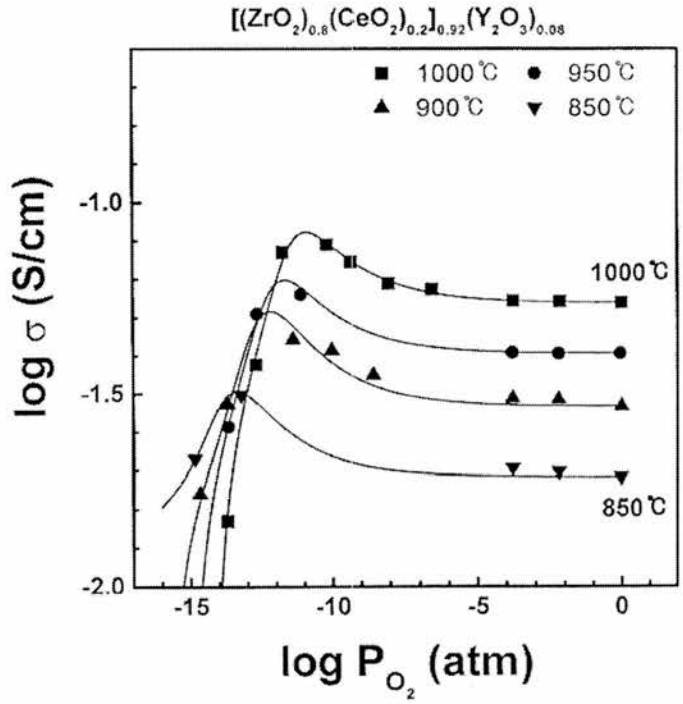

Figure 1.8: Conductivity of $(CeO_2)_{0.2}(ZrO_2)_{0.8}(Y_2O_3)_{0.08}$ vs. pO_2 [59].

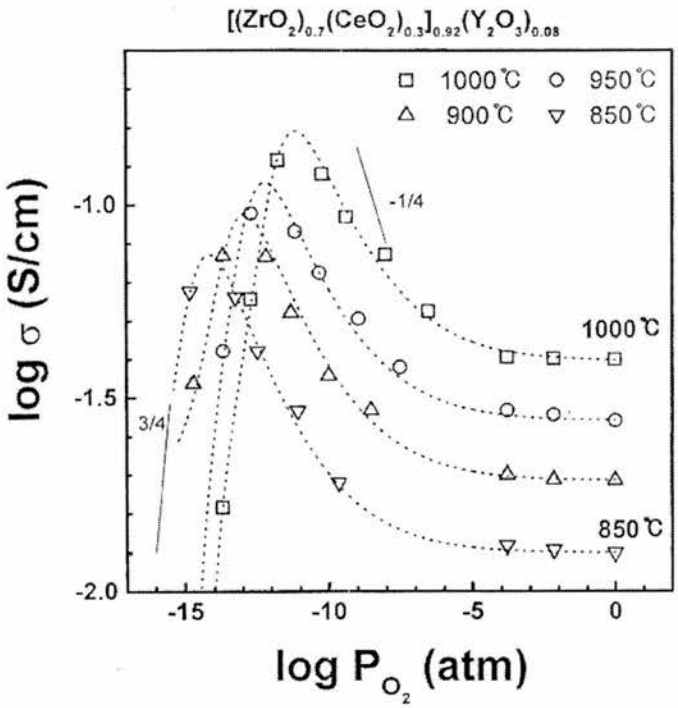

Figure 1.9: Conductivity of $(CeO_2)_{0.3}(ZrO_2)_{0.7}(Y_2O_3)_{0.08}$ vs. pO_2 [59].

For compositions where x=0 to 0.5, conductivity falls with increasing Ce content, although it was suggested that the reason for this was structural, as opposed to a change in charge carrier concentration. This was suggested, as the pre-exponential factors ranged from $5*10^5$ to $1*10^6$, suggesting that the charge carrier concentrations did not differ significantly. The activation energy, however, increased with increasing Ce composition from 0.89 eV (x=0) to 1.16 eV (x=0.5), which is indicative of species mobility getting worse with increasing Ce content.

Overall, it was concluded that the large conductivity fall at low pO_2 was due to a combination of both ionic and electronic conductivity decreasing. The falling electronic conductivity was also believed to be due to a fall in the amount of hopping carriers and falling electron mobility.

Structural investigation of this system looked at whether or not the conductivity behaviour was due to the formation of a secondary phase caused by Ce addition. The unit cell of the $(CeO_2)_x(ZrO_2)_{1-x}(Y_2O_3)_{0.08}$ system increased with increasing Ce content in a linear fashion from 5.14Å where x=0 (no Ce present) to 5.224Å where x=0.30, implying that the solubility limit for Ce had not been reached for this system [59]. Hence, there did not appear to be a second phase formed by the addition of CeO_2 into YSZ. Annealing at 10^{-15} atm pO_2 showed that reduction did not cause the formation of secondary phases either.

Other investigations into the CeO_2-YSZ system were centred on comparing the conductivity of 12 mol% CeO_2-ZrO_2 with 12 mol% CeO_2-ZrO_2 doped with Y_2O_3 [66]. For undoped 12 mol% CeO_2-ZrO_2, the ionic conductivity ranged from $9*10^{-4}$ Scm^{-1} at 800°C to $5*10^{-3}$ Scm^{-1} at 1,100°C. The EDB (electrolytic domain boundary), which is the onset of electronic conductivity, shifts to higher pO_2 with higher temperature from 10^{-12} atm at 800°C to 10^{-7} atm at 1,100°C.

For the 12 mol% CeO_2-ZrO_2-Y_2O_3 materials, adding just 2 mol% Y_2O_3 had significant effects on the conductivity/ pO_2 behaviour, as the conductivity was increased at least tenfold (0.01 Scm^{-1} at 800°C and 0.06 Scm^{-1} at 1,100°C). Also, the onset of electronic conductivity was shifted down to a lower pO_2 ($\sim10^{-17}$ atm at 800°C). Generally, the presence of Y_2O_3 increased ionic conductivity and extended the ionic domain to $\sim10^{-17}$ atm pO_2.

The effect of increasing Y_2O_3 content was to increase ionic conductivity until it reached a maximum of ~0.1 Scm^{-1} at 1,100°C at the saturation point, which was at 7-12 mol% Y_2O_3, followed by decreasing conductivity at Y_2O_3 levels beyond this point (Conductivities were still higher than for the composition containing no Y_2O_3). Activation energies were mostly independent of Y_2O_3 concentration below 14 mol%. Between 0 and 14 mol% Y_2O_3 content, E_{act} ranged from 0.9 - 1 eV, followed by a rise to 1.5 eV at the 18 mol% Y_2O_3 level. It is believed that CeO_2 has a role in this, in that it may be reducing defect association or altering the energy of defect migration in this system and this reduces the conductivity drop present at high doping concentrations [66].

The overall findings of this investigation into the CeO_2-ZrO_2 and CeO_2-YSZ systems indicated that in the CeO_2-ZrO_2 system, ionic conductivity was due to oxygen vacancy formation encouraged by the size effect caused by the Ce^{4+} ions being larger than Zr^{4+} ions. For the CeO_2-YSZ system, the effects were due to the trivalent Y^{3+} cations replacing tetravalent cations, leading to the creation of additional oxygen vacancies to maintain electro neutrality, enhancing ionic conductivity and electrolytic stability.

1.10: Aims of this work

The aim of this work is to examine the effect(s) of doping with ceria on a particular YZT material. The starting point was YZT with the formula $Y_{0.20}Zr_{0.62}Ti_{0.18}O_{1.90}$.
The CeO_2-doped YZTs, also known as YZTC compounds involve the substitution of one or more of the YZT components with cerium and were of the form YZTC: $Y_{0.20-x}Zr_{0.62-y}Ti_{0.18-z}Ce_{x+y+z}O_{1.9+x/2}$.

There were deliberate reasons for choosing $Y_{0.20}Zr_{0.62}Ti_{0.18}O_{1.90}$ as a starting point. Out of a range of YZTs, σ_e was at a maximum when the Ti content was 18 at%. (0.18 Scm^{-1} at low pO_2). Ionic conductivity was 0.01 Scm^{-1} for a composition containing 20 at% Y (Conductivities were measured at 930°C in a 97% H_2-3% H_2O atmosphere, corresponding to an effective pO_2 of 10^{-19} atm [55]). Finally, it is believed that doping YZT with ceria could pose some interesting challenges.

Firstly, will the YZTC materials maintain the cubic fluorite structure?

This is important, as the common SOFC electrolyte is YSZ, another cubic fluorite material. Thus, if a YZTC or YZTC-based cermet was to be used as a SOFC anode and it kept the cubic structure, then it would be compatible with the YSZ electrolyte.

Previous studies on adding TiO_2 and CeO_2 separately into Y_2O_3-ZrO_2 have indicated that there is a fairly extensive cubic fluorite region in the Y_2O_3-ZrO_2-CeO_2 system, although for the Y_2O_3-ZrO_2-TiO_2 system, the cubic phase is limited to 15-60 at% Y and up to 20 at% Ti. The extent of cubic phase formation of these ternary systems is shown in Figures 1.10 [67] and 1.11 [68, 69].

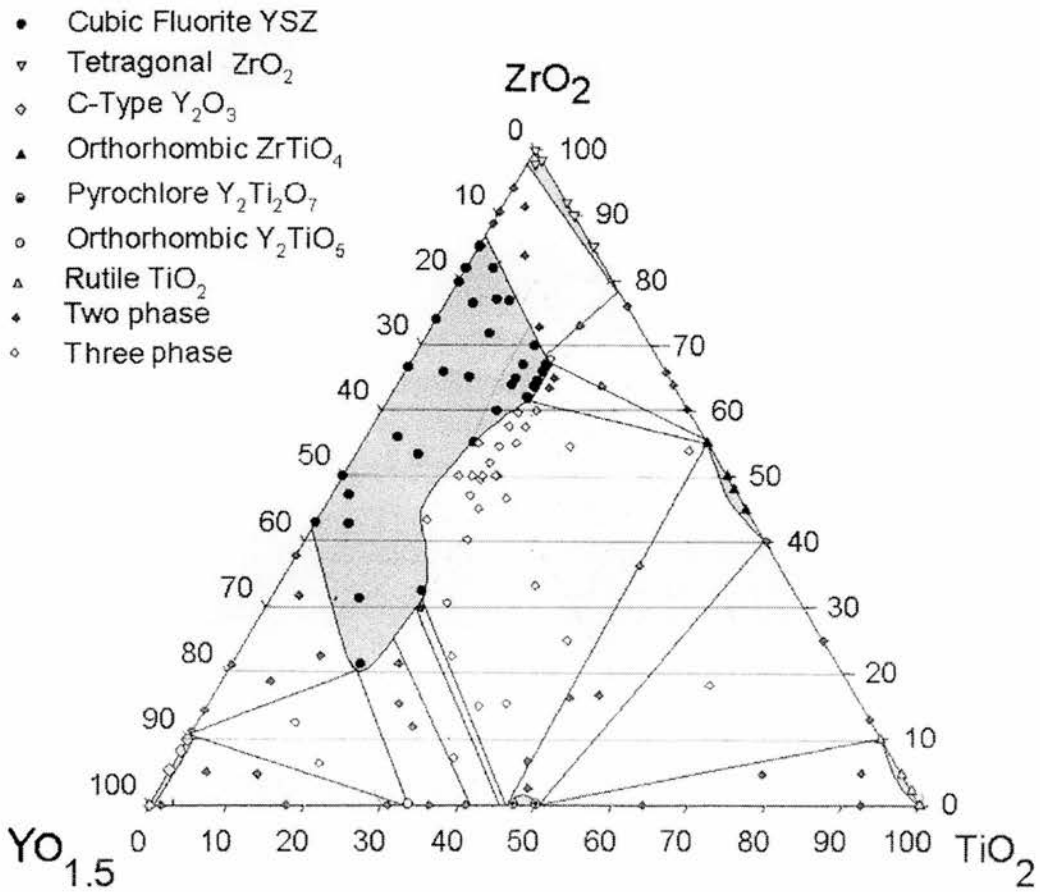

Figure 1.10: Ternary phase diagram of the Y_2O_3-ZrO_2-TiO_2 system at 1,500°C [67]

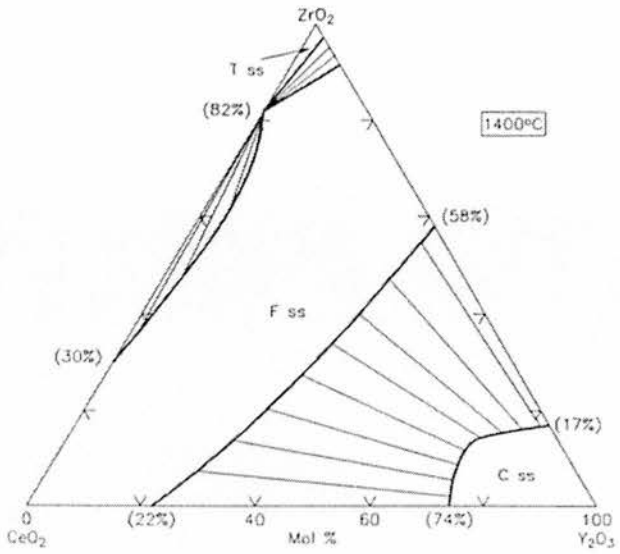

Figure 1.11: Ternary phase diagram of the Y_2O_3-ZrO_2-CeO_2 system at 1,400°C [68, 69]

Secondly, in order to minimise wear and tear on a SOFC during its operational life, the components must have matching thermal expansion properties. A thermal expansion mismatch between components would cause cracks in the cell when heated up to or cooled down from the SOFC operating temperature.

The reason for raising this concern is that the thermal expansion coefficient of CeO_2 is 10-20% higher than that of YSZ. This is especially of concern in a reducing environment, as CeO_2 expands considerably when reduced, as the ionic radius of the Ce cations increases from 0.97 to 1.14Å when going from Ce^{4+} to Ce^{3+}. [70]

It is likely that there could be a means to control this through the relative content of Ti and Ce, as TiO_2 shrinks on reduction and there could be a Ti: Ce ratio where the shrinkage and expansion effects combine to cancel each other out.

Thirdly, what effect will doping with CeO_2 have on ionic, electronic and total conductivity? The relevance is that the resultant YZTC material could have contributions to conductivity from the presence of Y_2O_3, which imparts ionic conductivity in YSZ, TiO_2 in YZT and CeO_2 itself.

References:

[1]: N.Q. Minh, *J. Am. Ceram. Soc*, 1993, **76**, 563-588

[2]: W.R. Grove, *Philos. Mag*, 1839, **14**, 127-130

[3]: W. Nernst, *Z. Elektrochem*, 1899, **6**, 41-43

[4]: E. Baur, H. Preis, *Z. Elektrochem*, 1937, **43**, 727-732

[5]: A.B. Stambouli, E. Traversa, *Renewable and Sustainable Energy Reviews*, 2002, **6**, 433-455

[6]: Online article obtained from WWW site Fuel Cells 2000, located at http://www.fuelcells.org/fctypes.htm

[7]: S.C. Singhal, Solid State Ionics, 2002, **152-153**, 405-410

[8]: A-L. Sauvet, J. Guindet, J. Fouletier, *Proceedings of the 4th Solid Oxide Fuel Cell Forum*, 2000, 567-577.

[9]: S.P.S. Badwal, *Solid State Ionics*, 2001, **143**, 39-46

[10]: T. Takahashi, H. Iwahara, Y. Nagai, *J. Appl. Electrochem*, 1972, **2**, 97-104

[11]: M. Miyayama, T. Nishi, H. Yanagida, *J. Mater. Sci*, 1987, **22**, 2624-2628

[12]: M.J. Verkerk, K. Keizer, A.J. Burggraaf, *J. Appl. Electrochem*, 1980, **10**, 81-90

[13]: A. Ahmad-Khanlou, F. Tietz, D. Stöver, *Solid State Ionics*, 2000, **135**, 543-547

[14]: J.B. Goodenough, *Phys. Rev*, 1955, **100**, 564-573

[15]: S. Srilomsak, D.P. Schilling, H.U. Anderson, *Proceedings of the 1st International Symposium on Solid Oxide Fuel Cells*, The Electrochemical Society, Pennington, NJ, 1989, 129-140

[16]: H. Yokokawa, T. Horita, N. Sakai, M. Dokiya, T. Kawada, *Solid State Ionics*, 1996, **86-88**, 1161

[17]: J.A.M. van Roosmallen, E.H.P. Cordfunke, *Solid State Ionics*, 1992, **52**, 303

[18]: Y. Teraoka, T. Nobunaga, K. Okamoto, N. Miura, N. Yamazoe, *Solid State Ionics*, 1991, **48**, 207-212

[19]: H.Y. Tu, Y. Takeda, N. Imanishi, O. Yamamoto, *Solid State Ionics*, 1997, **100**, 283-288

[20]: M. Godickemeier, K. Sasaki, L.J. Gauckler, I. Reiss, *Solid State Ionics*, 1996, **86-88**, 1996, 691-701

[21]: Y. Takeda, H. Ueno, N. Imanishi, O. Yamamoto, N. Sammes, M.B. Phillipps, *Solid State Ionics*, 1996, **86-88**, 1187-1190

[22]: G.C. Kostogloudis, C. Ftikos, *Solid State Ionics*, 1999, **126**, 143

[23]: S. Carter, A. Selcuk, R.J. Chater, J. Kajda, J.A. Kilner, B.C.H. Steele, *Solid State Ionics*, 1992, **53-56**, 597

[24]: L-W. Tao, M.M. Nasrallah, H.U. Anderson, *Proceedings of the 3rd International Symposium on Solid Oxide Fuel Cells*, The Electrochemical Society, Pennington, 1993, 241.

[25]: E. Maguire, B. Gharbage, F.M.B. Marques, J.A. Labrincha, *Solid State Ionics*, 2000, **127**, 329-355

[26]: L. Qiu, T. Ichikawa, A. Hirano, N. Imanishi, Y. Takeda, *Solid State Ionics*, 2003, **158**, 55-65

[27]: A.J. Jennings, S. J. Skinner, *Solid State Ionics*, 2002, **152-153**, 663-667

[28]: S.P.S. Badwal, *Solid State Ionics*, 2001, **143**, 39-46

[29]: S.C. Singhal, *Solid State Ionics*, 2000, **135**, 305-313

[30]: H.U. Anderson, *Solid State Ionics*, 1992, **52**, 33-41

[31]: N.Q. Minh, T. Takahashi, Science and Technology of Ceramic Fuel Cells, Elsevier, Amsterdam, 1995

[32]: B.C.H Steele, Electrochemistry and Clean Energy, Royal Society of Chemistry, 1994, 8

[33]: W.Z. Zhu, S.C. Deevi, *Materials Science and Engineering*, 2003, **A348**, 227-243

[34]: W.Z. Zhu, S.C. Deevi, *Materials Research Bulletin*, 2003, **38**, 957-972

[35]: I.G. Wright, B.A. Pint, C.S. Simpson, P.F. Tortorelli, *Mater. Sci. Forum*, 1997, **251/254**, 195

[36]: L. Jian, J. Huezo, D.G. Ivey, *Journal of Power Sources*, 2003, **123**, 151-162

[37]: W.J. Quadakkers, H. Greiner, W. Kock, Proceedings of the 1st European Solid Oxide Fuel Cell Forum, 1994, vol 1, 525-535.

[38]: P. Kofstad, Proceedings of the 2nd European Solid Oxide Fuel Cell Forum, 1996, 2, 479.

[39]: B.E. Liebert, *Proceedings of the 6th International Symposium on Solid Oxide Fuel Cells*, The Electrochemical Society, Pennington, 1999, 722-730.

[40]: J. Urbanek, M. Miller, H. Schmidt, K. Llipert, Proceedings of the 4th European Solid Oxide Fuel Cell Forum, 2000, 2, 567

[41]: D. Dulieu, J. Cotton, H. Greiner, *Proceedings of the 3rd European Solid Oxide Fuel Cell Forum*, 1998, 447

[42]: Y. Matsuzaki, I. Yasuda, *Solid State Ionics*, 2000, **132**, 271

[43]: W.J. Quadakkers, T. Malkow, P. Albellau, Proceedings of the 4th European Solid Oxide Fuel Cell Forum, 2000, vol 2, 827

[44]: M. Ueda, H. Taimatsu, Proceedings of the 4th European Solid Oxide Fuel Cell Forum, 2000, vol 2, 837

[45]: T. Brylewski, M. Nanko, T. Maruyama, K. Przybylski, *Solid State Ionics*, 2001, **143**, 131-150

[46]: T. Kadowaki, T. Shiomitsu, E. Matsuda, H. Nakagawa, H. Tsuneizumi, T. Maruyama, *Solid State Ionics*, 1993, **67**, 65

[47]: S.C. Singhal, *Mater. Res. Soc. Bull*, 2000, **25**, 16

[48]: U.B. Pal, S.C. Singhal, *J. Electrochem. Soc*, 1990, **137**, 2937

[49]: L.J.H. Kuo, S.D. Vora, S.C. Singhal, *J. Am. Ceram. Soc*, 1997, **80**, 589

[50]: J.W. Kim, A. Virkar, K-Z. Fung, K. Mehta, S.C. Singhal, *J. Electrochem. Soc*, 1999, **146**, 69

[51]: S.J. Visco, C.P. Jacobson, L.C. De Jonghe, *Proceedings of the 6th International Symposium on Solid Oxide Fuel Cells*, PV 99-19, The Electrochemical Society, Pennington, NJ, 1999, 861

[52]: S.P. Simner, J.W. Stevenson, K.D. Meinhardt, N.L. Canfield, *Proceedings of the 7th International Symposium on Solid Oxide Fuel Cells*, PV 2001-16, The Electrochemical Society, Pennington, NJ, 2001, 1051

[53]: S.P. Simner, Pacific Northwest National Laboratory, Unpublished work, 2001

[54]: Y. Matsuzaki, I. Yasuda, *Solid State Ionics*, 2000, **132**, 261-269

[55]: A. Kelaidopoulou, A. Siddle, A.L. Dicks, A. Kaiser, J.T.S. Irvine, *Proceedings of the 4th European Solid Oxide Fuel Cell Forum*, 2000, 537-546

[56]: J.T.S. Irvine, P.R. Slater, A. Kaiser, J.L. Bradley, P. Holtappels, M. Mogensen, *Proceedings of the 4th European Solid Oxide Fuel Cell Forum*, 2000

[57]: H. Naito, H. Arashi, *Solid State Ionics*, 1992, **53-56**, 436-441

[58]: H.U. Anderson, *Solid State Ionics*, 1992, **52**, 33-41

[59]: C.H. Lee, G.M. Choi, *Solid State Ionics*, 2000, 135, 653-661

[60]: K. Kobayashi, Y. Kai, S. Yamaguchi, N. Fukatsu, T. Kawashima, Y. Iguchi, *Solid State Ionics*, 1997, **93**, 193-199

[61]: E. Ramirez-Cabrera, A. Atkinson, D. Chadwick, *Proceedings of the 4th European Solid Oxide Fuel Cell Forum*, 2000, 49-57

[62]: G. Chiodelli, G. Flor, M. Scagliotti, *Solid State Ionics*, 1996, **91**, 109-121

[63]: M. Mogensen, N.M. Sammes, G.A. Tompsett, *Solid State Ionics*, 2000, **129**, 63-94

[64]: G. Chiodelli, A. Magistris, E. Lucchini, S. Meriani, *Science of Ceramics Vol. 14*, Institute of Ceramics, 1998, 903

[65]: M. Panhans, R.N. Blumenthal, *Solid State Ionics*, 1993, **60**, 279

[66]: J.H. Lee, S.M. Yoon, B-K. Kim, J. Kim, H-W. Lee, H-S. Song, *Solid State Ionics*, 2001, **144**, 175-184

[67]: A.J. Feighery, PhD. Thesis, University of St. Andrews, 1998

[68]: V. Longo, L. Podda, *Ceramica (Florence)*, 1984, **37** [5], 18-20

[69]: I. Barbariol, L. Kucich-Podda, S. Riotti, *Mater. Engl.*, 1990, **1** [3], 959-964

[70]: R.D. Shannon, C.T. Prewitt, *Acta Crystallographica*, 1969, **B25**, 925-929

Chapter 2: Experimental

Contents

2: Experimental

2.1: Preparation

Table 2.1 shows the reagents used to prepare the materials. The Y, Zr and Ti oxides were white powders, while the cerous nitrate was as colourless crystals. In addition, cobalt nitrate hexahydrate was in the form of red crystals. The entries in brackets indicate a change of supplier.

Table 2.1: Reagents used in this work.

Reagent	Purity & Supplier
Y_2O_3	Aldrich, 99.99%
	(Alfa Aesar, 99.9%)
TiO_2	Aldrich, 99.9+%
ZrO_2	Fluka, 99%
	(Riedel-de-Haen, 99%)
Fe_2O_3	Alfa Aesar, 99.8%
$Ce(NO_3)_3.6H_2O$	Alfa Aesar, 99.5% Reacton
$Co(NO_3)_2.6H_2O$	Aldrich, 98+% ACS reagent

The YZT and YZTC materials were synthesised by grinding up and mixing the appropriate quantities of metal oxides/ nitrates in an agate mortar and pestle. Then, the YZTC mixes were heated to at least 500°C for calcination, in order to decompose the cerous nitrate to become ceria. To confirm that this was complete, the mass of the powder mix was determined before and after calcination, to see if the mass lost was in line with expectations. Also, the powder mix became yellow afterwards, due to the presence of pale yellow ceria.

This step was not required for YZT, as nitrates were not used in its synthesis. After calcination, the resultant powder mix was mixed up and ground up again, using a solvent such as ethanol or acetone as a dispersing agent. Then, the powders were fired in alumina or platinum crucibles at a suitable temperature to allow solid-state reaction to occur. In some cases, the powders were pressed uniaxially into pellets before firing and fired as pellets. The firing temperatures were dependent on the material composition, as some of the YZTC materials could be fired at ~1,400°C, whereas others required firing temperatures of ~1,500°C (especially the YZT and YZTC compositions containing 3 at% Ti).

When firing was complete, a small amount of sample was examined using X-ray diffraction, to determine if the sample was phase pure (single phase with no peaks due to starting materials). If this was not the case, then the sample was re-ground and fired again, at a higher temperature than before and this was repeated, if necessary, until the material was

phase pure or it was decided that the composition was multi-phase at equilibrium. Masses recorded in this work were subject to uncertainties of up to ± 0.3 mg.

2.2: Instrumental Measurements

2.2.1: X-ray powder diffraction

Without internal standard

X-ray diffraction was used to determine the phase purity of materials after firing, as well as the structures of products from experiments such as reduction, oxidation, etc. Two instruments were used for diffraction. The instruments used were a STOE Stadi-P automated X-ray diffractometer in transmission mode and a Philips X'Pert diffractometer operating in reflectance mode. X-rays were generated by copper sources and passed through curved germanium monochromators. The X-rays of interest were the Cu $K\alpha_1$ X-rays, which had a wavelength of 1.5406 Å. On occasion, Cu $K\alpha_2$ X-rays, which had a wavelength of 1.5444 Å and half of the intensity of the accompanying $K\alpha_1$ X-rays, were found and could be removed by $K\alpha_2$-stripping methods present in the software accompanying the instruments.

Sample preparation for the STOE instrument involved a few milligrams of powder held between two thin acetate sheets with Vaseline. The resultant disc was placed in a circular metal disc placed in the instrument sample holder. During each experiment, the sample holder was spinning continuously, in order to minimise effects from preferred orientations, which would lead to significant errors in peak intensities.

For the Philips X-ray instrument, up to several hundred milligrams of sample were placed in a trench area of an aluminium plate and a glass slide was then used to ensure that the sample surface was flat, in order to reduce background.

The X-ray patterns were run over a 2θ range of 5-90°. Some runs were carried out over 2θ ranges of 20-110°. Some peaks that cropped up in XRD runs could be ignored. These were peaks due to Vaseline, present at 21.2-21.5° and 23.6-24.0° 2θ for STOE measurements and aluminium peaks from the sample holder were sometimes present on runs carried out on the Philips instrument, where there was not enough sample present on the aluminium plate.

The software accompanying the instruments was used to help manually index the diffraction patterns from a list of peaks generated from the raw data. This was after removal of residual spikes that were due to random spikes or Cu $K\alpha_2$ X-rays. Then, the peak list was used to obtain an approximation of the unit cell parameter, a, as follows:

$$a = \frac{\lambda\sqrt{(h^2 + k^2 + l^2)}}{2\sin\theta} = d\sqrt{(h^2 + k^2 + l^2)}$$

After that, least squares refinement was carried out on the data, using the approximate result as a starting point for generating refined values of the 2θ zero point (start point) and the unit cell parameter.

Internal Standard

In order to provide more certainty to XRD results obtained for the YZT and YZTC materials, XRD experiments of some of the materials were run again, using an internal standard for reference. The internal standard used was fine, black, crystalline silicon powder (325 mesh, 99.5%, Alfa Aesar). As a test, the standard was run on its own over a 2θ range of 10-95°. This was to determine whether or not one could discriminate between the silicon peaks from peaks due to the sample of interest.

The silicon standard peaks were as a cubic F-type lattice, with a unit cell parameter of 5.4312 (7) Å. This indicated that the silicon peaks were not going to interfere with those from the YZT and YZTC materials, which had unit cells of ~5.1-5.2 Å. In order to determine the proximity of the Si peak positions to where they should be, they were compared to JCPDS-ICDD powder diffraction file entry 27-1402.

The silicon standard runs were run just like any other X-ray powder diffraction, but with some silicon added to the material of interest. Of course, the diffraction pattern showed peaks due to the material of interest and silicon. The silicon peaks were compared with the PDF database information and the deviations in d-spacing and 2θ angle between the two sets of information were used to create a 'correction curve' of corrections needed to be applied to the measured Si peaks, so that their positions were where they should be. Then, the equation describing the correction curve was applied to the YZT/YZTC peaks to adjust them relative to the 'corrected' Si peaks.

2.2.2: Pellet preparation

Pellets of up to 16 mm thickness were pressed uniaxially in a 13mm diameter die using a SPECAC press and up to 8g of powder. A variety of different types of pellets were made for samples that were used for a range of measurements, such as conductivity, dilatometry and pellets for reaction. The load used was 2-4 tons, which corresponds to a

pressure ranging from 148 – 296 MPa applied for up to 5 minutes. After that, the pellets were sintered at temperatures up to those used to fire the pellets for up to 12 hours.

Some pellets were made to be more porous than others. This was done by adding graphite into the pellet powder mix, which burns out and forms pores in the structure. This was not so perfect, however, as some of the resultant pellets were not stable or collapsed after the graphite was burnt off.

After quenching to room temperature in air, the physical dimensions of each pellet were measured, to determine the densities of the pellets. Also, the density of each pellet was compared to theoretical density values for each material. Theoretical density was calculated as:

$$T.Density = \frac{ZM}{NV}$$

Z = Number of formula units that make up the unit cell of the material. In the case of the cubic fluorite structure, Z=4.

M = mass of 1 mole of the material/ g mol^{-1}

N = Avogadro's number, $6.0221367*10^{23}$ mol^{-1}

V = unit cell volume/ cm^3.

2.2.3: Tube furnace heating

In some cases, samples of YZTC materials were heated in a tube furnace, with a view to reduction and re-oxidation studies using larger quantities of material that can be handled by a TGA instrument.

Pellets of the materials of interest were placed in an alumina boat that was inserted into the internal alumina tube of the furnace. Then, the samples were heated for at least 24-48 hours at 1,000°C in a flowing atmosphere of either 5% H_2/argon or argon for reduction or oxygen for oxidation experiments. In addition, for reduction experiments, a piece of copper foil was placed either underneath the samples in the boat or in a separate alumina boat. This foil was used as an oxygen getter and leakage monitor, based on how much mass gain (if any) was present in the foil.

Heating of the furnace was controlled by a Eurotherm temperature controller, in conjunction with a type K (chromel/ alumel) thermocouple wire that was wrapped around the centre of the internal alumina tube. The main aim of these experiments was to provide information on the reduction and oxidation behaviour of these materials.

2.2.4: Simultaneous TG-DTA

Simultaneous TG-DTA experiments were carried out on a TA Instruments SDT 2960 instrument. These experiments were done in order to determine if the materials used in this work could be re-oxidised fully after being reduced.

The conditions used for the oxidation runs were as follows: ~20-30mg of sample was measured out into a 4mm high, 6mm diameter alumina crucible. Alongside, another alumina crucible was filled with a similar mass of alumina to act as a reference for DTA and a counter mass for TGA measurements.

The atmosphere used was air, flowing at a rate of 110 cm^3 min^{-1}. The samples were heated from ambient to 1,200°C at 10°C min^{-1}, then cooled at 20°C min^{-1} to ambient temperature.

In addition, a 'blank' TG-DTA run was carried out before the experiments to act as a baseline for TGA and DTA signals, to account for background and buoyancy that can be experienced in such runs. For this 'blank', this was a normal experiment, except that the sample was alumina, as it is a material that should not show any endo- or exothermic DTA transitions or any mass change processes under the experimental conditions.

2.2.5: TGA

TGA measurements were carried out using a RheoTherm TG1000M+ instrument capable of heating up to 950°C at heating rates of up to 999°C min^{-1}, using a water-cooled furnace. A type R (Pt/Pt-13% Rh) thermocouple located 0.5-1mm below the sample pan was used to determine the sample temperature. The furnace temperature was measured using a type K thermocouple . This instrument was set up to use dry or 'wet' atmospheres of either Ar or 5% H_2/Argon.

A 'wet' atmosphere was one where the gas of interest was passed through a glass tube containing wet fibreglass or cotton wool. Thus, this would humidify the atmosphere before it enters the instrument. This was done, because passing the gas through a bubbler containing water would have caused disruptions to the signal baseline, due to potential variability and disruptions to the gas flow, which should be a steady stream of gas. The flow rates used were 20-30 cm^3 min^{-1}.

The TGA studies involved a set temperature program applied to a set of runs of powders of YZTC materials under reducing conditions in a 5% H_2/Argon atmosphere. The mass signal was subject to possible uncertainties of up to ± 3 μg.

2.2.6: 2-terminal AC Impedance Spectroscopy

For 2-terminal AC impedance spectroscopy, the samples used were pellets of ~13mm in diameter with densities equal to at least 65% of calculated theoretical density. Platinum terminals were painted onto both circular faces of the pellets using platinum paste and covered the entirety of each of the faces. Afterwards, the paste was heated overnight at ~100°C to dry off most of the solvent and then fired for 1 hour at 900°C in static air.

The measurements involved a Pt wire compression jig that was designed 'in-house', as shown in Figure 2.1. A type K thermocouple was used to measure the sample temperature. For temperature-based measurements, the jig was inserted into a small horizontal tube furnace controlled by a Eurotherm 900 series programmer and heated up to the desired temperature. When this temperature was reached, the system was given at least 45-120 minutes to let the sample equilibrate to a stable and (more or less) constant temperature. After that time, the conductivity measurement was taken.

The atmosphere used for these conductivity experiments was static air.

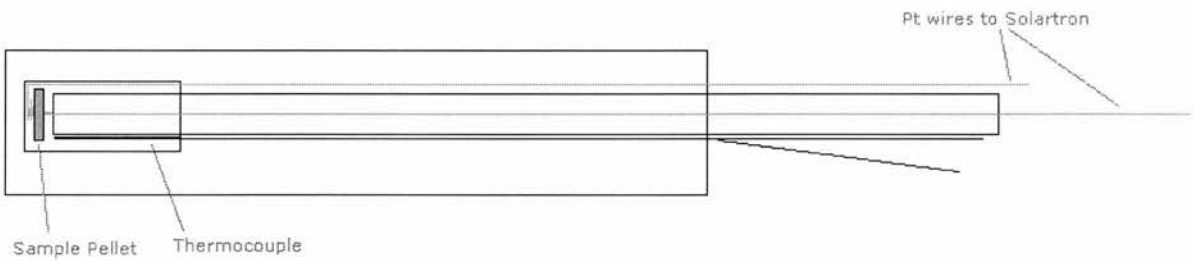

Figure 2.1: Pt wire jig used for AC impedance measurements

The conductivity determinations involved connecting up the Pt wires of the jig to a Solartron SI1260 Impedance/ Gain-Phase analyser. Using this system, the imaginary and real responses were determined over a frequency range of 0.1 Hz – 8 MHz. Data measured at frequencies above 1 MHz was deemed unreliable, as the analyser instrument was not properly calibrated at frequencies above 1 MHz.

Interpretation of the results involved having to account for many factors before obtaining the final value of conductivity for a particular temperature. Normally, the response curve is plotted as the imaginary component of the resistance (Z'') as the y-axis against the real component of the resistance (Z') as the x-axis and the simple response of interest is in the

form of a semicircle. The initial resistance value, R' (Ω), is determined from the points where the semicircle intercepts the Z' axis. A (somewhat idealised) example of this response curve, known as a Nyquist plot is shown in Figure 2.2:

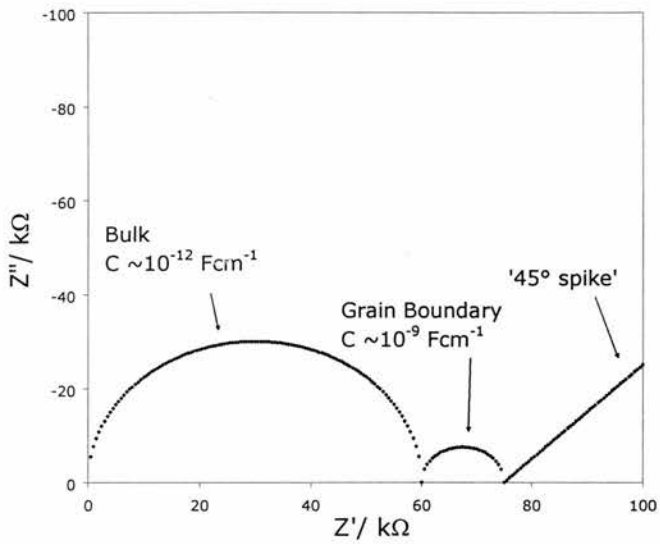

Figure 2.2: Example of a Nyquist plot.

This value R' accounts for the sample resistance value and the resistance of the jig (R_{jig}) at the temperature of interest. Values of R_{jig} were determined previously by impedance measurements carried out on a short-circuit, in order that any resistance is due to the wires of the jig over a range of temperatures up to 1,000°C.

To obtain the corrected resistance R, R_{jig} for the temperature of interest was subtracted from R'. Then R was inverted to obtain the conductance σ'' in units of S (Ω^{-1}) and in order to obtain the true conductivity value, σ'' is then normalised for sample density and geometry. To normalise for the sample geometry, σ'' is multiplied by geometric factor g (cm^{-1}) and g is calculated as T/A, where A (cm^2) is the area of the circular face of the sample pellet and T (cm) is the thickness of the pellet. This now yields conductivity value σ' (Scm^{-1}), which then has to be normalised for sample density.

To do this, σ' was multiplied by $\rho_{theoretical}/\rho_{measured}$, where $\rho_{theoretical}$ represents the theoretical density for the sample material and $\rho_{measured}$ represents the actual sample density. This now yields the fully normalised conductivity value σ (Scm^{-1}). That said, however, density normalisation only works for samples that have a density of at least 65 - 75% of the theoretical density if linearity is to be a fair approximation [2.1]. The ideal situation would be to work with pellets that are fully dense.

Finally, for a range of conductivity measurements carried out on the same sample at different temperatures, the activation energy of the conductivity process can be calculated

using an Arrhenius plot of ln σT ($Scm^{-1}K$) against T^{-1} (K^{-1}). This should lead to a straight-line plot where the slope is E/R (K) and multiplying this slope by R will yield the activation energy, E ($J\ mol^{-1}$). E is normally expressed in units of eV, where 1 eV = 96,485 $J\ mol^{-1}$. This is the expected behaviour for a small polaron-based mechanism.

AC Impedance spectroscopy does not only have the capability to measure the conductivity of a material. It can also establish the nature of the conductivity. This is due to the property called capacitance in parallel to resistance. It can be derived from the response curve used to calculate the conductivity values. The capacitance of the process is derived from the equation $2\pi RCf_{max} = 1$, meaning that $f_{max}=1/(2\pi RC')$.

R is the resistance of the process, C' is the capacitance and f_{max} is the frequency of maximum loss in the impedance spectrum. f_{max} can be found from the plot at the point in the semicircle where Z'' is at is highest and f_{max} is the frequency at which this happens.
After determining C', it is corrected for the capacitance of the jig by subtracting the previously known capacitance value from C'. Then, C' is normalised for sample geometry in the same way as it was for conductivity by multiplying C' by geometric factor g to yield the final capacitance C (Fcm^{-1}).
The capacitance value C can indicate of the type of process, as shown by Table 2.2.

Capacitance/ Fcm^{-1}	Phenomenon Responsible
10^{-12}	Bulk
10^{-11}	Minor, 2nd phase
$10^{-11} \rightarrow 10^{-8}$	Grain boundary
$10^{-10} \rightarrow 10^{-9}$	Bulk ferroelectric
$10^{-9} \rightarrow 10^{-7}$	Surface layer
$10^{-7} \rightarrow 10^{-5}$	Sample-Electrode interface
10^{-4}	Electrochemical reactions

Table 2.2: Capacitance values and associated phenomena [2.2]

2.2.7: 4-terminal DC conductivity measurements

The aim of DC conductivity measurements is to measure the dependence of the conductivity of a material upon partial oxygen pressure (pO_2) at a particular temperature. The samples were pellets of the materials of interest with 4 platinum terminals fixed onto one side of each pellet. They were prepared by painting 4 lines of platinum paste onto the pellet. Then, thin strips of Pt foil were stuck onto these lines as terminals. After that, the pellets were dried for several hours at ~100°C, to remove the solvent, terpineol, then heated up to 900°C, in order to remove the organic content and fire the Pt electrodes, fixing the terminals into position.

The arrangement of the electrodes on the sample pellet is shown in Figure 2.3 and a schematic of the system used for the measurements is shown in Figure 2.4. A yttria-zirconia sensor was used to determine the partial oxygen pressure (pO_2) and its operation is based upon the Nernst equation.

$$V_o = \frac{RT}{4F} \ln \frac{pO_2}{pO_{2(ref)}}$$

The electrochemical cell potential is V_o and $pO_{2(ref)}$ represents the pO_2 in equilibrium with the reference electrode. V_o was measured by a Solartron 7065 microprocessor voltmeter and converted into a pO_2 value using the Nernst equation above.

T is the sample temperature measured by a type R thermocouple connected to a Keithley 182 sensitive digital voltmeter, showing the thermocouple signal as a voltage. To obtain the true temperature, one had to account for a reference junction at 20°C (At 20°C, the thermocouple signal was 0 V). This correction was done by adding 0.111mV to the voltmeter reading. This final voltage signal was converted into a temperature by referring to a standard R-type ITS-90 thermocouple table.

Two more instruments were used to determine the conductivity of the sample. Firstly, DC current was applied to the outer electrodes by a Keithley 220 programmable current source and a Solartron 7150 digital multimeter measured the voltage across distance l, between the inner electrodes.

From voltage and current measurements, conductivity was determined as $\sigma=I/V$ in Siemens (S). Next, an adjustment factor was applied to account for the sample geometry. This geometric factor, g/ cm^{-1}, was based on the physical dimensions of the sample pellet and the distances between the electrodes, as shown in Figure 2.3. g=l/dt, where l is the distance between the centres of the two inner electrodes, d is the diameter of the pellet and t is the pellet thickness.

Finally, normalised conductivity was obtained by multiplying σ by g to obtain conductivity in units of S cm^{-1}. This particular geometry is not a perfect model, however, and there is a possible uncertainty of ±10%. Geometric correction is usually frequently ratified by AC impedance studies on samples of similar size, as the geometry involved in a sample for 2-terminal AC impedance studies is better defined.

Principally, conductivity measurements involved heating the sample to the required temperature. Then, the system was left for a few minutes to allow the sample temperature to settle down, as this temperature was used in the pO_2 calculations, as shown previously. The first half of the experiment was to slowly reduce the sample with a very low flow rate of 5%

H_2/Ar gas over a period of 24 hours, to allow time for the system environment to equilibrate at low pO_2 levels. After that, the second half of the experiment involved slowly oxidising the sample back to its original pO_2 level by allowing air to leak in air very slowly, over a period of several hours.

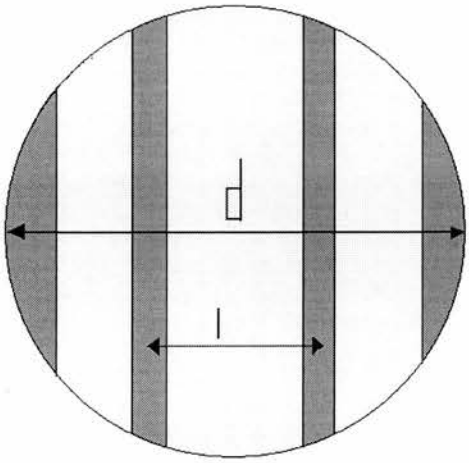

Figure 2.3: Arrangement of Pt electrodes for sample pellet

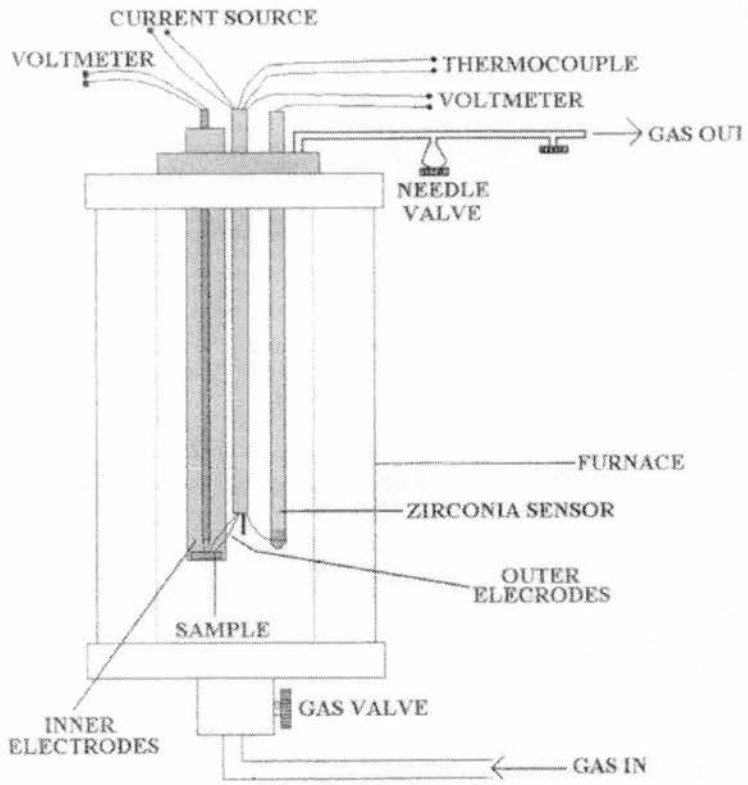

Figure 2.4: Pt wire jig used for 4-terminal DC conductivity measurements in controlled atmospheres

2.2.8: Dilatometry

Dilatometry is defined as "A technique in which a dimension of a substance under negligible load is measured as a function of temperature while the substance is subjected to a controlled temperature program." (ICTA, ASTM E 473-85)

Thermal expansion measurements were carried out on a Netzsch DIL 402C horizontal pushrod dilatometer. The way in which the instrument measures the thermal expansion is that while in the sample holder, the change in sample length is transmitted by the pushrod to a LVDT (linear variable displacement transducer). The LVDT converts this length change into an electrical signal, translated by an analogue to digital converter. Sample temperature is measured by a type S (Pt/90% Pt-10% Rh) thermocouple.

The experiments were in two parts. In the first part, a 'correction' sample was run using the experimental conditions that will be used in the actual sample experiment with a dummy of similar dimensions to the test sample. The second part of the experiment was a repeat of the run, using the actual sample of interest. The main aim of these experiments was to determine the thermal expansion properties of the YZTC materials in a variety of atmospheres.

The experiment conditions used for oxidising atmosphere runs were that the sample was heated in oxygen flowing at 50 cm^3 min^{-1} at 5°C min^{-1} from ambient to 1,100°C and back to ambient at 5 to 10°C min^{-1}. Other runs were done in argon and 5% H_2/ argon atmospheres. The experiments run in argon were run using the same temperature regime as the experiments in oxygen.

The experiments in 5% H_2/ Argon, however, were slightly different, in that the heating was only done to 1,000°C, in order to minimise potential degradation of the sample thermocouple. Before the runs in argon or 5% H_2/argon, however, the sample pellets were pre-reduced in the atmosphere of interest by heating up to 1,000°C in a tube furnace for at least 24-48 hours.

The 'correction' samples were 10 mm diameter alumina cylinders that had lengths ranging from 6 – 15mm. Ideally, for the most accurate results, the sample length had to be as close to that of the blank as possible, usually within ± 0.5 mm.

In terms of theory, the length change measured by the system is a combination of the expansion of the sample holder and the sample. In order to correct for this, a correction run is carried out under the same conditions as the intended sample using a standard reference

material such as alumina. Then, the system compares measured data with reference data and allows correction accordingly.

$$\Delta l_{sys} = \Delta l_{stt} - \Delta l_{stm}$$

$$\Delta l_{sa} = \Delta l_{sam} + \Delta l_{sys}$$

In equations x and y, the terms are defined as follows:

Δl_{sys} = correction curve for expansion of measuring system

Δl_{stt} = tabulated reference expansion data for standard

Δl_{stm} = measured expansion of standard (uncorrected)

Δl_{sa} = actual expansion of sample (corrected)

Δl_{sam} = measured expansion of sample (uncorrected)

The coefficient of thermal expansion (α) is calculated by the following equation:

$$\alpha_m = \frac{l_{T2} - l_{T1}}{L_0(T2 - T1)} = \frac{\Delta l / L_0}{\Delta T}$$

In the above equation, L_0 is the original sample length; l_{T1} and l_{T2} are the sample lengths at temperatures T1 and T2 respectively. Δl is the change in sample length between the temperatures T1 and T2.

References:

[2.1]: A.J. Feighery, PhD Thesis, University of St. Andrews, 1998

[2.2]: J.T.S. Irvine, D.C. Sinclair, A.R. West, *Advanced Materials*, 1990, **2**, 132-138

Chapter 3: Synthesis and Characterisation

Contents

3: Synthesis and Characterisation

3.1: X-ray Powder Diffraction Analysis

3.1.1: Structural Background

Most, but not all of the compositions investigated were single phase cubic fluorite. Generally, doping YZT with ceria (another fluorite material) did not cause a change in the crystallographic phase of YZT. The cubic forms have F-type lattices of space group Fm3m.

The fluorite structure is found for certain compounds of the form MX_2 (X= F or O) and an inverted form, antifluorite, exists and comprises of materials of the type M_2E, where E can be O, S, Se or Te. This structure consists of a cubic close-packed array of cations and tetrahedral anions. With an anion: cation ratio of 2:1, the cations are 8-coordinate and the anions are 4-coordinate. This is the other way around for the antifluorite structure, as the cation and anion sites are swapped around.

The fluorite structure can be envisaged in one of two ways. The first way is to describe it as a 3-dimensional network of MX_8 cubes and XM_4 tetrahedra. Alternatively, it can be thought of as a primitive cubic anion array where 8-coordinate sites at the cube body centres alternate between being empty and occupied by a cation. Overall, the lattice type is face-centred cubic and the primitive cube accounts for only 1/8 of the unit cell [3.1]. The unit cell is of the formula M_4X_8, as illustrated in Figure 3.1 [3.2].

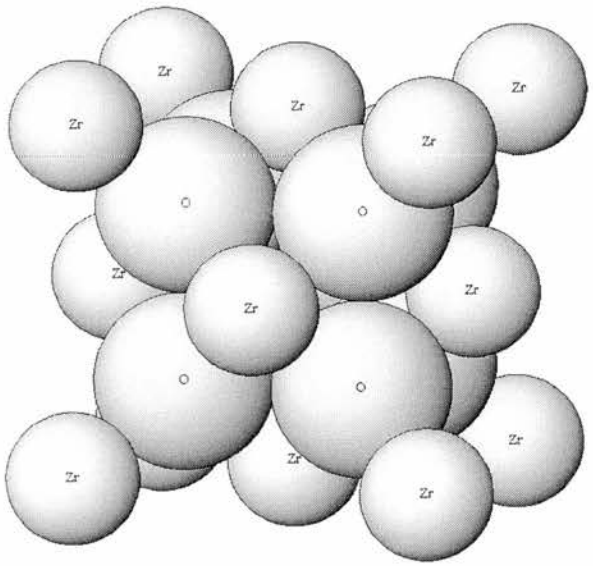

Figure 3.1: 3-dimensional view of the cubic fluorite structure. [3.2]

The other main MX_2 structure is rutile, most commonly found for TiO_2. In general, this structure is found for cations that are too small to form the fluorite structure with O or F anions. The unit cell is tetragonal with the formula M_2X_4 and is illustrated in Figure 3.2 [3.3].

The cations are located in two sites, the body centre and the corners. The oxygen positions are variable and usually determined experimentally. The cations are in a 6-coordinate octahedral environment, although the octahedron involving the body centre cation is in a different orientation to that of the octahedra containing the corner cations. The anions are in 3-coordinate trigonal environments and as they form the corners of the MX_6 octahedra, each corner anion is shared between three octahedra. These octahedra then form a 3-dimensional network by sharing edges and corners [3.1].

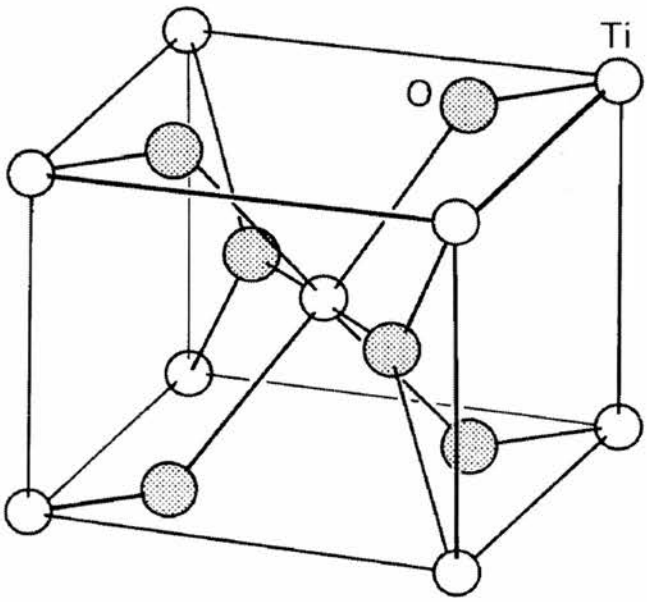

Figure 3.2: Rutile structure [3.3]

Nature of ZrO_2

It is known that for pure ZrO_2, there are three possible forms. First, there is the low-temperature, monoclinic baddeleyite structure, where the Zr cations are in a 7-coordinate environment [3.4], as shown in Figure 3.3 [3.5]. Dark spheres represent oxygens and the grey sphere represents Zr.

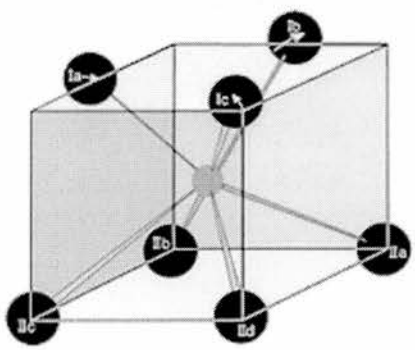

Figure 3.3: Representation of the ZrO_7 polyhedron in baddeleyite ZrO_2 [3.5]

At ~1,100°C, the structure changes from monoclinic to tetragonal, where the Zr cations enter into an 8-coordinate environment [3.6]. The tetragonal ZrO_2 structure can be considered to be a slightly distorted fluorite, where Zr is coordinated to two sets comprising 4 oxygen ions each. The Zr-O distance for the first set is ~2.08 Å, while the Zr-O distance for the second set is ~2.38Å [3.7]. Figure 3.4 illustrates this [3.8].

In this diagram, the small black spheres represent the Zr cations and the large spheres represent the oxygen ions. These are coloured white and grey to represent the two sets of oxygens that Zr is coordinated to, mutually displaced in the opposite direction of the c-axis, causing the tetragonal distortion and two sets of Zr-O distances [3.8].

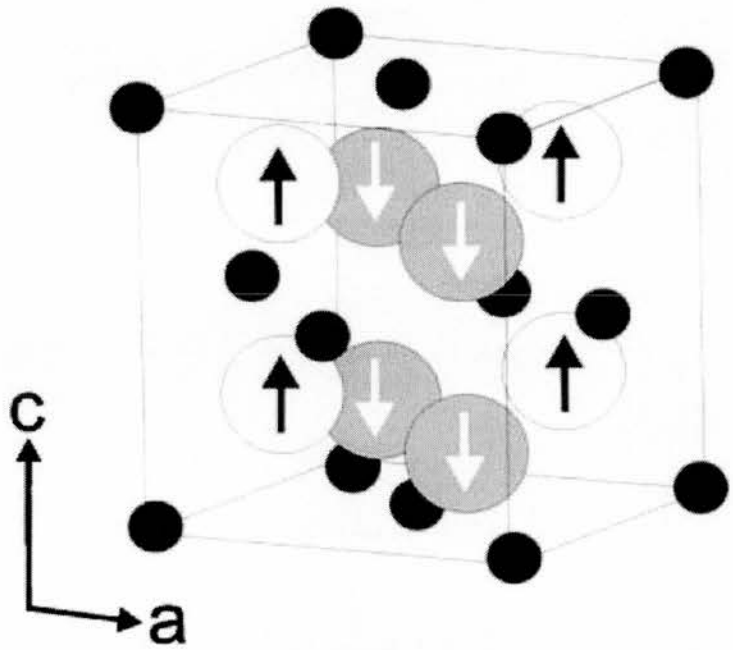

Figure 3.4: Schematic of tetragonal ZrO_2 [3.8]

Finally, there is the cubic fluorite ZrO_2 structure that is only stable at temperatures above 2,377°C [3.9]. The explanation of why this phase is unstable at lower temperatures was suggested by semi-empirical rules proposed by Pauling that were based on the 'ionic radius ratio' (r_{cation}/ r_{anion}) [3.10]. Two assumptions required for it to work are that the cation must be in contact with the anions, placing a minimum size requirement for a cation to be suitable for a particular type of site. Secondly, the anions may or may not be in contact. The minimum radius ratios for the 6-coordinate octahedral and 8-coordinate cubic sites were calculated to be 0.414 and 0.732, respectively. These can be illustrated in Figure 3.5, based on the radius of O^{2-} being 1.40Å [3.11]. It is noted, however, that in ZrO_2, Zr prefers to be in 7-fold coordination.

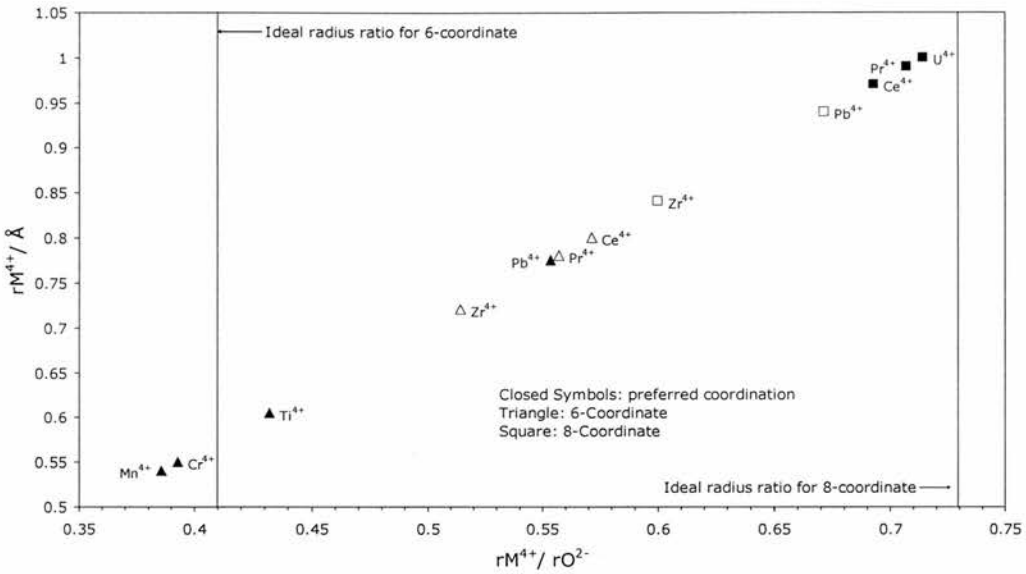

Figure 3.5: Plot of cation radius vs. cation/anion radius ratio for MO_2 oxides in normal state.

For ZrO_2, the ionic radius ratio is too low for effective 8-coordination, but can be suitable for a 6 or 7-coordinate environment. This means that the Zr cation is too small for ZrO_2 to attain the cubic fluorite structure but would be large enough to form structures of lower coordination numbers such as 6-coordinate rutile or 7-coordinate baddeleyite [3.8, 3.1].

3.1.2: Materials, as synthesised in air

The results of X-ray diffraction determinations on these materials, as synthesised in air were shown in Tables 3.1-3.4. Figures 3.6 – 3.11 represent X-ray diffraction patterns for YZT and certain YZTC materials. In these Figures, peaks marked 'I' represent peaks that are not due to the cubic phase, but could be due to an additional, tetragonal or lower symmetry phase and not due to starting materials.

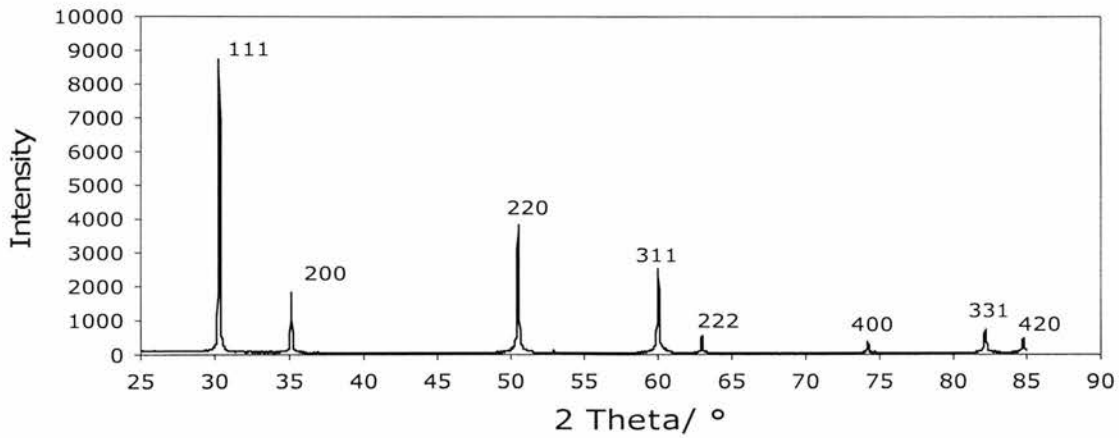

Figure 3.6: X-ray diffraction pattern for $Y_{0.20}Zr_{0.62}Ti_{0.18}O_{1.90}$

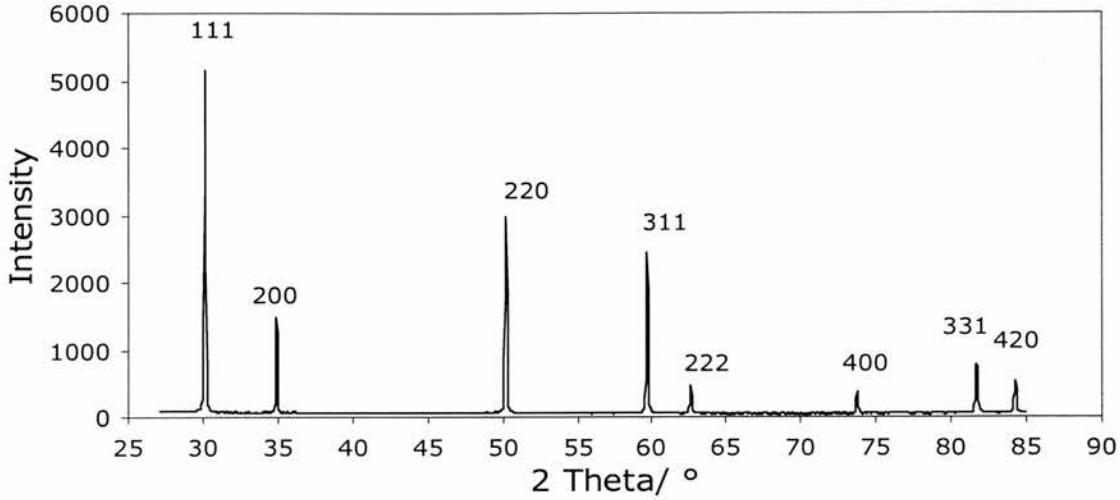

Figure 3.7: X-ray diffraction pattern for $Y_{0.20}Zr_{0.62}Ti_{0.13}Ce_{0.05}O_{1.90}$

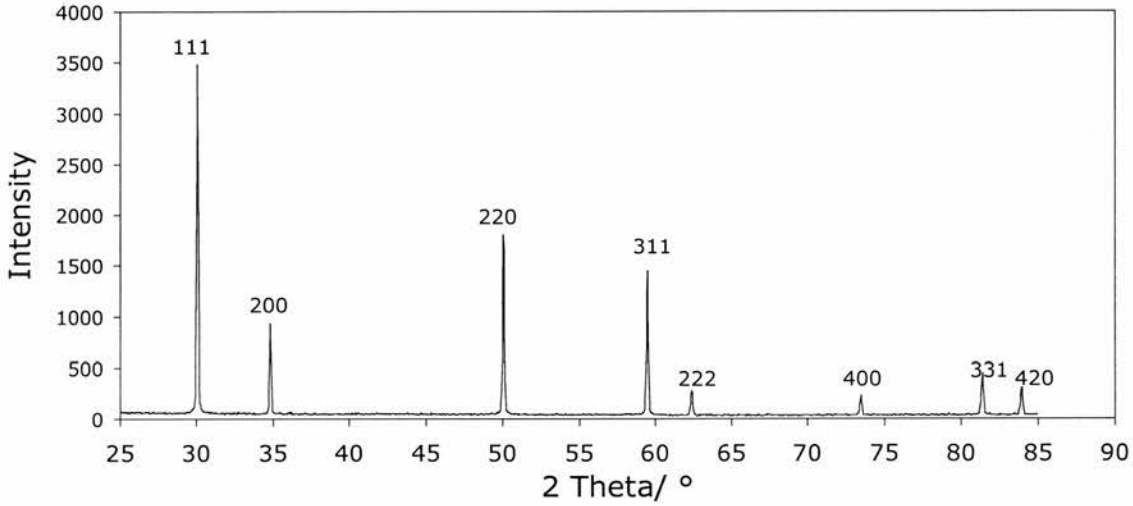

Figure 3.8: X-ray diffraction pattern for $Y_{0.20}Zr_{0.57}Ti_{0.13}Ce_{0.10}O_{1.90}$

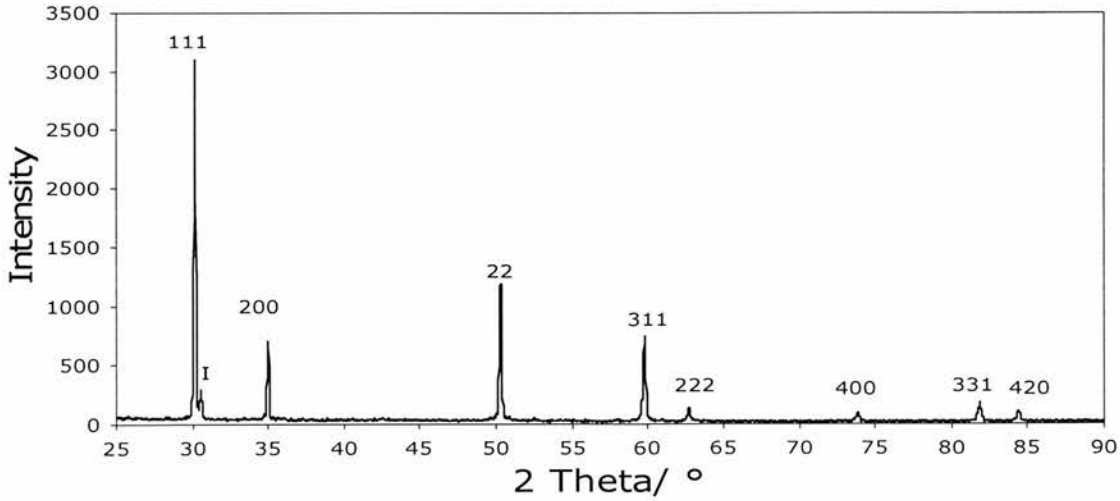

Figure 3.9: X-ray diffraction pattern for $Y_{0.15}Zr_{0.62}Ti_{0.18}Ce_{0.05}O_{1.925}$

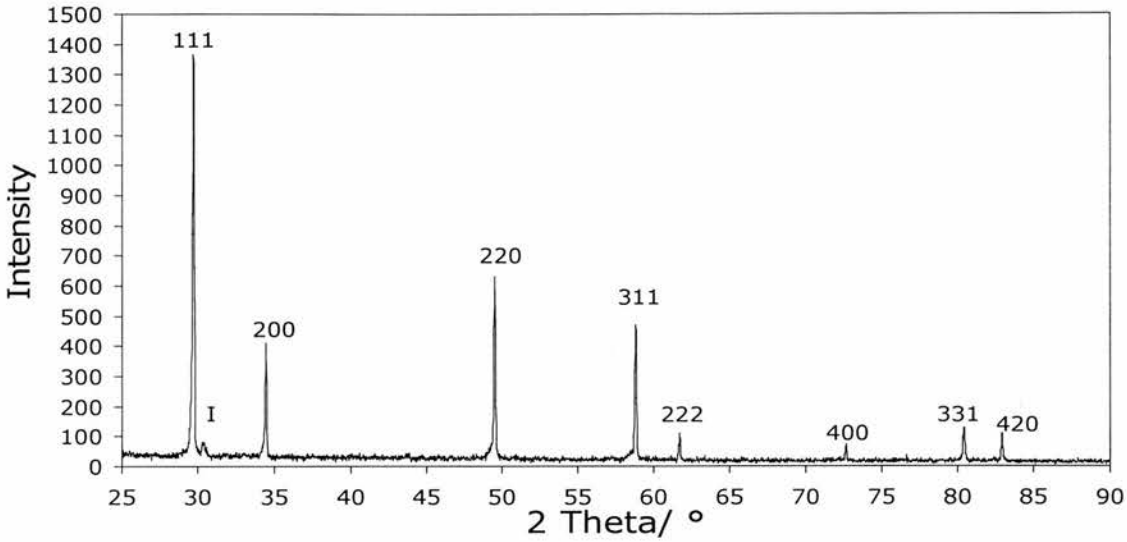

Figure 3.10: X-ray diffraction pattern for $Y_{0.10}Zr_{0.52}Ti_{0.13}Ce_{0.25}O_{1.95}$

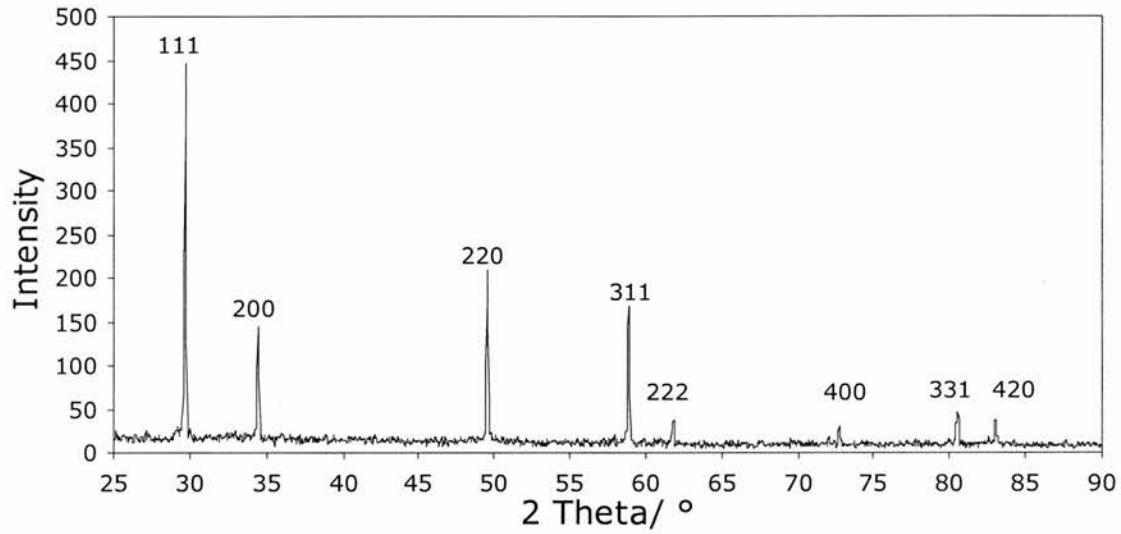

Figure 3.11: X-ray diffraction pattern for $Y_{0.125}Zr_{0.52}Ti_{0.13}Ce_{0.225}O_{1.9375}$

Table 3.1: Structures of YZTC materials containing 18+ at% Ti.

Formula	Type	Cubic unit cell/ Å
$Y_{0.20}Zr_{0.62}Ti_{0.18}O_{1.90}$	C	5.1111
$Y_{0.20}Zr_{0.57}Ti_{0.18}Ce_{0.05}O_{1.90}$	C	5.1272
$Y_{0.10}Zr_{0.62}Ti_{0.18}Ce_{0.10}O_{1.95}$	T	-
$Y_{0.15}Zr_{0.62}Ti_{0.18}Ce_{0.05}O_{1.925}$	C/T	-
$Y_{0.08}Zr_{0.62}Ti_{0.18}Ce_{0.12}O_{1.96}$	T	-
$Y_{0.10}Zr_{0.57}Ti_{0.18}Ce_{0.15}O_{1.95}$	C/T	-
$Y_{0.12}Zr_{0.62}Ti_{0.18}Ce_{0.08}O_{1.94}$	C/T	-
$Y_{0.125}Zr_{0.57}Ti_{0.18}Ce_{0.125}O_{1.9375}$	C/T	-
$Y_{0.125}Zr_{0.52}Ti_{0.18}Ce_{0.175}O_{1.9375}$	C/T	-
$Y_{0.15}Zr_{0.57}Ti_{0.18}Ce_{0.10}O_{1.925}$	C/T	-
$Y_{0.15}Zr_{0.52}Ti_{0.18}Ce_{0.15}O_{1.925}$	C/T	-
$Y_{0.20}Zr_{0.52}Ti_{0.20}Ce_{0.08}O_{1.90}$	C/T	-
$Y_{0.20}Zr_{0.47}Ti_{0.20}Ce_{0.13}O_{1.90}$	C/T	-

Table 3.2: Structures of YZTC materials containing 13 at% Ti.

Formula	Type	Cubic unit cell/ Å
$Y_{0.20}Zr_{0.62}Ti_{0.13}Ce_{0.05}O_{1.90}$	C	5.1357
$Y_{0.20}Zr_{0.57}Ti_{0.13}Ce_{0.10}O_{1.90}$	C	5.1518
$Y_{0.15}Zr_{0.57}Ti_{0.13}Ce_{0.15}O_{1.925}$	C	5.1664
$Y_{0.15}Zr_{0.52}Ti_{0.13}Ce_{0.20}O_{1.925}$	C	5.1860
$Y_{0.15}Zr_{0.62}Ti_{0.13}Ce_{0.10}O_{1.925}$	C	5.1499
$Y_{0.10}Zr_{0.52}Ti_{0.13}Ce_{0.25}O_{1.95}$	C/T	-
$Y_{0.10}Zr_{0.47}Ti_{0.13}Ce_{0.30}O_{1.95}$	C/T	-
$Y_{0.125}Zr_{0.52}Ti_{0.13}Ce_{0.225}O_{1.9375}$	C	5.1964
$Y_{0.125}Zr_{0.47}Ti_{0.13}Ce_{0.275}O_{1.9375}$	C/T	-
$Y_{0.20}Zr_{0.52}Ti_{0.13}Ce_{0.15}O_{1.90}$	C	5.1699

Table 3.3: Structures of YZTC materials containing 8 at% Ti.

Formula	Type	Cubic unit cell/ Å
$Y_{0.15}Zr_{0.52}Ti_{0.08}Ce_{0.25}O_{1.925}$	C	5.2055
$Y_{0.15}Zr_{0.57}Ti_{0.08}Ce_{0.20}O_{1.925}$	C	5.2024
$Y_{0.15}Zr_{0.62}Ti_{0.08}Ce_{0.15}O_{1.925}$	C	5.1733
$Y_{0.20}Zr_{0.52}Ti_{0.08}Ce_{0.20}O_{1.90}$	C	5.2000
$Y_{0.20}Zr_{0.57}Ti_{0.08}Ce_{0.15}O_{1.90}$	C	5.1810
$Y_{0.10}Zr_{0.52}Ti_{0.08}Ce_{0.30}O_{1.95}$	C/T	-
$Y_{0.125}Zr_{0.47}Ti_{0.08}Ce_{0.325}O_{1.9375}$	C	5.2232
$Y_{0.125}Zr_{0.52}Ti_{0.08}Ce_{0.275}O_{1.9375}$	C	5.2116
$Y_{0.125}Zr_{0.57}Ti_{0.08}Ce_{0.225}O_{1.9375}$	C	5.1950
$Y_{0.20}Zr_{0.62}Ti_{0.08}Ce_{0.10}O_{1.90}$	C	5.1622
$Y_{0.125}Zr_{0.62}Ti_{0.08}Ce_{0.175}O_{1.9375}$	C	5.1865

Table 3.4: Structures of YZTC materials containing 3 at% Ti.

Formula	Type	Cubic unit cell/ Å
$Y_{0.20}Zr_{0.62}Ti_{0.03}Ce_{0.15}O_{1.90}$	C	5.1868
$Y_{0.15}Zr_{0.62}Ti_{0.03}Ce_{0.20}O_{1.925}$	C	5.1991
$Y_{0.20}Zr_{0.57}Ti_{0.03}Ce_{0.20}O_{1.90}$	C	5.1956
$Y_{0.15}Zr_{0.57}Ti_{0.03}Ce_{0.25}O_{1.925}$	C	5.2025
$Y_{0.20}Zr_{0.52}Ti_{0.03}Ce_{0.25}O_{1.90}$	C	5.2111
$Y_{0.15}Zr_{0.52}Ti_{0.03}Ce_{0.30}O_{1.925}$	C	5.2280
$Y_{0.125}Zr_{0.57}Ti_{0.03}Ce_{0.275}O_{19375}$	C	5.2181
$Y_{0.10}Zr_{0.62}Ti_{0.03}Ce_{0.25}O_{1.95}$	C	5.2200

From Tables 3.1-4, it appears that many of the materials, especially those with low Y or high Ti content are not single phase cubic. These materials show structures that are either a two-phase mixture of cubic and tetragonal phases, where the cubic structure is not fully stabilised or they are fully tetragonal. For example, yttria-stabilised zirconia requires at least 8 mol% of yttria to stabilise the cubic structure (8 mol% YSZ approximates to $Y_{0.15}Zr_{0.85}O_{1.925}$).

The effect of changing composition on the unit cell sizes of the cubic YZTC materials is shown in Figures 3.12 and 3.13. It was found that the unit cell increased linearly with increasing CeO_2 content and decreased with TiO_2 content. The unit cell parameters ranged from 5.111 to 5.228Å for up to 30 mol% CeO_2 content. Also, if too much Y is removed, the

structure was no longer single-phase cubic and would become either a two-phase cubic/tetragonal mixture or simply tetragonal. It is likely that the reason for this is that with only $Y_{0.10}$, this is not enough to stabilise the cubic ZrO_2 structure.

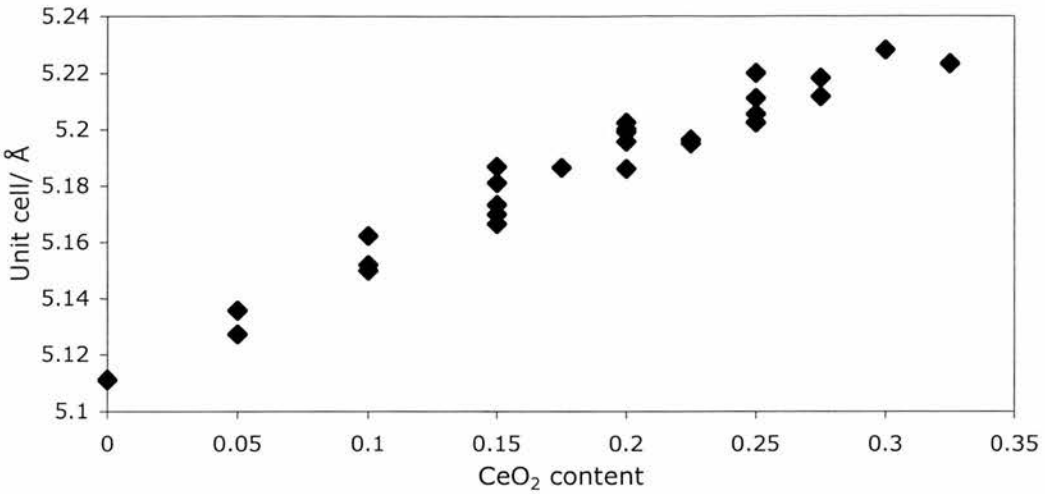

Figure 3.12: Effect of CeO_2 content on unit cell size

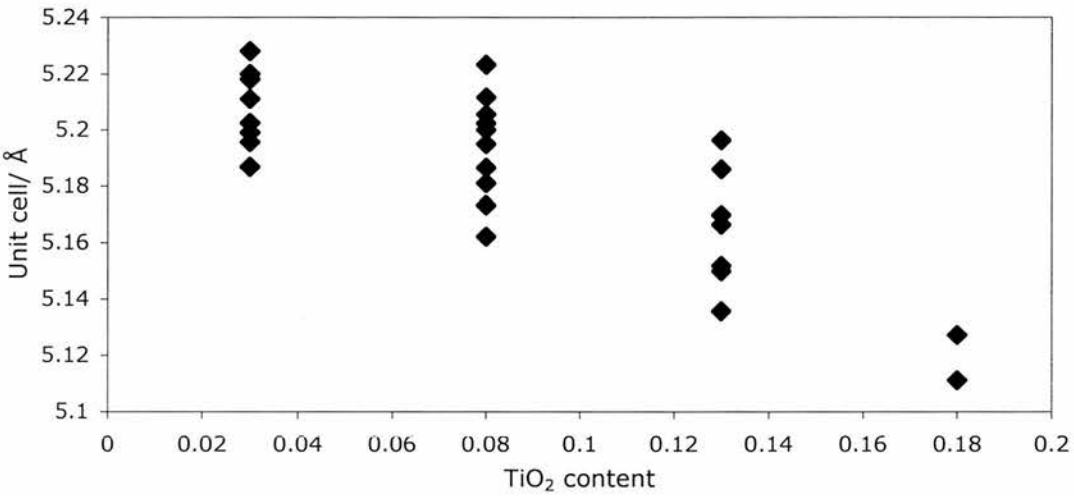

Figure 3.13: Effect of TiO_2 content on unit cell size

If there is too much Ti present, this also makes it less easy to form cubic structures. The reason for this is that in the cubic fluorite structure, the cations are in an 8-coordinate environment. The ideal ionic radius ratio of cation: anion for this environment is ($\sqrt{3}$ -1) or 0.732. The ionic radius of O^{2-} is 1.38Å [3.11] in the 4-coordinate anion environment. So, the ideal cation radius is 1.01Å in this case.

The ionic radius of Ti^{4+} is only 0.605Å, which is too small to be suited to the 8-coordinate environment and it prefers to be in a 6-coordinate environment, as is found in tetragonal structures. Thus, if a lot of Ti is present, it would be very difficult to attain a cubic structure.

With an ionic radius of 0.84Å, the Zr^{4+} cation (MO_8) is bigger than Ti^{4+}, larger than usual for a 6-coordinate environment but not quite enough to be ideally suited to the cubic 8-coordinate environment. The size of the Ti^{4+} cation could also raise the question of whether or not the Ti cations are sitting in the normal cation sites of the cubic structure or if they are located elsewhere. Finally, it appears that the amount of Y_2O_3 that can be removed from the system without distorting the structure increases with decreasing TiO_2 content, as materials containing only 3 at% Ti could still have cubic structures, even with only 10 at% Y.

3.1.2: More Detailed Unit Cell Parameter Analysis

The aim of this section was to determine the accuracy of some of the XRD results from reduction and oxidation, as there were some apparent contradictions. So, certain XRD runs were attempted again, although with an internal standard present, in order to yield more accurate results. The internal standard used was silicon (99.5% pure, 325 mesh, Alfa Aesar).

Table 3.5 lists the peak positions due to silicon, as obtained from JCPDS-ICDD powder diffraction file entry 27-1402. The structure of silicon is based on a tetrahedral framework, like diamond and the XRD pattern is cubic with an F-type lattice. The unit cell edge of silicon was 5.431Å, meaning that the silicon peaks did not interfere with the YZT or YZTC peaks in the diffraction patterns. The silicon peaks in each experiment were compared with what they should have been. Then, the differences between these results were used to correct the YZT or YZTC peaks, in the form of a 'correction curve'. The first set of experiments involved YZT, YZTC1, YZTC2 and YZTC3 materials with the silicon standard present. The unit cell parameters before and after correcting for the positions of the silicon peaks were shown in Table 3.6. Table 3.7 shows a comparison between the results with and without silicon present.

Table 3.5: Silicon standard information

(hkl)	111	220	311	400	331	422	511	440
D/ Å	3.136	1.920	1.638	1.358	1.246	1.109	1.045	0.960
2θ/ °	28.44	47.30	56.12	69.13	76.38	88.03	94.95	106.72

Table 3.6: Results for YZT, YZTC 1-3 materials

Unit cell/ Å	YZT	YZTC1	YZTC2	YZTC3
Before correction	5.1113 (1)	5.1403 (2)	5.1317 (10)	5.1591 (3)
After correction	5.1101 (1)	5.1387 (5)	5.1326 (6)	5.1607 (5)
difference	-0.0012	-0.0016	+0.0009	+0.0016

Table 3.7: Comparison of XRD results with and without silicon standard

Unit cell/ Å	YZT	YZTC1	YZTC2	YZTC3
Without Si standard	5.1124 (18)	5.1377 (27)	5.1272 (4)	5.1530 (16)
With Si standard	5.1101 (1)	5.1387 (5)	5.1326 (6)	5.1607 (5)
difference	-0.0023	+0.0010	+0.0054	+0.0077

Small differences in the unit cell lengths of YZT and YZTC materials are present when the results from experiments with and without corrections based on the silicon standard are compared. The size of the deviations ranged from –0.002 to 0.008Å. While these deviations increased with increasing Ce content, this could just be a coincidence, as the correction factors based on silicon standard peaks involved a non-linear correction.

3.2: Phase stability

In terms of the phase stability of the YZTC system, the true phase diagram required to represent this 4-component system would have to be in the form of a tetrahedron. Unfortunately, one problem with a tetrahedral quaternary phase diagram is that it is a purely 3-dimensional structure that cannot be represented properly on a 2-dimensional medium such as a computer screen or a sheet of paper. The way in which this can be worked around is shown below in Figure 3.14. Here, one can imagine the tetrahedron being sliced into triangular sections along one of the 4 axes. Each slice is a ternary diagram, where one component is assumed to be the same for all of the compositions shown on the diagram and the other three components are variable.

For the quaternary representation and ternary slices of the diagram, the component used as the 'constant' for the ternary slices was the TiO_2 content, with CeO_2, ZrO_2 and $YO_{1.5}$ as 'variable' components. The TiO_2 content was the 'constant' component, in order to keep the number of ternary phase diagrams to a minimum. Also, the TiO_2 content was very important in determining whether or not a particular YZTC composition would yield a cubic structure. Also, this would show the evolution of deviation of the YZTC structures away from cubic with increasing TiO_2 content.

The main goal in choosing what compositions to investigate was based on the doping of CeO_2 into YZT ($Y_{0.20}Zr_{0.62}Ti_{0.18}O_{1.90}$). The compositions investigated were of the general formula $Y_{0.20-x}Zr_{0.62-y}Ti_{0.18-z}Ce_{(x+y+z)}O_{1.9+x/2}$. Thus, there were restrictions placed on the scope of the ternary phase diagrams that follow.

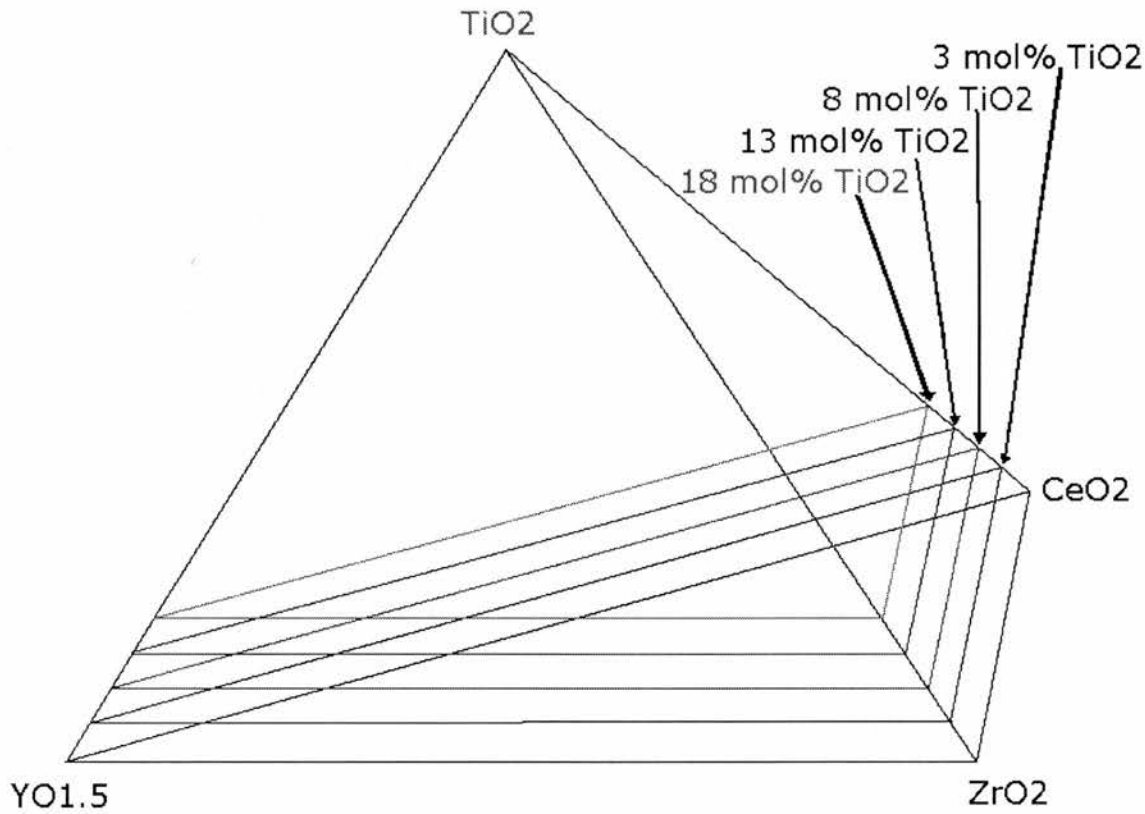

Figure 3.14: Quaternary representation and ternary slices of the YZTC phase diagram

Figure 3.15 shows the phase diagram of the Y_2O_3-ZrO_2-CeO_2 system, illustrating phase formation without TiO_2 present [3.12-3.14]. Figures 3.16 – 3.19 show the phase formation for YZTC materials containing 3 at% Ti (3.16), 8 at% Ti (3.17), 13 at% Ti (3.18) and 18 at% Ti (3.19) respectively. Single-phase cubic structures are represented by blue symbols. Purple symbols represent two-phase structures, green symbols represent tetragonal structures and grey symbols represent three-phase structures. Additional points representing compositions with no CeO_2 content were derived from prior literature [3.14]

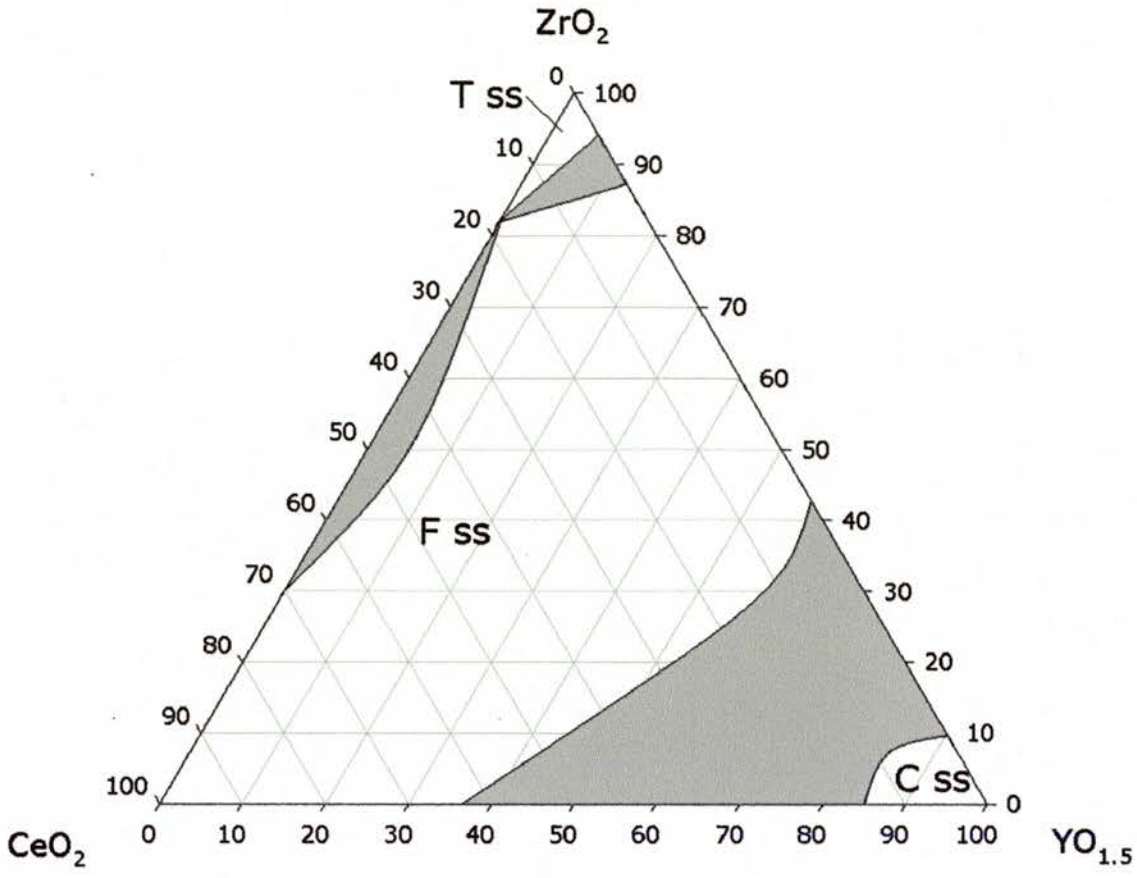

Figure 3.15: Phase diagram for Y_2O_3-ZrO_2-CeO_2 system [3.12-3.14]

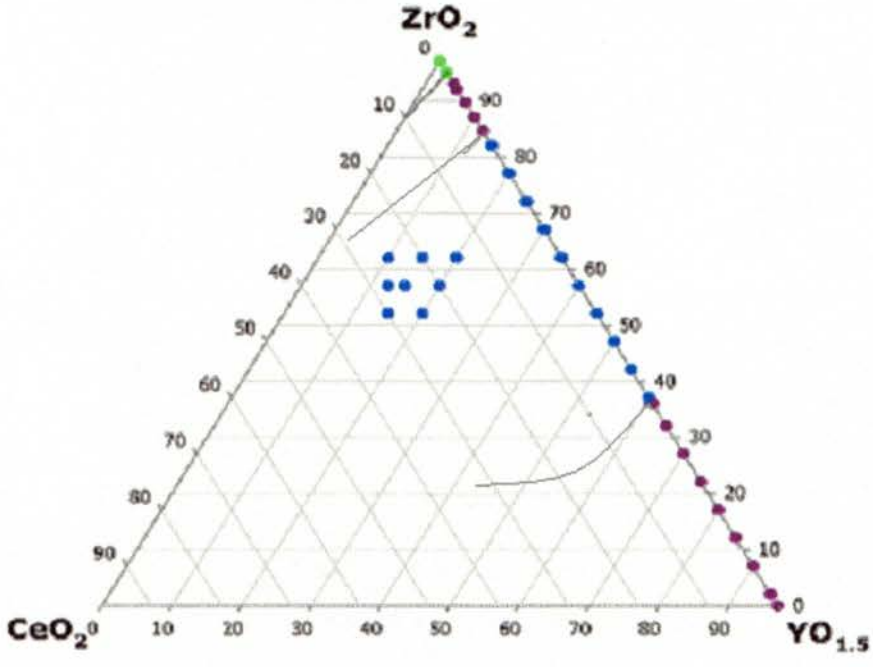

Figure 3.16: Partial phase diagram for YZTC materials containing 3 at% Ti, suggested position of phase boundary lines estimated by inspection of neighbouring sections of the ternary system.

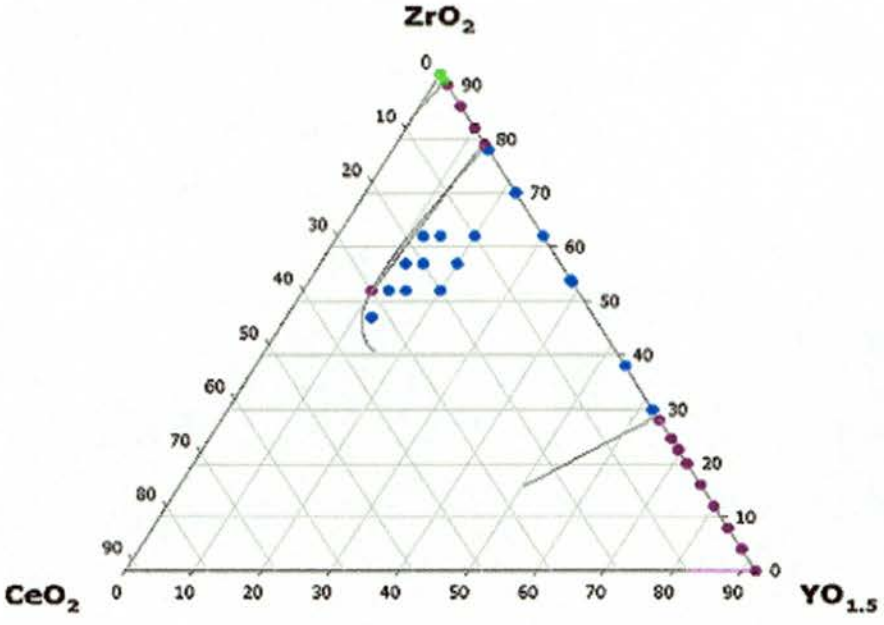

Figure 3.17: Partial phase diagram for YZTC materials containing 8 at% Ti.

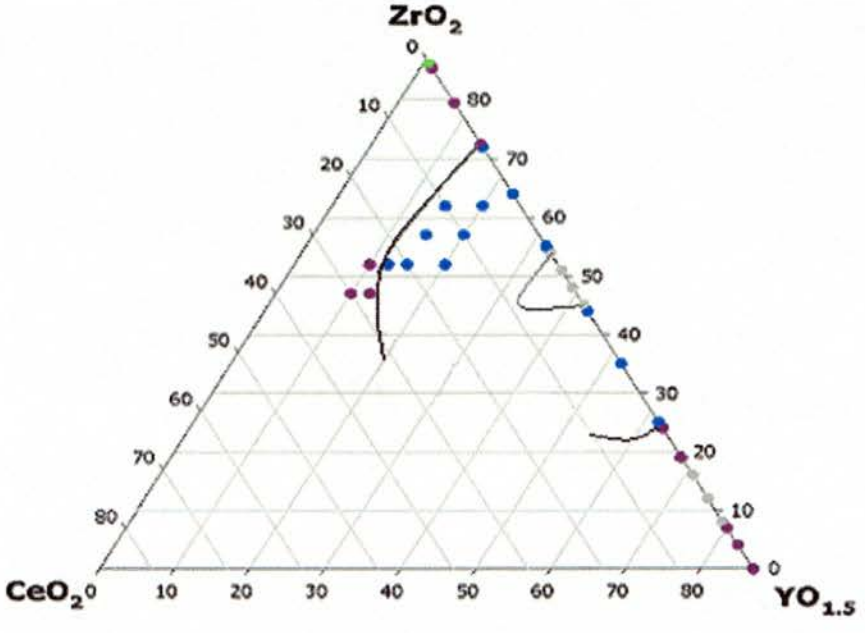

Figure 3.18: Partial phase diagram for YZTC materials containing 13 at% Ti.

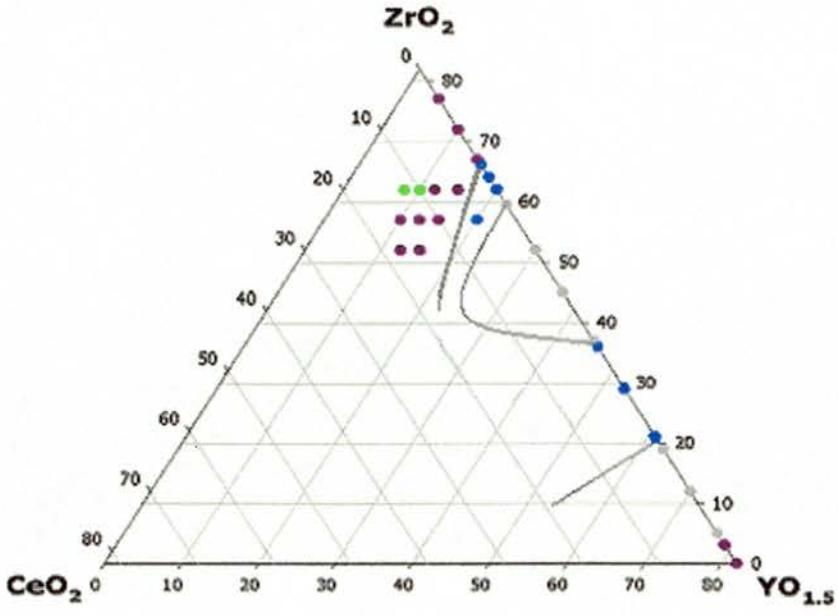

Figure 3.19: Partial phase diagram for YZTC materials containing 18 at% Ti.

From Figure 3.16, all of the examined compositions containing 3 at% Ti exhibited the cubic structure. This was even true of the compositions with less than 15 at% Y, which is the level of Y content that corresponds to 8 mol% Y_2O_3. The importance of the 8 mol% Y_2O_3 level is that it is the minimum Y_2O_3 content required to stabilise the cubic fluorite structure of the Y_2O_3-ZrO_2 system down to 1,000°C. The lowest Y content was 10 at% (corresponding to 5.26 mol% Y_2O_3) and the cubic structure was still maintained. Perhaps the key to the cubic structure being so stable is that the Ti content is very low. This is probably helped by the compositions containing 15-30 at% Ce, as the size effect of the large Ce cations can help stabilise the cubic structure. Thus, it is possible to stabilise the cubic structure of YZTC compositions with lower levels of Y_2O_3 than is required for stabilising the cubic structure of YSZ. In the later diagrams for compositions containing higher Ti content, the cubic structure gets more and more difficult to obtain.

From Figure 3.17, the vast majority of compositions examined containing 8 at% Ti exhibited the cubic structure. The only composition that did not show a perfectly cubic structure for this set of compositions was the one that contained 10 at% Y. That particular composition yielded a two-phase mixture of cubic and tetragonal phases. The compositions containing at least 12.5 at% Y exhibited the cubic structure and this corresponds to a Y_2O_3 content of 6.67 mol%. While there is a minimum limit for the amount of Y_2O_3 required for cubic YZTC compositions containing 8 at% Ti, this limit of 6.67 mol% is still less than the 8 mol% Y_2O_3 required for cubic YSZ.

From Figure 3.18, it is shown that the cubic structure for YZTC is more difficult to obtain for compositions containing 13 at% Ti. All compositions that contain 15 and 20 at% Y exhibited the cubic structure and at the 12.5 at% Y level, the system is at the borderline between single-phase cubic and the two-phase mixtures. This is shown where the composition $Y_{0.125}Zr_{0.52}Ti_{0.13}Ce_{0.225}O_{1.9375}$ is cubic but $Y_{0.125}Zr_{0.47}Ti_{0.13}Ce_{0.275}O_{1.9375}$ is two-phase. Thus, the limiting composition for the cubic structure for YZTC materials containing 13 at% Ti is $Y_{0.125}Zr_{0.52}Ti_{0.13}Ce_{0.225}O_{1.9375}$. The compositions containing 10 at% Y were all two-phase mixtures.

For compositions at this low Y and high Ce end of the diagram, the compositions were two-phase when the Ce content was 25 at% or higher. This implies that there is a limit to how much CeO_2 can be added (22.5 – 25 at%) to the structure with that amount of Ti present.

In Figure 3.19, however, it is shown that it is very difficult to get a cubic structure for a YZTC composition containing 18 at% Ti. Only the compositions containing 20 at% Y were cubic. Most of the compositions were two-phase and they contained 10-15 at% Y and there appears to be a borderline between the two-phase compositions and the single-phase tetragonal compositions. The maximum limiting composition for the tetragonal structure is $Y_{0.10}Zr_{0.62}Ti_{0.18}Ce_{0.10}O_{1.95}$, in that any compositions with higher Y or Ce content are in the two-phase region. It also appeared that for low Y content (10 at% Y or less), the structure moved away from tetragonal to being two-phase with increasing Ce content. Thus, it appears that the solubility of Ce into cubic YZT containing 18 at% Ti is very low, although the Ti and Y content also have their parts to play. Thus, it appears that increasing Ti^{4+} content leads to reducing the solubility of Ce^{4+} into the cubic YZT phase.

The fact that the cubic structure is becoming more and more difficult to obtain with high Ti content is due to disruption caused by the Ti cations being in 8-coordinate cubic sites that they are too small for that type of site. Ti cations are more suited to 6-coordinate environments. Also, low Y content helps hinder the cubic structure, as there would be less oxygen vacancies and large cations present to help stabilise the structure.

Overall, it appears that the main limiting factors in terms of obtaining cubic structures in the YZTC system are decreasing Y and increasing Ti content. It appears that Ti content has more of a limiting effect on cubic structures than the Y content. This is shown in the four phase diagrams when the increasing Ti content makes it more and more difficult to obtain single-phase cubic structures, in that the cubic structure requires more and more yttria to stabilise it. At the 3 at% Ti level, the cubic structure could be stabilised with only 5.26 mol% Y_2O_3, whereas 6.67 mol% Y_2O_3 was required for the 8 at% Ti compositions. For the 13 at%

Ti compositions, however, it was possible to stabilise the cubic structure at some cases with only 6.67 mol% Y_2O_3 but 8 mol% was required to be absolutely certain. Finally, for the 18 at% Ti compositions, at least 11 mol% Y_2O_3 was required for obtaining cubic structures.

The fact that more and more Y was needed to obtain a cubic structure for compositions containing more and more Ti was also true for the Y_2O_3-TiO_2-ZrO_2 (YZT) system, as indicated in additional points in the ternary phase diagrams. It was found that increasing the amount of Y^{3+} increased the solubility of Ti^{4+} in the YZT system, allowing more Ti^{4+} to be incorporated into the cubic phase. The explanation given for this behaviour was that in the defect fluorite structure, there were a lot of oxygen vacancies (especially due to the lower valency Y cations). This allowed the Ti cations to attain the preferred 6-coordinate environment within the structure [3.14].

It was also said that in stabilised ZrO_2, these vacancies that would normally associate with the Zr cations can also associate with small dopant cations to form MO_6 polyhedra [3.15]. Thus, where the Y content is high enough, the oxygen vacancies help the Ti cations into a coordination environment that is more suitable for them.

3.3: TGA reduction

3.3.1: Reduction in 5% H_2/ Argon

Quantitative determinations on the reduction of YZTC materials involved TGA experiments on some of the materials prepared. The first run carried out was a 'blank', where there was no sample present in the sample pan and the experimental conditions used were the same as those used in the main experiments. This 'blank' was used as a baseline run, from which corrections could be made on the main experimental runs for baseline drift and buoyancy. The TGA plots for sample runs were shown in Figures 3.20 to 3.25. For these diagrams, corrections for buoyancy and/ or baseline drift were not determined until after the blank run was carried out.

The results were shown in Table 3.8. The first mass loss stage involves the mass change after heating from ambient to 350°C and is likely to be due to moisture present. The second mass loss stage involves the mass change after heating from 350°C to 950°C and should indicate the mass change due to sample reduction. From Figure 3.26, the corrections that had to be made from the blank were as shown in Table 3.9 and Table 3.10 represents the results from Table 3.8 corrected for the blank. The blank showed two apparent mass loss

stages, like the other runs, so the magnitudes of these apparent losses were subtracted from the corresponding mass change stages on the other runs.

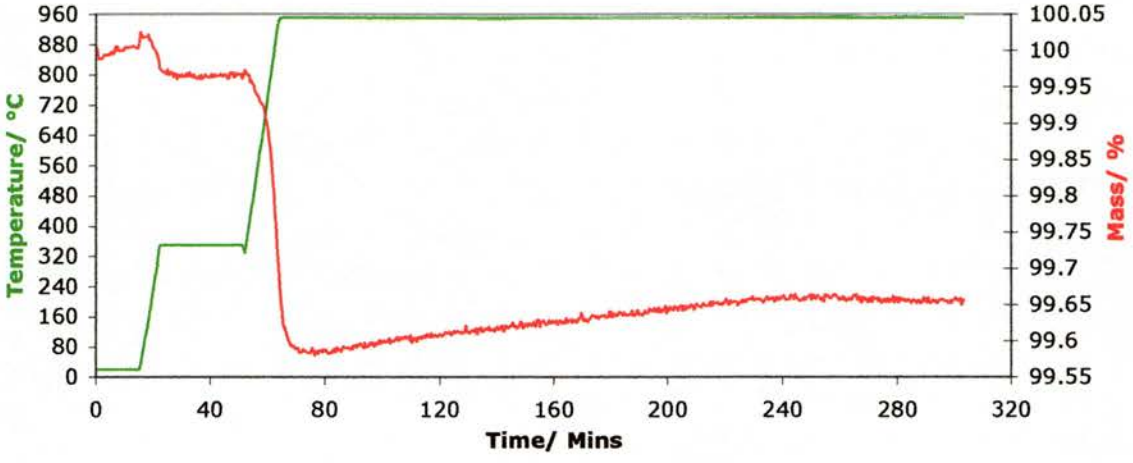

Figure 3.20: TGA plot for $Y_{0.20}Zr_{0.62}Ti_{0.13}Ce_{0.05}O_{1.90}$ (Mass: 27.87 mg)

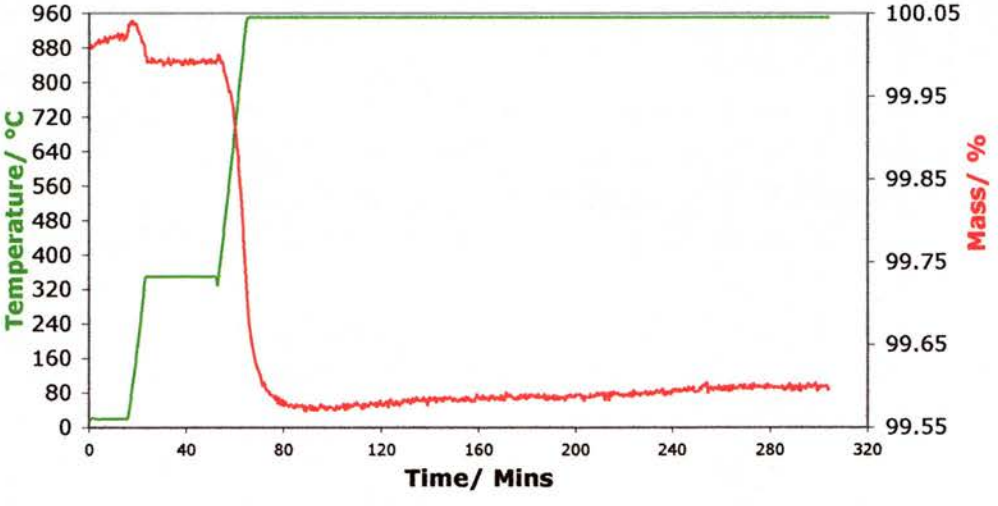

Figure 3.21: TGA plot for $Y_{0.20}Zr_{0.57}Ti_{0.18}Ce_{0.05}O_{1.90}$ (Mass: 28.34 mg)

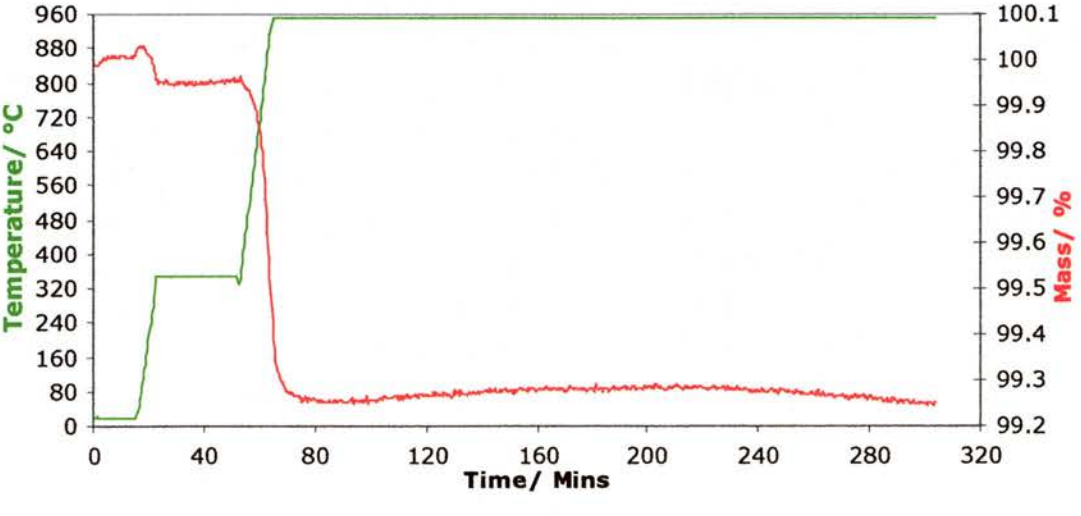

Figure 3.22: TGA plot for $Y_{0.20}Zr_{0.57}Ti_{0.13}Ce_{0.10}O_{1.90}$ (Mass: 20.10 mg)

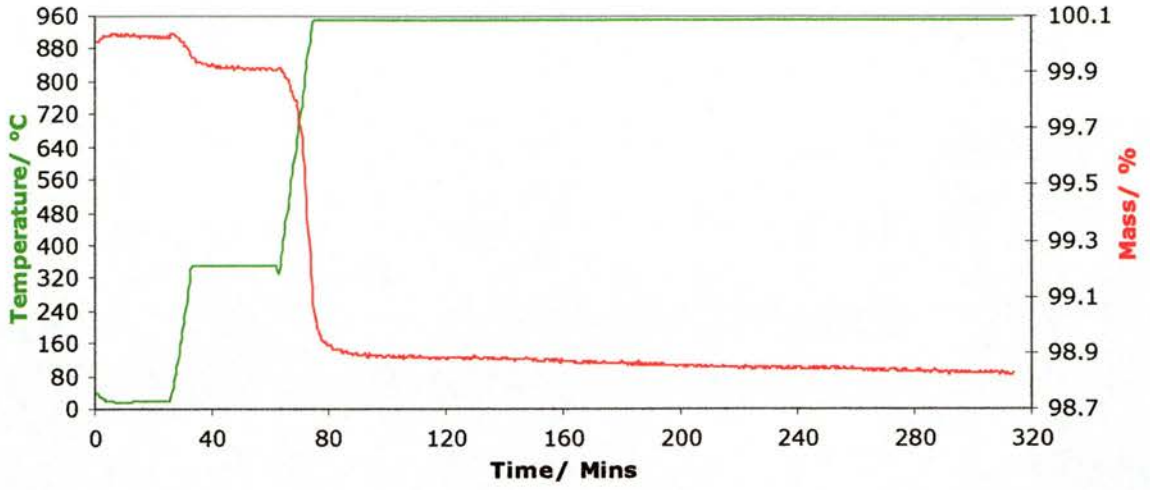

Figure 3.23: TGA plot for $Y_{0.15}Zr_{0.57}Ti_{0.13}Ce_{0.15}O_{1.925}$ (Mass: 26.33 mg)

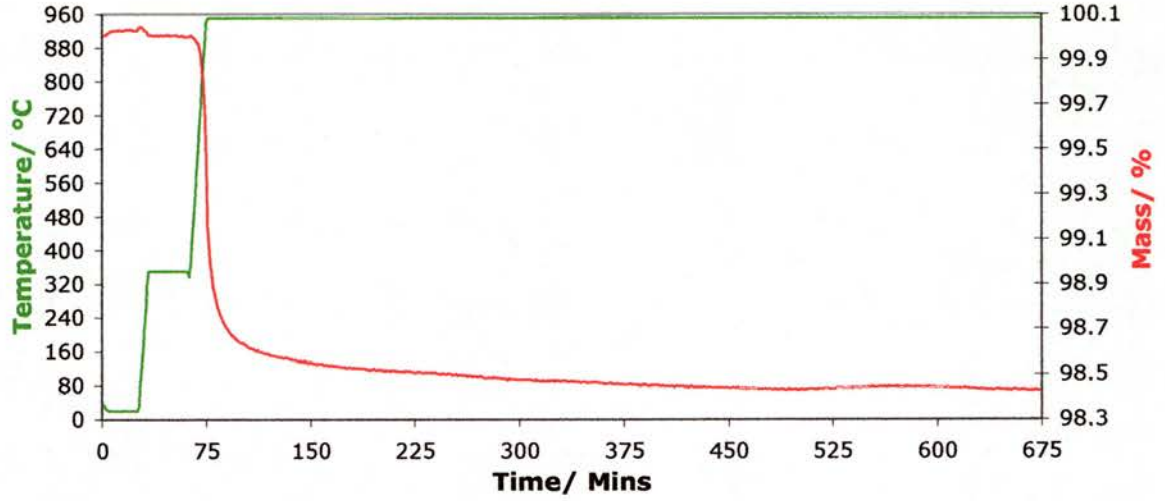

Figure 3.24: TGA plot for $Y_{0.15}Zr_{0.52}Ti_{0.08}Ce_{0.25}O_{1.925}$ (Mass: 32.71 mg)

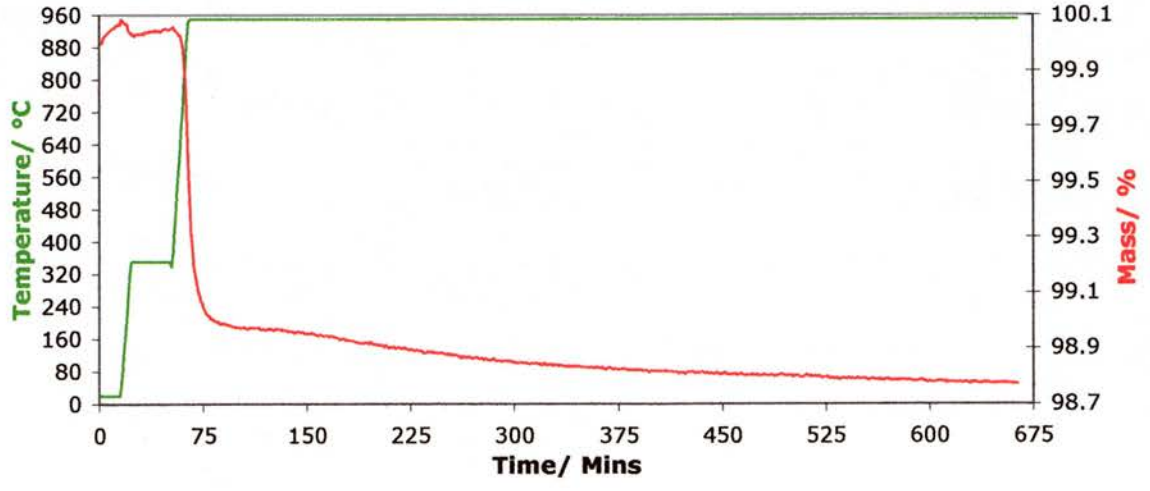

Figure 3.25: TGA plot for $Y_{0.15}Zr_{0.57}Ti_{0.08}Ce_{0.20}O_{1.925}$ (Mass: 24.95 mg)

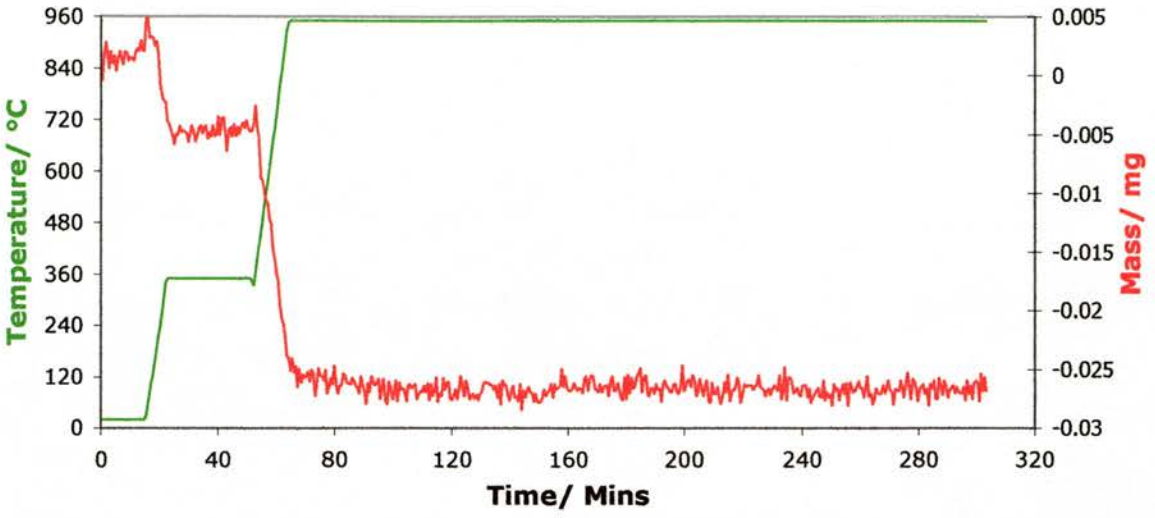

Figure 3.26: TGA plot for empty pan

Table 3.8: Uncorrected TGA reduction results

Material	Mass/ mg	Mass loss 1/ % (μg)	Mass loss 2/ % (μg)
$Y_{0.20}Zr_{0.62}Ti_{0.13}Ce_{0.05}O_{1.90}$	27.870	0.0424 (11.82)	0.3864 (107.70)
$Y_{0.20}Zr_{0.57}Ti_{0.18}Ce_{0.05}O_{1.90}$	28.335	0.0321 (9.10)	0.4178 (110.19)
$Y_{0.20}Zr_{0.57}Ti_{0.13}Ce_{0.10}O_{1.90}$	20.102	0.0630 (12.66)	0.6980 (140.31)
$Y_{0.15}Zr_{0.57}Ti_{0.13}Ce_{0.15}O_{1.925}$	26.329	0.1176 (30.96)	1.0825 (285.01)
$Y_{0.15}Zr_{0.52}Ti_{0.08}Ce_{0.25}O_{1.925}$	32.705	0.0306 (10.01)	1.5614 (510.66)
$Y_{0.15}Zr_{0.57}Ti_{0.08}Ce_{0.20}O_{1.925}$	24.953	0.0401 (10.01)	1.2549 (313.14)

Table 3.9: Corrections to be applied to results in Table 3.8

Corrections	Mass stage 1/ μg	Mass stage 2/ μg
Blank	-6.37	-21.85

Table 3.10: Corrected TGA reduction results corresponding to oxygen loss on reduction

Material	Mass/ mg	Mass loss 2/ % (μg)	Formula O loss
$Y_{0.20}Zr_{0.62}Ti_{0.13}Ce_{0.05}O_{1.90}$	27.870	0.3080 (85.85)	0.023
$Y_{0.20}Zr_{0.57}Ti_{0.18}Ce_{0.05}O_{1.90}$	28.335	0.3118 (88.34)	0.026
$Y_{0.20}Zr_{0.57}Ti_{0.13}Ce_{0.10}O_{1.90}$	20.102	0.5893 (118.46)	0.044
$Y_{0.15}Zr_{0.57}Ti_{0.13}Ce_{0.15}O_{1.925}$	26.329	0.9995 (263.16)	0.077
$Y_{0.15}Zr_{0.52}Ti_{0.08}Ce_{0.25}O_{1.925}$	32.705	1.4946 (488.81)	0.122
$Y_{0.15}Zr_{0.57}Ti_{0.08}Ce_{0.20}O_{1.925}$	24.953	1.1674 (291.30)	0.093

After the TGA runs were finished, the residues from those experiments were retained for XRD determinations and their results are shown in Table 3.11.

Table 3.11: XRD results for YZTC materials before and after reduction

Unit cell/ Å	$Y_{0.20}Zr_{0.62}Ti_{0.13}Ce_{0.05}O_{1.90}$	$Y_{0.20}Zr_{0.57}Ti_{0.18}Ce_{0.05}O_{1.90}$	$Y_{0.20}Zr_{0.57}Ti_{0.13}Ce_{0.10}O_{1.90}$	$Y_{0.15}Zr_{0.57}Ti_{0.13}Ce_{0.15}O_{1.925}$
Before	5.1377 (27)	5.1272 (4)	5.1530 (16)	5.1673 (12)
After	5.1432 (4)	5.1277 (7)	5.1589 (5)	5.1854 (7)
Difference	+0.0055	+0.0005	+0.0060	+0.0181
Oxygen loss	0.023	0.026	0.044	0.077

These materials retained the cubic fluorite structure after reduction 5% H_2/Argon at 950°C. Table 3.11 indicates that in general, reduction of a YZTC material in 5% H_2/ Argon causes an increase in the unit cell edge. $Y_{0.20}Zr_{0.57}Ti_{0.18}Ce_{0.05}O_{1.90}$ showed a negligible unit cell expansion due to reduction of 0.0005Å (probably due to high TiO_2 content). $Y_{0.15}Zr_{0.57}Ti_{0.13}Ce_{0.15}O_{1.925}$ showed the largest expansion of 0.0181Å that is likely to be due to its higher Ce content.

Overall, the changes in the materials upon reduction at 950°C were that the powders changed in colour from pale yellow/ brown to a medium-dark brown. Small mass changes were observed. These are likely to be due to one or some of the following effects:

a) Reduction of Ce^{4+} to Ce^{3+}

b) Reduction of Ti^{4+} to Ti^{3+}

c) Oxygen vacancies will form alongside, due to the loss of oxygen

The most likely factor is the reduction of Ce^{4+} to Ce^{3+}, as reduction of CeO_2 to CeO_{2-x} causes a change of colour from pale yellow to dark blue or black. Ti^{4+} is more difficult to reduce. It is possible, however, that the effect of reduction on unit cell size could be due to the effects of Ce and Ti reduction and resultant oxygen vacancies. This is because the changes in unit cell did not show an obvious or direct trend with Ce content. Formation of Ti^{3+} tends to reduce the size of the lattice. Thus, the change in unit cell size is the due to a combination of two effects. The mass changes on reduction as shown by TGA appear to increase with increasing Ce content, with possibly a small contribution to the mass loss from Ti reduction.

Another consideration is the extent to which the samples were reduced, with a view to whether or not the Ce^{4+} was fully reduced to Ce^{3+} at 950°C in 5% H_2/Argon. This was done by comparing the mass loss measured in TGA reduction with that predicted by the formula if all of the Ce^{4+} was reduced to Ce^{3+}, as shown in Table 3.12. The 'extent of reduction' column estimates how much of the Ce^{4+} was reduced to Ce^{3+} in 5% H_2/ Argon.

Table 3.12: Comparison between actual and predicted mass losses for reduction

Material	Mass loss 2/ %	Predicted mass loss/ %	Extent of Ce^{4+} reduction/ %
$Y_{0.20}Zr_{0.62}Ti_{0.13}Ce_{0.05}O_{1.90}$	0.3080	0.3391	90.84
$Y_{0.20}Zr_{0.57}Ti_{0.18}Ce_{0.05}O_{1.90}$	0.3118	0.3454	90.27
$Y_{0.20}Zr_{0.57}Ti_{0.13}Ce_{0.10}O_{1.90}$	0.5893	0.6644	88.70
$Y_{0.15}Zr_{0.57}Ti_{0.13}Ce_{0.15}O_{1.925}$	0.9995	0.9726	100.00
$Y_{0.15}Zr_{0.52}Ti_{0.08}Ce_{0.25}O_{1.925}$	1.4946	1.5333	97.48
$Y_{0.15}Zr_{0.57}Ti_{0.08}Ce_{0.20}O_{1.925}$	1.1674	1.2501	93.38

From Table 3.12, the mass losses due to reduction at 950°C were generally slightly lower than those predicted by the formulae of the materials studied. Almost all of the Ce^{4+} is reduced to Ce^{3+}, although the extent of reduction does vary with composition.

Another set of reduction in experiments was performed in 5% H_2/ Argon, with a different heating programme. The heating regime involved holding isothermally for 30 minutes at 25°C, then the system was heated up to 350°C, followed by holding at 350°C for 30 minutes, then heating up to 900°C and holding for at least 4 hours at 900°C.

The first run was on $Y_{0.125}Zr_{0.52}Ti_{0.08}Ce_{0.275}O_{1.9375}$ and the TGA plot is shown in Figure 3.27. This shows that there was a mass loss of 0.0135% from moisture, followed by the main mass loss that was in two stages. The first stage was during the heating up to 900°C and the first hour of holding at 900°C, over which the sample lost 1.3231% mass. The second stage of the main mass loss started just over 60 minutes into the isothermal hold, running until the end of the experiment and in this stage, the sample lost a further 0.2379% mass. Thus, over the main mass loss from 350-900°C, the total mass loss was 1.5610% due to reduction.

It is predicted that for the Ce content to be fully reduced from Ce^{4+} to Ce^{3+}, this would involve a mass loss of 1.6677%. So, based on the measured mass loss, which was 93.6% of the predicted mass loss, the sample was almost fully reduced.

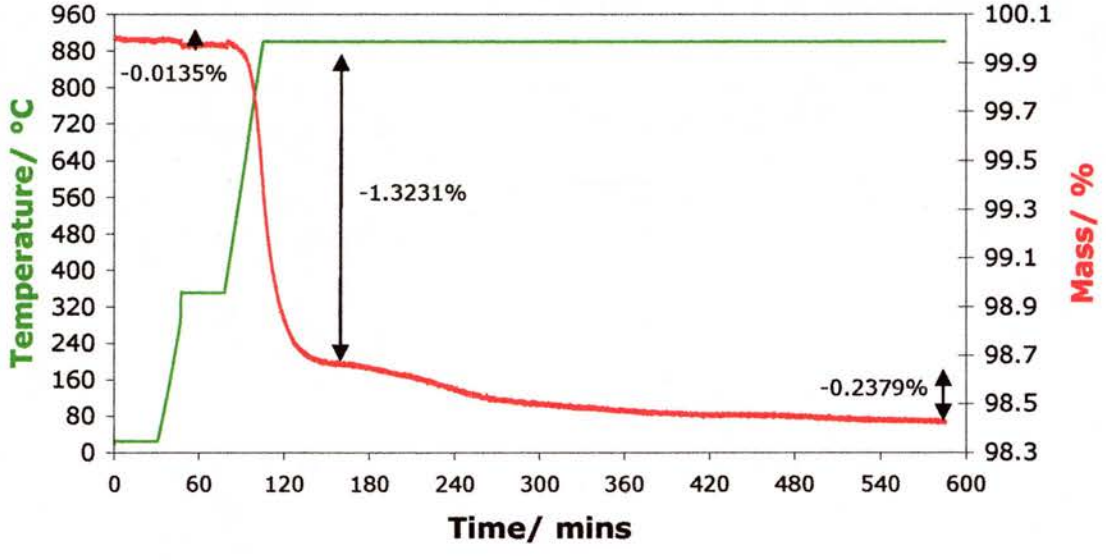

Figure 3.27: TGA plot of $Y_{0.125}Zr_{0.52}Ti_{0.08}Ce_{0.275}O_{1.9375}$.

The second experiment in this set was done on $Y_{0.20}Zr_{0.52}Ti_{0.08}Ce_{0.20}O_{1.90}$. The profile of this experiment is shown in Figure 3.28. This shows that the reduction was not complete, even after holding at 900°C for just over 6 hours. The mass loss due to moisture (up to 350°C) was 0.0413% and the mass loss stage due to reduction indicated that the process was not complete after that amount of time, as the mass trace had not settled down to a plateau during that time and was still falling at the end of the experiment. The mass loss of the incomplete reduction stage was 0.8263%. The level of mass loss required to fully reduce the Ce^{4+} content

higher extent of reduction would have been obtained if the isothermal hold was extended even longer. The low extent of reduction is due to the powder particles being too large.

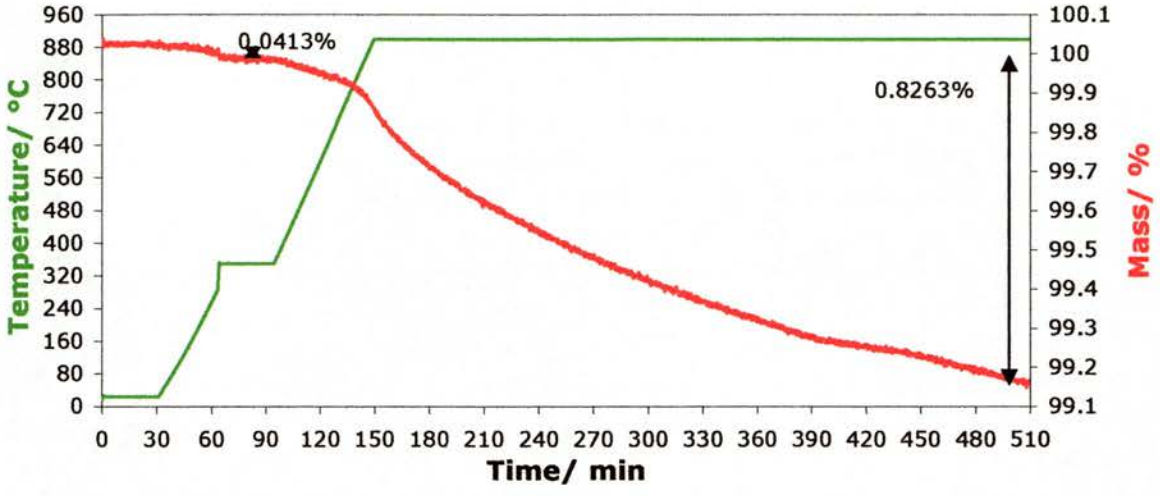

Figure 3.28: TGA plot for the reduction of $Y_{0.20}Zr_{0.52}Ti_{0.08}Ce_{0.20}O_{1.90}$ at 900°C.

3.3.2: Reduction in argon

These experiments involved looking at the reduction of the YZTC materials up to 900°C in argon. The heating regime involved holding isothermally for 30 minutes at 25°C, then the system was heated up to 350°C, followed by holding at 350°C for 30 minutes, then heating up to 900°C and holding for at least 4 hours at 900°C. The heating rates used ranged from 10 - 20°C min^{-1} and the atmospheres used were argon and 5% H_2/ argon.

The general appearance of the runs was as follows: the first mass loss stage involves the mass change after heating from ambient to 350°C and is likely to be due to moisture present. The second mass loss stage involves the change in mass after heating from 350°C to 950°C and should indicate the mass change due to reduction of the samples.

Firstly, a 'blank' experiment was carried out using an empty sample pan under the same conditions as the other experiments, in order to determine if there were any mass effects present due to buoyancy or baseline drift. This is illustrated in Figure 3.29. This 'blank' run showed two mass loss stages. The first stage represented the change in mass from holding isothermally at ambient to the isothermal hold at 350°C. The second stage represented the mass change from heating up from 350°C to the end of the isothermal hold at 900°C. In these cases, the first mass stage showed a loss of 10.75 μg. In the second stage, there was a mass loss of 23.32 μg during heating, although there was some upwards drift of 3.55 μg during the isothermal hold, leading to an overall mass loss of 19.77 μg.

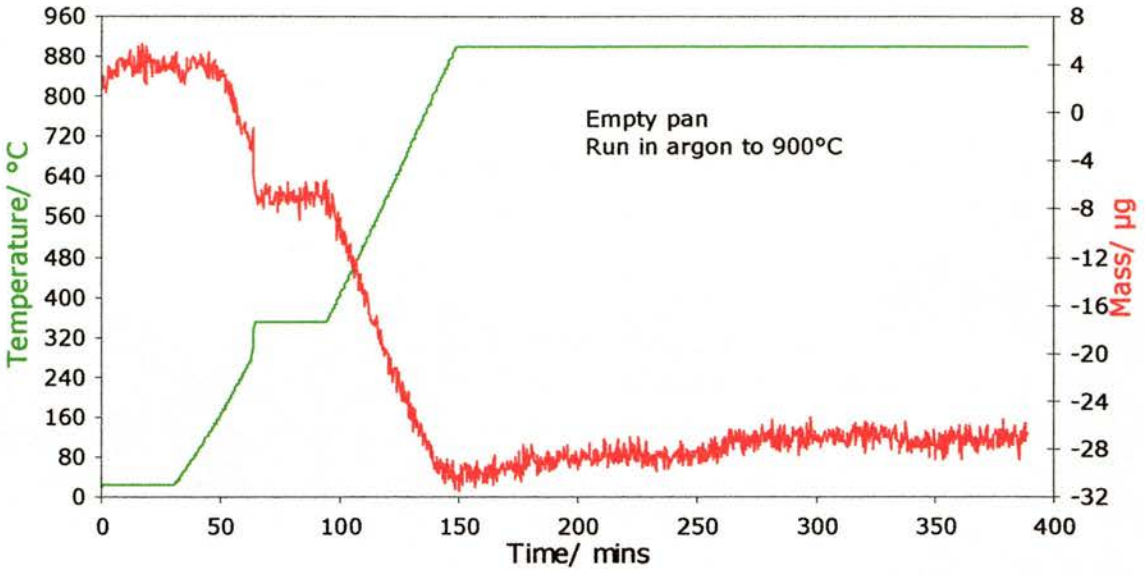

Figure 3.29: TGA plot of empty pan

The first sample was $Y_{0.20}Zr_{0.52}Ti_{0.08}Ce_{0.20}O_{1.90}$ and the TGA plot is shown in Figure 3.30.

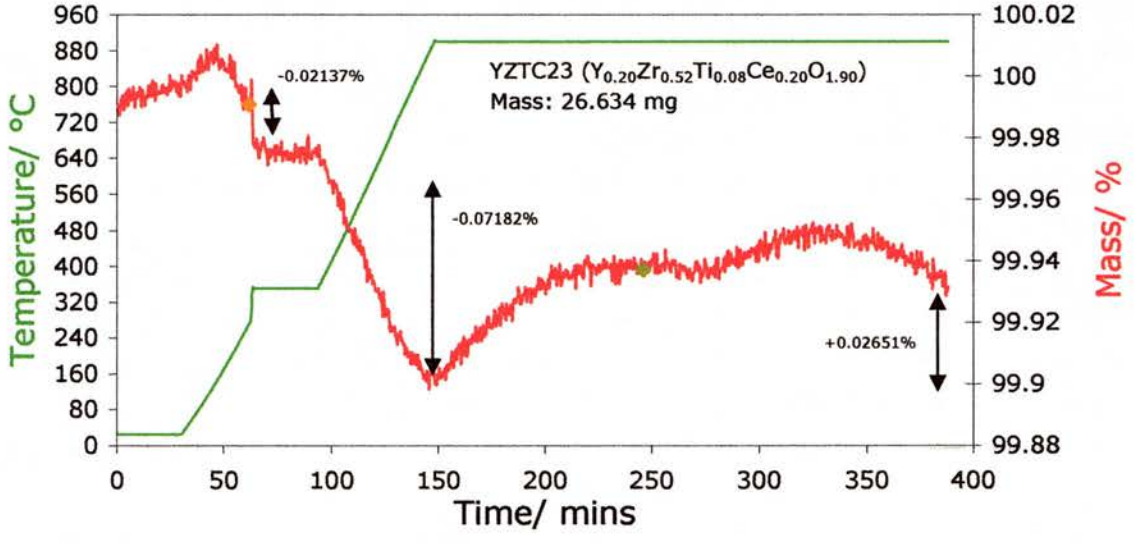

Figure 3.30: TGA plot in argon for $Y_{0.20}Zr_{0.52}Ti_{0.08}Ce_{0.20}O_{1.90}$.

From Figure 3.30, there was a small mass loss up to 350°C. The second mass loss was an event that peaked at the point when the isothermal hold at 900°C began. This led to a mass loss, followed by some upward drift during the isothermal hold. Overall, these mass losses stages were 5.69 and 12.07µg respectively. When corrected for background, however, these mass changes became small mass gains. The second run involved the reduction of $Y_{0.20}Zr_{0.57}Ti_{0.08}Ce_{0.15}O_{1.90}$. The resultant plot from this run is shown as Figure 3.31.

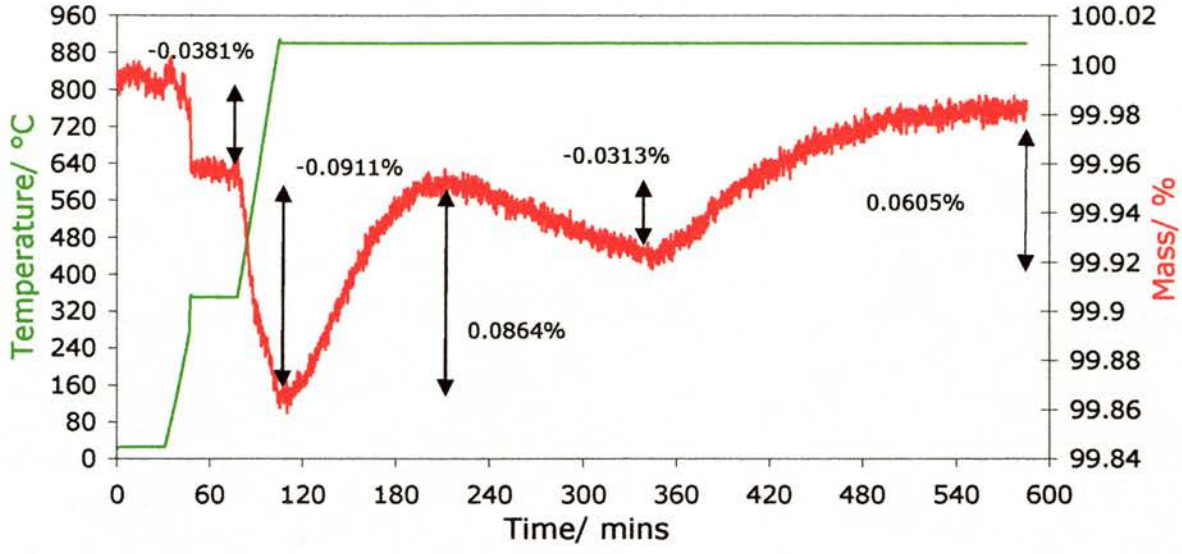

Figure 3.31: TGA plot of $Y_{0.20}Zr_{0.57}Ti_{0.08}Ce_{0.15}O_{1.90}$

From Figure 3.31, there was an initial mass loss up to 350°C of 0.0381%. Then, in the second heating stage, there was a mixture of mass losses and gains during the isothermal hold at 900°C. Overall, the mass trace indicated a small mass gain.

The third run involved the reduction of $Y_{0.20}Zr_{0.52}Ti_{0.03}Ce_{0.25}O_{1.90}$. The resultant plot from this run is shown as Figure 3.32. This shows behaviour similar to the previous run, where in the second heating/ mass loss stage, the mass falls, then rises and falls during the isothermal hold at 900°C. Overall, the TGA experiments in argon indicate that there were small mass gains, which may make sense later on.

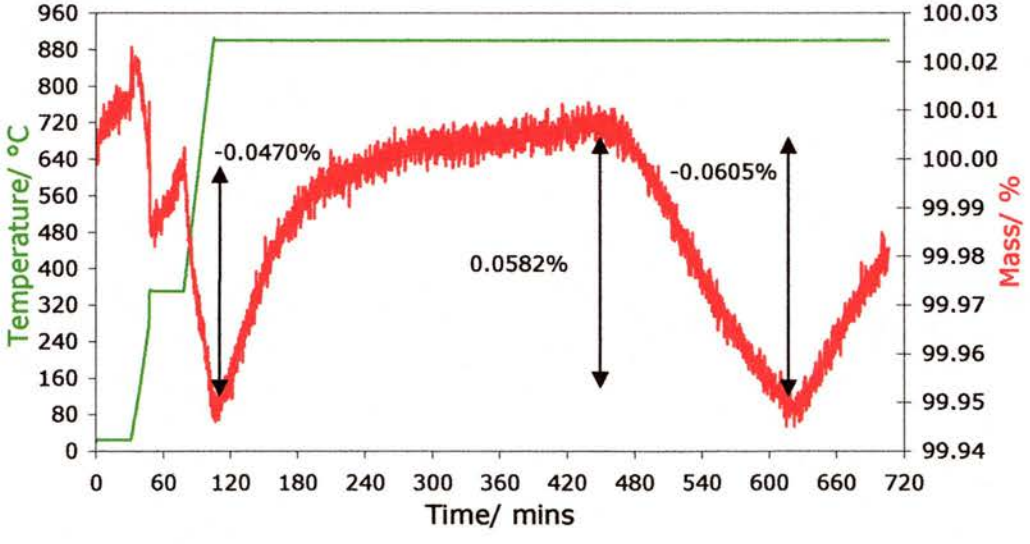

Figure 3.32: TGA plot of $Y_{0.20}Zr_{0.52}Ti_{0.03}Ce_{0.25}O_{1.90}$.

3.4: Qualitative reduction studies

Studies on the reduction of these materials were carried out on several sets of pellets of the YZTC materials. This was done, in order to carry out reduction on a larger scale than is possible with TGA experiments. So, despite possible systematic errors, fairly good accuracy is possible.

With this form of reduction, one cannot differentiate between mass losses due to moisture and that due to reduction. Pellets are less susceptible to surface moisture than powders, so one can reasonably assume that the mass loss will be due to reduction. Masses measured in this work were subject to an uncertainty of up to ± 0.0003g.

3.4.1: Reduction in 5% H_2/ Argon

The results of several sets of measurements when reduced in 5% H_2/ Argon at 1,000°C are summarised in Table 3.13. During these experiments, pieces of copper foil were placed in the tube furnace along with the sample pellets to act as an oxygen getter. It was found that in these experiments, the copper gained very little or no mass, implying that there was no significant presence of residual oxygen or leaks.

Table 3.13: Mass losses due to reduction

	Mass loss/ %				Average	Predicted Mass loss/%	Ce Reduction Extent/ %
$Y_{0.20}Zr_{0.62}Ti_{0.18}O_{1.90}$	0.0085	0.0222			0.0154		
$Y_{0.20}Zr_{0.62}Ti_{0.13}Ce_{0.05}O_{1.90}$	0.2485	0.2323	0.2710	0.2361	0.2470	0.3391	72.84
$Y_{0.20}Zr_{0.57}Ti_{0.18}Ce_{0.05}O_{1.90}$	0.3880	0.3482	0.2794		0.3385	0.3454	98.00
$Y_{0.20}Zr_{0.57}Ti_{0.13}Ce_{0.10}O_{1.90}$	0.5966	0.6570	0.6359		0.6298	0.6644	94.79
$Y_{0.15}Zr_{0.57}Ti_{0.13}Ce_{0.15}O_{1.925}$	0.7713	0.8827	1.0001	0.8771	0.8828	0.9726	90.77
$Y_{0.15}Zr_{0.52}Ti_{0.13}Ce_{0.20}O_{1.925}$	1.3814				1.3814	1.2716	108.63
$Y_{0.15}Zr_{0.62}Ti_{0.13}Ce_{0.10}O_{1.925}$	0.5184	0.6554			0.5869	0.6615	88.72
$Y_{0.15}Zr_{0.62}Ti_{0.08}Ce_{0.15}O_{1.925}$	1.0167	0.9992			1.0080	0.9558	105.46
$Y_{0.125}Zr_{0.52}Ti_{0.13}Ce_{0.225}O_{1.9375}$	1.4866				1.4866	1.4140	105.13
$Y_{0.20}Zr_{0.52}Ti_{0.08}Ce_{0.20}O_{1.90}$	1.0732				1.0732	1.2552	85.50
$Y_{0.20}Zr_{0.57}Ti_{0.08}Ce_{0.15}O_{1.90}$	0.8948				0.8948	0.9598	93.23
$Y_{0.125}Zr_{0.47}Ti_{0.08}Ce_{0.325}O_{1.9375}$	1.8056				1.8056	1.9351	93.31
$Y_{0.125}Zr_{0.52}Ti_{0.08}Ce_{0.275}O_{1.9375}$	1.6162				1.6162	1.6677	96.91
$Y_{0.125}Zr_{0.57}Ti_{0.08}Ce_{0.225}O_{1.9375}$	1.5246	1.3524			1.4385	1.3903	103.47
$Y_{0.20}Zr_{0.62}Ti_{0.03}Ce_{0.15}O_{1.90}$	0.9643				0.9643	0.9434	102.22
$Y_{0.15}Zr_{0.62}Ti_{0.03}Ce_{0.20}O_{1.925}$	1.2772	1.1734			1.2253	1.2293	99.67

Table 3.13 suggests that after 48+ hours in 5% H_2/Argon at 1,000°C, all but three of the YZTC compositions showed mass losses that indicated at least 90% of the Ce^{4+} was reduced to Ce^{3+} or even full reduction. The extent of reduction in the other three compositions ranged from 72.8 to 88.7%, which could be due to the samples being of higher density than

the others, these compositions could be less susceptible to reduction than the others or there could be other factors that may have been exposed to as hot or reducing an environment. The compositions that were not as fully reduced were $Y_{0.20}Zr_{0.62}Ti_{0.13}Ce_{0.05}O_{1.90}$, $Y_{0.15}Zr_{0.62}Ti_{0.13}Ce_{0.10}O_{1.925}$ and $Y_{0.20}Zr_{0.52}Ti_{0.08}Ce_{0.20}O_{1.90}$. The YZT $Y_{0.20}Zr_{0.62}Ti_{0.18}O_{1.90}$ did not appear to lose mass at all, as the amount of mass loss observed was within the limits of uncertainty in the mass measurement. Thus, it is doubtful that YZT lost mass at all.

There was no trend between the extent of reduction of Ce and formula to help explain this situation, although it was found that the amount of mass lost due to reduction increased with increasing Ce content.

XRD studies were done on some of the reduced materials to examine the effect of reduction on the structure. It was found that the cubic structure was maintained, although the reduction caused the unit cell parameters to increase by different amounts. The unit cell parameters of reduced materials were shown in Table 3.14.

Table 3.14: Effects of reduction on unit cell size.

Formula	a (reduced)/ Å		Average	a (non-reduced)/ Å	Δa/ Å
$Y_{0.20}Zr_{0.62}Ti_{0.13}Ce_{0.05}O_{1.90}$	5.1349	5.1397	5.1373	5.1357	0.0016
$Y_{0.20}Zr_{0.57}Ti_{0.18}Ce_{0.05}O_{1.90}$	5.1299	5.1277	5.1288	5.1272	0.0016
$Y_{0.20}Zr_{0.57}Ti_{0.13}Ce_{0.10}O_{1.90}$	5.1633	5.1643	5.1638	5.1518	0.0120
$Y_{0.15}Zr_{0.57}Ti_{0.13}Ce_{0.15}O_{1.925}$	5.1799	5.1828	5.1814	5.1664	0.0150
$Y_{0.20}Zr_{0.62}Ti_{0.03}Ce_{0.15}O_{1.90}$	5.2087		5.2087	5.1868	0.0219
$Y_{0.15}Zr_{0.62}Ti_{0.03}Ce_{0.20}O_{1.925}$	5.2231		5.2231	5.1991	0.0240
$Y_{0.20}Zr_{0.57}Ti_{0.03}Ce_{0.20}O_{1.90}$	5.2225		5.2225	5.1956	0.0269
$Y_{0.125}Zr_{0.57}Ti_{0.08}Ce_{0.225}O_{1.9375}$	5.2217		5.2217	5.1950	0.0267
$Y_{0.125}Zr_{0.52}Ti_{0.08}Ce_{0.275}O_{1.9375}$	5.2484		5.2484	5.2116	0.0368
$Y_{0.125}Zr_{0.47}Ti_{0.08}Ce_{0.325}O_{1.9375}$	5.2765		5.2765	5.2232	0.0533

Table 3.14 indicates that reduction in 5% H_2/ Argon causes an increase in unit cell parameter of 0.0016 – 0.0533 Å. The most common effect present is that this difference increased with increasing Ce content and there was some slight indication that increasing Ti content can hinder this increase. One example was that the increase in unit cell edge was almost the same for the pair $Y_{0.20}Zr_{0.62}Ti_{0.13}Ce_{0.05}O_{1.90-\delta}$ & $Y_{0.20}Zr_{0.57}Ti_{0.18}Ce_{0.05}O_{1.90-\delta}$ at 0.0016 Å and for the pair $Y_{0.20}Zr_{0.57}Ti_{0.03}Ce_{0.20}O_{1.90-\delta}$ & $Y_{0.125}Zr_{0.57}Ti_{0.08}Ce_{0.225}O_{1.9375-\delta}$ at 0.0267 – 0.0269 Å.

It was also found that the reduction of the YZTC materials also had an effect on the colour of the samples. In the as-fired form, these materials tend to be pale yellow or light brown in colour. After reduction, there was a colour change, where the pellets became dark brown or black and when ground up, the resultant powders were brown. This is likely to be

due to the reduction of the cerium present in the material from Ce^{4+} to Ce^{3+}, as pure CeO_2 tends to darken to black or dark blue on reduction to CeO_{2-x} [3.16].

In addition, oxidation studies were carried out on the reduced materials to determine how easily these materials could revert back to normal oxygen stoichiometry. This involved oxidation of some reduced materials in oxygen at 1,000°C. It was found that the materials could be oxidised just as easily as they were reduced, as the mass gains from oxidation were within a few percent of the amount of mass lost due to reduction. Also, oxidation caused the reduced powders or pellets to change from dark brown/ black to pale yellow.

3.4.2: Reduction in argon

For comparison, one set of pellets that was used in the qualitative reduction in 5% H_2/ Argon was oxidised and reduced in argon at 1,000°C for ~60 hours. The mass changes associated with the reduction in argon were shown in Table 3.15.

Table 3.15: Mass changes on reduction in argon.

	Before reduction/ g	After reduction/ g	Mass loss/ g	Mass loss/ %
$Y_{0.20}Zr_{0.62}Ti_{0.03}Ce_{0.15}O_{1.90}$	2.7747	2.7721	0.0026	0.094
$Y_{0.15}Zr_{0.62}Ti_{0.03}Ce_{0.20}O_{1.925}$(a)	1.1650	1.1640	0.0010	0.086
$Y_{0.15}Zr_{0.62}Ti_{0.03}Ce_{0.20}O_{1.925}$(b)	3.1048	3.1057	-0.0009	-0.029
$Y_{0.20}Zr_{0.57}Ti_{0.03}Ce_{0.20}O_{1.90}$	2.2785	2.2788	-0.0003	-0.013

Table 3.15 shows that there were very small mass changes of <0.1%, much less than was observed for reduction in 5% H_2/ Argon. Two of the samples lost mass, whereas the other two gained negligible amounts of mass. $Y_{0.20}Zr_{0.57}Ti_{0.13}Ce_{0.20}O_{1.90-\delta}$ did not show any noticeable mass change at all, as the amount of mass gain was within the uncertainty limits of the balance used for measuring mass.

In terms of appearance, the samples were slightly darker than they were in the oxidised form, but not to the extent shown for reduction in 5% H_2/ Argon. Then, parts of the reduced pellets were ground up and examined by XRD, with the results shown in Table 3.16. This indicates that for these materials, the unit cell edge shrinks slightly by 0.0029 – 0.0049Å upon reduction in argon. This could imply that as the pO_2 decreases, there could be an initial shrinkage of the unit cell, followed by an expansion.

An alternative explanation is that argon at 900-1,000°C is less reducing than firing at 1,500°C in static air. In some cases, YZTC pellets were dark yellow or black in colour when fired at 1,400-1,500°C in air, implying that some of the Ce is reduced to Ce^{3+} on firing, to a

further extent than would happen in argon at 900-1,000°C. This could explain the mass gains observed here and in the TGA experiments in argon at 900°C.

Table 3.16: Unit cells before and after reduction in argon

Unit cell/ Å	Before reduction	After reduction	Difference
$Y_{0.20}Zr_{0.62}Ti_{0.03}Ce_{0.15}O_{1.90}$	5.1868	5.1834	-0.0034
$Y_{0.15}Zr_{0.62}Ti_{0.03}Ce_{0.20}O_{1.925}$	5.1991	5.1942	-0.0049
$Y_{0.20}Zr_{0.57}Ti_{0.03}Ce_{0.20}O_{1.90}$	5.1956	5.1927	-0.0029

3.5: Reduction studies at controlled pO_2 levels

3.5.1: Reduction in argon

This set of measurements involved the reduction of a range of pre-oxidised pellets in Argon for ~48 hours at 1,000°C, along with some copper foil present as an oxygen getter. To monitor the pO_2 level in the furnace, a Pt-wire jig containing a type K thermocouple and YSZ tube pO_2 sensor were placed at one end of the tube furnace.

The voltage from the sensor and the temperature reading from the thermocouple were used to calculate the pO_2 level, as per equation (a). V is the voltage signal from the YSZ sensor tube, T is the temperature from the thermocouple, pO_2' is the reference pO_2 level inside the sensor tube (0.209 atm, the pO_2 of air at normal atmospheric pressure) and pO_2'' is the pO_2 level that is being measured by the sensor. pO_2'' can be determined directly from equation (b).

$$V = \frac{RT}{4F}\ln\left(\frac{pO_2'}{pO_2''}\right) \text{ (a) } \quad pO_2'' = pO_2'\exp\left(\frac{-4VF}{RT}\right) \text{ (b)}$$

After letting the furnace reach 1,000°C and stay there for several hours, the pO_2 was measured using the sensor setup. The voltage from the sensor was 0.1906 V and the temperature was 963°C. From equation (b), the measured pO_2 was $1.63*10^{-4}$ atm. During the run, this calculation was repeated several times and for at least 24 hours, the pO_2 was more or less the same, although it did rise slightly to $1.65*10^{-4}$ atm a few hours before heating at 1,000°C finished. The results of reduction in argon are shown in Table 3.17.

Table 3.17: Results of reduction in argon.

	Before reduction/ g	After reduction/ g	Mass change/ g	Mass change/ %
$Y_{0.20}Zr_{0.57}Ti_{0.18}Ce_{0.05}O_{1.90}$	5.8214	5.8164	-0.0050	-0.0859
$Y_{0.15}Zr_{0.52}Ti_{0.13}Ce_{0.20}O_{1.925}$	1.8790	1.8797	+0.0007	+0.0373
$Y_{0.15}Zr_{0.62}Ti_{0.13}Ce_{0.10}O_{1.925}$	5.7606	5.7615	+0.0009	+0.0156
$Y_{0.15}Zr_{0.62}Ti_{0.08}Ce_{0.15}O_{1.925}$	5.6724	5.6708	-0.0016	-0.0282
$Y_{0.125}Zr_{0.52}Ti_{0.13}Ce_{0.225}O_{1.9375}$	5.4422	5.4369	-0.0053	-0.0974
$Y_{0.20}Zr_{0.52}Ti_{0.08}Ce_{0.20}O_{1.90}$	5.7314	5.7279	-0.0035	-0.0611
$Y_{0.20}Zr_{0.57}Ti_{0.08}Ce_{0.15}O_{1.90}$	5.7346	5.7359	+0.0013	+0.0227

From Table 3.17, it appears that there are very small mass changes (<0.1%) for the samples reduced in argon. Some of the mass changes are losses and others appear to show gains for some unknown reason (perhaps due to errors in the balance or in measuring of the masses). It is most likely that the mass gains are the norm, when taking previous results into account. In terms of appearance, all of the sample pellets were of darker shades of the original sample pellet colours. The amount of darkening of the pellets was not as extensive as has been seen for pellets reduced in 5% H_2/ Argon, however. In the case of pellets reduced in 5% H_2/ Argon, they tended to be very dark brown or black and the pellets reduced in argon were not as dark as that. This is in line with expectations, as argon is not as strong a reducing atmosphere as 5% H_2/ Argon. Overall, this suggests that in argon at 900-1,000°C, Ce^{4+} is more stable than when fired at 1,400-1,500°C in static air.

3.5.2: Reduction in 5% H_2/ Argon

In addition to the reduction in argon, the pellets reduced in argon were reduced again in the tube furnace at 1,000°C for 50 hours in 5% H_2/ Argon. As for the reduction in argon, the pO_2 was monitored using the same pO_2 sensor as was used in the previous section. The same pellets were used in this experiment, as were used in the reduction in argon. The results of this reduction are shown in Table 3.18. This showed that the cerium content of the samples was effectively fully reduced from Ce^{4+} to Ce^{3+}. In addition, the sample pellets were dark brown/ black in colour.

Table 3.18: Results of reduction in 5% H_2/ Argon.

	Before reduction/ g	After reduction/ g	Mass loss/ g	Mass loss/ %
$Y_{0.20}Zr_{0.57}Ti_{0.18}Ce_{0.05}O_{1.90}$	5.8211	5.7917	0.0294	0.5051
$Y_{0.15}Zr_{0.52}Ti_{0.13}Ce_{0.20}O_{1.925}$	1.8781	1.8531	0.0250	1.3311
$Y_{0.15}Zr_{0.62}Ti_{0.13}Ce_{0.10}O_{1.925}$	5.7609	5.7168	0.0441	0.7655
$Y_{0.15}Zr_{0.62}Ti_{0.08}Ce_{0.15}O_{1.925}$	5.6685	5.6145	0.0540	0.9526
$Y_{0.125}Zr_{0.52}Ti_{0.13}Ce_{0.225}O_{1.9375}$	5.4431	5.3635	0.0796	1.4624
$Y_{0.20}Zr_{0.52}Ti_{0.08}Ce_{0.20}O_{1.90}$	5.7278	5.6582	0.0696	1.2151
$Y_{0.20}Zr_{0.57}Ti_{0.08}Ce_{0.15}O_{1.90}$	5.7326	5.6779	0.0547	0.9542

During the course of the reduction, the pO_2 varied due to a slight increase in the flow rate, as at one point, it appeared that the gas flow had stopped for a while, so the flow rate was increased. The pO_2 was monitored at various points of the process after the tube furnace held at 1,000°C.

Early in the run, the sample temperature was 963°C and the voltage at the sensor was 0.987 V. This translated into a pO_2 level of $1.67*10^{-17}$ atm. After 1 day, the temperature was 962°C, with a sensor voltage of 1.1485 V. This resulted in a pO_2 level of $3.74*10^{-20}$ atm.

Then, in the final day of the run, the first measurement was at 966°C, with a sensor voltage of 1.123 V, yielding a pO_2 of $1.12*10^{-19}$ atm. In the final measurement before the furnace temperature was turned down, the temperature was 963°C and the sensor voltage was 1.167 V, yielding a final pO_2 level of $1.93*10^{-20}$ atm. Thus, the pO_2 level in the 5% H_2/ Argon atmosphere ranged from 10^{-17} to 10^{-20} atm and this was enough to fully reduce the sample pellets.

After this reduction, parts of the reduced pellets were ground up and examined by XRD. All of the structures were still single-phase cubic after reduction. Table 3.19 shows the effect of reduction on the unit cells of these materials. Depending on the material that was reduced, the unit cell edge increased by up to 0.023Å.

Table 3.19: Unit cells before and after reduction in 5% H_2/ Argon.

Unit cell/ Å	Before reduction	After reduction	Difference
$Y_{0.15}Zr_{0.62}Ti_{0.13}Ce_{0.10}O_{1.925}$	5.1499	5.1529 (4)	0.0030
$Y_{0.15}Zr_{0.62}Ti_{0.08}Ce_{0.15}O_{1.925}$	5.1733	5.1892 (5)	0.0159
$Y_{0.125}Zr_{0.52}Ti_{0.13}Ce_{0.225}O_{1.9375}$	5.1964	5.2171 (6)	0.0207
$Y_{0.20}Zr_{0.52}Ti_{0.08}Ce_{0.20}O_{1.90}$	5.2000	5.2230 (2)	0.0230
$Y_{0.20}Zr_{0.57}Ti_{0.08}Ce_{0.15}O_{1.90}$	5.1810	5.1962 (4)	0.0152

3.5.3: Reduction of powder in Argon

A portion of the $Y_{0.20}Zr_{0.52}Ti_{0.08}Ce_{0.20}O_{1.90}$ pellet that was reduced at 1,000°C in the previous section was ground up and re-oxidised in oxygen at 1,000°C. Then, some of the resultant powder was heated up again in argon in the tube furnace at 1,000°C, with some copper foil present to remove residual oxygen. The pO_2 sensor system used earlier in this section was used again to monitor the pO_2 of the atmosphere in the furnace. The mass of powder used was 1.1459g and according to the pO_2 sensor, the pO_2 varied between $7.9*10^{-5}$ atm and $1.0*10^{-4}$ atm.

After the reduction, the sample lost 0.0024g of mass, corresponding to a 0.2094% loss in mass. This means that the extent of reduction of the sample was 16.7%. The powder was very light brown in colour, slightly darker than the non-reduced form, which is bright yellow in colour. From XRD, the unit cell of the reduced material is 5.1925(8) Å. This unit cell parameter size is 0.0075 Å lower than the material 'as-fired' at 1,400-1,500°C and 0.0305 Å lower than the fully reduced form of the material, as was reduced in 5% H_2/ Argon. The extent of mass loss indicates that this was reduction of a fully oxidised sample in argon. This is as opposed to reduction of the material 'as-fired', which would be reduced to some extent already.

3.5.4: Reduction of powder in 'wet' 5% H_2/ Argon

Some of the $Y_{0.20}Zr_{0.52}Ti_{0.08}Ce_{0.20}O_{1.90}$ pellet that was reduced at 1,000°C previously was ground up and re-oxidised in oxygen at 1,000°C. Then, some of the resultant powder was heated up again in 'wet' 5% H_2/ Argon (5% H_2/ Argon bubbled through water) in the tube furnace at 1,000°C, with some copper foil present to remove residual oxygen. The pO_2 sensor system used earlier in this section was used again to monitor the pO_2 of the atmosphere in the furnace. The mass of powder used was 2.7178 g and according to the pO_2 sensor, the pO_2 of the environment was $4.5 - 6.0*10^{-16}$ atm.

After the reduction, the sample lost 0.0347g of mass, corresponding to a 1.2768% loss in mass. This means that the sample was fully reduced in the 'wet' 5% H_2/ Argon environment and there may have been a small amount of moisture present, as the mass loss was slightly greater than the expected 1.2552%. The unit cell of the reduced material was 5.2210(8) Å, 0.002 Å lower than when reduced in dry 5% H_2/ Argon.

The results from measurements on this material were combined to form a plot of unit cell parameter a and δ, the amount of formula oxygen lost on reduction against pO_2. This is shown in Figure 3.33. Assuming that the 'as-fired' material is already slightly reduced, the unit cell size of 5.2000 Å would correspond to a pO_2 of approximately 10^{-7} atm at 900-1,000°C and δ of 0.04.

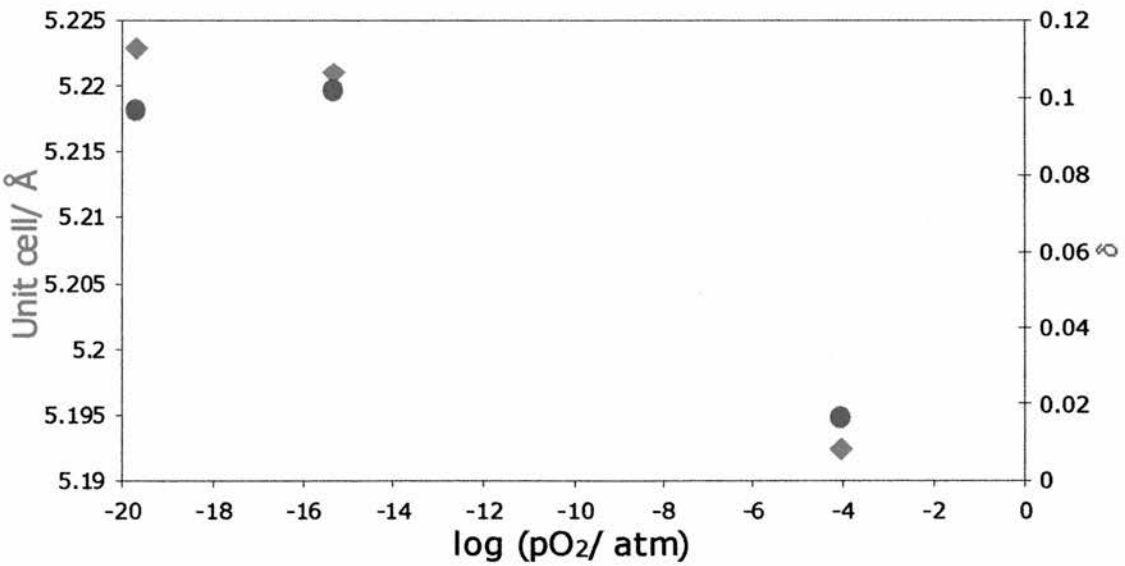

Figure 3.33: plot of a and δ vs. pO_2 for $Y_{0.20}Zr_{0.52}Ti_{0.08}Ce_{0.20}O_{1.9-\delta}$.

3.6: Summary of Reduction/ Oxidation Studies

3.6.1: Mass Changes

When reduced in argon, the main results from pellets were somewhat conflicting, in that some materials showed mass losses and others showed gains of <0.1%. Overall, the trend was a mass gain. This was most likely due to Ce^{4+} being more stable in argon at 900-1,000°C than the YZTC firing conditions of 1,400-1,500°C in static air. This also implies that the samples 'as-fired' were slightly more reduced in firing than in argon.

There was a result from the reduction of fully oxidised $Y_{0.20}Zr_{0.52}Ti_{0.08}Ce_{0.20}O_{1.90}$ powder in argon. In this case, the sample was slightly reduced, showing a mass loss of 0.2094%. This corresponded to the formula changing from $Y_{0.20}Zr_{0.52}Ti_{0.08}Ce_{0.20}O_{1.90}$ to $Y_{0.20}Zr_{0.52}Ti_{0.08}Ce_{0.20}O_{1.883}$, a loss of 0.017 O. This also implies that 17% of the Ce was reduced from Ce^{4+} to Ce^{3+}. Thus, reduction in argon is enough to reduce some, but not all of the Ce. There was a sign of reduction, as samples reduced in argon were slightly darker in colour than the oxidised form.

From the qualitative and quantitative measurements in 5% H_2/ Argon, most of the YZTC materials can be mostly or even fully reduced in 5% H_2/ Argon, although some materials tend to be more difficult to reduce than others. This was shown in Figure 3.34, where the mass loss due to reduction was compared to predicted values that are based on how much mass loss there would be if all of the Ce^{4+} was reduced to Ce^{3+}. In some cases, the mass losses are very close to the predicted values, implying that most of these materials were either mostly or even fully reduced. There are some materials that appear to be harder to reduce than others, although this trend did not follow a compositional pattern. Unsurprisingly, the amount of mass lost due to reduction increased with increasing CeO_2 content.

Another sign that implied a change in the YZTC materials when reduced in 5% H_2/ Argon was that the samples changed in colour from pale yellow/ light brown to dark brown/ black, which is almost typical of darkening that occurs when CeO_2 is reduced at low pO_2. Thus, it can be said that reduction is more prominent in 5% H_2/ Argon than it is in argon and in most YZTC materials; it is possible to fully reduce the Ce content at 1,000°C.

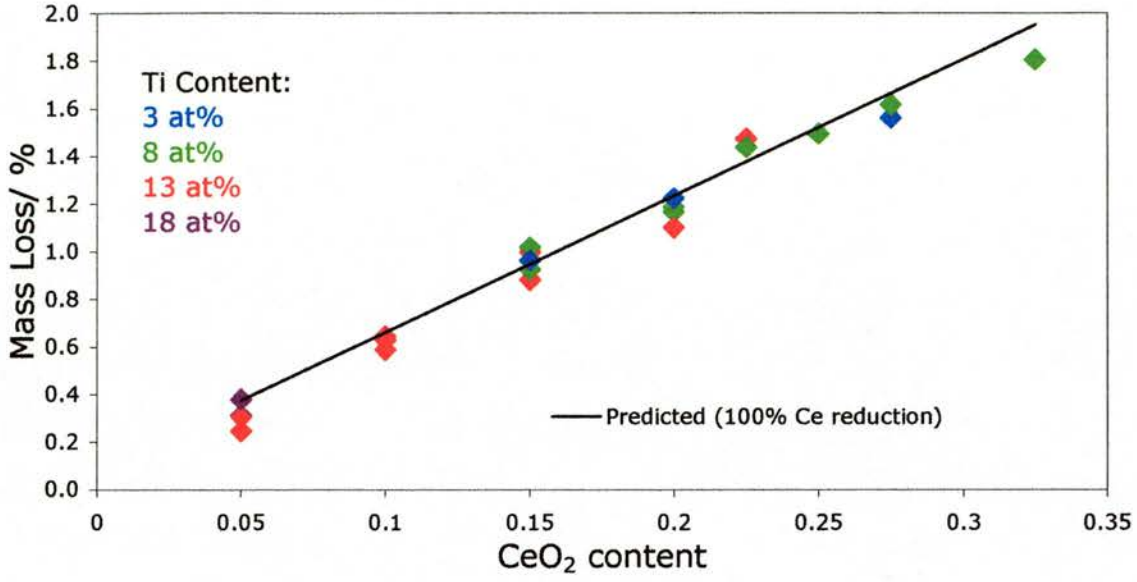

Figure 3.34: Mass losses due to reduction in 5% H_2/ Argon.

3.6.2: Structural Changes on Reduction

It was found that when a YZTC material is reduced in argon, corresponding to a pO_2 of $10^{-5} - 10^{-4}$ atm, the effects are somewhat slight. The pellets and powders change in colour from a light yellow/ brown to a light/ medium grey. The cubic structure was maintained, although the unit cell size was up to 0.0075 Å lower than 'as-fired' materials, depending on composition. This reduction in unit cell size would imply that annealing in argon at 900-1,000°C caused less reduction of Ce^{4+} than firing at 1,400-1,500°C in static air.

Reduction up to 1,000°C in 5% H_2/ Argon, corresponding to a pO_2 of ~10^{-20} atm (dry) or ~10^{-16} atm ('wet'), had a more profound effect on the structure. The reduced YZTC materials retained the cubic structure, although the unit cell increased in size. The unit cell size of the reduced samples increased linearly with increasing CeO_2 content and decreased with increasing TiO_2 content. Also, the extent of unit cell expansion increased with increasing CeO_2 content, up to 0.0533Å for a sample containing 32.5 mol% CeO_2. These trends are shown in Figures 3.35 and 3.36. Figure 3.37 shows the effect of pO_2 on unit cell in argon and 5% H_2/Argon.

Compared to the unit cell sizes in argon and 5% H_2/ Argon, the unit cells of the YZTC materials 'as-fired' at 1,400-1,500°C corresponded to a sample reduced at a pO_2 of approximately 10^{-7} atm (fired at 1,400°C) or up to 10^{-5} atm (fired at 1,500°C).

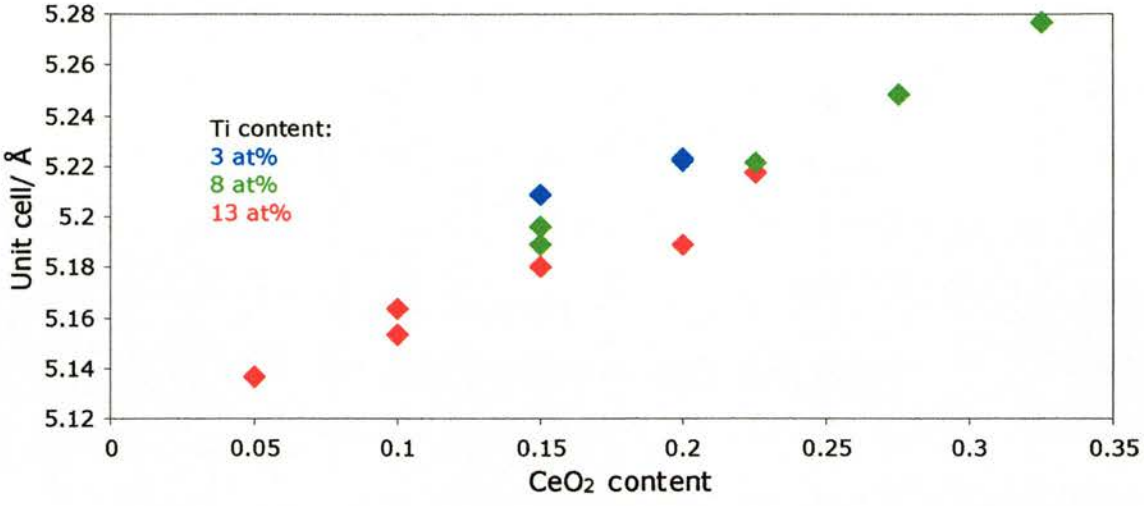

Figure 3.35: Unit cell sizes of YZTC materials reduced in 5% H_2/ Argon.

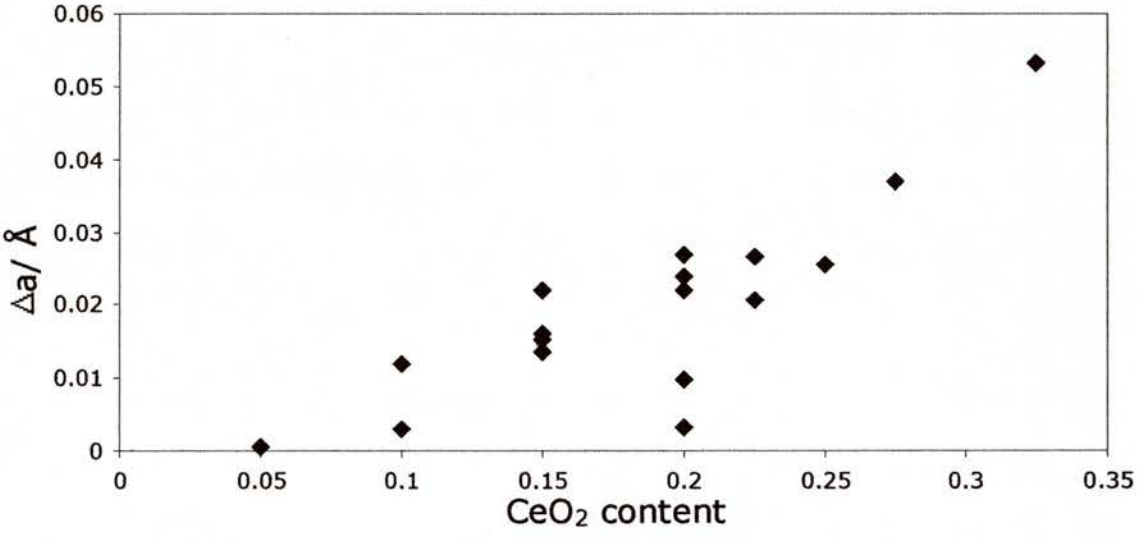

Figure 3.36: Unit cell size increase due to reduction in 5% H_2/ Argon

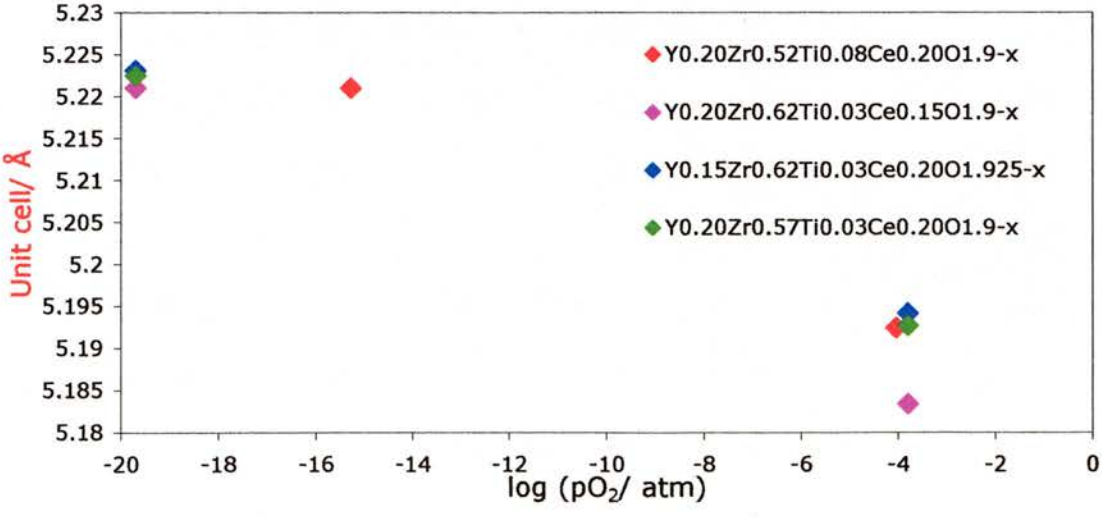

Figure 3.37: Effect of pO_2 on unit cell size

3.7: Thermal Expansion Results

3.7.1: Measurements in oxygen

The first set of measurements was carried out in oxygen on some YZTC materials up to 1,100°C. Figure 3.38 shows a typical plot of expansion with temperature.

All of the measurements behaved basically as shown in Figure 3.38. The thermal expansion coefficients (α) for the materials were calculated overall from 200-1,025°C. α is not constant between 200-1,025°C but increases with temperature, although the expansion was close to linear overall, as shown in Figure 3.39.

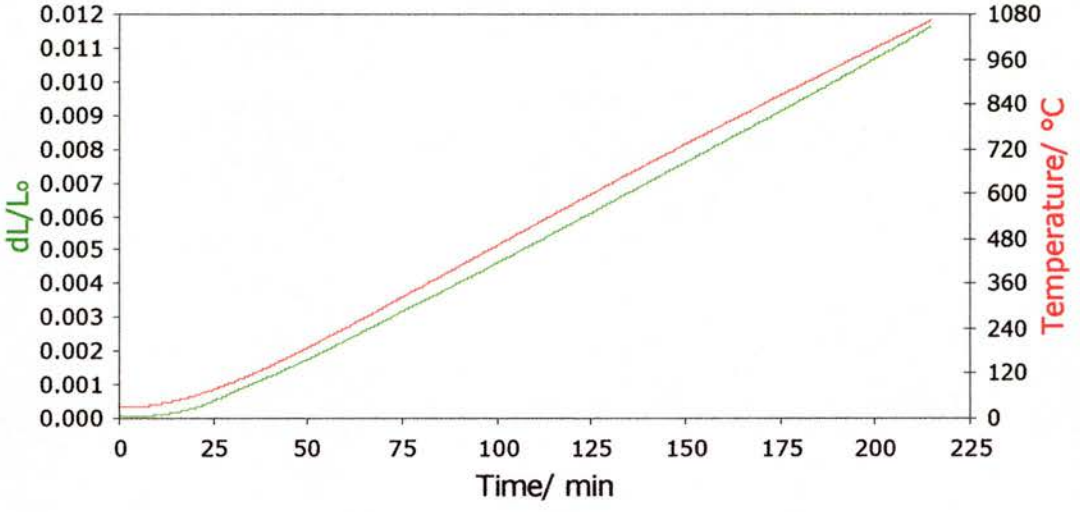

Figure 3.38: Thermal expansion plot for $Y_{0.15}Zr_{0.57}Ti_{0.13}Ce_{0.15}O_{1.925}$

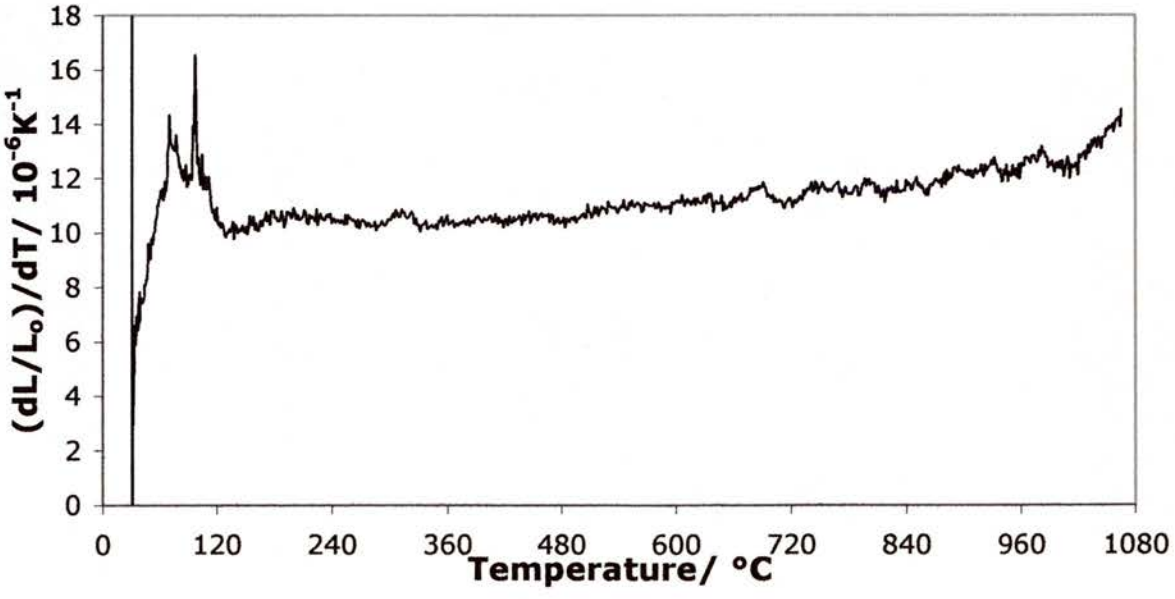

Figure 3.39: Plot of (dL/Lo)/dT vs. temperature for $Y_{0.15}Zr_{0.57}Ti_{0.13}Ce_{0.15}O_{1.925}$.

Table 3.20: Thermal expansion coefficients for YZTC materials in oxygen

Formula	α/ 10^{-6} K^{-1} (200-1,025°C)	Unit cell edge/Å
$Y_{0.20}Zr_{0.62}Ti_{0.18}O_{1.90}$	10.25	5.1111
$Y_{0.20}Zr_{0.62}Ti_{0.13}Ce_{0.05}O_{1.90}$	10.74	5.1357
$Y_{0.20}Zr_{0.57}Ti_{0.18}Ce_{0.05}O_{1.90}$	10.99	5.1272
$Y_{0.15}Zr_{0.62}Ti_{0.13}Ce_{0.10}O_{1.925}$	11.10	5.1499
$Y_{0.20}Zr_{0.57}Ti_{0.13}Ce_{0.10}O_{1.90}$	11.34	5.1518
$Y_{0.15}Zr_{0.57}Ti_{0.13}Ce_{0.15}O_{1.925}$	11.21	5.1664
$Y_{0.15}Zr_{0.62}Ti_{0.08}Ce_{0.15}O_{1.925}$	11.06	5.1733
$Y_{0.20}Zr_{0.57}Ti_{0.08}Ce_{0.15}O_{1.90}$	11.01	5.1810
$Y_{0.15}Zr_{0.52}Ti_{0.13}Ce_{0.20}O_{1.925}$	11.05	5.1860
$Y_{0.20}Zr_{0.52}Ti_{0.08}Ce_{0.20}O_{1.90}$	11.44	5.2000
$Y_{0.125}Zr_{0.52}Ti_{0.13}Ce_{0.225}O_{1.9375}$	11.67	5.1964
$Y_{0.125}Zr_{0.52}Ti_{0.08}Ce_{0.275}O_{1.9375}$	11.68	5.2116
$Y_{0.125}Zr_{0.47}Ti_{0.08}Ce_{0.325}O_{1.9375}$	11.68	5.2232
$Y_{0.15}Zr_{0.62}Ti_{0.03}Ce_{0.20}O_{1.925}$	11.20	5.1991
$Y_{0.20}Zr_{0.57}Ti_{0.03}Ce_{0.20}O_{1.90}$	11.36	5.1956
$Y_{0.15}Zr_{0.57}Ti_{0.03}Ce_{0.25}O_{1.925}$	11.29	5.2025

The results from Table 3.20 were plotted against composition and cubic unit cell size and these plots are shown as Figures 3.40-3.44.

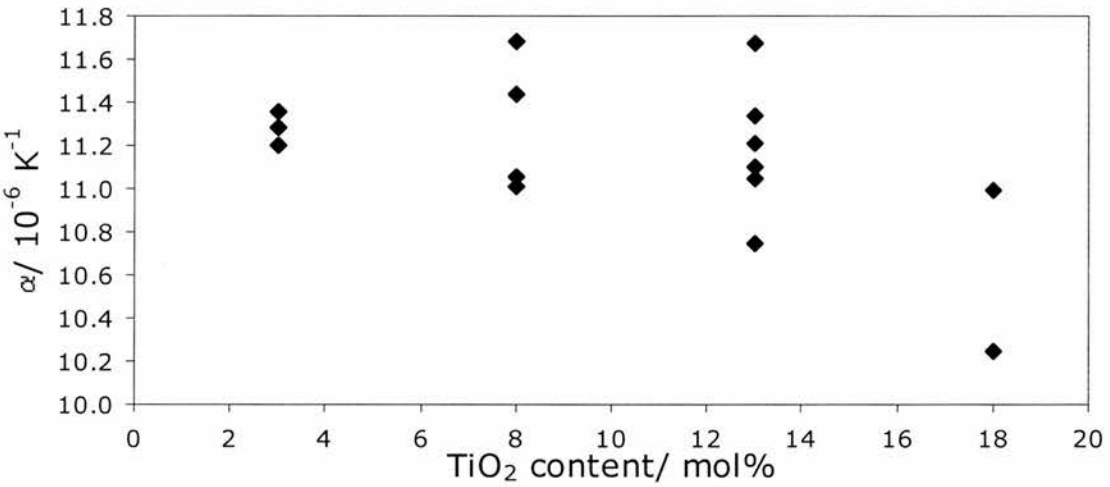

Figure 3.40: Dependence between α and TiO_2 content

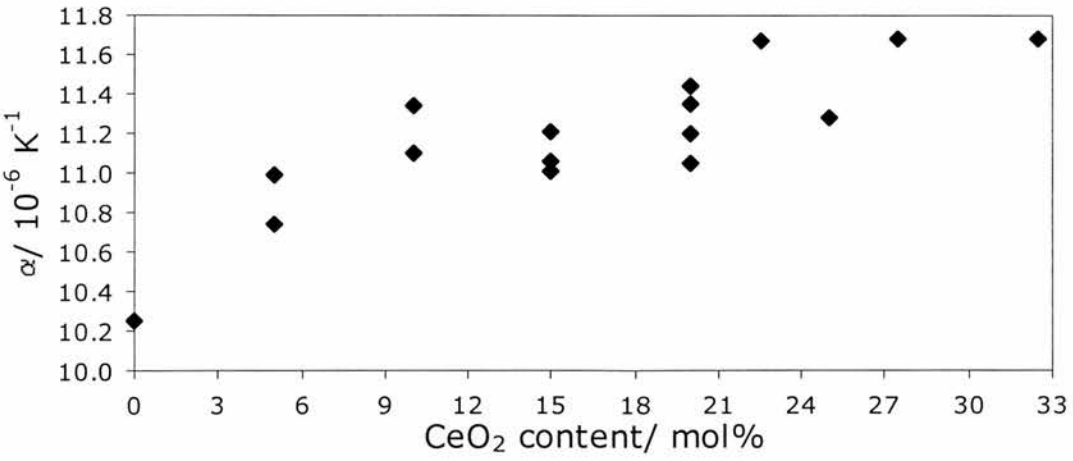

Figure 3.41: Dependence between α and CeO_2 content

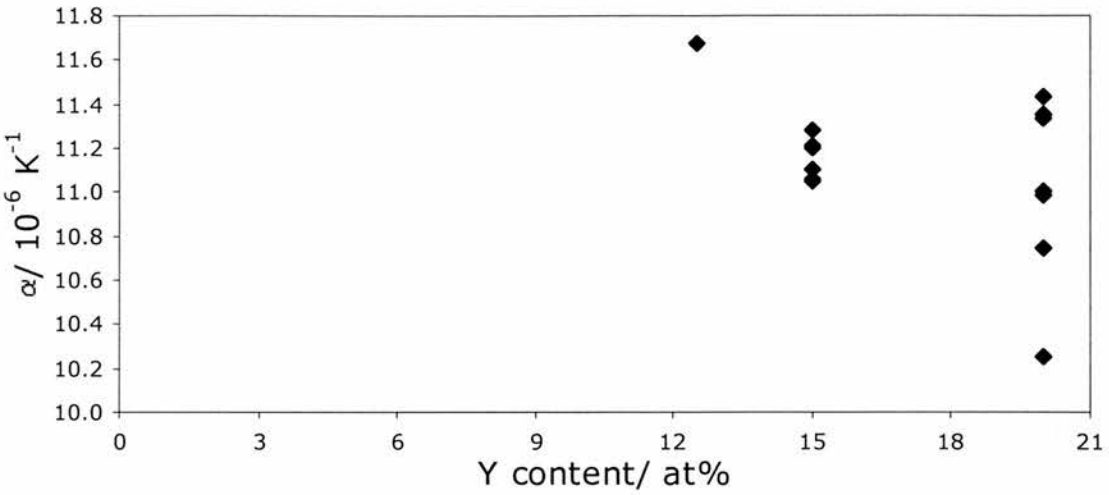

Figure 3.42: Dependence between α and Y content

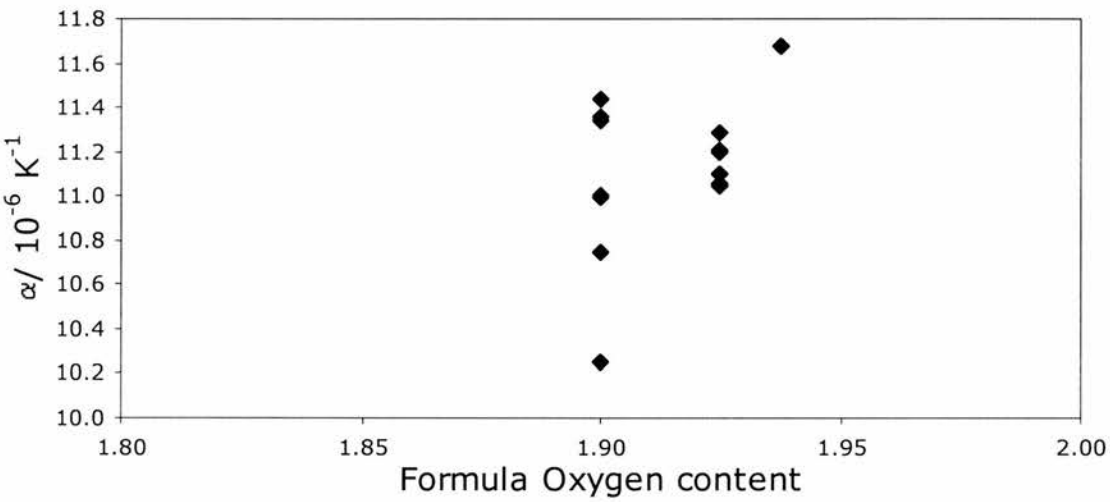

Figure 3.43: Dependence between α and O content

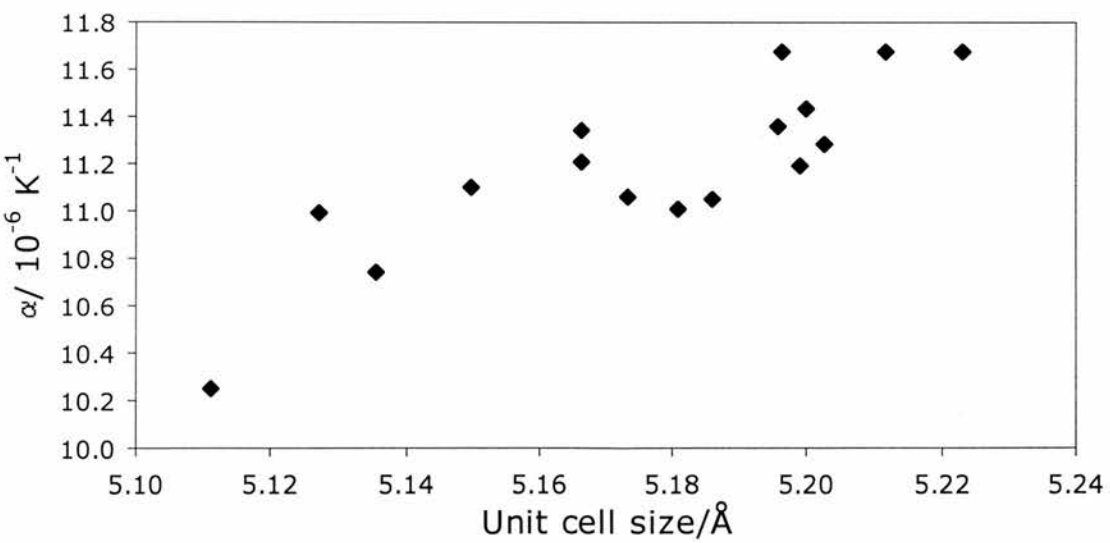

Figure 3.44: Dependence between α and cubic unit cell size

From Table 3.20 and Figures 3.40-3.44, there appear to be a series of trends involving thermal expansion. Firstly, α increases linearly with increasing CeO_2 content for compositions that contain CeO_2. Also, α decreases with increasing TiO_2 and Y content in what appears to be a linear trend and finally, α increases with increasing cubic unit cell size in a trend similar to that observed for CeO_2 content. The variability in α for the plots at fixed levels of Ti or Ce is due to a set of materials that have the same Ti or Ce content but the rest of the composition is varied (different Y:Zr:Ti or Y:Zr:Ce ratios).

3.7.2: Measurements in 5% H_2/ Argon

The second set of thermal expansion measurements was carried out on YZTC pellets which were pre-reduced in 5% H_2/Argon at 1,000°C for 48 hours. The conditions used for these measurements were that samples were heated up at 5°C min^{-1} to 1,000°C in 5% H_2/Argon. The aim of this set of measurements was to determine the effect of reduction on the thermal expansion of these materials. Table 3.21 shows the thermal expansion results. Figure 3.45 shows the plot of the expansion of a reduced YZTC material with time.

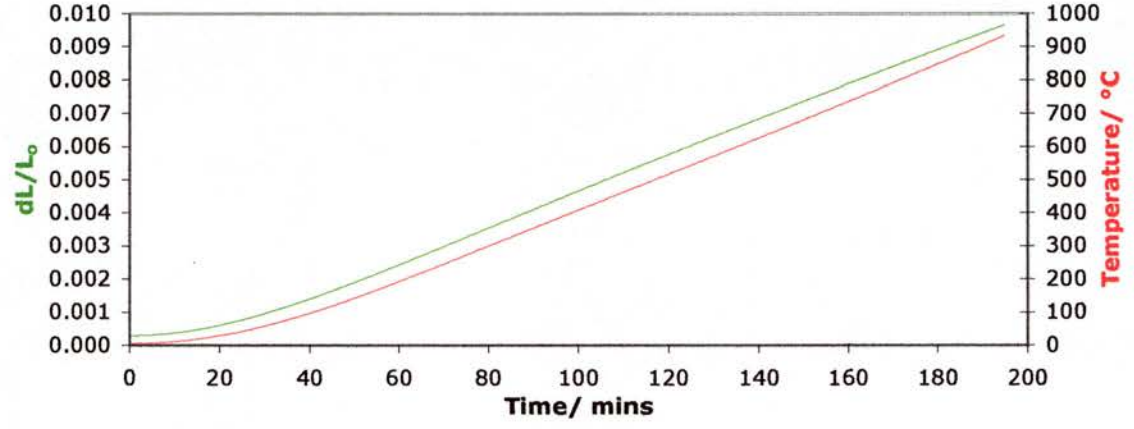

Figure 3.45: Thermal expansion plot for $Y_{0.20}Zr_{0.57}Ti_{0.08}Ce_{0.15}O_{1.90-\delta}$

Table 3.21: Thermal expansion coefficients for reduced YZTC materials in 5% H_2/Argon

Formula	α/ 10^{-6} K^{-1} (200-950°C)	Unit Cell edge/ Å
$Y_{0.20}Zr_{0.62}Ti_{0.13}Ce_{0.05}O_{1.90-\delta}$	10.42	5.1373
$Y_{0.20}Zr_{0.57}Ti_{0.18}Ce_{0.05}O_{1.90-\delta}$	10.30	5.1288
$Y_{0.20}Zr_{0.57}Ti_{0.13}Ce_{0.10}O_{1.90-\delta}$	10.63	5.1638
$Y_{0.15}Zr_{0.57}Ti_{0.13}Ce_{0.15}O_{1.925-\delta}$	10.48	5.1814
$Y_{0.15}Zr_{0.62}Ti_{0.08}Ce_{0.15}O_{1.925-\delta}$	10.30	5.1892
$Y_{0.20}Zr_{0.57}Ti_{0.08}Ce_{0.15}O_{1.90-\delta}$	10.17	5.1962
$Y_{0.15}Zr_{0.62}Ti_{0.13}Ce_{0.10}O_{1.925-\delta}$	10.58	5.1529
$Y_{0.20}Zr_{0.62}Ti_{0.03}Ce_{0.15}O_{1.90-\delta}$	10.54	5.2087
$Y_{0.15}Zr_{0.62}Ti_{0.03}Ce_{0.20}O_{1.925-\delta}$	10.22	5.2231
$Y_{0.15}Zr_{0.57}Ti_{0.03}Ce_{0.25}O_{1.925-\delta}$	10.38	-
$Y_{0.125}Zr_{0.57}Ti_{0.03}Ce_{0.275}O_{1.9375-\delta}$	10.19	-

All of the measurements behaved as shown in Figure 3.45. The thermal expansion coefficients (α) for the materials, as shown in Table 3.21 were calculated overall from 200-950°C. α is not constant between 200-950°C but it increases with increasing temperature, although the expansion was close to linear overall. This is illustrated in Figure 3.46. Figures 3.47-3.49 are plots of α for the reduced materials against TiO_2, CeO_2 content and unit cell size, respectively.

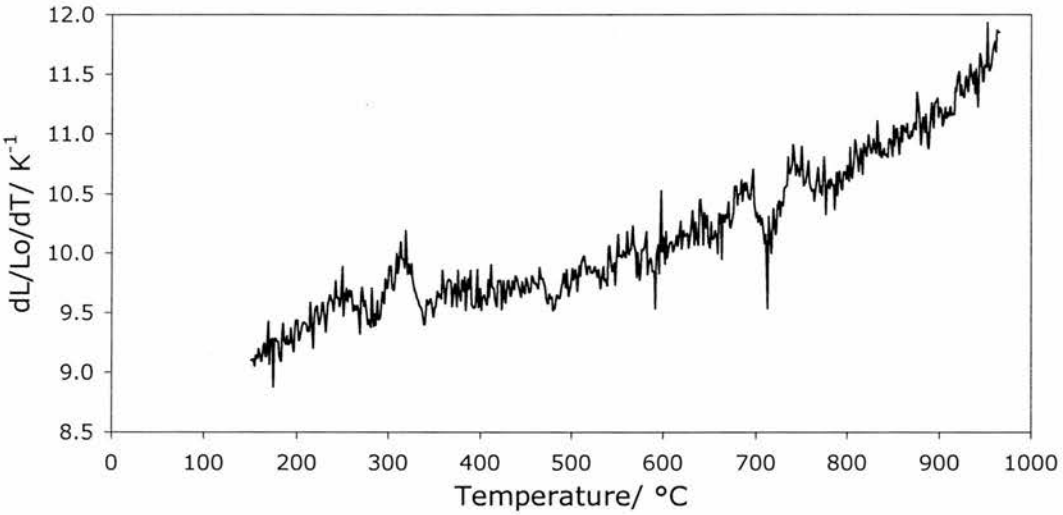

Figure 3.46: Plot of (dL/Lo)/dT vs. temperature for Reduced $Y_{0.20}Zr_{0.57}Ti_{0.08}Ce_{0.15}O_{1.90-\delta}$

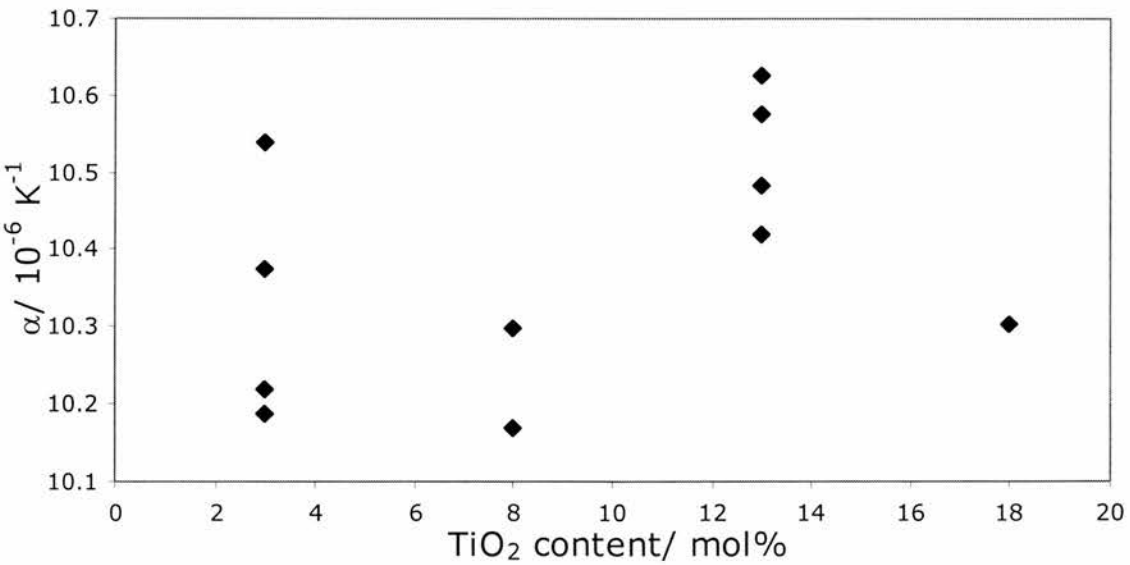

Figure 3.47: Dependence between α and TiO_2 content for reduced YZTC pellets.

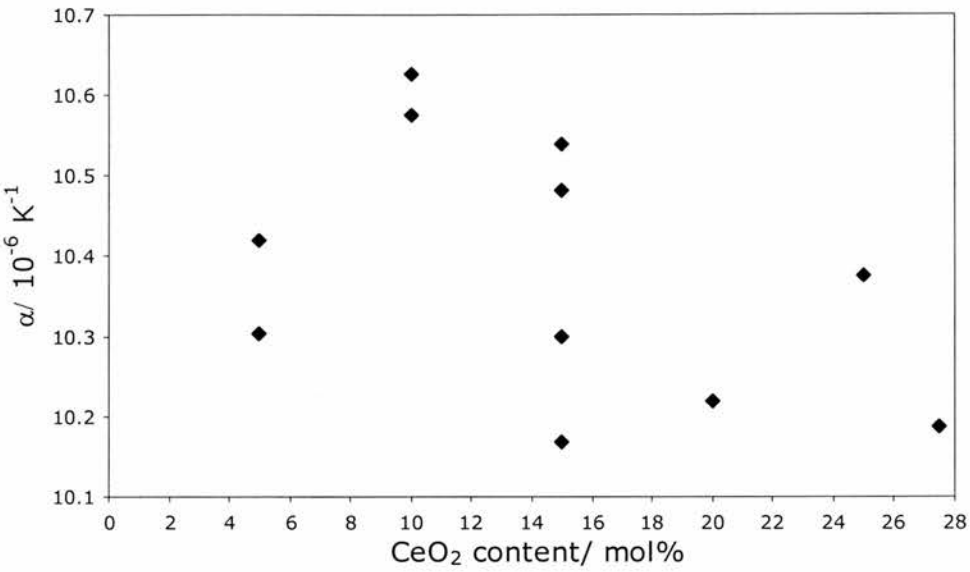

Figure 3.48: Dependence between α and CeO_2 content for reduced YZTC pellets.

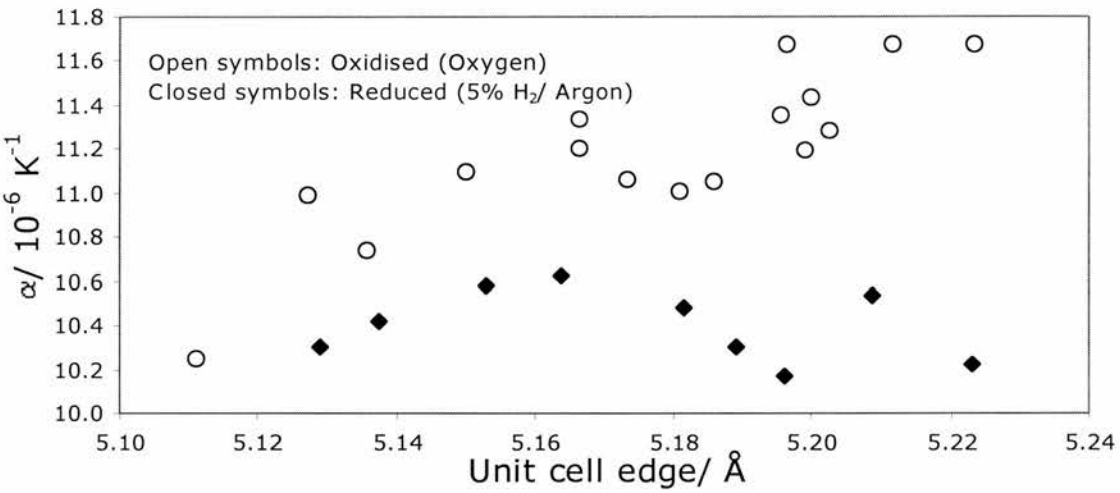

Figure 3.49: Dependence between α and unit cell edge for YZTC pellets.

From Figures 3.47 and 3.48, for samples reduced in 5% H_2/ Argon, α appears to be independent of TiO_2 content, whereas it decreases with increasing CeO_2 content. In Table 3.22, the levels of α in oxygen and 5% H_2/ Argon were compared and there was a slight trend where α is higher in oxygen than it is in 5% H_2/ Argon by between $0.32 - 0.98*10^{-6}$ K^{-1}. The extent of difference in α in going from oxygen to 5% H_2/ Argon is compared with composition in Figures 3.50 and 3.51, which show that the difference increases with increasing CeO_2 content and decreases with increasing TiO_2 content.

It was also found from Figure 3.49, in the comparison of α with the unit cell edge of the reduced materials, the following was found. Initially, α increases with increasing unit cell edge up to 5.164Å, then decreases with increasing unit cell edge between 5.164 and 5.196 Å.

Table 3.22: Comparison of α for reduced and non-reduced YZTC materials

Formula	$\alpha/ 10^{-6} K^{-1}$ (Oxygen)	$\alpha/ 10^{-6} K^{-1}$ (5% H_2/Argon)	$\Delta\alpha/ 10^{-6} K^{-1}$
$Y_{0.15}Zr_{0.62}Ti_{0.13}Ce_{0.10}O_{1.925-\delta}$	11.10	10.58	0.52
$Y_{0.15}Zr_{0.62}Ti_{0.08}Ce_{0.15}O_{1.925-\delta}$	11.06	10.30	0.77
$Y_{0.15}Zr_{0.57}Ti_{0.13}Ce_{0.15}O_{1.925-\delta}$	11.21	10.48	0.72
$Y_{0.20}Zr_{0.62}Ti_{0.13}Ce_{0.05}O_{1.90-\delta}$	10.74	10.42	0.32
$Y_{0.20}Zr_{0.57}Ti_{0.18}Ce_{0.05}O_{1.90-\delta}$	10.99	10.30	0.69
$Y_{0.20}Zr_{0.57}Ti_{0.13}Ce_{0.10}O_{1.90-\delta}$	11.34	10.63	0.71
$Y_{0.15}Zr_{0.57}Ti_{0.03}Ce_{0.25}O_{1.925-\delta}$	11.29	10.38	0.91
$Y_{0.20}Zr_{0.57}Ti_{0.08}Ce_{0.15}O_{1.90-\delta}$	11.01	10.17	0.84
$Y_{0.15}Zr_{0.62}Ti_{0.03}Ce_{0.20}O_{1.925-\delta}$	11.20	10.22	0.98

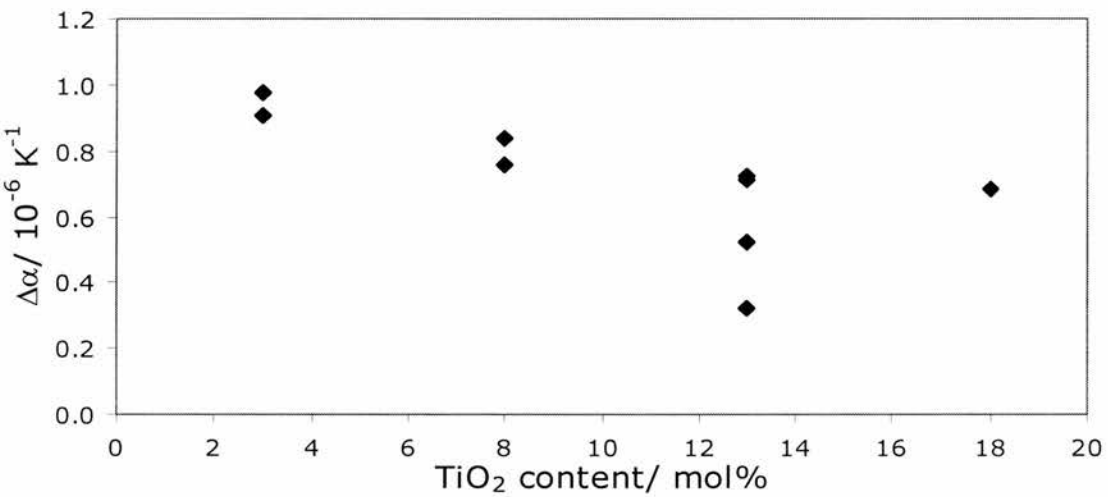

Figure 3.50: Dependence of Δα with TiO_2 content

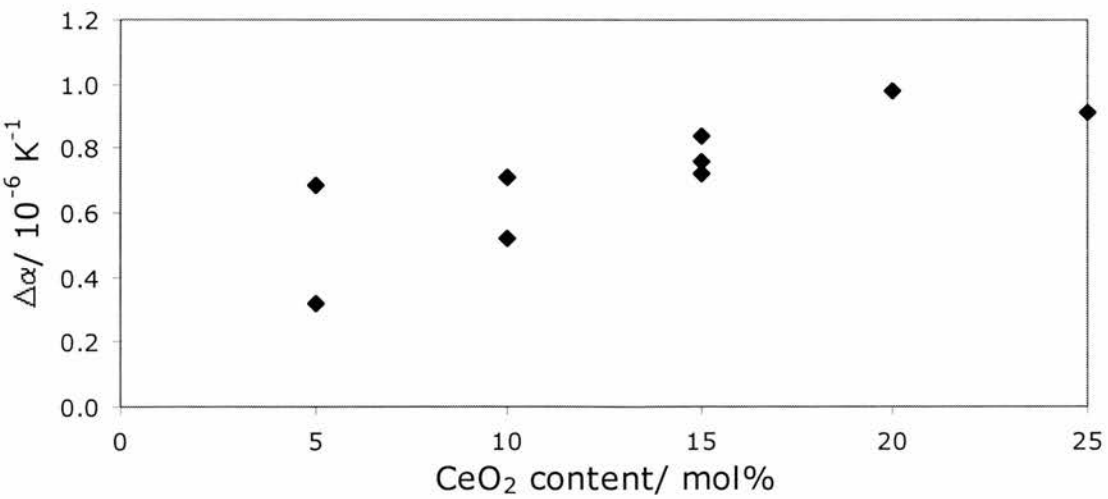

Figure 3.51: Dependence of Δα with CeO_2 content

3.7.3: Measurements in Argon

The third set of thermal expansion measurements was carried out on YZTC pellets that were pre-reduced in Argon at 1,000°C for 48 hours. The conditions used for these measurements were that the samples were heated up at 5°C min^{-1} to 1,100°C in Argon. The reason for doing this set of measurements was to determine the effect of reduction in argon on the thermal expansion of these materials. Table 3.23 shows the thermal expansion results. Figure 3.52 shows the plot of the expansion of a reduced YZTC material with temperature.

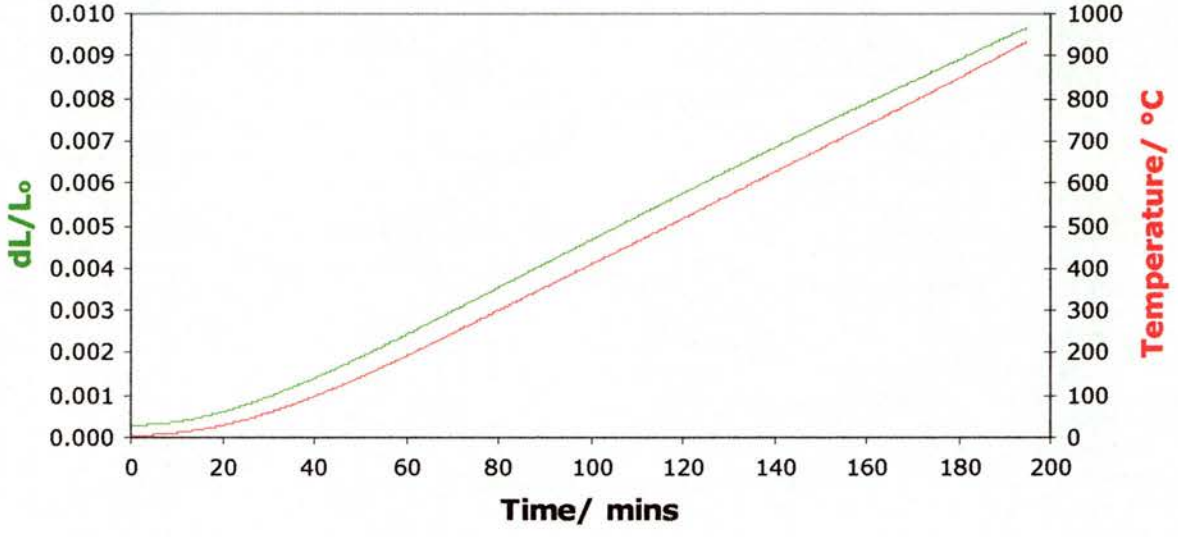

Figure 3.52: Thermal expansion plot for $Y_{0.20}Zr_{0.57}Ti_{0.08}Ce_{0.15}O_{1.90-\delta}$

Table 3.23: Thermal expansion coefficients for reduced YZTC materials in Argon

Formula	α/ 10^{-6} K^{-1} (200-1,025°C)
$Y_{0.15}Zr_{0.62}Ti_{0.13}Ce_{0.10}O_{1.925-\delta}$	11.13
$Y_{0.20}Zr_{0.62}Ti_{0.03}Ce_{0.15}O_{1.90-\delta}$	10.97
$Y_{0.15}Zr_{0.62}Ti_{0.03}Ce_{0.20}O_{1.925-\delta}$	11.36
$Y_{0.15}Zr_{0.57}Ti_{0.03}Ce_{0.25}O_{1.925-\delta}$	11.28
$Y_{0.15}Zr_{0.52}Ti_{0.03}Ce_{0.30}O_{1.925-\delta}$	11.44
$Y_{0.15}Zr_{0.62}Ti_{0.08}Ce_{0.15}O_{1.925-\delta}$	11.42
$Y_{0.20}Zr_{0.57}Ti_{0.08}Ce_{0.15}O_{1.90-\delta}$	10.87
$Y_{0.125}Zr_{0.57}Ti_{0.03}Ce_{0.275}O_{1.9375-\delta}$	11.37
$Y_{0.20}Zr_{0.57}Ti_{0.13}Ce_{0.10}O_{1.90-\delta}$	11.13
$Y_{0.20}Zr_{0.52}Ti_{0.03}Ce_{0.25}O_{1.90-\delta}$	11.07

All of the measurements behaved basically as shown in Figure 3.48. The thermal expansion coefficients (α) were calculated overall from 200-1,025°C. α is not constant between 200 and 1,025°C but it increases with increasing temperature, although the expansion was basically linear overall. This is illustrated in Figure 3.53. Figures 3.54 and 3.55 are plots of α for the reduced materials against TiO_2 and CeO_2 content, respectively.

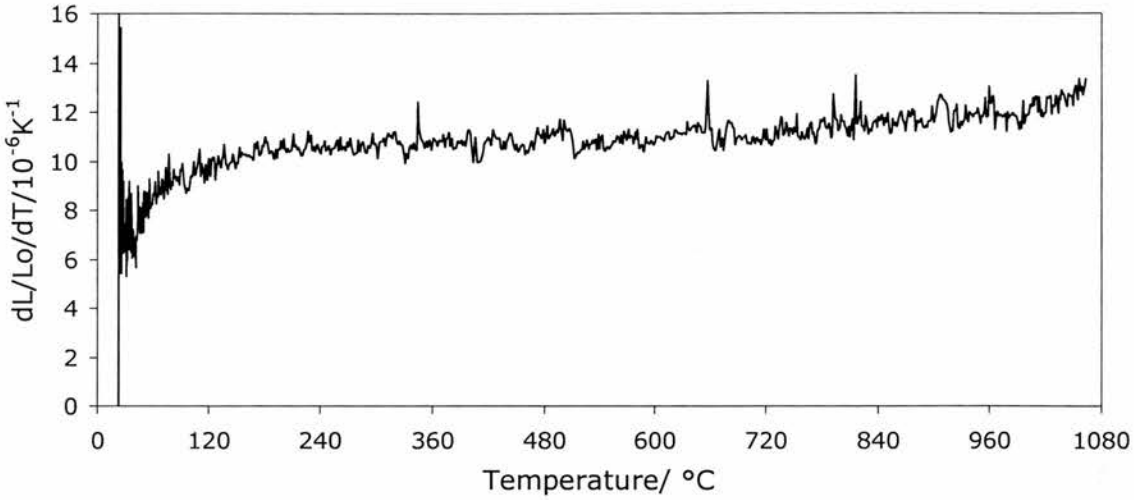

Figure 3.53: Plot of (dL/Lo)/dT vs. temperature for reduced $Y_{0.15}Zr_{0.62}Ti_{0.13}Ce_{0.10}O_{1.925-\delta}$.

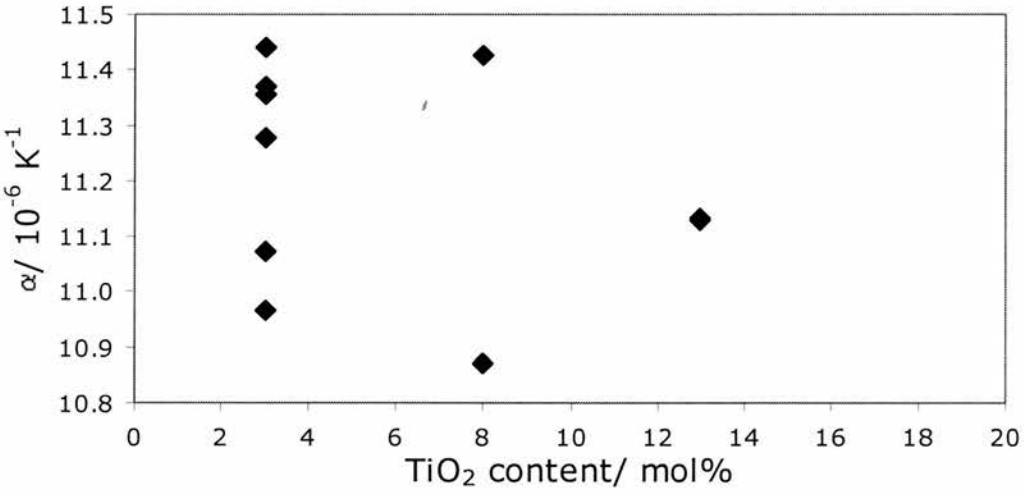

Figure 3.54: Dependence between α and TiO_2 content for reduced YZTC pellets run in Argon.

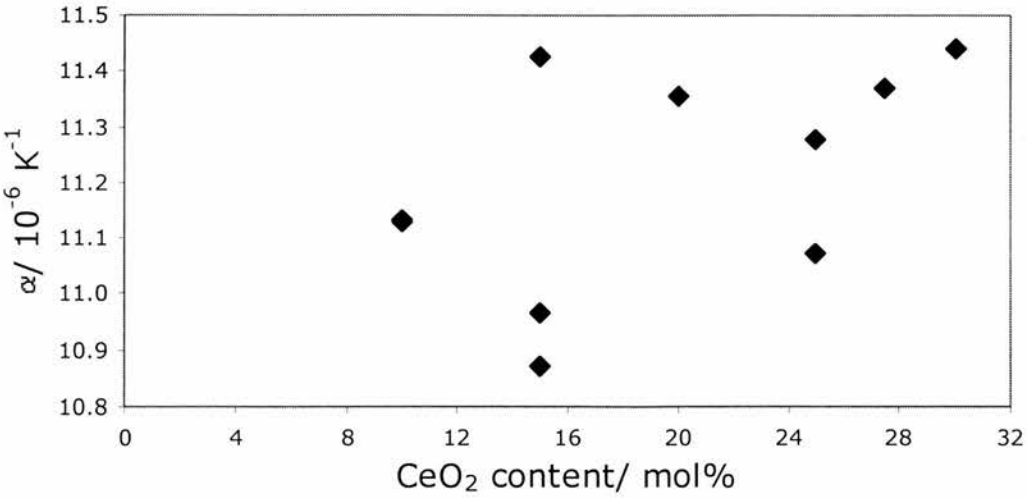

Figure 3.55: Dependence between α and CeO_2 content for YZTC pellets run in Argon.

Table 3.24: Comparison of α for reduced and non-reduced YZTC materials

Formula	$\alpha/ 10^{-6} K^{-1} (O_2)$	$\alpha/ 10^{-6} K^{-1} (Ar)$	$\Delta\alpha/ 10^{-6}K^{-1}$
YZTC 3 ($Y_{0.20}Zr_{0.57}Ti_{0.13}Ce_{0.10}O_{1.90-\delta}$)	11.34	11.13	0.21
YZTC 24 ($Y_{0.20}Zr_{0.57}Ti_{0.08}Ce_{0.15}O_{1.90-\delta}$)	11.01	10.87	0.14
YZTC 13 ($Y_{0.15}Zr_{0.62}Ti_{0.13}Ce_{0.10}O_{1.925-\delta}$)	11.10	11.13	-0.03
YZTC 14 ($Y_{0.15}Zr_{0.62}Ti_{0.08}Ce_{0.15}O_{1.925-\delta}$)	11.06	11.42	-0.37
YZTC 35 ($Y_{0.15}Zr_{0.62}Ti_{0.03}Ce_{0.20}O_{1.925-\delta}$)	11.20	11.36	-0.16
YZTC 37 ($Y_{0.15}Zr_{0.57}Ti_{0.03}Ce_{0.25}O_{1.925-\delta}$)	11.28	11.28	0.01

From Table 3.24, the thermal expansion coefficients in argon appear to be similar to those when the samples were run in oxygen. In some cases, α is higher in oxygen than it is for argon, and in the other cases, the opposite is true. The difference in α in going from oxygen to argon atmospheres varies from -0.37 to $0.21*10^{-6}$ K^{-1}. There does not appear to be a trend between composition and Δα.

3.7.4: Overall comparison

Table 3.25 shows the overall comparison of thermal expansion coefficients of materials run in oxygen, 5% H_2/ Argon and argon atmospheres.

Table 3.25: Comparison of thermal expansion in various atmospheres

Formula	α (O_2)/ $10^{-6} K^{-1}$	α (5% H_2/Ar)/ $10^{-6} K^{-1}$	α (Ar)/ $10^{-6}K^{-1}$
$Y_{0.20}Zr_{0.57}Ti_{0.13}Ce_{0.10}O_{1.90-\delta}$	11.34	10.63	11.13
$Y_{0.20}Zr_{0.57}Ti_{0.08}Ce_{0.15}O_{1.90-\delta}$	11.01	10.17	10.87
$Y_{0.15}Zr_{0.62}Ti_{0.13}Ce_{0.10}O_{1.925-\delta}$	11.10	10.58	11.13
$Y_{0.15}Zr_{0.62}Ti_{0.08}Ce_{0.15}O_{1.925-\delta}$	11.06	10.30	11.42
$Y_{0.15}Zr_{0.62}Ti_{0.03}Ce_{0.20}O_{1.925-\delta}$	11.20	10.22	11.36
$Y_{0.15}Zr_{0.57}Ti_{0.03}Ce_{0.25}O_{1.925-\delta}$	11.28	10.38	11.28

Figures 3.56 – 3.57 illustrate the differences between the levels of α with atmosphere.

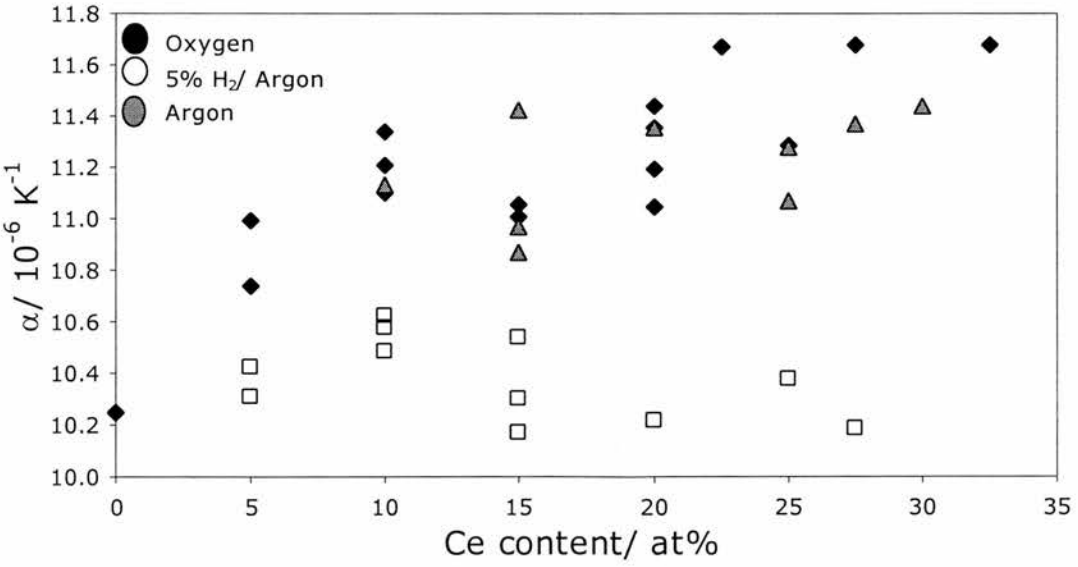

Figure 3.56: Overall comparison with dependence on Ce content

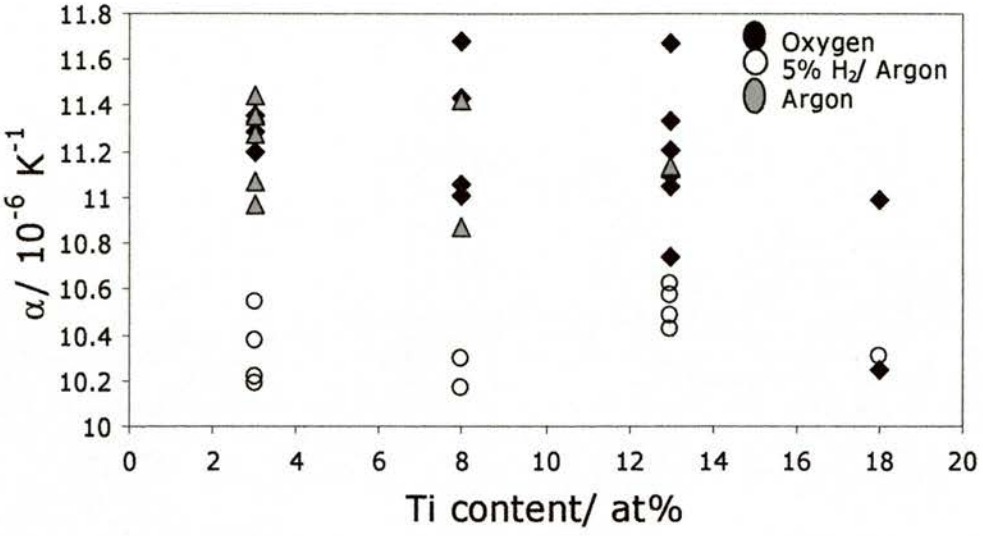

Figure 3.57: Overall comparison with dependence on Ti content

3.7.5: Effect of reduction on expansion of oxidised pellets

Another study on the thermal expansion of YZTC materials investigated the extent of expansion (or shrinkage) when the pellets are being reduced in argon or 5% H_2/ argon. Oxidised pellets were heated at 5°C min^{-1} to 1,100°C in argon or 1,000°C in 5% H_2/ argon. The cooling rate was 5 - 10°C min^{-1}.

a) $Y_{0.15}Zr_{0.62}Ti_{0.03}Ce_{0.20}O_{1.925}$

The first specimen pellet was $Y_{0.15}Zr_{0.62}Ti_{0.03}Ce_{0.20}O_{1.925}$. In the first experiment, a pellet 9.750mm in length was reduced in 5% H_2/ Argon. The thermal expansion plot on heating is shown in Figure 3.58 and Figure 3.59 represents the thermal expansion on cooling.

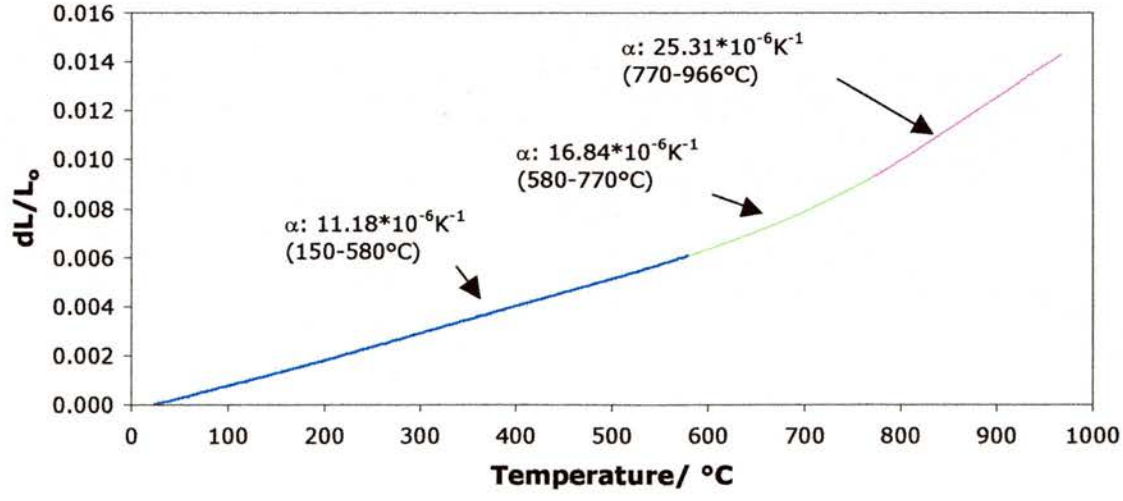

Figure 3.58: Thermal expansion plot of reduction in 5% H_2/ Argon on heating

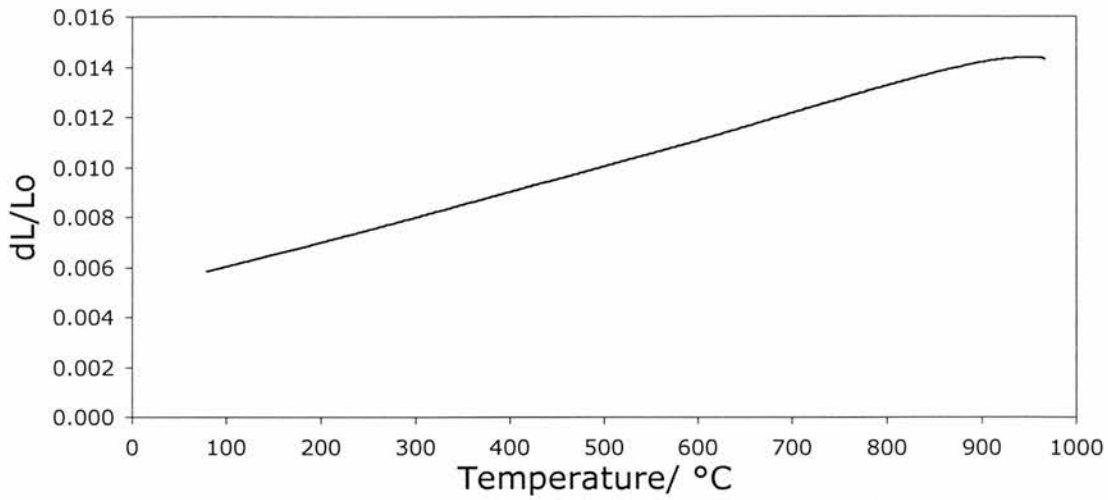

Figure 3.59: Thermal expansion plot of reduction in 5% H_2/ Argon on cooling

From Figure 3.58, it appears that between 150 and 580°C, the sample has not yet started reduction, as the thermal expansion coefficient of $11.18*10^{-6} K^{-1}$ is similar to that observed for this material when run in oxygen. Above 580°C, the reduction starts to begin, as shown by the thermal expansion coefficient increasing to $16.84*10^{-6} K^{-1}$ and by 770°C, the sample has been mostly reduced, as the thermal expansion coefficient rises to $25.31*10^{-6} K^{-1}$.

Figure 3.59 suggests that perhaps the sample pellet has been fully reduced in the 5% H_2/ argon atmosphere up to 960°C, as there was only one slope observed on cooling, with a thermal expansion coefficient of $10.34*10^{-6} K^{-1}$. This is similar to the expansion coefficient observed from the measurements done in 5% H_2/ argon on a pellet that was pre-reduced. This implies that the sample pellet was as fully reduced up to 960°C as the one that was pre-reduced at 1,000°C.

Also, from Figure 3.58, one can try to estimate how much extra expansion of the sample was caused by its reduction in 5% H_2/ argon. This involved extrapolating the effect of the first stage of the plot (150-580°C) to 960°C, using the thermal expansion coefficient in that temperature range to determine how much the sample would have expanded by up to 960°C if it was not reducible in these experimental conditions. Then, this was compared by how much the sample had expanded by at 960°C and the difference in the two values would indicate the extent of expansion due to reduction.

In doing this, up to 960°C, the sample expanded by a total of 1.425%. Extrapolating the thermal expansion observed from 150-580°C up to 960°C implied that the sample would have expanded by 1.041% if it was a non-reducing atmosphere. This gives a difference of

0.384%, implying that reduction up to 960°C in 5% H_2/ Argon caused the sample to expand by 0.384%.

Then, the pellet was oxidised before carrying out the second experiment, although the pellet had to be re-fired, as it broke shortly after oxidation. The second experiment involved examining the effect of reduction in argon. The sample pellet was 9.082 mm in length. Figure 3.60 shows the thermal expansion plot on heating.

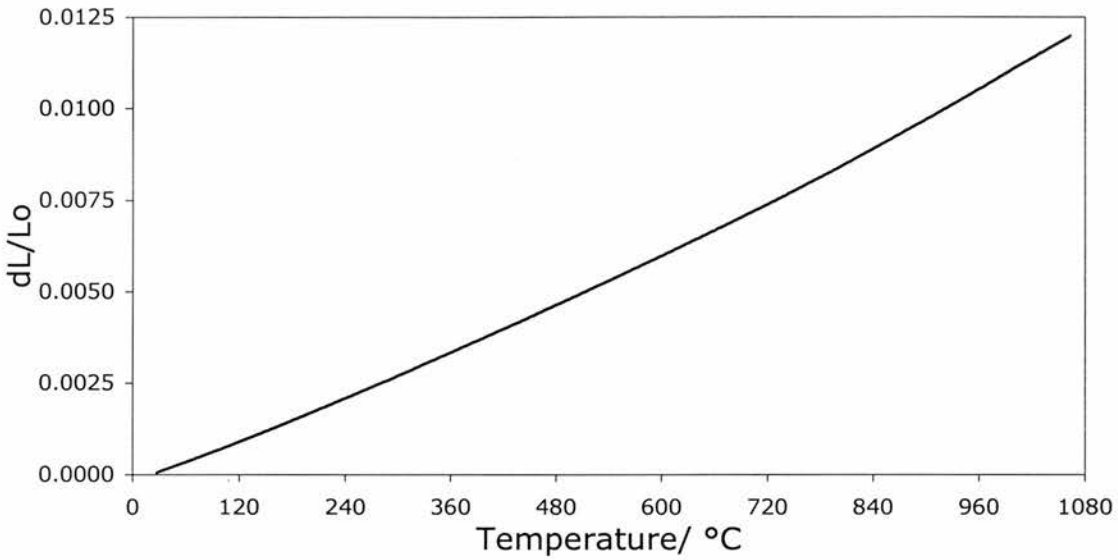

Figure 3.60: Thermal expansion of $Y_{0.15}Zr_{0.62}Ti_{0.03}Ce_{0.20}O_{1.925}$ pellet being reduced in argon.

After the experiment finished, it appeared that the sample was reduced to some extent, as the pellet changed colour from pale yellow to medium grey. When looking at Figure 3.60, there appeared to be two main regions. The first was an imperfect slope region up to approximately 700°C (the thermal expansion coefficient is not an absolute constant, it is temperature-dependent, increasing with temperature). In the first region, the pellet was in a non-reduced state and the thermal expansion coefficient (measured from 300-600°C) was $10.96*10^{-6}$ K^{-1}. Above 700°C, however, the slope became steeper and it is likely that this was due to partial reduction of the sample in argon. The thermal expansion coefficient (measured from 840-1,040°C) was $13.77*10^{-6}$ K^{-1}. It is likely that this is associated with expansion of the sample due to partial reduction, as the change in slope appears to be more than what would be expected from the normal observation of the thermal expansion coefficient rising by a small amount with increasing temperature. So, the effect of reduction in argon was slight.

To estimate the amount of expansion associated with partial reduction in argon, the thermal expansion coefficient between 300 and 600°C was extrapolated from 300°C to the

end of the heating stage at 1,065°C. This extrapolation implied that the amount of total expansion without this effect would have been 1.11%. The total expansion at the end of heating was 1.20%. Thus, it is estimated that partial reduction in argon caused an expansion of 0.09%.

Thus, it can be said that when an oxidised YZTC pellet is reduced in an inert or reducing atmosphere, the reduction causes an additional expansion that decreases with increasing pO_2. This was due to an expansion of 0.38% when the $Y_{0.15}Zr_{0.62}Ti_{0.03}Ce_{0.20}O_{1.925}$ pellet was reduced in 5% H_2/ Argon (pO_2 ~10^{-19} atm), whereas the sample expanded 0.09% when reduced in argon (pO_2 ~10^{-5} atm).

b) $Y_{0.125}Zr_{0.47}Ti_{0.08}Ce_{0.325}O_{1.9375}$

The second sample was an oxidised pellet of $Y_{0.125}Zr_{0.47}Ti_{0.08}Ce_{0.325}O_{1.9375}$. In the first measurement, a pellet of length 13.361 mm was reduced in argon. The thermal expansion plot is shown in Figure 3.61.

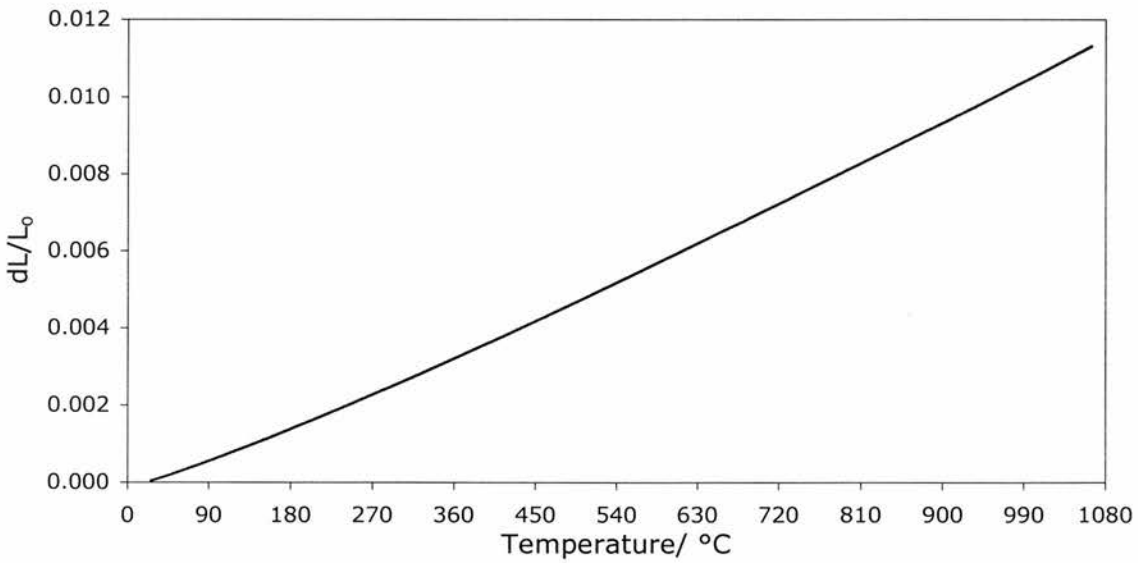

Figure 3.61: Thermal expansion plot of $Y_{0.125}Zr_{0.47}Ti_{0.08}Ce_{0.325}O_{1.9375}$ reduced in argon

In Figure 3.61, the appearance of the run was that the thermal expansion was not absolutely constant but increased slowly with increasing temperature, which is typical for this type of measurement. In the range 180 – 380°C, α was $10.20*10^{-6}$ K^{-1}, rising to $11.26*10^{-6}$ K^{-1} from 380 – 790°C and ultimately to $11.90*10^{-6}$ K^{-1} from 790 – 1,065°C (region where it is possible that reduction happens). In comparison with measurements in oxygen, the material does not expand as much in argon as it does in oxygen, as the values of α are lower.

In terms of evidence of reduction of the material, the sample pellet was slightly darkened after the experiment and an estimate was determined to see if there was additional expansion that was not due to just an increase in temperature. This estimated the extent of total sample expansion (dL/Lo) if α was the same from 790 – 1,065°C as it was from 380 - 790°C. In doing this at 1,065°C, dL/Lo was 1.114%, as opposed to the actual dL/Lo of 1.132%, indicating that the sample may have expanded by a very small amount of 0.018% due to reduction in argon. So, the effect of reduction in argon on the thermal expansion behaviour of $Y_{0.125}Zr_{0.47}Ti_{0.08}Ce_{0.325}O_{1.9375}$ was minimal.

After that, the sample pellet was re-oxidised at 1,000°C in static air, before determining the effect of reduction in 5% H_2/ Argon on thermal expansion. In the reduction experiment, the sample length was 13.362 mm and heating was up to 1,000°C in 5% H_2/ Argon. The behaviour of this run was shown in Figure 3.62.

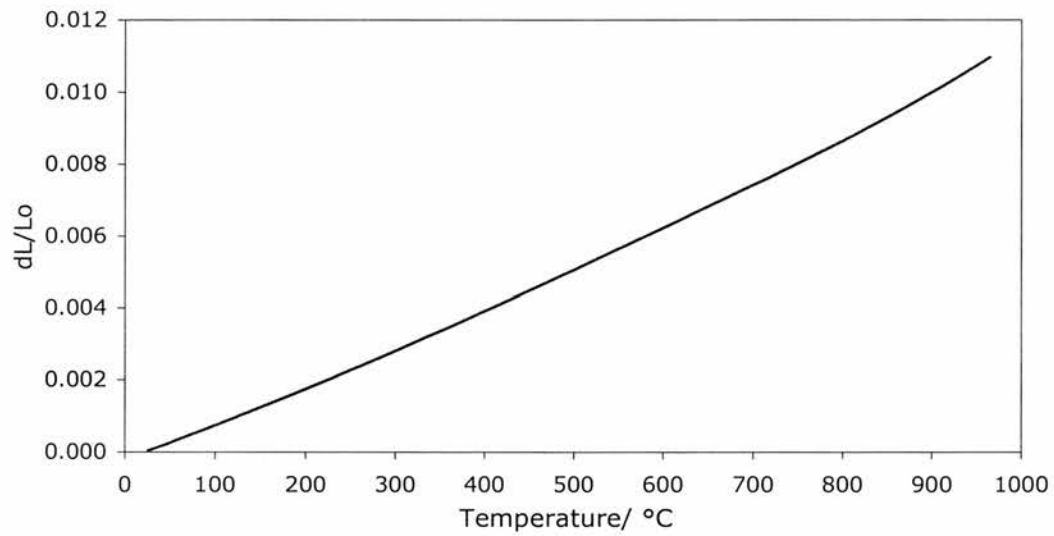

Figure 3.62: Thermal expansion plot of $Y_{0.125}Zr_{0.47}Ti_{0.08}Ce_{0.325}O_{1.9375}$ reduced in 5% H_2/ Argon.

From Figure 3.62, it appears that there are two regions of interest. The first is between 300 and 730°C, where α is $11.56*10^{-6}$ K^{-1} and this appears to be non-reduced sample behaviour, as α is comparable to that seen when run in oxygen. In the second region between 730 and 965°C, however, it appears that the sample is being reduced, as α rises to $13.66*10^{-6}$ K^{-1}, indicating some additional expansion due to reduction in 5% H_2/ Argon.

One estimate to how much additional expansion was due to reduction was to assume that α between 730 and 965°C was $11.56*10^{-6}$ K^{-1} and not what it was, then determine what dL/Lo was at 965°C and compare it with what was found in the actual measurement. Any

difference in these two values would indicate any additional expansion caused by sample reduction. In this extrapolation, dL/Lo at 965°C was calculated as 1.049%, as opposed to 1.099% from the actual experiment. This gives a difference of 0.05%, implying that the sample expanded an additional 0.05% in length when reduced in 5% H_2/ Argon. Also, the reduced pellet was dark brown/ black in colour. It is likely that this sample was of a higher density than the previous one, leading to less reduction and less expansion.

c) $Y_{0.125}Zr_{0.62}Ti_{0.08}Ce_{0.175}O_{1.9375}$

Finally, the comparisons between the effects of thermal expansion on reducing an oxidised pellet in argon and 5% H_2/ argon were determined for the material $Y_{0.125}Zr_{0.62}Ti_{0.08}Ce_{0.175}O_{1.9375}$. In the first experiment, a pellet of length 11.229 mm was reduced in argon at up to 1,100°C. The behaviour of this material in argon is shown in Figure 3.63.

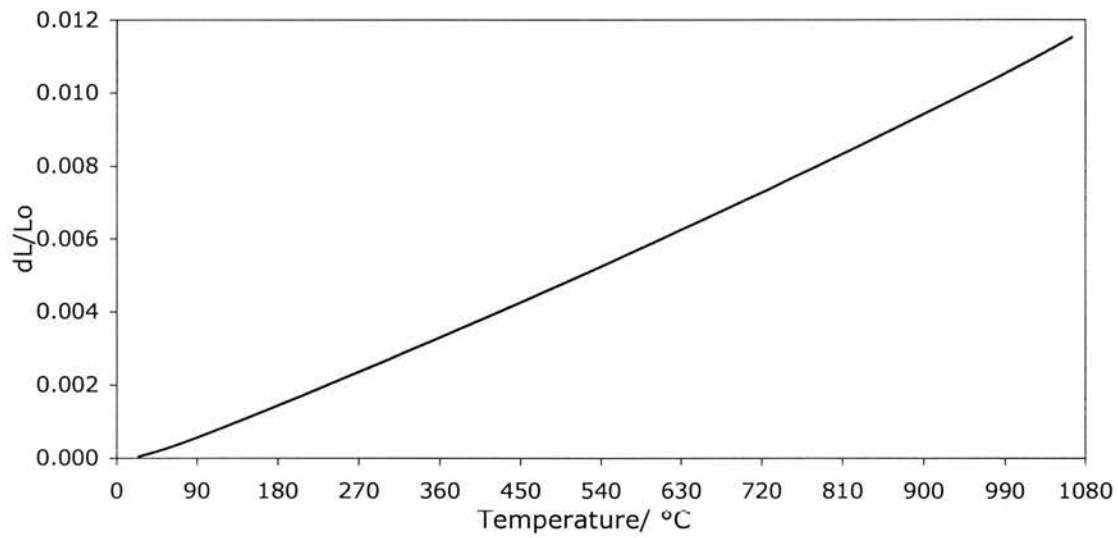

Figure 3.63: Thermal expansion plot of $Y_{0.125}Zr_{0.62}Ti_{0.08}Ce_{0.175}O_{1.9375}$ reduced in argon.

Figure 3.63 showed two important regions, where the first region was between 300 and 730°C, while the second region was between 730 and 965°C, where it is likely that changes in the sample due to partial reduction were happening. In the first region, α was $10.98*10^{-6}$ K^{-1}, while in the second region, α was $12.35*10^{-6}$ K^{-1}. It is possible that there may be a small additional expansion due to reduction.

The estimate of additional expansion due to reduction was based on assuming that there was no additional expansion from 730-965°C and that α was the same as for the first region. In doing this, this yielded a dL/Lo at 965°C of 1.107%, as opposed to 1.153% from

the actual run. This implied that the sample length expanded by 0.046% when being reduced in argon. Afterwards, the sample was re-oxidised at 1,000°C in static air for up to 48 hours. Then, the pellet was measured again, although the sample was heated up to 1,000°C in 5% H_2/ Argon. The sample length was 11.222 mm. The thermal expansion behaviour of $Y_{0.125}Zr_{0.62}Ti_{0.08}Ce_{0.175}O_{1.9375}$ being reduced in 5% H_2/ Argon is shown in Figure 3.64.

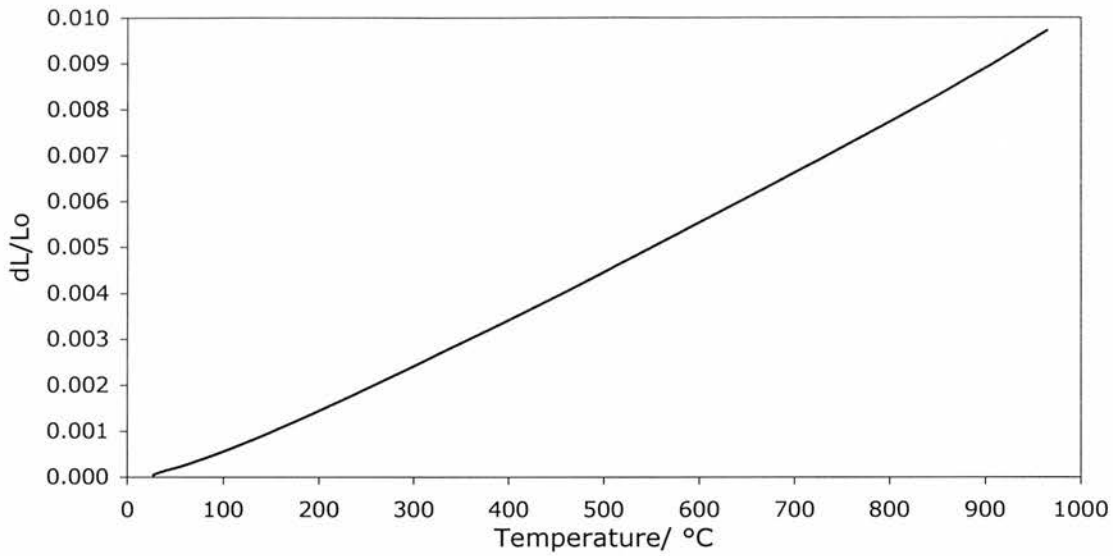

Figure 3.64: Thermal expansion plot of $Y_{0.125}Zr_{0.62}Ti_{0.08}Ce_{0.175}O_{1.9375}$ in 5% H_2/ Argon.

From Figure 3.64, the behaviour of this material when being reduced in 5% H_2/ Argon is similar to that of a normal run where a sample is heated up in oxygen. α is not constant throughout the run, as it is expected that α increases by a small amount with increasing temperature. Between 300 and 730°C, α was $10.56*10^{-6}$ K^{-1}, whereas from 730°C onwards, α increased to $11.74*10^{-6}$ K^{-1}. So, there could have been a very small expansion due to reduction (if any). If there was any additional expansion of sample length due to reduction, it was estimated to be no higher than 0.028%, based on continuing the level of α of $10.56*10^{-6}$ K^{-1} from 300°C to 965°C.

3.8: Conclusions/ Trends

The conclusions and trends that can be derived from these structural studies are as follows:

Most of the YZTC compositions investigated had cubic structures, with unit cell edges ranging from 5.111 to 5.228 Å. The unit cell edge increased with increasing CeO_2 content and decreasing TiO_2 content. In terms of phase formation, it was found that single-phase cubic structures were more difficult to attain with increasing TiO_2 content. All compositions containing 3 mol% TiO_2 were single-phase cubic, even with a Y content of only 10 at%, implying that at this level, single-phase cubic structures were very easy to attain, helped by the size effect of the Ce^{4+} ions. For compositions containing 8 mol% TiO_2, at least 6.67 mol% Y_2O_3 was required for single-phase cubic structures. At least 8 mol% Y_2O_3 was required in the case of compositions containing 13 mol% TiO_2. In the case of compositions containing 18 mol% TiO_2, single-phase cubic structures were the exception, as they could only be attained with the presence of 11 mol% Y_2O_3.

Reduction studies indicated that some changes occur when the YZTC materials are reduced in argon or 5% H_2/ Argon. In argon, there is some reduction of fully oxidised materials, as up to 17% of the Ce is reduced from Ce^{4+} to Ce^{3+}, while in 5% H_2/ Argon, the extent of reduction was almost 100%, due to the lower pO_2. Further evidence of reduction was that the materials turned light grey in argon, then dark brown/ black in 5% H_2/ Argon. Compared to samples, as fired in static air at 1,400-1,500°C, mass gains were observed when annealed in argon, implying that there is less reduction of Ce in argon than the firing conditions.

The effect reduction had on structure was that with falling pO_2, the unit cell edge decreased slightly in argon by up to 0.0075Å, relative to materials 'as-fired', then rising more significantly in 5% H_2/ Argon by up to 0.0533Å, increasing with CeO_2 content.
Finally, in terms of thermal expansion, α ranged from $10.25 - 11.68*10^{-6}\ K^{-1}$ in oxygen. α increases with increasing CeO_2 content and decreasing TiO_2 content. In argon, the levels of α vary slightly from those in oxygen, with the difference in α in the range $-0.37 - +0.21*10^{-6}\ K^{-1}$, depending on composition. Then, in 5% H_2/ Argon, α was $0.32 - 0.98*10^{-6}\ K^{-1}$ lower than α in oxygen and tended to decrease with increasing CeO_2 content.

References:

[3.1]: A.R. West, Basic Solid State Chemistry, John Wiley & Sons Ltd, Chichester

[3.2]: http://unit.aist.go.jp/greenlife/ii/STRUCIMAGES/ZrO2-cubic.gif

[3.3]: http://www.tulane.edu/~inorg/PDF%20Files/Solid%20State/Rutile%20Structure.pdf

[3.4]: J.D. McCullough, A.M. Heuer, *Acta Crystallographica*, 1959, **12**, 507

[3.5]: http://www.zrchem.com/zrchemistry.htm

[3.6]: G. Teufer, *Acta Crystallographica*, 1962, **15**, 1187

[3.7]: F. Capel, M.A. Bañares, C. Moure, P. Durán, *Materials Letters*, 1999, **38**, 331-335

[3.8]: N. Shibata, J. Katamura, A. Kuwabara, Y. Ikuhara, T. Sakuma, *Materials Science and Engineering*, 2001, **A312**, 90-98.

[3.9]: R.J. Ackermann, E.D. Rauh, C.A. Alexander, *High Temp*, 1975, **7**, 304

[3.10]: Kingery, Bowen, Uhlmann, Introduction to Ceramics, 2nd Edition, Wiley-Interscience Publications, 1975

[3.11]: R.D. Shannon, C.T. Prewitt, *Acta Crystallographica*, 1969, **B25**, 925-929

[3.12]: V. Longo, L. Podda, *Ceramica (Florence)*, 1984, **37** [5], 18-20

[3.13]: I. Barbariol, L. Kucich-Podda, S. Riotti, *Mater. Engl.*, 1990, **1** [3], 959-964

[3.14]: A.J. Feighery, PhD Thesis, University of St. Andrews, 1998

[3.15]: P. Li, I-W. Chen, *Denki Kagaku*, 1993, **64**, 690

[3.16]: M. Mogensen, N.M. Sammes, G.A. Tompsett, *Solid State Ionics*, 2000, **129**, 63-94

Chapter 4: Conductivity

Contents

4: Conductivity

4.1: AC Impedance Spectroscopy Measurements

The AC Impedance spectroscopy measurements were carried out on a wide range of YZTC materials over temperature ranges between 300 and 1,000°C, in static air. In general, there were two sets of behaviour that were found in these sets of measurements. These are shown in Figures 4.1 and 4.2, respectively.

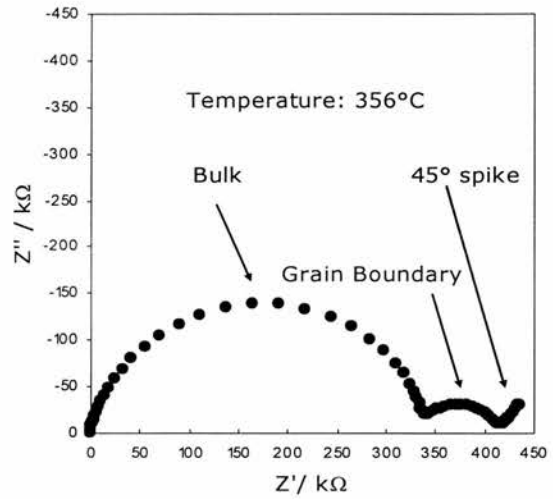

Figure 4.1: Example Impedance Response 1 from $Y_{0.15}Zr_{0.62}Ti_{0.08}Ce_{0.15}O_{1.925}$

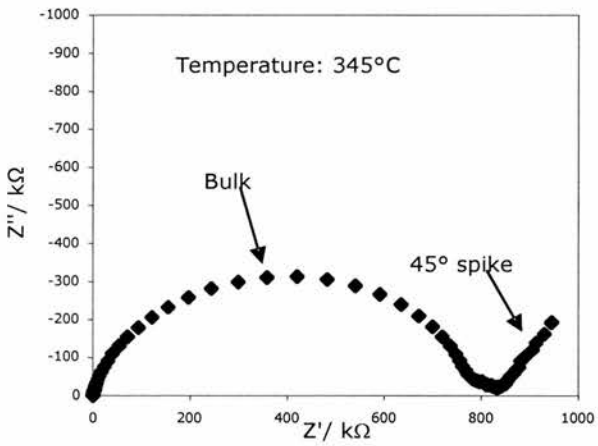

Figure 4.2: Example Impedance Response 2 from $Y_{0.20}Zr_{0.62}Ti_{0.13}Ce_{0.05}O_{1.90}$

The main difference between Figures 4.1 and 4.2 is that in Figure 4.2, the bulk is dominant, making the grain boundary contribution difficult to extract. At times, there can even be situations where there is no grain boundary response. The low frequency spike becomes a semicircle due to electrochemical processes at temperatures over 650-700°C.

In the tables listing conductivity results, the following abbreviations are used: σ_{bulk} for bulk conductivity, σ_{gb} for grain boundary conductivity and σ_{elec} for conductivity due to electrochemical processes. All element conductivities were corrected for geometry to Scm^{-1}, which is suitable for bulk and grain boundary. For convenience, the electrochemical conductivity was also expressed in Scm^{-1}. As it is an interface process, however, it would be more appropriate in units of Scm^{-2}.

4.1.1: Measurements in Static Air

$Y_{0.20}Zr_{0.62}Ti_{0.13}Ce_{0.05}O_{1.90}$

Measurements were performed from 345-835°C. The Nyquist plots showed a bulk semicircle, low frequency spike/ electrochemical semicircle and part of a grain boundary semicircle, although this was small compared to the bulk and could not be determined with any confidence. The conductivity results are shown in Table 4.1, capacitances are in Table 4.2 and the Arrhenius plots were shown in Figure 4.3. From the Arrhenius plots, at 900°C, σ_{bulk} was $4.226*10^{-3}$ Scm^{-1} and σ_{elec} was $9.235*10^{-2}$ Scm^{-1}.

Table 4.1: Conductivity results

Temperature/ °C	σ_{bulk}/ Scm^{-1}	σ_{elec}/ Scm^{-1}
345	$2.589*10^{-7}$	-
368	$5.388*10^{-7}$	-
392	$1.251*10^{-6}$	-
421	$2.572*10^{-6}$	-
445	$5.317*10^{-6}$	-
478	$1.047*10^{-5}$	-
501	$1.893*10^{-5}$	-
539	$3.755*10^{-5}$	-
562	$6.312*10^{-5}$	-
604	$1.185*10^{-4}$	$2.163*10^{-5}$
627	-	$5.103*10^{-5}$
668	$2.994*10^{-4}$	$3.073*10^{-4}$
692	$4.425*10^{-4}$	$7.852*10^{-4}$
738	$7.572*10^{-4}$	$2.567*10^{-3}$
761	$1.053*10^{-3}$	$6.494*10^{-3}$
835	$2.144*10^{-3}$	$1.118*10^{-2}$

Table 4.2: Additional Parameters

C_{bulk}/ Fcm^{-1}	C_{elec}/ Fcm^{-1}
$3.56*10^{-12}$	$2.51*10^{-5}$

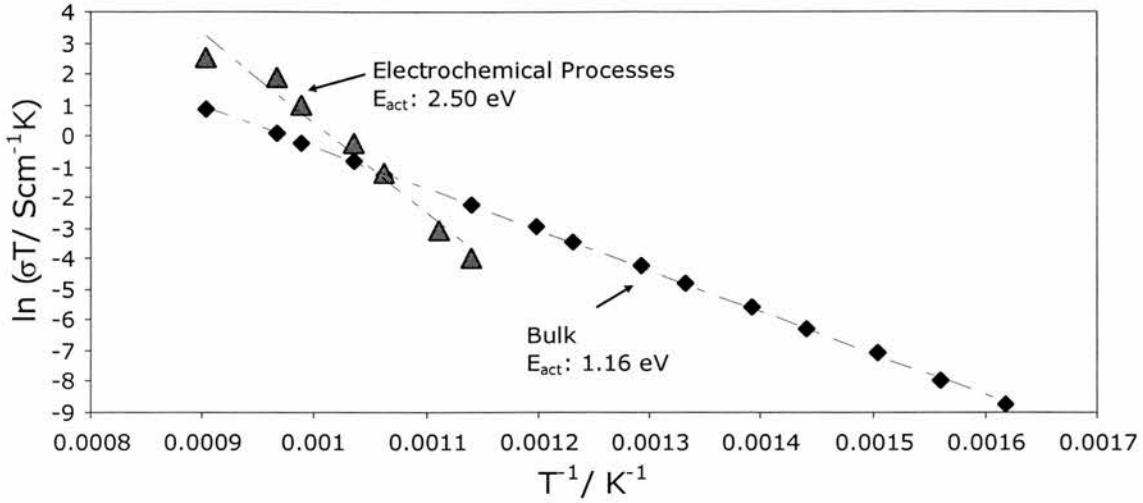

Figure 4.3: Arrhenius plots for $Y_{0.20}Zr_{0.62}Ti_{0.13}Ce_{0.05}O_{1.90}$ measured in air

$Y_{0.20}Zr_{0.57}Ti_{0.13}Ce_{0.10}O_{1.90}$

Measurements were from 351-898°C. The Nyquist plots showed a bulk semicircle, low frequency spike/ electrochemical semicircle and part of a grain boundary semicircle, although this was mostly merged in with the bulk. The grain boundary response could only be determined up to 448°C and was not seen above 570°C. The conductivity results are shown in Table 4.3, capacitances in Table 4.4 and the Arrhenius plots were shown in Figure 4.4. From the Arrhenius plots, at 900°C, σ_{bulk} was $3.806*10^{-3}$ Scm^{-1}, σ_{gb} was $2.168*10^{-2}$ Scm^{-1} and σ_{elec} was 1.509 Scm^{-1}.

Table 4.3: Conductivity results

Temperature/ °C	σ_{bulk}/ Scm^{-1}	σ_{gb}/ Scm^{-1}	σ_{elec}/ Scm^{-1}
351	$4.237*10^{-7}$	$9.119*10^{-7}$	-
359	$4.016*10^{-7}$	$1.204*10^{-6}$	-
405	$2.042*10^{-6}$	$5.618*10^{-6}$	-
423	$2.528*10^{-6}$	$7.332*10^{-6}$	-
448	$5.944*10^{-6}$	$1.858*10^{-5}$	-
504	$1.993*10^{-5}$	-	-
570	$6.885*10^{-5}$	-	$4.464*10^{-5}$
607	$1.078*10^{-4}$	-	$1.156*10^{-4}$
645	$2.208*10^{-4}$	-	$1.191*10^{-3}$
690	$4.049*10^{-4}$	-	$5.277*10^{-3}$
739	$7.659*10^{-4}$	-	$2.600*10^{-2}$
787	$1.340*10^{-3}$	-	$7.156*10^{-2}$
795	$1.426*10^{-3}$	-	$9.659*10^{-2}$
860	$2.536*10^{-3}$	-	-
898	$3.582*10^{-3}$	-	-

Table 4.4: Additional Parameters

C_{bulk}/ Fcm^{-1}	C_{gb}/ Fcm^{-1}	C_{elec}/ Fcm^{-1}
$4.60*10^{-12}$	$6.99*10^{-10}$	$5.34*10^{-5}$

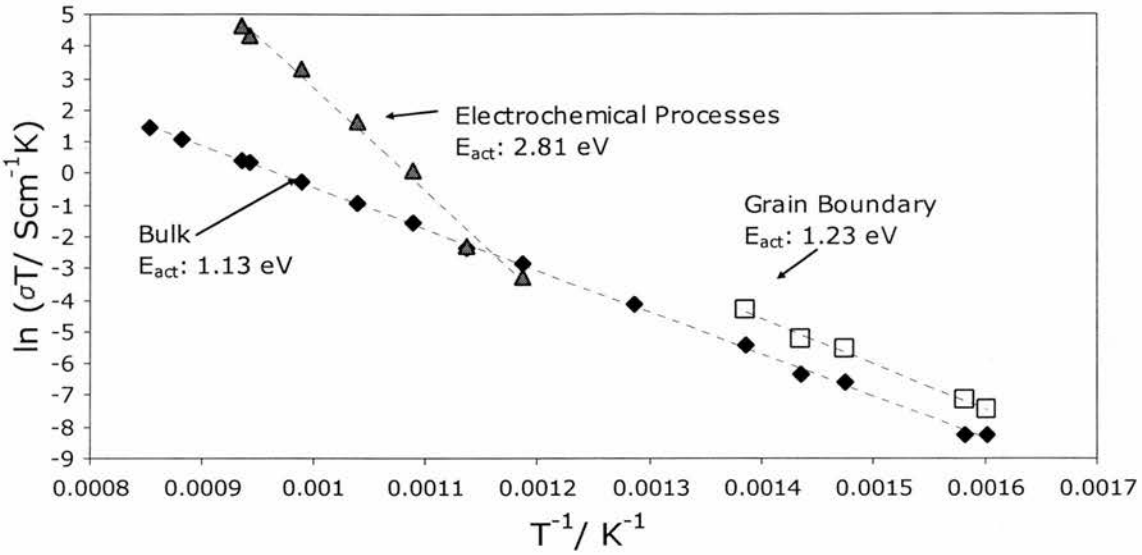

Figure 4.4: Arrhenius plots for $Y_{0.20}Zr_{0.57}Ti_{0.13}Ce_{0.10}O_{1.90}$ measured in air

$Y_{0.15}Zr_{0.52}Ti_{0.08}Ce_{0.25}O_{1.925}$

Measurements were from 289-776°C. The Nyquist plots showed a bulk semicircle, low frequency spike/ electrochemical semicircle and part of a grain boundary semicircle, although this was mostly merged in with the bulk. The grain boundary response could only be determined up to 464°C and was not seen above 572°C. The conductivity results are shown in Table 4.5, capacitances in Table 4.6 and the Arrhenius plots were shown in Figure 4.5. It was also estimated from the Arrhenius plot that at 900°C, σ_{bulk} was $5.601*10^{-3}$ Scm^{-1}, $5.407*10^{-3}$ Scm^{-1} for σ_{gb} and 1.122 Scm^{-1} for σ_{elec}.

Table 4.5: Conductivity results

Temperature/ °C	σ_{bulk}/ Scm^{-1}	σ_{gb}/ Scm^{-1}	σ_{elec}/ Scm^{-1}
289	$2.381*10^{-8}$	-	-
352	$2.659*10^{-7}$	$1.284*10^{-6}$	-
382	$7.271*10^{-7}$	$2.177*10^{-6}$	-
409	$1.664*10^{-6}$	$6.414*10^{-6}$	-
433	$3.212*10^{-6}$	$1.145*10^{-5}$	-
464	$7.154*10^{-6}$	$1.703*10^{-5}$	-
487	$1.248*10^{-5}$	-	-
519	$2.516*10^{-5}$	-	-
540	$4.088*10^{-5}$	-	-
572	$7.422*10^{-5}$	-	-
596	$1.135*10^{-4}$	-	$4.921*10^{-5}$
631	-	-	$2.864*10^{-4}$
655	$2.832*10^{-4}$	-	$7.868*10^{-4}$
695	$5.292*10^{-4}$	-	$2.983*10^{-3}$
718	$7.174*10^{-4}$	-	$7.120*10^{-3}$
776	$1.483*10^{-3}$	-	$3.506*10^{-2}$

Table 4.6: Additional Parameters

C_{bulk}/ Fcm^{-1}	C_{gb}/ Fcm^{-1}	C_{elec}/ Fcm^{-1}
$4.20*10^{-12}$	$7.25*10^{-10}$	$5.40*10^{-5}$

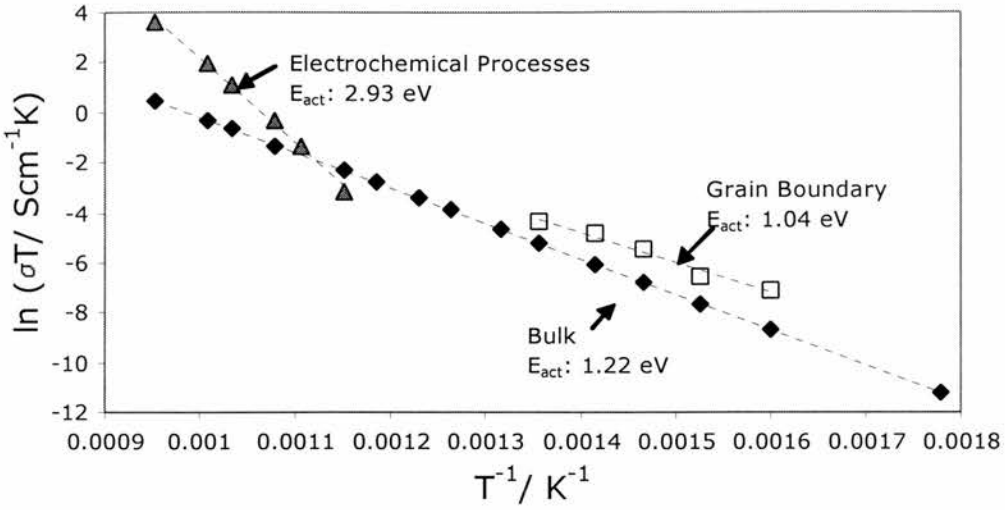

Figure 4.5: Arrhenius plots for $Y_{0.15}Zr_{0.52}Ti_{0.08}Ce_{0.25}O_{1.925}$ measured in air

$Y_{0.15}Zr_{0.52}Ti_{0.13}Ce_{0.20}O_{1.925}$

Measurements were from 333-902°C. The Nyquist plots showed a bulk semicircle, low frequency spike/ electrochemical semicircle and part of a grain boundary semicircle, although this could not be determined with any confidence. The conductivity results are shown in Table 4.7, capacitances in Table 4.8 and the Arrhenius plots were shown in Figure 4.6. At 900°C, σ_{bulk} was $3.003*10^{-3}$ Scm^{-1} and σ_{elec} was $3.642*10^{-2}$ Scm^{-1}.

Table 4.7: Conductivity Results

Temperature/ °C	σ_{bulk}/ Scm^{-1}	σ_{elec}/ Scm^{-1}
333	$5.923*10^{-8}$	-
371	$2.117*10^{-7}$	-
382	$3.238*10^{-7}$	-
431	$1.339*10^{-6}$	-
433	$1.506*10^{-6}$	-
482	$5.326*10^{-6}$	-
489	$5.998*10^{-6}$	-
534	$1.729*10^{-5}$	-
552	$2.319*10^{-5}$	-
588	$4.969*10^{-5}$	-
614	$7.516*10^{-5}$	-
647	$1.343*10^{-4}$	$1.381*10^{-4}$
682	$2.150*10^{-4}$	$4.033*10^{-4}$
705	$3.198*10^{-4}$	$1.247*10^{-3}$
750	$5.609*10^{-4}$	$2.736*10^{-3}$
767	$7.181*10^{-4}$	$4.292*10^{-3}$
823	$1.306*10^{-3}$	$8.722*10^{-3}$
902	$2.981*10^{-3}$	$2.951*10^{-2}$

Table 4.8: Additional Parameters

C_{bulk}/ Fcm^{-1}	C_{elec}/ Fcm^{-1}
$4.11*10^{-12}$	$1.56*10^{-5}$

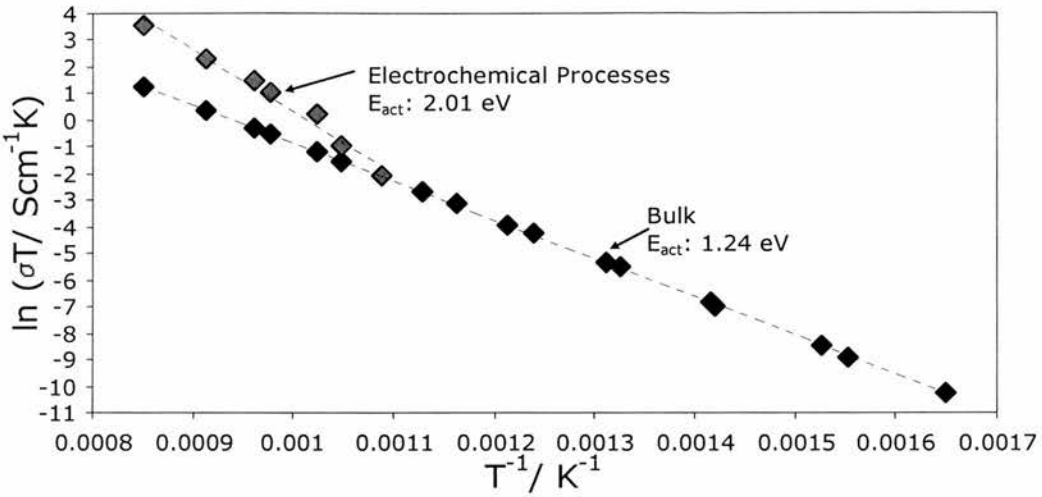

Figure 4.6: Arrhenius plots for $Y_{0.15}Zr_{0.52}Ti_{0.13}Ce_{0.20}O_{1.925}$ measured in air

$Y_{0.125}Zr_{0.52}Ti_{0.13}Ce_{0.225}O_{1.9375}$

Measurements were from 343-845°C. The Nyquist plots showed a bulk semicircle, low frequency spike/ electrochemical semicircle and part of a grain boundary semicircle, although this could not be determined with any confidence. Conductivity results are shown in Table 4.9, capacitances in Table 4.10 and Arrhenius plots were shown in Figure 4.7. At 900°C, σ_{bulk} was $2.613*10^{-3}$ Scm^{-1} and σ_{elec} was $2.887*10^{-2}$ Scm^{-1}.

Table 4.9: Conductivity Results

Temperature/ °C	σ_{bulk}/ Scm^{-1}	σ_{elec}/ Scm^{-1}
343	$1.247*10^{-7}$	-
391	$6.098*10^{-7}$	-
404	$6.849*10^{-7}$	-
448	$2.746*10^{-6}$	-
462	$3.289*10^{-6}$	-
500	$9.278*10^{-6}$	-
523	$1.333*10^{-5}$	-
557	$2.965*10^{-5}$	-
589	$4.771*10^{-5}$	-
613	$8.250*10^{-5}$	-
655	$1.405*10^{-4}$	$1.352*10^{-4}$
679	-	$7.272*10^{-4}$
716	$3.303*10^{-4}$	$1.002*10^{-3}$
734	-	$2.830*10^{-3}$
771	$6.594*10^{-4}$	$3.004*10^{-3}$
800	$1.048*10^{-3}$	$7.556*10^{-3}$
827	$1.187*10^{-3}$	-
845	$1.619*10^{-3}$	$9.714*10^{-3}$

Table 4.10: Additional Parameters

C_{bulk}/ Fcm^{-1}	C_{elec}/ Fcm^{-1}
$3.54*10^{-12}$	$6.85*10^{-6}$

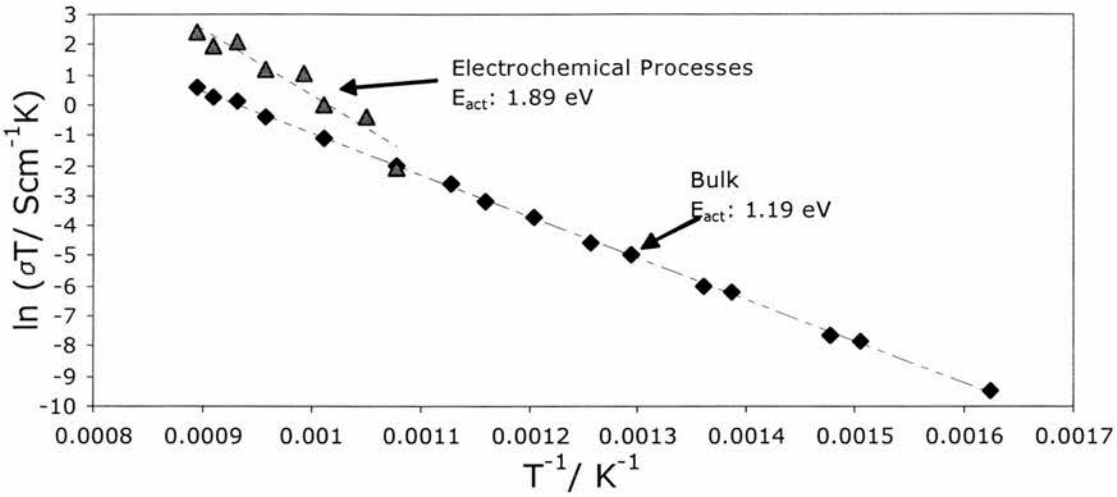

Figure 4.7: Arrhenius plots for $Y_{0.125}Zr_{0.52}Ti_{0.13}Ce_{0.225}O_{1.9375}$ measured in air

$Y_{0.15}Zr_{0.57}Ti_{0.03}Ce_{0.25}O_{1.925}$

Measurements were from 363 - 901°C. The Nyquist plots showed a bulk and grain boundary semicircles, along with the low frequency spike/ electrochemical semicircle. Conductivity results are shown in Table 4.11, capacitances in Table 4.12 and Arrhenius plots in Figure 4.8. At 901°C, σ_{bulk} was $6.094*10^{-3}$ Scm^{-1}, σ_{gb} was 0.1986 Scm^{-1} and σ_{elec} was 0.0818 Scm^{-1}.

Table 4.11: Conductivity Results

Temperature/ °C	σ_{bulk}/ Scm^{-1}	σ_{gb}/ Scm^{-1}	σ_{elec}/ Scm^{-1}
363	$5.526*10^{-7}$	$9.487*10^{-7}$	
416	$2.914*10^{-6}$	$3.076*10^{-6}$	
471	$1.028*10^{-5}$	$1.881*10^{-5}$	
526	$3.755*10^{-5}$	$4.963*10^{-5}$	
581	$1.009*10^{-4}$	$2.456*10^{-4}$	
636	$2.978*10^{-4}$	$4.594*10^{-4}$	$2.294*10^{-4}$
690	$6.024*10^{-4}$	$2.819*10^{-3}$	$2.317*10^{-3}$
746	$1.318*10^{-3}$	$3.848*10^{-3}$	$5.746*10^{-3}$
802	$2.223*10^{-3}$	$2.200*10^{-2}$	$2.299*10^{-2}$
845	$3.615*10^{-3}$	$2.531*10^{-2}$	$2.526*10^{-2}$
901	$6.094*10^{-3}$	$1.986*10^{-1}$	$8.180*10^{-2}$

Table 4.12: Additional Parameters

C_{bulk}/ Fcm^{-1}	C_{gb}/ Fcm^{-1}	C_{elec}/ Fcm^{-1}
$4.09*10^{-12}$	$1.43*10^{-9}$	$6.78*10^{-4}$

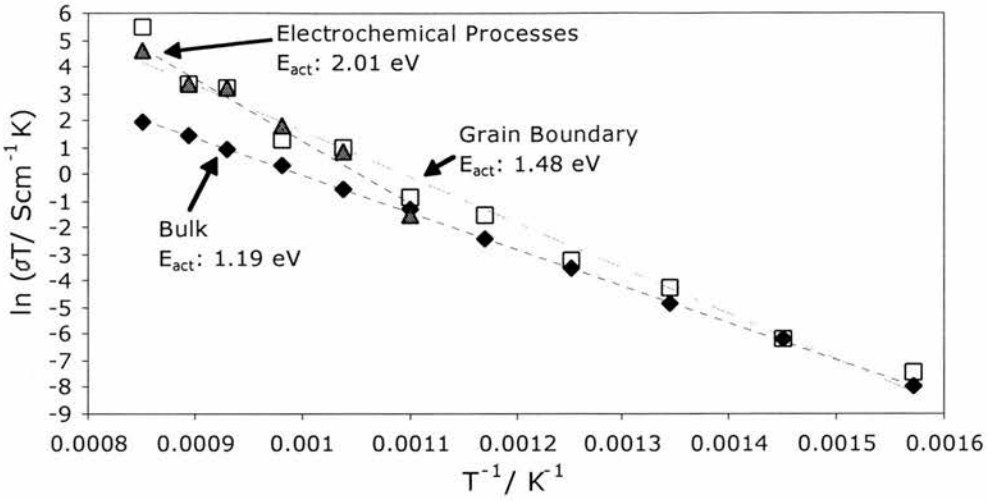

Figure 4.8: Arrhenius plots for $Y_{0.15}Zr_{0.57}Ti_{0.03}Ce_{0.25}O_{1.925}$ measured in air

$Y_{0.15}Zr_{0.62}Ti_{0.08}Ce_{0.15}O_{1.925}$

Measurements were from 356 - 897°C. The Nyquist plots showed a bulk and grain boundary semicircles, along with the low frequency spike/ electrochemical semicircle. The grain boundary response could only be determined up to 748°C, merging fully with the electrochemical semicircle at higher temperatures. Conductivity results are shown in Table 4.13, capacitances in Table 4.14 and Arrhenius plots were shown in Figure 4.9. At 900°C, σ_{bulk} was $6.684*10^{-3}$ Scm^{-1}, σ_{gb} was $2.377*10^{-1}$ Scm^{-1} and σ_{elec} was 3.646 Scm^{-1}.

Table 4.13: Conductivity results

Temperature/ °C	σ_{bulk}/ Scm^{-1}	σ_{gb}/ Scm^{-1}	σ_{elec}/ Scm^{-1}
356	$8.924*10^{-7}$	$3.389*10^{-6}$	-
396	$2.702*10^{-6}$	$9.396*10^{-6}$	-
431	$7.094*10^{-6}$	$3.475*10^{-5}$	-
469	$1.632*10^{-5}$	$7.597*10^{-5}$	-
504	$3.610*10^{-5}$	$2.149*10^{-4}$	-
540	$7.148*10^{-5}$	$3.976*10^{-4}$	-
574	$1.351*10^{-4}$	$1.025*10^{-3}$	$1.882*10^{-4}$
610	$2.315*10^{-4}$	$1.890*10^{-3}$	$3.185*10^{-4}$
643	$4.064*10^{-4}$	$5.182*10^{-3}$	$1.537*10^{-3}$
679	$6.349*10^{-4}$	$6.618*10^{-3}$	$3.761*10^{-3}$
712	$1.039*10^{-3}$	$2.958*10^{-2}$	$1.905*10^{-2}$
748	$1.252*10^{-3}$	$8.762*10^{-2}$	$3.369*10^{-2}$
781	$2.166*10^{-3}$	-	$3.709*10^{-1}$
817	$3.047*10^{-3}$	-	$5.828*10^{-1}$
850	$4.367*10^{-3}$	-	-
897	$6.626*10^{-3}$	-	-

Table 4.14: Additional Parameters

C_{bulk}/ Fcm^{-1}	C_{gb}/ Fcm^{-1}	C_{elec}/ Fcm^{-1}
$3.45*10^{-12}$	$5.16*10^{-9}$	$5.11*10^{-5}$

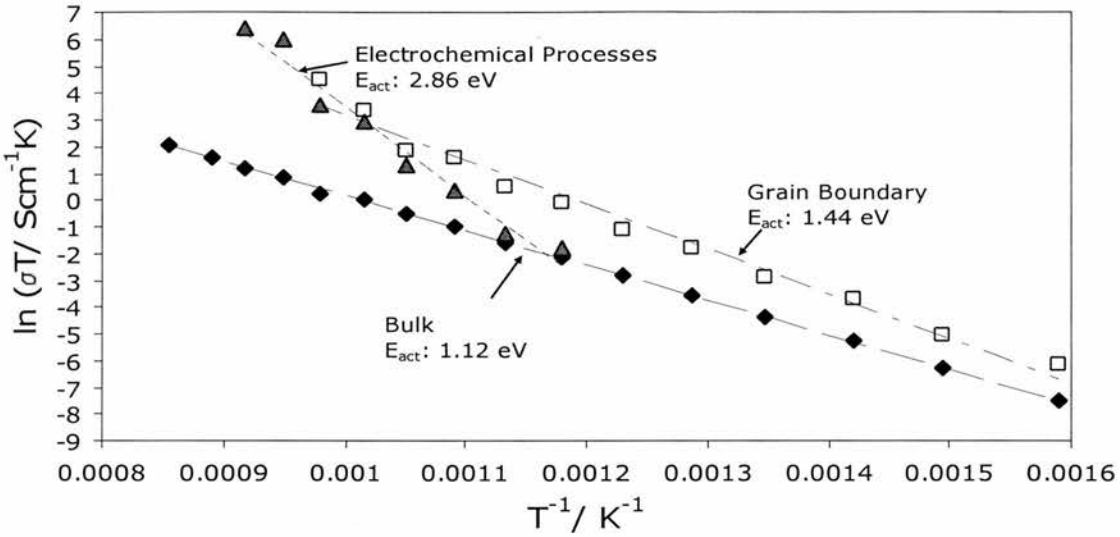

Figure 4.9: Arrhenius plots for $Y_{0.15}Zr_{0.62}Ti_{0.08}Ce_{0.15}O_{1.925}$ measured in air

$Y_{0.15}Zr_{0.57}Ti_{0.08}Ce_{0.20}O_{1.925}$

Measurements were from 361 - 997°C. The Nyquist plots showed a bulk and grain boundary semicircles, along with the low frequency spike/ electrochemical semicircle. The grain boundary response could only be determined up to 691°C, merging with the electrochemical semicircle at higher temperatures. Conductivity results are shown in Table 4.15, capacitances in Table 4.16 and Arrhenius plots were shown in Figure 4.10. At 900°C, σ_{bulk} was $6.702*10^{-3}$ Scm^{-1}, $7.531*10^{-2}$ Scm^{-1} for σ_{gb} and $5.769*10^{-2}$ Scm^{-1} for σ_{elec}.

Table 4.15: Conductivity results.

Temperature/ °C	σ_{bulk}/ Scm^{-1}	σ_{gb}/ Scm^{-1}	σ_{elec}/ Scm^{-1}
361	$7.256*10^{-7}$	$1.315*10^{-6}$	-
416	$4.049*10^{-6}$	$7.596*10^{-6}$	-
470	$1.356*10^{-5}$	$2.086*10^{-5}$	-
581	$1.331*10^{-4}$	$3.741*10^{-4}$	-
635	$3.203*10^{-4}$	$1.590*10^{-3}$	-
691	$6.709*10^{-4}$	$7.470*10^{-3}$	$9.697*10^{-4}$
701	$7.735*10^{-4}$	-	-
799	$2.480*10^{-3}$	-	$1.001*10^{-2}$
834	$3.531*10^{-3}$	-	-
866	$4.867*10^{-3}$	-	$2.615*10^{-2}$
931	$8.590*10^{-3}$	-	$8.369*10^{-2}$
997	$1.539*10^{-2}$	-	$3.072*10^{-1}$

Table 4.16: Additional Parameters

C_{bulk}/ Fcm^{-1}	C_{gb}/ Fcm^{-1}	C_{elec}/ Fcm^{-1}
$4.59*10^{-12}$	$5.75*10^{-8}$	$5.66*10^{-4}$

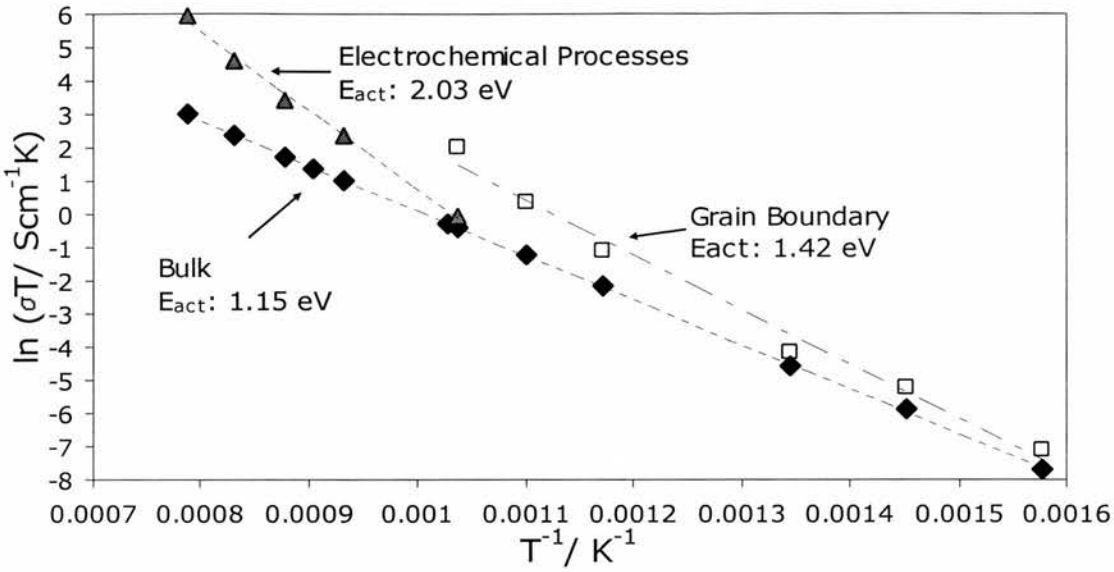

Figure 4.10: Arrhenius plots for $Y_{0.15}Zr_{0.57}Ti_{0.08}Ce_{0.20}O_{1.925}$ measured in air

$Y_{0.20}Zr_{0.62}Ti_{0.08}Ce_{0.10}O_{1.90}$

Measurements were from 365 - 932°C. The Nyquist plots showed a bulk and grain boundary semicircles, along with the low frequency spike/ electrochemical semicircle. The grain boundary response could only be determined up to 529°C, as it merges with the electrochemical semicircle at higher temperatures. Conductivity results are shown in Table 4.17, capacitances in Table 4.18 and Arrhenius plots were shown in Figure 4.11. At 900°C, σ_{bulk} was $7.830*10^{-3}$ Scm^{-1}, σ_{gb} was $3.575*10^{-2}$ Scm^{-1} and σ_{elec} was 0.138 Scm^{-1}.

Table 4.17: Conductivity results

Temperature/ °C	σ_{bulk}/ Scm^{-1}	σ_{gb}/ Scm^{-1}	σ_{elec}/ Scm^{-1}
365	$1.015*10^{-6}$	$4.155*10^{-6}$	-
420	$5.214*10^{-6}$	$1.790*10^{-5}$	-
473	$1.843*10^{-5}$	$8.737*10^{-5}$	-
529	$6.462*10^{-5}$	$2.336*10^{-4}$	-
669	$5.917*10^{-4}$	-	-
720	$1.251*10^{-3}$	-	$6.133*10^{-3}$
768	$2.072*10^{-3}$	-	$1.317*10^{-2}$
823	$3.714*10^{-3}$	-	$5.037*10^{-2}$
877	$7.473*10^{-2}$	-	$7.473*10^{-2}$
932	$1.011*10^{-2}$	-	$2.486*10^{-1}$

Table 4.18: Additional Parameters

C_{bulk}/ Fcm^{-1}	C_{gb}/ Fcm^{-1}	C_{elec}/ Fcm^{-1}
$4.82*10^{-12}$	$1.11*10^{-9}$	$3.69*10^{-4}$

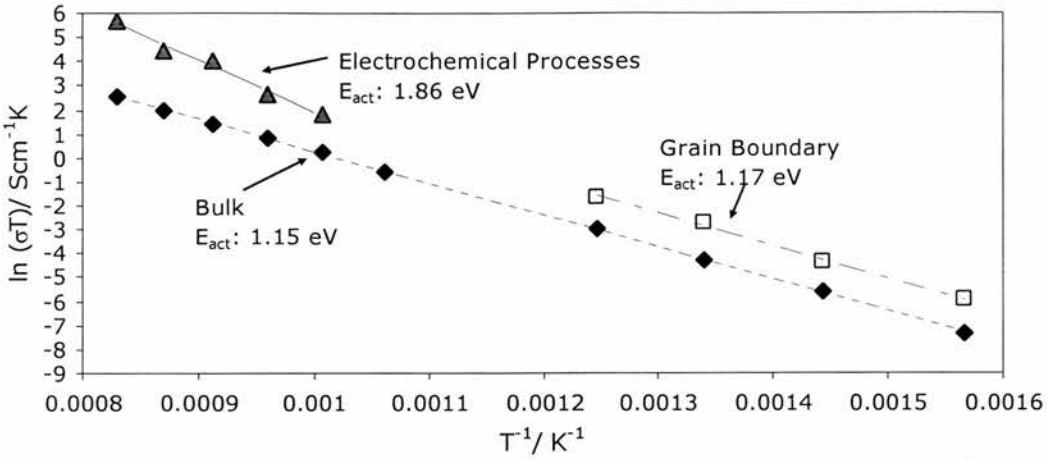

Figure 4.11: Arrhenius plots for $Y_{0.20}Zr_{0.62}Ti_{0.08}Ce_{0.10}O_{1.90}$ measured in air

$Y_{0.15}Zr_{0.62}Ti_{0.03}Ce_{0.20}O_{1.925}$

Measurements were from 418 - 907°C. The Nyquist plots showed a bulk and grain boundary semicircles, along with the low frequency spike/ electrochemical semicircle. The grain boundary response could only be determined up to 769°C, merging with the electrochemical semicircle at higher temperatures. Conductivity results are shown in Table 4.19, capacitances in Table 4.20 and Arrhenius plots were shown in Figure 4.12. At 900°C, σ_{bulk} was $7.911*10^{-3}$ Scm^{-1}, σ_{gb} was $6.063*10^{-2}$ Scm^{-1} and σ_{elec} was $2.473*10^{-2}$ Scm^{-1}.

Table 4.19: Conductivity results

Temperature/ °C	σ_{bulk}/ Scm^{-1}	σ_{gb}/ Scm^{-1}	σ_{elec}/ Scm^{-1}
418	$4.814*10^{-6}$	$8.481*10^{-6}$	$5.426*10^{-7}$
472	$1.934*10^{-5}$	$3.590*10^{-5}$	$2.415*10^{-6}$
526	$5.939*10^{-5}$	$1.246*10^{-4}$	$4.602*10^{-6}$
581	$4.064*10^{-4}$	$4.455*10^{-4}$	-
635	$3.507*10^{-4}$	$1.300*10^{-3}$	$6.164*10^{-5}$
659	$6.001*10^{-4}$	$1.328*10^{-3}$	$1.296*10^{-4}$
769	$2.128*10^{-3}$	$1.958*10^{-2}$	$2.500*10^{-3}$
800	$3.101*10^{-3}$	-	$1.473*10^{-2}$
825	$3.776*10^{-3}$	-	$9.232*10^{-3}$
855	$5.142*10^{-3}$	-	$1.684*10^{-2}$
907	$8.326*10^{-3}$	-	$3.920*10^{-2}$

Table 4.20: Additional Parameters

C_{bulk}/ Fcm^{-1}	C_{gb}/ Fcm^{-1}	C_{elec}/ Fcm^{-1}
$5.15*10^{-12}$	$2.23*10^{-9}$	$3.40*10^{-5}$

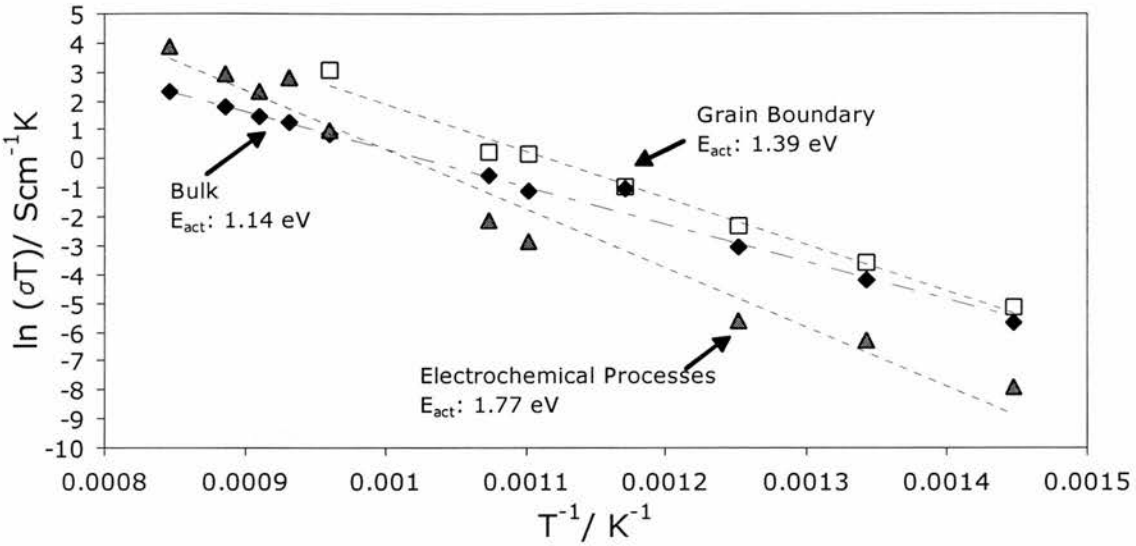

Figure 4.12: Arrhenius plots for $Y_{0.15}Zr_{0.62}Ti_{0.03}Ce_{0.20}O_{1.925}$ measured in air

$Y_{0.10}Zr_{0.62}Ti_{0.03}Ce_{0.25}O_{1.95}$

Measurements were from 363 - 910°C. The Nyquist plots showed a bulk and grain boundary semicircles, along with the low frequency spike/ electrochemical semicircle. The grain boundary response could only be determined up to 717°C, as it merged with the electrochemical semicircle at higher temperatures. Conductivity results are shown in Table 4.21, capacitances in Table 4.22 and Arrhenius plots were shown in Figure 4.13. At 900°C, σ_{bulk} was $9.951*10^{-3}$ Scm^{-1}, σ_{gb} was 0.101 Scm^{-1} and σ_{elec} was 0.113 Scm^{-1}.

Table 4.21: Conductivity results

Temperature/ °C	σ_{bulk}/ Scm^{-1}	σ_{gb}/ Scm^{-1}	σ_{elec}/ Scm^{-1}
363	$1.449*10^{-6}$	$1.615*10^{-6}$	-
418	$7.396*10^{-6}$	$9.842*10^{-6}$	-
473	$2.721*10^{-5}$	$4.831*10^{-5}$	-
527	$8.420*10^{-5}$	$1.918*10^{-4}$	-
581	-	$6.581*10^{-4}$	-
606	$3.371*10^{-4}$	$1.131*10^{-3}$	$8.325*10^{-6}$
636	$5.558*10^{-4}$	$1.976*10^{-3}$	$5.820*10^{-5}$
692	$1.133*10^{-3}$	$8.979*10^{-3}$	$7.855*10^{-4}$
717	$1.422*10^{-3}$	-	$1.741*10^{-3}$
746	$2.123*10^{-3}$	-	$3.608*10^{-3}$
801	$3.907*10^{-3}$	-	$1.050*10^{-2}$
828	$4.880*10^{-3}$	-	$1.423*10^{-2}$
856	$6.729*10^{-3}$	-	$2.445*10^{-2}$
910	$1.059*10^{-2}$	-	-

Table 4.22: Additional Parameters

C_{bulk}/ Fcm^{-1}	C_{gb}/ Fcm^{-1}	C_{elec}/ Fcm^{-1}
$4.60*10^{-12}$	$4.54*10^{-9}$	$5.43*10^{-5}$

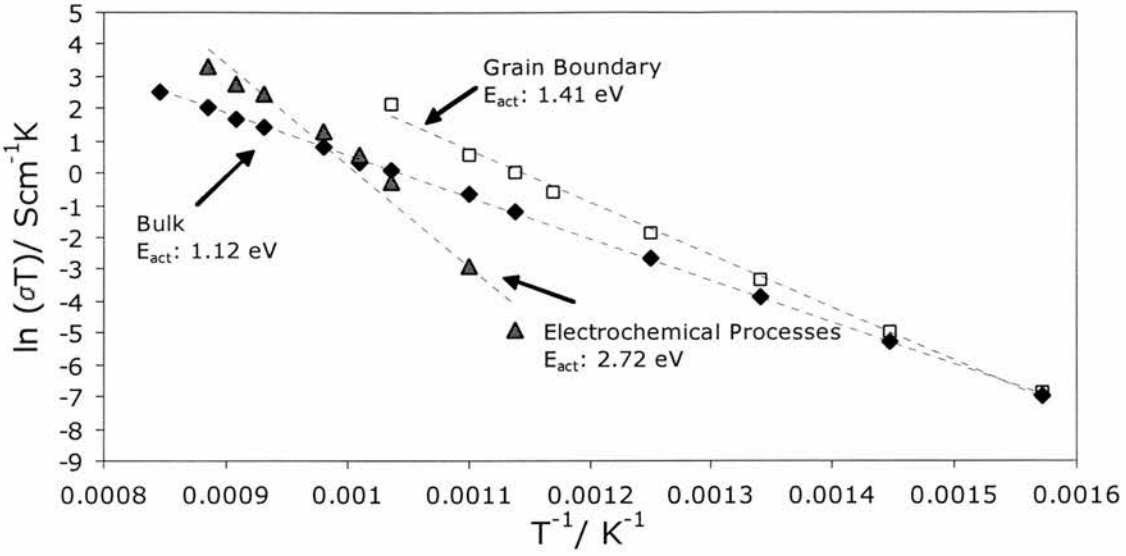

Figure 4.13: Arrhenius plots for $Y_{0.10}Zr_{0.62}Ti_{0.03}Ce_{0.25}O_{1.95}$ measured in air

$Y_{0.125}Zr_{0.47}Ti_{0.08}Ce_{0.325}O_{1.9375}$

Measurements were from 357 - 912°C. The Nyquist plots showed a bulk semicircle, along with the low frequency spike/ electrochemical semicircle. Conductivity results are shown in Table 4.23, capacitances in Table 4.24 and Arrhenius plots were shown in Figure 4.14. At 900°C, σ_{bulk} was $4.758*10^{-3}$ Scm^{-1} and σ_{elec} was $2.435*10^{-2}$ Scm^{-1}.

Table 4.23: Conductivity results.

Temperature/ °C	σ_{bulk}/ Scm^{-1}	σ_{elec}/ Scm^{-1}
357	$3.698*10^{-7}$	-
411	$1.859*10^{-6}$	-
466	$7.551*10^{-6}$	-
523	$2.530*10^{-5}$	-
577	$7.152*10^{-5}$	-
633	$1.836*10^{-4}$	-
687	$4.214*10^{-4}$	$5.675*10^{-4}$
743	$9.046*10^{-4}$	$3.016*10^{-3}$
800	$1.804*10^{-3}$	$9.447*10^{-3}$
829	$2.234*10^{-3}$	$5.492*10^{-3}$
855	$3.353*10^{-3}$	$2.380*10^{-2}$
912	$5.461*10^{-3}$	$1.803*10^{-2}$

Table 4.24: Additional Parameters

C_{bulk}/ Fcm^{-1}	C_{elec}/ Fcm^{-1}
$6.14*10^{-12}$	$9.54*10^{-4}$

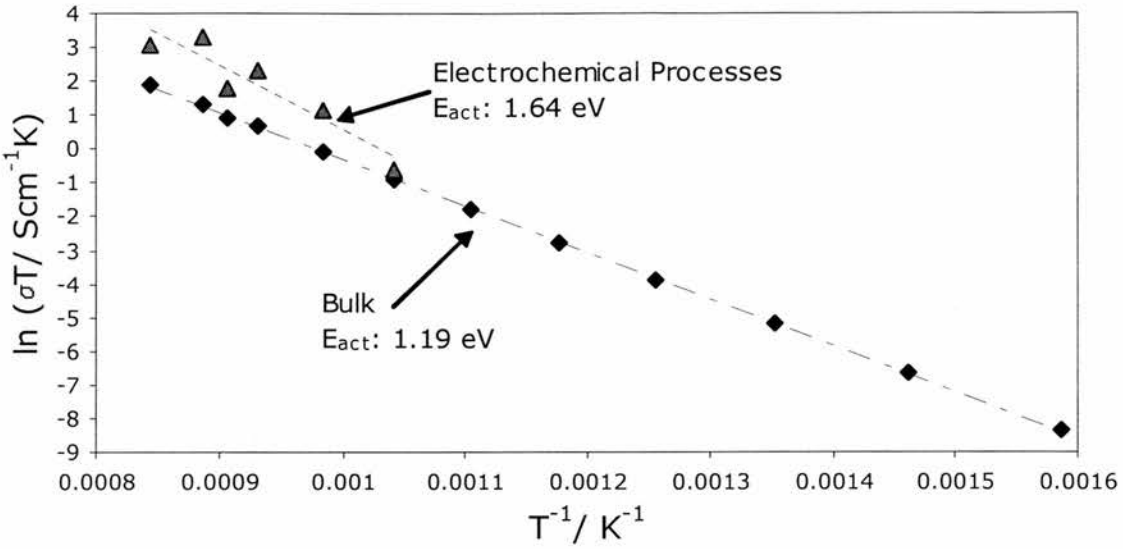

Figure 4.14: Arrhenius plots for $Y_{0.125}Zr_{0.47}Ti_{0.08}Ce_{0.325}O_{1.9375}$ measured in air

$Y_{0.20}Zr_{0.52}Ti_{0.03}Ce_{0.25}O_{1.90}$

Measurements were from 359 - 913°C. The Nyquist plots showed a bulk and grain boundary semicircles, along with the low frequency spike/ electrochemical semicircle. The grain boundary response could only be determined up to 802°C, merging with the electrochemical semicircle at higher temperatures. Conductivity results are shown in Table 4.25, capacitances in Table 4.26 and Arrhenius plots were shown in Figure 4.15. At 900°C, σ_{bulk} was $7.103*10^{-3}$ Scm^{-1}, σ_{gb} was 0.264 Scm^{-1} and σ_{elec} was $1.671*10^{-2}$ Scm^{-1}.

Table 4.25: Conductivity results.

Temperature/ °C	σ_{bulk}/ Scm^{-1}	σ_{gb}/ Scm^{-1}	σ_{elec}/ Scm^{-1}
359	$4.201*10^{-7}$	-	-
416	$2.626*10^{-6}$	$1.260*10^{-5}$	-
471	$1.232*10^{-5}$	$6.765*10^{-5}$	-
503	$2.294*10^{-5}$	$1.323*10^{-4}$	-
526	$3.785*10^{-5}$	-	-
582	$1.184*10^{-4}$	$8.087*10^{-4}$	-
612	$1.844*10^{-4}$	$1.678*10^{-3}$	-
637	$2.972*10^{-4}$	$3.690*10^{-3}$	-
692	$6.712*10^{-4}$	$1.195*10^{-2}$	$1.403*10^{-4}$
721	$9.563*10^{-4}$	$2.210*10^{-2}$	$4.973*10^{-4}$
748	$1.357*10^{-3}$	$4.799*10^{-2}$	$1.118*10^{-3}$
802	$2.601*10^{-3}$	-	$3.862*10^{-3}$
831	$3.444*10^{-3}$	-	$4.893*10^{-3}$
858	$4.656*10^{-3}$	-	$9.251*10^{-3}$
913	$7.834*10^{-3}$	-	$1.367*10^{-2}$

Table 4.26: Additional Parameters

C_{bulk}/ Fcm^{-1}	C_{gb}/ Fcm^{-1}	C_{elec}/ Fcm^{-1}
$4.27*10^{-12}$	$4.67*10^{-9}$	$1.97*10^{-4}$

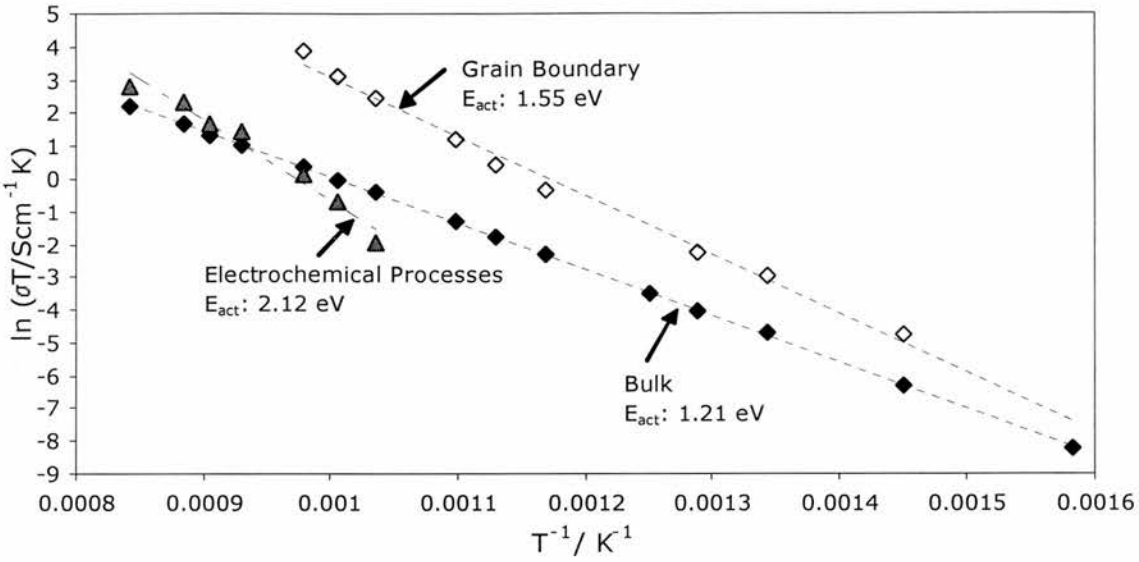

Figure 4.15: Arrhenius plots for $Y_{0.20}Zr_{0.52}Ti_{0.03}Ce_{0.25}O_{1.90}$ measured in air

$Y_{0.125}Zr_{0.62}Ti_{0.08}Ce_{0.175}O_{1.9375}$

Measurements were from 364 - 963°C. The Nyquist plots showed the bulk and grain boundary semicircles, along with the low frequency spike/ electrochemical semicircle. The grain boundary response could only be determined up to 713°C, as it became more difficult to determine with higher temperature, merging with the electrochemical semicircle at higher temperatures. Conductivity results are shown in Table 4.27, capacitances in Table 4.28 and Arrhenius plots were shown in Figure 4.16. At 900°C, σ_{bulk} was $6.508*10^{-3}$ Scm^{-1}, σ_{gb} was $8.202*10^{-2}$ Scm^{-1} and σ_{elec} was $1.822*10^{-2}$ Scm^{-1}.

Table 4.27: Conductivity results

Temperature/ °C	σ_{bulk}/ Scm^{-1}	σ_{gb}/ Scm^{-1}	σ_{elec}/ Scm^{-1}
364	$9.484*10^{-7}$	$1.853*10^{-6}$	-
441	$8.022*10^{-6}$	$2.560*10^{-5}$	-
495	$2.766*10^{-5}$	$8.803*10^{-5}$	-
550	$8.089*10^{-5}$	$2.655*10^{-4}$	-
604	$1.971*10^{-4}$	$9.661*10^{-4}$	-
659	-	$2.472*10^{-3}$	$9.877*10^{-5}$
713	$9.532*10^{-4}$	$1.246*10^{-2}$	$7.328*10^{-4}$
768	$1.794*10^{-3}$	-	$2.399*10^{-3}$
823	$3.190*10^{-3}$	-	$6.415*10^{-3}$
878	$5.302*10^{-3}$	-	$1.246*10^{-2}$
921	$7.199*10^{-3}$	-	$1.579*10^{-2}$
963	$1.137*10^{-2}$	-	$5.090*10^{-2}$

Table 4.28: Additional Parameters

C_{bulk}/ Fcm^{-1}	C_{gb}/ Fcm^{-1}	C_{elec}/ Fcm^{-1}
$6.01*10^{-12}$	$1.23*10^{-9}$	$3.71*10^{-4}$

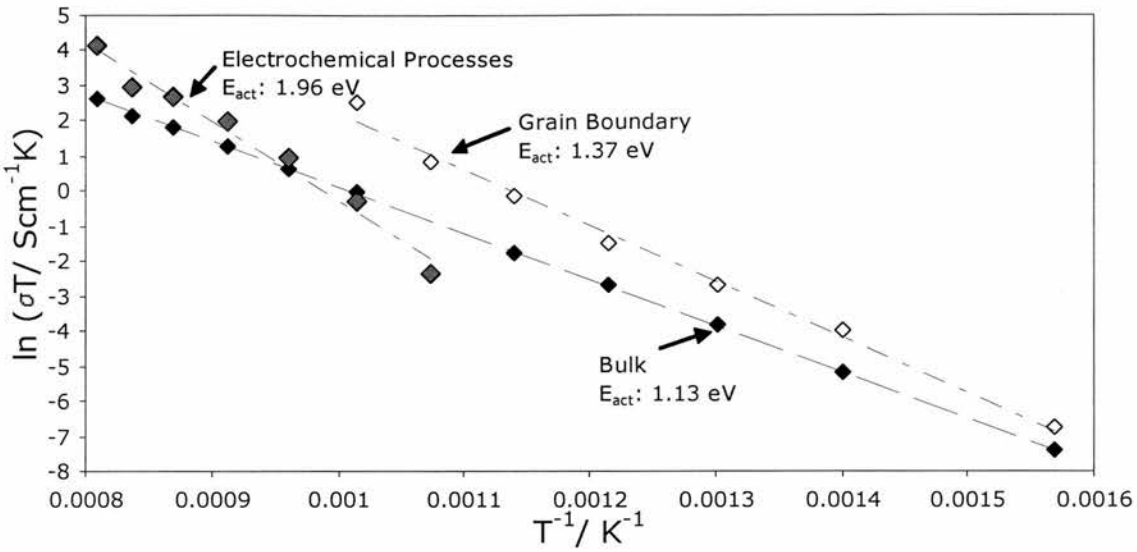

Figure 4.16: Arrhenius plots for $Y_{0.125}Zr_{0.62}Ti_{0.08}Ce_{0.175}O_{1.9375}$ measured in air

$Y_{0.20}Zr_{0.52}Ti_{0.08}Ce_{0.20}O_{1.90}$

Measurements were from 392 - 911°C. The Nyquist plots showed the bulk and low frequency spike/ electrochemical semicircles. The grain boundary response was almost impossible to determine reliably. Conductivity results are shown in Table 4.29, capacitances in Table 4.30 and Arrhenius plots were shown in Figure 4.17. At 900°C, σ_{bulk} was $5.114*10^{-3}$ Scm^{-1}, and σ_{elec} was $2.383*10^{-2}$ Scm^{-1}.

Table 4.29: Conductivity results

Temperature/ °C	σ_{bulk}/ Scm^{-1}	σ_{elec}/ Scm^{-1}
392	$1.048*10^{-6}$	-
502	$1.711*10^{-5}$	-
529	$3.557*10^{-5}$	-
584	$9.908*10^{-5}$	-
610	$1.311*10^{-4}$	-
638	-	-
693	$5.486*10^{-4}$	$9.413*10^{-4}$
720	$6.687*10^{-4}$	$4.312*10^{-4}$
747	$1.072*10^{-3}$	$3.841*10^{-3}$
803	$2.007*10^{-3}$	$1.061*10^{-2}$
831	$2.352*10^{-3}$	$4.801*10^{-3}$
858	$3.518*10^{-3}$	$2.225*10^{-2}$
911	$5.288*10^{-3}$	$1.847*10^{-2}$

Table 4.30: Additional Parameters

C_{bulk}/ Fcm^{-1}	C_{elec}/ Fcm^{-1}
$4.68*10^{-12}$	$5.59*10^{-5}$

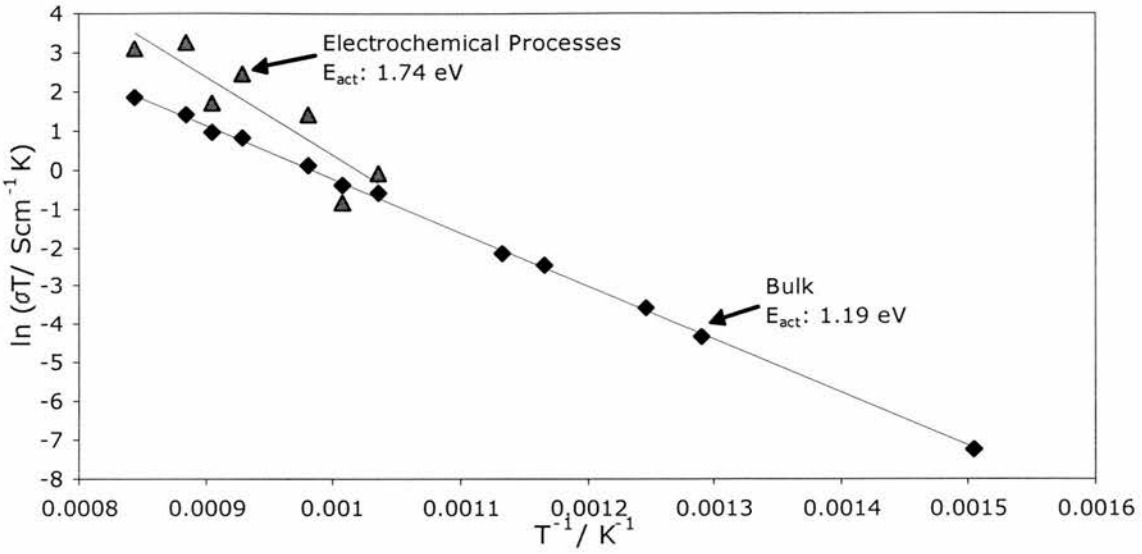

Figure 4.17: Arrhenius plots for $Y_{0.20}Zr_{0.52}Ti_{0.08}Ce_{0.20}O_{1.90}$ measured in air

$Y_{0.20}Zr_{0.57}Ti_{0.08}Ce_{0.15}O_{1.90}$

Measurements were from 363 - 912°C. The Nyquist plots showed a bulk along with the low frequency spike/ electrochemical semicircle. Conductivity results are shown in Table 4.31, capacitances in Table 4.32 and Arrhenius plots were shown in Figure 4.18. At 900°C, σ_{bulk} was $5.229*10^{-3}$ Scm^{-1} and σ_{elec} was $3.844*10^{-2}$ Scm^{-1}.

Table 4.31: Conductivity results

Temperature/ °C	σ_{bulk}/ Scm^{-1}	σ_{elec}/ Scm^{-1}
363	$6.033*10^{-7}$	-
420	$3.215*10^{-6}$	-
474	$1.265*10^{-5}$	-
530	$4.082*10^{-5}$	-
584	$1.101*10^{-4}$	-
612	$1.432*10^{-4}$	-
638	$2.633*10^{-4}$	-
694	$6.033*10^{-4}$	$2.617*10^{-4}$
720	$7.108*10^{-4}$	$3.149*10^{-4}$
747	$1.173*10^{-3}$	$1.506*10^{-3}$
802	$2.180*10^{-3}$	$5.058*10^{-3}$
831	$2.454*10^{-3}$	-
857	$3.782*10^{-3}$	$1.339*10^{-2}$
912	$5.366*10^{-3}$	-

Table 4.32: Additional Parameters

C_{bulk}/ Fcm^{-1}	C_{elec}/ Fcm^{-1}
$4.88*10^{-12}$	$4.02*10^{-5}$

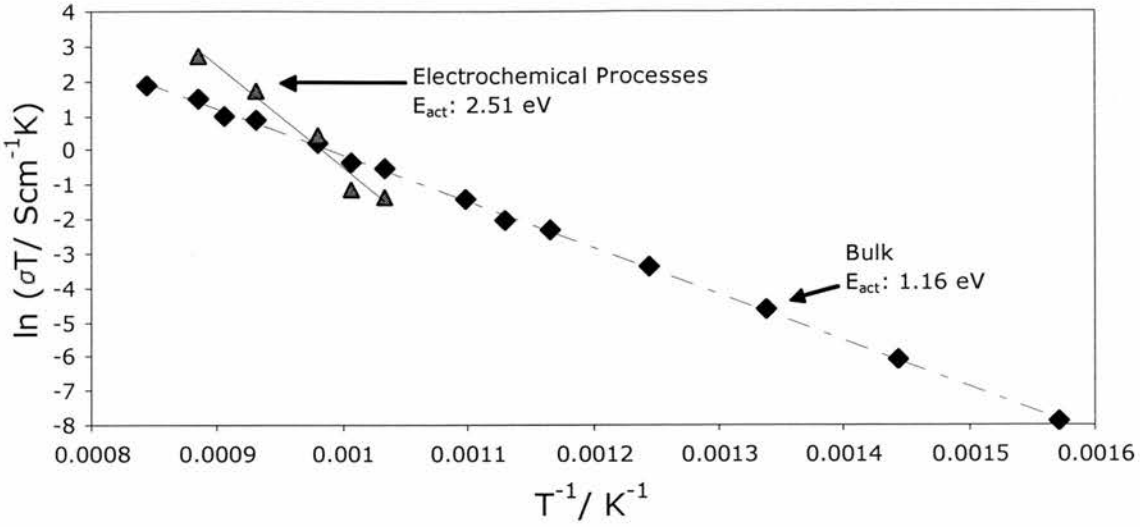

Figure 4.18: Arrhenius plots for $Y_{0.20}Zr_{0.57}Ti_{0.08}Ce_{0.15}O_{1.90}$ measured in air

4.1.2: Measurement in 5% H_2/ Argon

These measurements were done on the material $Y_{0.20}Zr_{0.57}Ti_{0.13}Ce_{0.10}O_{1.90}$. Beforehand, the material was annealed in 5% H_2/ Argon for 24-48 hours, followed by the actual measurements in flowing 5% H_2/ Argon from 252 - 772°C.

The Nyquist plots only showed the bulk response initially, followed by an initially incomplete semicircle that developed with temperature from 400°C. The second response was due to electrochemical processes, as capacitances were in the order of 10^{-4} to 10^{-3} Fcm^{-1}. This is unlike the measurements in static air, where the grain boundary was present to some extent. Conductivity results are shown in Table 4.33, with the Arrhenius plots shown in Figure 4.19.

Conductivities at 900°C were $1.16*10^{-2}$ Scm^{-1} for bulk and 1.265 Scm^{-1} for electrochemical processes. Compared to the static air measurements, the bulk activation energy was 0.32 eV lower, while the electrochemical activation energy was 0.90 eV. The bulk conductivity of the reduced sample was 40 times as high as for the oxidised sample at 350°C, although the ratio decreases with increasing temperature. At 900°C, the reduced bulk conductivity is only treble that of the oxidised sample. This is shown in Figure 4.20.

The higher bulk conductivity could be due to less oxide ions and more oxygen vacancies in the lattice. Alternatively, it could be due to an electronic contribution. The lower activation energy indicates that there is more oxide ion mobility. The number of oxygen vacancies would only affect the activation energy if this number changed with temperature. In this case, it is due to the Ce^{3+} concentration increasing with increasing temperature. The lower

activation energy of the electrochemical response indicates increased electrochemical activity due to H_2, the loss of oxygen in the lattice due to reduction or both factors.

Table 4.33: Conductivity results

Temperature/ °C	σ_{bulk}/ Scm^{-1}	σ_{elec}/ Scm^{-1}
252	$1.685*10^{-6}$	-
299	$5.811*10^{-6}$	-
350	$1.684*10^{-5}$	-
357	$1.996*10^{-5}$	-
400	$4.452*10^{-5}$	$3.225*10^{-3}$
412	$5.792*10^{-5}$	$5.984*10^{-3}$
443	$9.521*10^{-5}$	$4.884*10^{-3}$
453	$1.233*10^{-4}$	$1.046*10^{-2}$
506	$2.776*10^{-4}$	-
570	$6.089*10^{-4}$	$2.349*10^{-2}$
578	$7.317*10^{-4}$	$2.876*10^{-2}$
637	$1.424*10^{-3}$	$1.858*10^{-1}$
656	$1.888*10^{-3}$	$3.368*10^{-1}$
701	$3.084*10^{-3}$	-
737	$4.256*10^{-3}$	-
772	$5.686*10^{-3}$	-

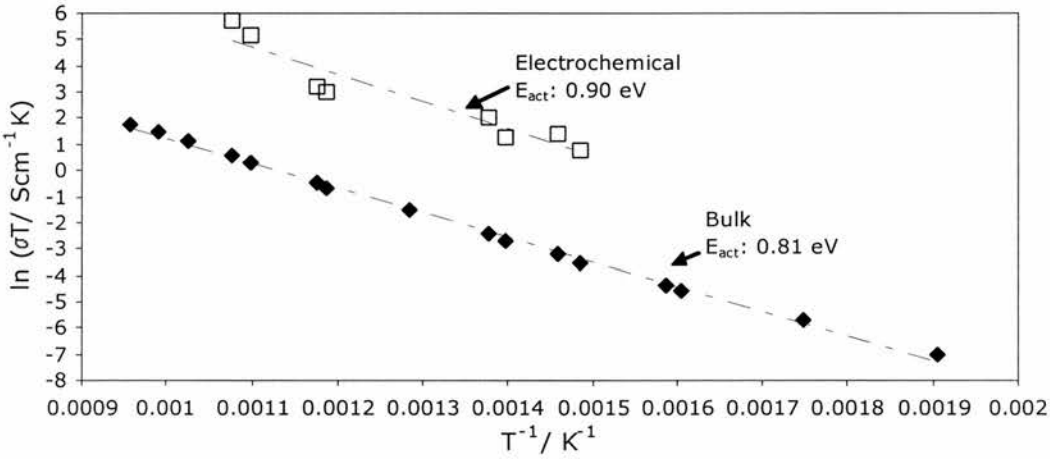

Figure 4.19: Arrhenius plots of $Y_{0.20}Zr_{0.57}Ti_{0.13}Ce_{0.10}O_{1.90-\delta}$ measured in 5% H_2/ Argon

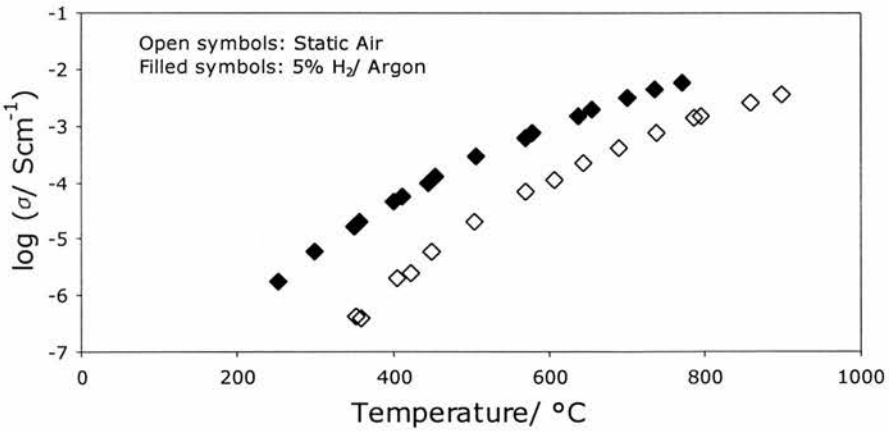

Figure 4.20: Comparison of bulk conductivity for reduced and non-reduced $Y_{0.20}Zr_{0.57}Ti_{0.13}Ce_{0.10}O_{1.90}$

4.1.3: Symmetrical cell tests

For the material $Y_{0.15}Zr_{0.57}Ti_{0.13}Ce_{0.15}O_{1.925}$, its performance as a potential SOFC electrode was determined using symmetrical cell impedance measurements [4.1]. Preparation of the cell involved two identical symmetrical layers of the material pasted on as a slurry on the faces of a 300μm thick YSZ/ 20% Al_2O_3 electrolyte. These were sintered at 1,200°C in air and then a layer of Pt paste was painted onto each face, covering the electrodes, followed by firing at 1,000°C. Three sets of measurements were from 500 – 900°C in air, 'wet' 5% H_2/ Ar and 'wet' 5% CH_4/ Ar. Examples of the symmetrical cell measurements in these atmospheres are shown in Figure 4.21-4.23, measured at 500, 700 and 900°C respectively.

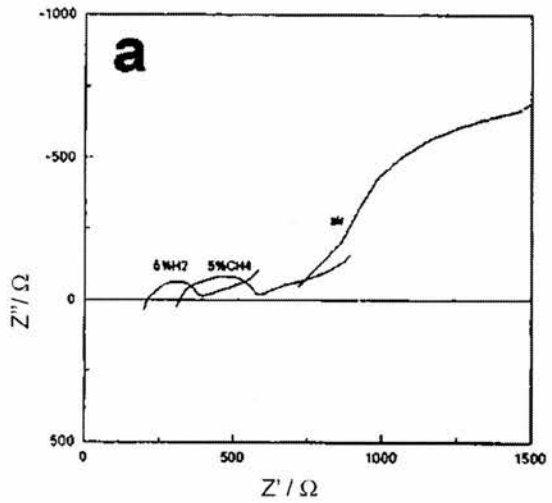

Figure 4.21: Symmetrical-cell measurements on $Y_{0.15}Zr_{0.57}Ti_{0.13}Ce_{0.15}O_{1.925}$ (500°C) [4.1]

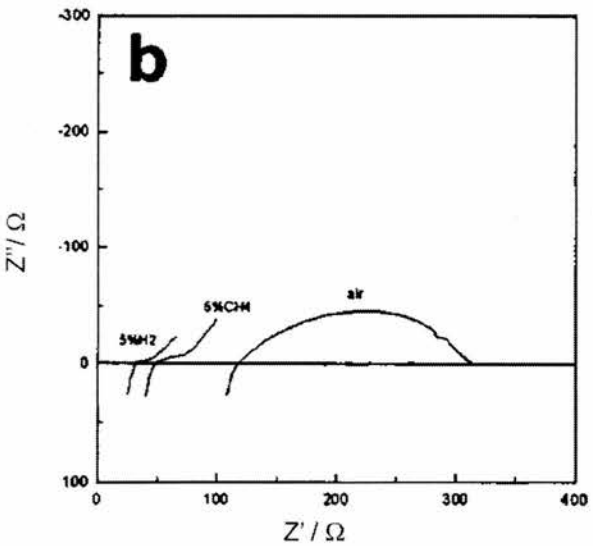

Figure 4.22: Symmetrical-cell measurements on $Y_{0.15}Zr_{0.57}Ti_{0.13}Ce_{0.15}O_{1.925}$ (700°C) [4.1]

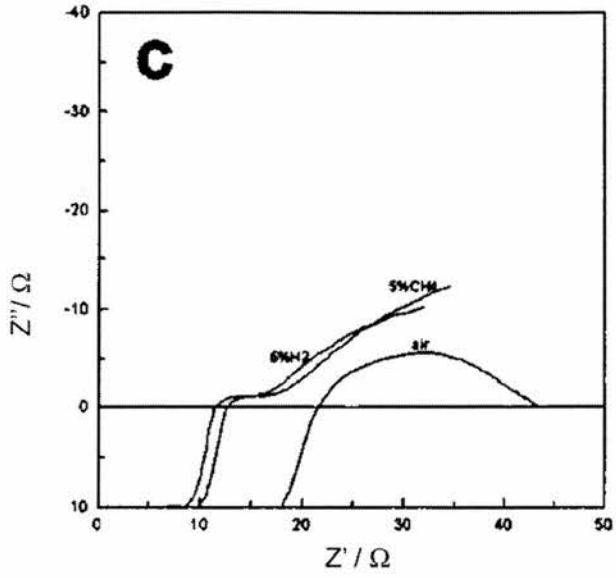

Figure 4.23: Symmetrical-cell measurements on $Y_{0.15}Zr_{0.57}Ti_{0.13}Ce_{0.15}O_{1.925}$ (900°C) [4.1]

At low temperatures, there was a well-resolved single arc, for which the high frequency intercept was equal to the series resistance of the electrolyte and electrode R_{series}. The value of R_{series} can be affected by the electrode in two ways. The series resistance of the electrode can contribute directly to R_{series}. Alternatively, there may be poor lateral connectivity between the electrode and electrolyte, reducing the effective contact area. As temperature increases, the arc becomes less well-defined, becoming distorted at high frequency due to inductance. The capacitance of the arc was 1-10μF and was related to electrode polarisation phenomena, as were additional low frequency arcs or diffusion features.

Arrhenius plots of the temperature dependences of R_{series} and $R_{polarisation+diffusion}$ are shown in Figure 4.24 and 4.25, respectively [4.1]. In both cases, resistances fell with increasing temperature. For R_{series}, the Arrhenius plots showed curvature below 600°C. In conductivity terms, σ was highest in 'wet' 5% H_2/ Argon, slightly higher than for 'wet' 5% CH_4/ Argon, although the difference narrows with increasing temperature to almost nothing at 900°C. In these reducing atmospheres, σ was 2-4 times as high for air, with the difference narrowing at higher temperatures.

For $R_{polarisation+diffusion}$, σ is slightly higher in 5% H_2/ Argon than 5% CH_4/ Argon throughout. In air, however, σ is initially much lower than for the reducing atmospheres up to 700°C but increases more rapidly with increasing temperature. At 750°C, σ equals that of 'wet' 5% CH_4/ Argon and at 850°C, σ equals that in 'wet' 5% H_2/ Argon, exceeding it at 900°C. Overall, the electrochemical performance of the electrode is similar in 'wet' 5% H_2/ Argon and 'wet' 5% CH_4/ Argon at high temperatures but at low temperatures, performance

was best in 'wet' 5% H_2/ Argon. It was noted that the measurements in 'wet' 5% CH_4/ Argon were carried out after those in 'wet' 5% H_2/ Argon. Thus, events that occurred when the sample was being heated in H_2 may be responsible to an extent for reduced performance in 'wet' 5% CH_4/ Argon [4.1], essentially agglomeration of Cu metal.

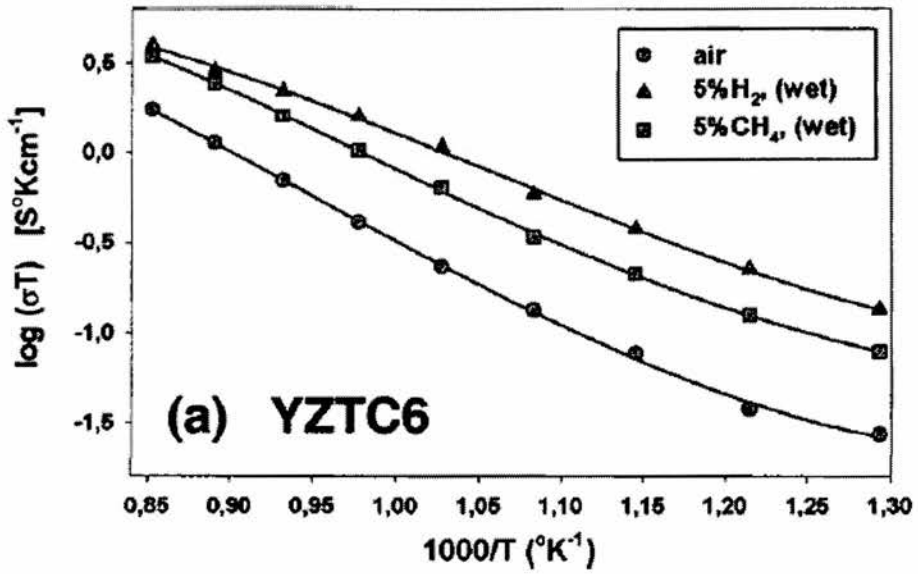

Figure 4.24: Temperature dependence of R_{series} [4.1]

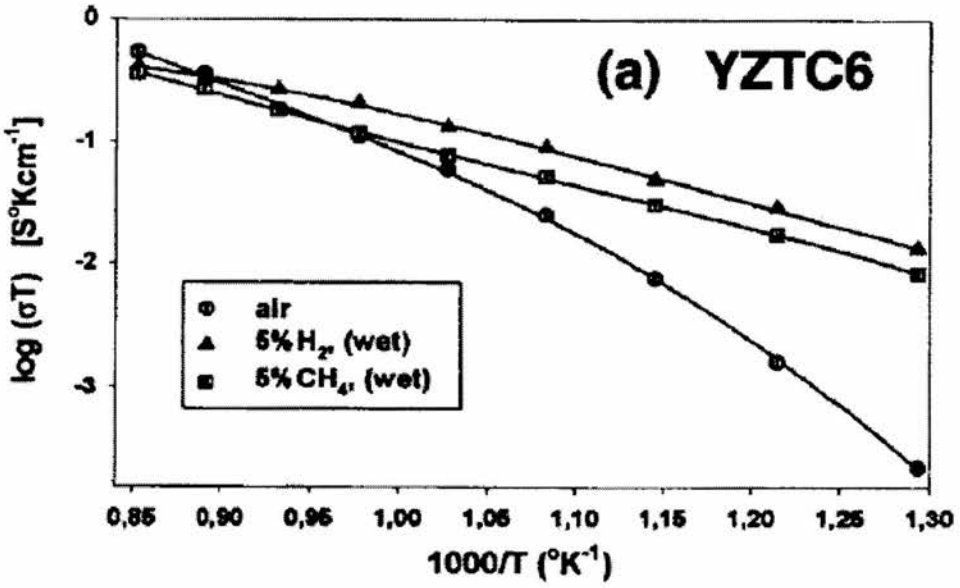

Figure 4.25: Temperature dependence of $R_{polarisation+diffusion}$ [4.1]

4.2: DC conductivity measurements

4.2.1: YZTC 3 ($Y_{0.20}Zr_{0.57}Ti_{0.13}Ce_{0.10}O_{1.90}$)

In this determination, the sample temperature ranged from 872°C to 885°C and was assumed to be constant during each separate measurement although due to changing thermal conductivity of the gas mix, a variation of ±5°C should be allowed for. The plot of log σ_{tot} (total conductivity) against log pO_2 is shown as Figure 4.26. The determination of electronic contribution was shown in Figure 4.27 for pO_2 rising.

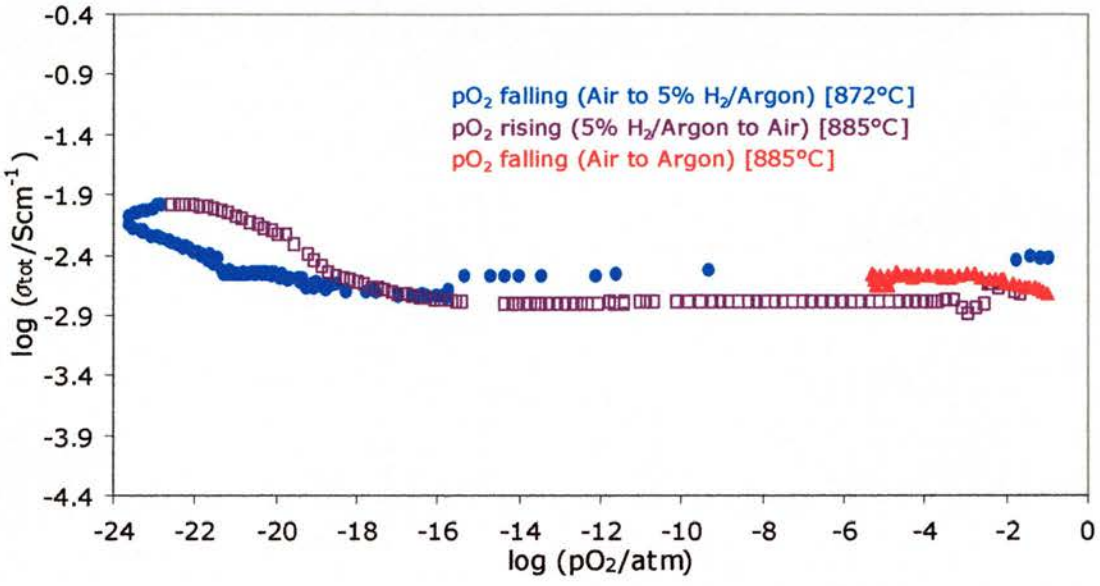

Figure 4.26: Overall plot of log σ_{tot} vs. log pO_2

In Figure 4.26, there were two regions in the σ/ pO_2 curve. Firstly, there was the pO_2-independent 'ionic domain' down to ~10^{-16} atm. Below 10^{-16} atm, there was the mixed ionic/ electronic conductivity region. Assuming that oxide ion conduction is pO_2-independent, the electronic contribution can be obtained by the equation $\sigma_{tot}=\sigma_i+\sigma_e$. In determining σ_e, it was based on $\sigma_i = 1.59*10^{-3}$ Scm^{-1} and in Figure 4.27, there was a slope of –0.27, implying that σ_e almost follows a $pO_2^{-1/4}$ dependence. σ_e reached a maximum of $8.85*10^{-3}$ Scm^{-1} at $2.7*10^{-23}$ atm. Finally, between 10^{-4} and 10^{-2} atm, there was a peak in the oxidation curve.

When reduced in argon, conductivity increased slightly with falling pO_2 between 0.1 and 10^{-3} atm, although this is likely to be due to rising temperature, rather than an n-type electronic contribution. At $<10^{-3}$ atm, there was the 'ionic domain'.

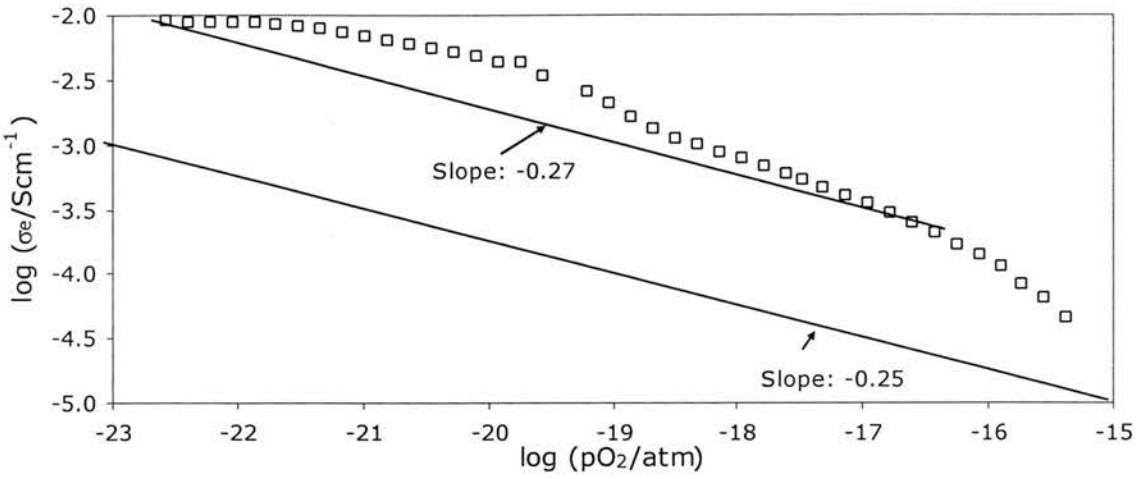

Figure 4.27: Electronic conductivity of $Y_{0.20}Zr_{0.57}Ti_{0.13}Ce_{0.10}O_{1.90}$ (during oxidation)

4.2.2: YZTC 6 ($Y_{0.15}Zr_{0.57}Ti_{0.13}Ce_{0.15}O_{1.925}$)

For this material, there were two determinations of the dependence of conductivity with pO_2. Firstly, pO_2 was reduced with 5% H_2/ Argon and secondly, pO_2 was reduced in Argon. Sample temperature was measured initially at 900°C, but it was not recorded during the experiment. There may have been variations of ± 5-10°C in temperature, due to differences in thermal conductivity between 5% H_2/ Argon and air. The plot of log σ against log pO_2 is shown in Figure 4.28 for reduction in 5% H_2/ Argon and reoxidation in air. The determination of electronic conductivity was shown in Figure 4.29

In Figure 4.28, there were two regions in the σ/ pO_2 curve. Firstly, there was the 'ionic domain' down to 10^{-13} atm during reduction or 10^{-15} atm during oxidation. Below these pO_2 levels, there was the mixed ionic/ electronic conductivity region, with a difference in behaviour between oxidation and reduction. Effectively, the ionic plateau is dominant, with a small n-type contribution at low pO_2. On oxidation, there are small peaks superimposed at high and low pO_2.

In determining electronic contribution, σ_i was estimated as $3.05*10^{-3}$ Scm^{-1} on reduction and on oxidation. On reduction, there was a slope in the curve of –0.33 between 10^{-12} and 10^{-18} atm, with maximum σ_e of $6.08*10^{-3}$ Scm^{-1} at $1.6*10^{-18}$ atm. On oxidation, there was a slope of –0.17 between 10^{-16} and 10^{-19} atm, with maximum σ_e of $4.18*10^{-3}$ Scm^{-1} at $7.0*10^{-21}$ atm.

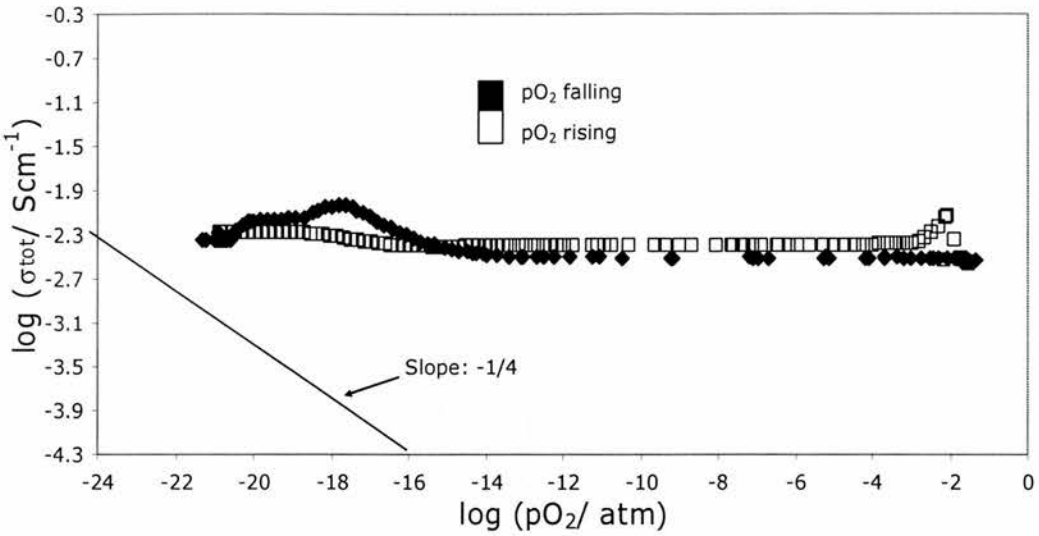

Figure 4.28: Overall plot of log σ_{tot} vs. log pO_2

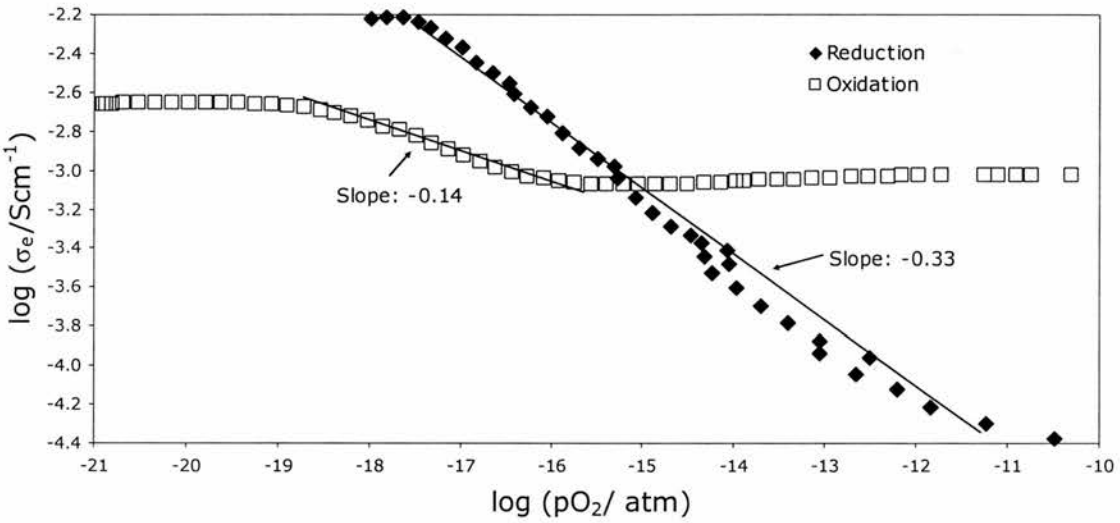

Figure 4.29: Determination of electronic conductivity of $Y_{0.15}Zr_{0.57}Ti_{0.13}Ce_{0.15}O_{1.925}$

4.2.3: YZTC 10 ($Y_{0.15}Zr_{0.52}Ti_{0.08}Ce_{0.25}O_{1.925}$)

In the first determination of the dependence of conductivity with pO_2, the pO_2 was reduced using 5% H_2/ Argon and reoxidised in air. The sample temperature was 900°C. The plot of conductivity against pO_2 is shown in Figure 4.30, although the data on reduction was unreliable and was omitted.

In Figure 4.30, there were two regions in the σ/ pO_2 curve. Firstly, there was the 'ionic domain' that ended at ~10^{-11} atm. At <10^{-11} atm, there was mixed conductivity, with a difference in behaviour between oxidation and reduction. On reduction, electronic contribution was n-type down to 10^{-17} atm, then conductivity decreased with decreasing pO_2

below 10^{-17} atm. On oxidation, conductivity increased with increasing pO_2. Finally, there was a peak on oxidation between 10^{-3} and 0.1 atm.

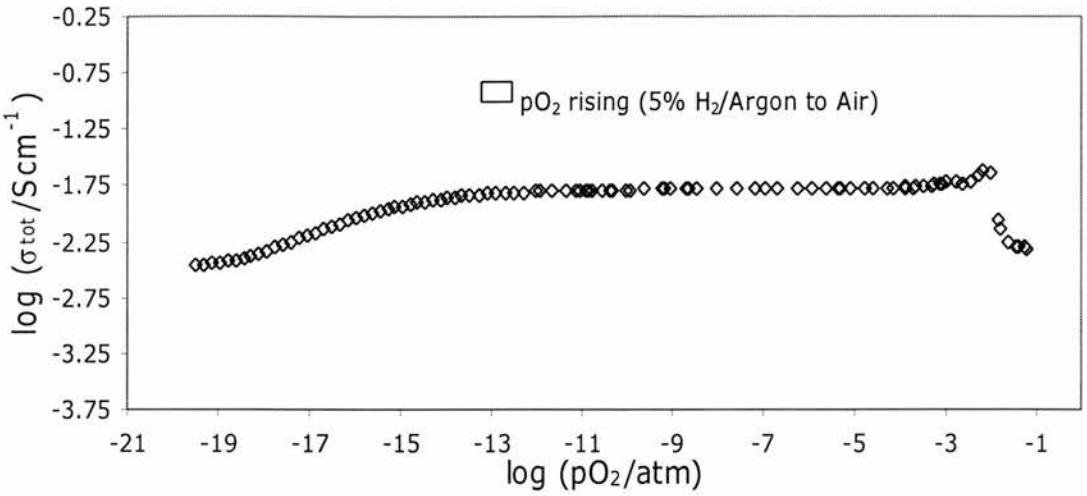

Figure 4.30: Plot of log σ vs. log pO_2 for 1st determination.

To determine if the observations in Figure 4.30 were real or not, the measurement was repeated and the plot of log σ vs. log pO_2 is shown in Figure 4.31. The sample temperature was initially 907°C. The determination of electronic contribution is in Figure 4.32.

In Figure 4.31, there were two regions in the σ/ pO_2 curve. Firstly, there was the 'ionic domain' down to ~10^{-12} atm. Below 10^{-12} atm, there was the mixed conductivity region, with a difference in behaviour between oxidation and reduction. On reduction, electronic contribution was n-type down to 10^{-18} atm, then conductivity decreased with decreasing pO_2 below 10^{-18} atm. On oxidation, conductivity increased with increasing pO_2. Finally, there was a peak on oxidation between 10^{-3} and 0.1 atm. Essentially, the behaviour was similar to Figure 4.30.

In calculating electronic contribution, σ_i was estimated as $4.79*10^{-3}$ Scm^{-1} on reduction. There was a slope in the curve of –0.34 between 10^{-12} and 10^{-18} atm, with maximum σ_e of $2.01*10^{-2}$ Scm^{-1} at $1.2*10^{-18}$ atm.

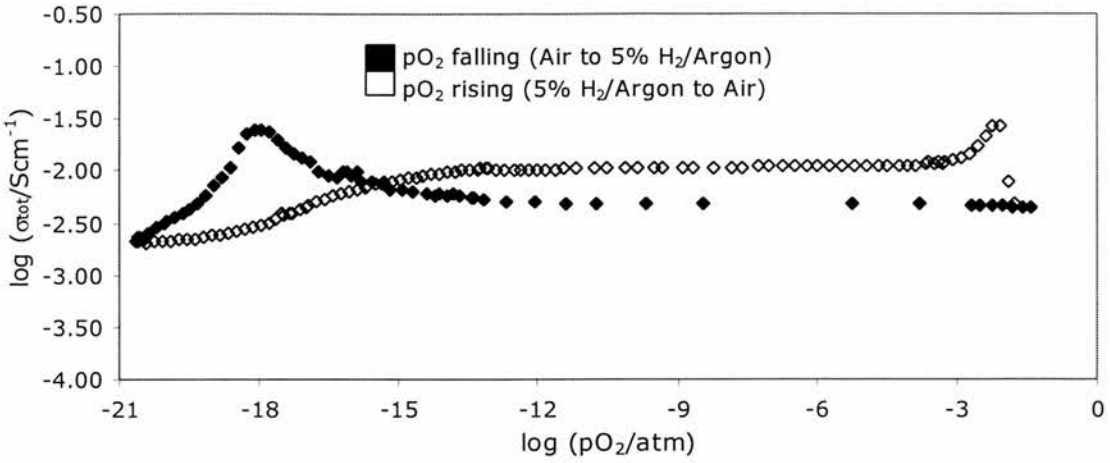

Figure 4.31: Plot of log σ vs. log pO_2 for the 2nd determination

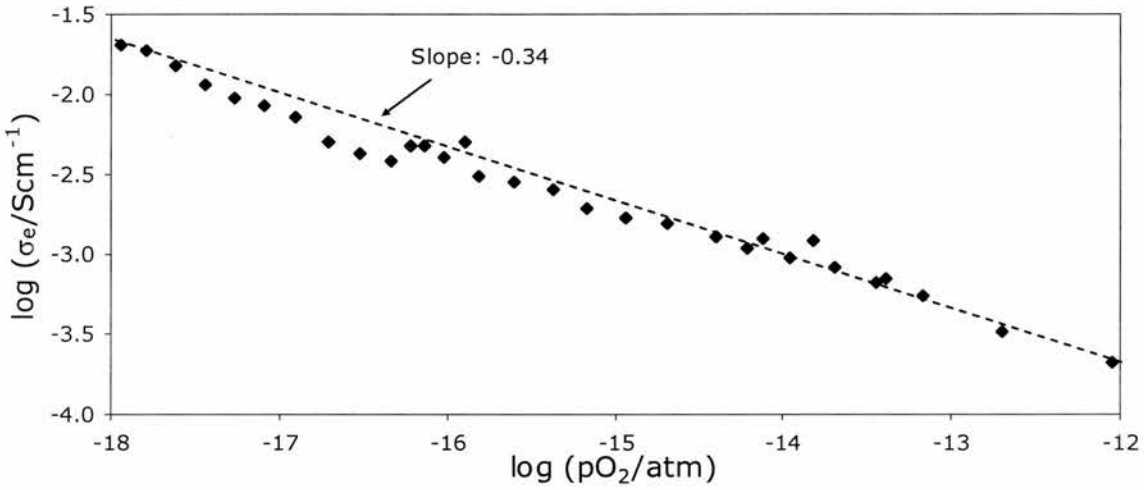

Figure 4.32: Plot of log σ_e vs. log pO_2 for pO_2 falling

In the third measurement, pO_2 was reduced using 'wet' 5% H_2/ Argon (gas was bubbled through water), limiting the minimum pO_2 to ~10^{-18} atm. The plot of log σ against log pO_2 is shown in Figure 4.33. Sample temperature was initially 908°C. The determination of electronic contribution is in Figure 4.34.

In Figure 4.34, there were two regions in the σ/ pO_2 curve. Firstly, there was the 'ionic domain' down to ~10^{-11} atm. Below 10^{-11} atm, there was the mixed conductivity region, with different behaviour on oxidation and reduction. On reduction, electronic contribution was n-type down to 10^{-17} atm, with conductivity decreasing with decreasing pO_2 below 10^{-17} atm. On oxidation, conductivity increased with increasing pO_2. Finally, there was a peak on oxidation between 10^{-3} and 0.1 atm. In estimating electronic conductivity, σ_i was assumed to

be $5.82*10^{-3}$ Scm^{-1} on reduction. There was a slope in the curve of –0.57 between 10^{-11} and 10^{-16} atm, with maximum σ_e of $2.17*10^{-2}$ Scm^{-1} at $1.7*10^{-16}$ atm.

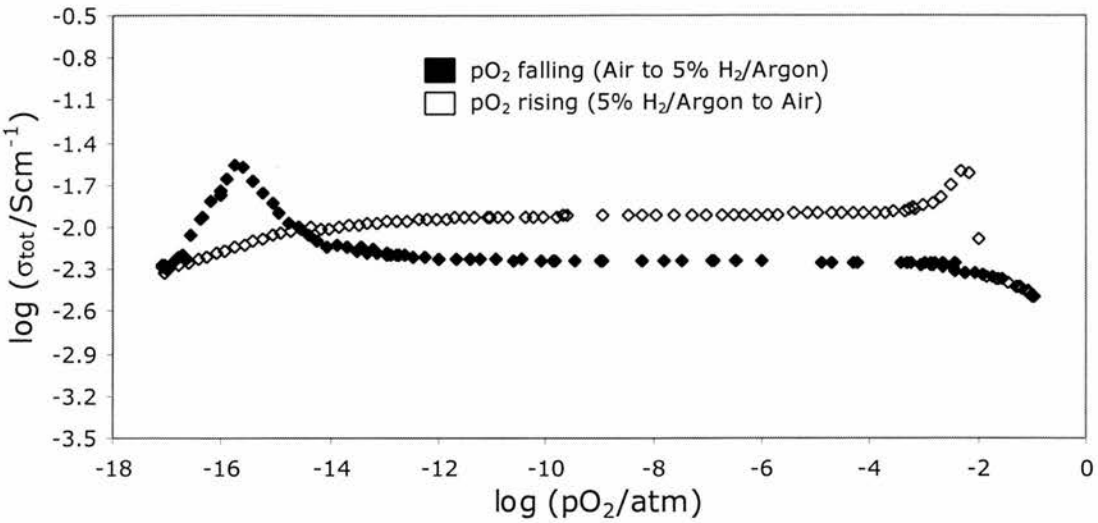

Figure 4.33: Plot of log σ vs. log pO_2 for the 3rd determination

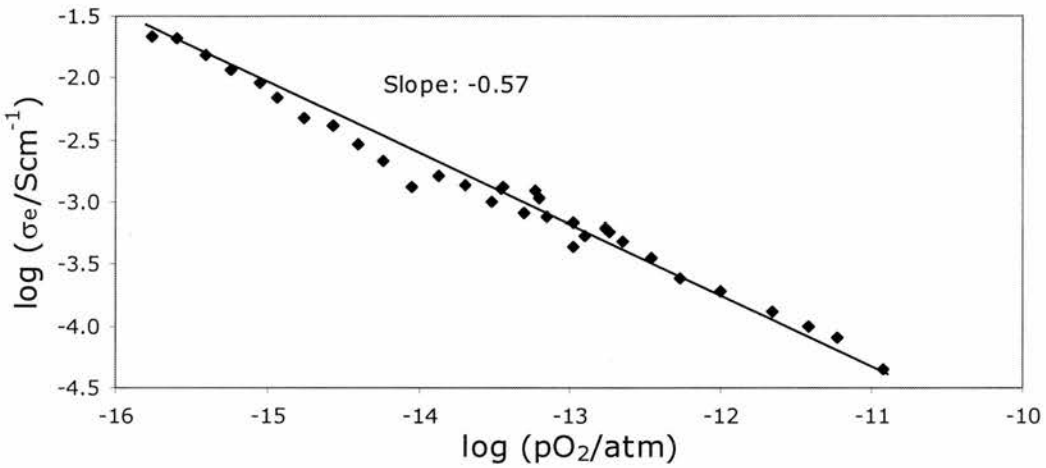

Figure 4.34: Plot of log σ_e vs. log pO_2 for pO_2 falling

For comparison, Figures 4.35 and 4.36 show the three sets of measurements on $Y_{0.15}Zr_{0.52}Ti_{0.08}Ce_{0.25}O_{1.925}$ when the pO_2 is falling and rising, respectively. The reduction experiments in dry 5% H_2/ Argon were not reproducible, as one showed higher conductivities than the other, as well as σ_e reaching a maximum at higher pO_2. This lack of reproducibility indicates that the conductivity behaviour is due to kinetic control, where there is a kinetic factor involved. This may be an effect of differences in gas flow rates used on reduction or differences in the rates of or extent of Ce reduction attained in the experiment.

Differences between conductivity behaviour on reduction and oxidation appear as an irreversible peak in conductivity only evident on reduction. There is a hysteresis present in the behaviour of conductivity decreasing with decreasing pO_2, where the peak moves 3 orders of

magnitude on reduction in different experiments. On oxidation, the peak is shifted up in pO_2 by ~16 orders of magnitude. This could be due to ordering of defects like oxygen vacancies on reduction, where it may start with a Ce^{3+} concentration of 60% but this may be present on oxidation even when the Ce^{3+} concentration is much lower.

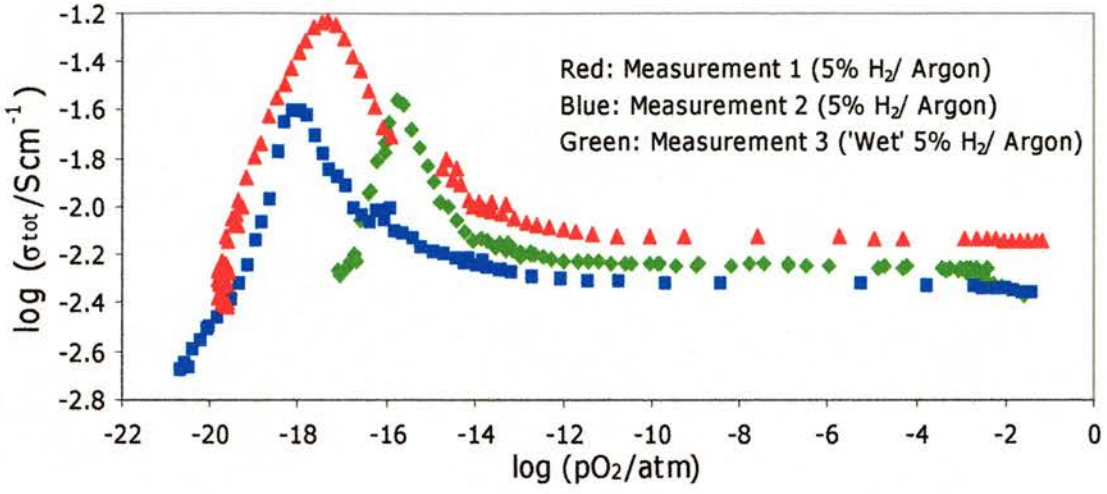

Figure 4.35: Comparison of determinations (pO_2 falling)

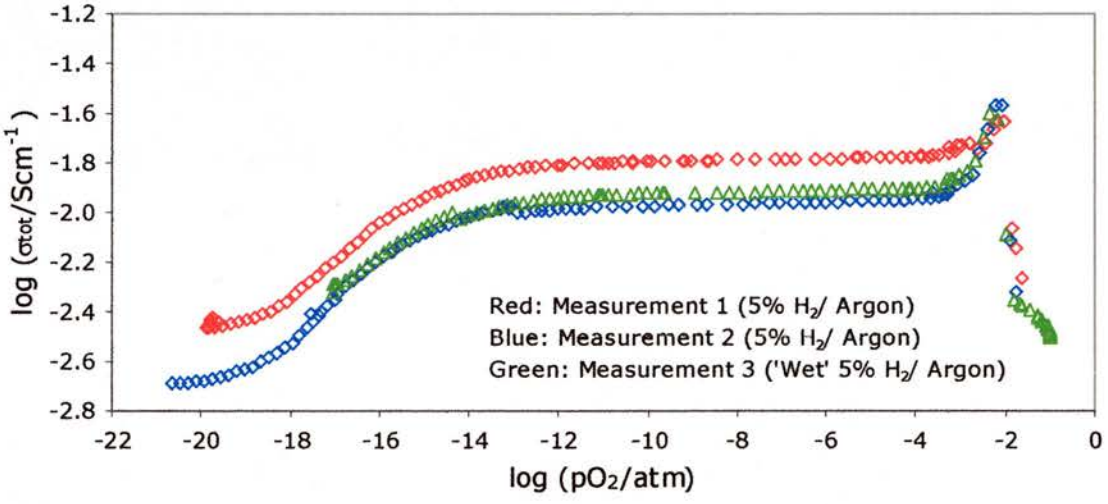

Figure 4.36: Comparison of determinations (pO_2 rising)

4.2.4: YZTC 37 ($Y_{0.15}Zr_{0.57}Ti_{0.03}Ce_{0.25}O_{1.925}$)

In this measurement, data was collected using an upgraded programme. The sample temperature started at 900°C and was logged throughout, unlike the previous experiments. The plot of log σ_{tot} (total conductivity) against log pO_2 is shown as Figure 4.37, with a plot of temperature against log pO_2 in Figure 4.38. The determination of electronic contribution was shown in Figure 4.39.

There are two main regions in the σ/ pO_2 curves. The first region is the 'ionic domain' down to 10^{-11} atm, with electronic conductivity below 10^{-11} atm. Initially, between 0.2 and $4.3*10^{-3}$ atm, σ increases slightly with decreasing pO_2, although this is due to sample temperature increasing ~4°C over this range, not electronic conductivity. Below this pO_2 region, the 'ionic domain' is more settled, as the temperature is more constant. There is a contrast in behaviour below 10^{-11} atm. On reduction, there is mixed conductivity down to $3.4*10^{-15}$ atm, followed by σ decreasing with decreasing pO_2 below $3.4*10^{-15}$ atm. In calculating electronic contribution, σ_i was $6.32*10^{-3}$ Scm^{-1} on reduction. There was a slope in the curve of –0.79 between $8*10^{-14}$ and $3.4*10^{-15}$ atm, where σ_e reached a maximum of $2.61*10^{-2}$ Scm^{-1}. On oxidation, only σ increasing with increasing pO_2 was observed in this region with a 'peak' in the 'ionic domain' region between 10^{-5} and 10^{-3} atm.

During the measurements, the sample temperature was fairly steady on oxidation between 906 and 908°C for most of the time but rising 3°C between 10^{-20} and 10^{-16} atm pO_2. On reduction, the sample temperature increased by 4-5°C from 10^{-15} to 10^{-18} atm pO_2, falling back at lower pO_2. These temperature increases are in the region of sample reduction and could be due to reaction between H_2 and oxygen in the sample or from air leaking in.

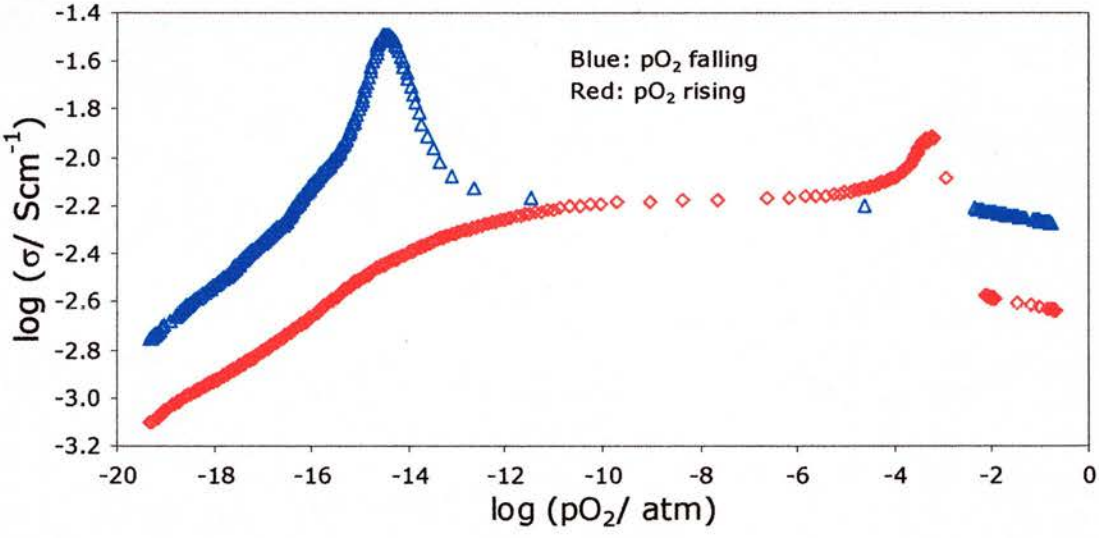

Figure 4.37: Overall plot of log σ vs. log pO_2

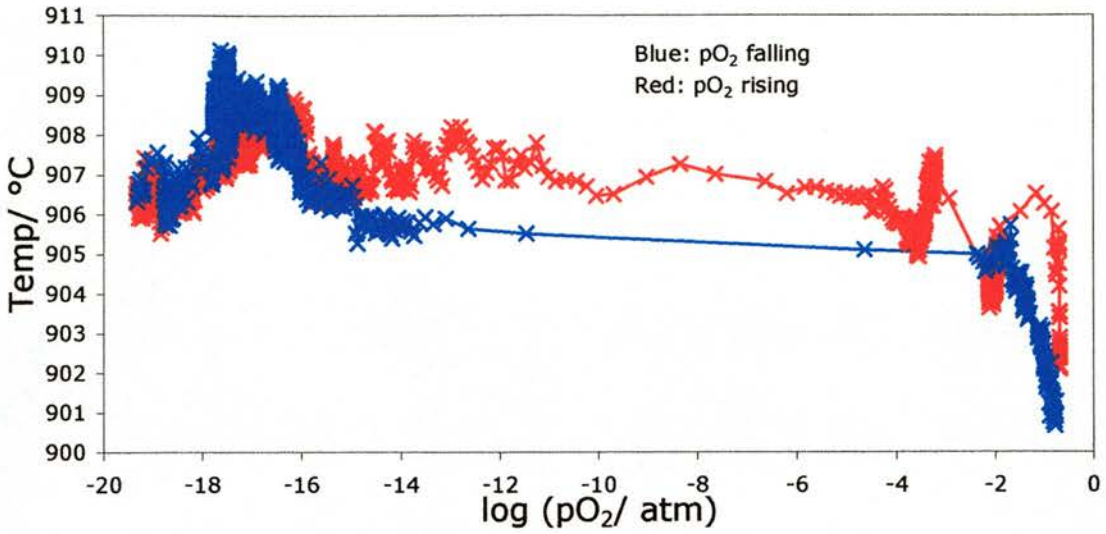

Figure 4.38: Plot of temperature vs. log pO_2

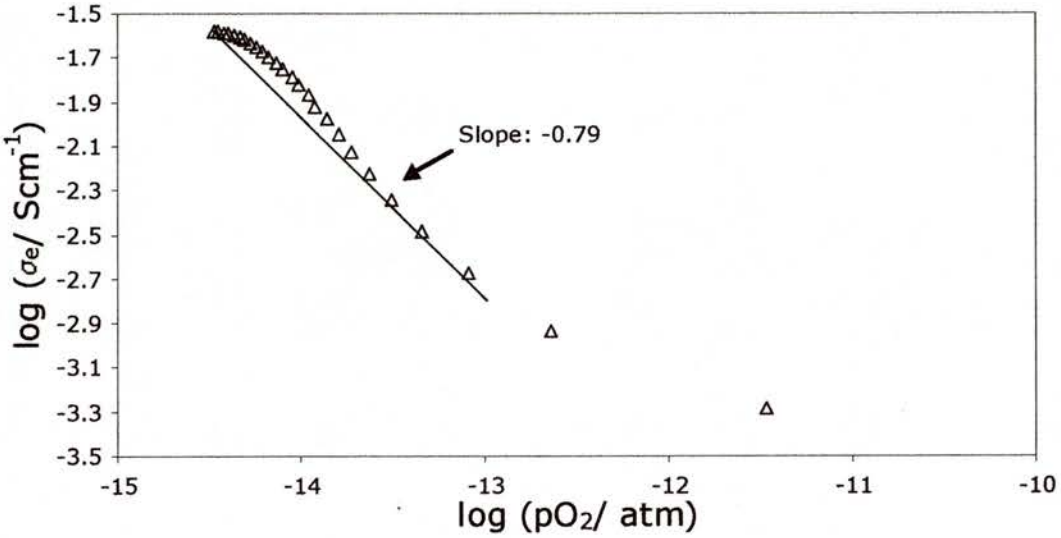

Figure 4.39: Plot of $\sigma-\sigma_i$ (at $pO_2=10^{-8}$ atm) as estimation of σ_e vs. pO_2 (pO_2 falling)

4.3: Summary of conductivity results

4.3.1: AC Impedance

Activation Energies

For comparison between the different materials investigated, the activation energies from the AC Impedance results were shown in Table 4.34 and in Figures 4.40-4.43, where gb indicates the grain boundary and elec indicates the electrochemical processes.

Table 4.34: Activation energies of conductivity processes

	E_{act} (bulk)/ eV	E_{act} (gb)/ eV	E_{act} (elec)/ eV
$Y_{0.20}Zr_{0.62}Ti_{0.13}Ce_{0.05}O_{1.90}$	1.16		2.50
$Y_{0.20}Zr_{0.57}Ti_{0.13}Ce_{0.10}O_{1.90}$	1.13	1.23	2.81
$Y_{0.15}Zr_{0.52}Ti_{0.08}Ce_{0.25}O_{1.925}$	1.22	1.04	2.93
$Y_{0.15}Zr_{0.52}Ti_{0.13}Ce_{0.20}O_{1.925}$	1.24		2.01
$Y_{0.125}Zr_{0.52}Ti_{0.13}Ce_{0.225}O_{1.9375}$	1.19		1.89
$Y_{0.15}Zr_{0.57}Ti_{0.03}Ce_{0.25}O_{1.925}$	1.19	1.48	2.01
$Y_{0.15}Zr_{0.62}Ti_{0.08}Ce_{0.15}O_{1.925}$	1.12	1.44	2.86
$Y_{0.15}Zr_{0.57}Ti_{0.08}Ce_{0.20}O_{1.925}$	1.15	1.42	2.03
$Y_{0.20}Zr_{0.62}Ti_{0.08}Ce_{0.10}O_{1.90}$	1.14	1.17	1.86
$Y_{0.15}Zr_{0.62}Ti_{0.03}Ce_{0.20}O_{1.925}$	1.14	1.39	1.77
$Y_{0.10}Zr_{0.62}Ti_{0.03}Ce_{0.25}O_{1.95}$	1.12	1.41	2.72
$Y_{0.125}Zr_{0.47}Ti_{0.08}Ce_{0.325}O_{1.9375}$	1.19		1.64
$Y_{0.20}Zr_{0.52}Ti_{0.03}Ce_{0.25}O_{1.90}$	1.21	1.55	2.12
$Y_{0.125}Zr_{0.62}Ti_{0.08}Ce_{0.175}O_{1.9375}$	1.13	1.37	1.96
$Y_{0.20}Zr_{0.52}Ti_{0.08}Ce_{0.20}O_{1.90}$	1.19		1.74
$Y_{0.20}Zr_{0.57}Ti_{0.08}Ce_{0.15}O_{1.90}$	1.16		2.51

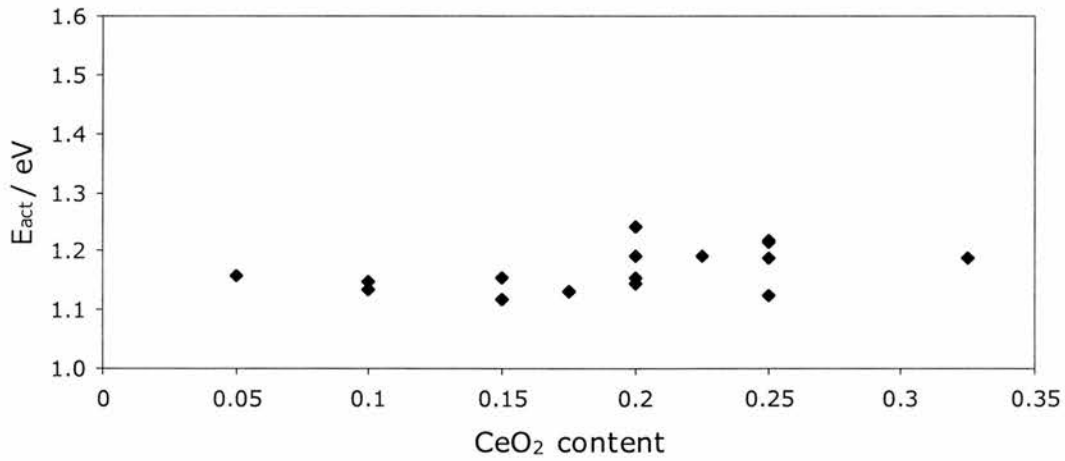

Figure 4.40: Activation energies for bulk conductivity

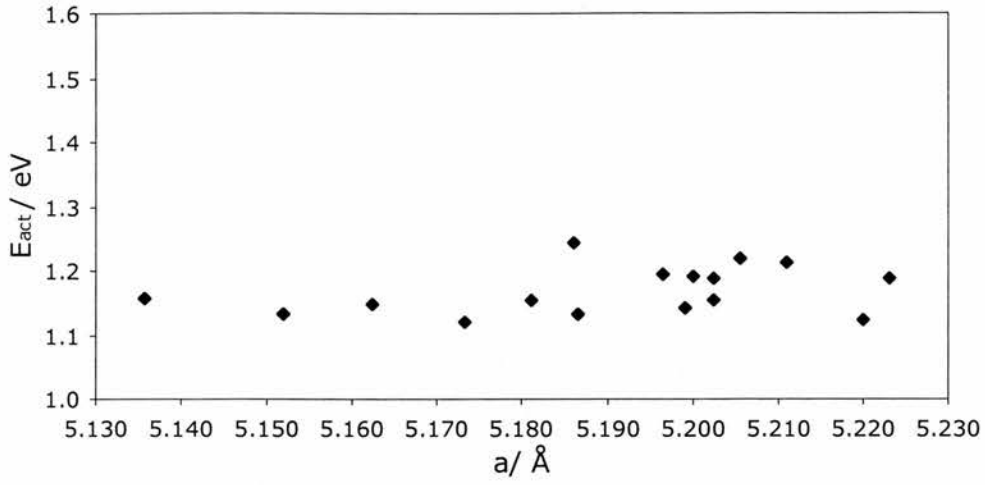

Figure 4.41: Bulk activation energies vs. unit cell parameter

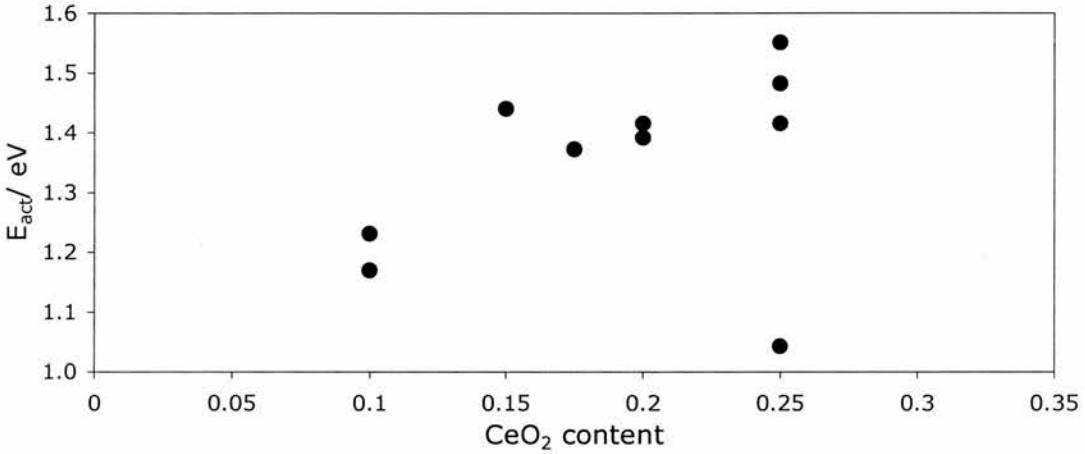

Figure 4.42: Activation energies for grain boundary conductivity

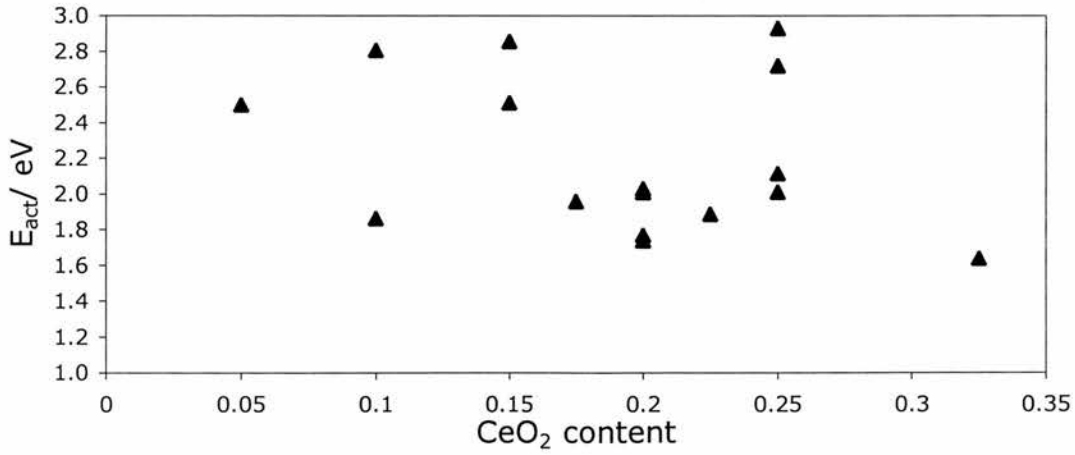

Figure 4.43: Activation energies for electrochemical processes conductivity

Bulk activation energies ranged from 1.12 eV for $Y_{0.15}Zr_{0.62}Ti_{0.08}Ce_{0.15}O_{1.925}$ to 1.24 eV for $Y_{0.15}Zr_{0.52}Ti_{0.13}Ce_{0.20}O_{1.925}$. There was no significant trend between activation energy and the amount of a particular component (Y_2O_3, ZrO_2, TiO_2 or CeO_2). It was also

independent of unit cell size. Of all of the conductivity processes, bulk activation energies were the lowest.

The grain boundary activation energy ranged from 1.04 eV for $Y_{0.15}Zr_{0.52}Ti_{0.08}Ce_{0.25}O_{1.925}$ to 1.55 eV for $Y_{0.20}Zr_{0.52}Ti_{0.03}Ce_{0.25}O_{1.90}$. Generally, the grain boundary activation was up to 0.34 eV higher than the bulk, although there were two cases where it was up to 0.18 eV lower than the bulk (as found for $Y_{0.15}Zr_{0.52}Ti_{0.08}Ce_{0.25}O_{1.925}$). This activation energy appeared to increase with increasing CeO_2 (and possibly ZrO_2) content and decrease with increasing TiO_2 content.

The activation energy for electrochemical processes ranged from 1.64 eV for $Y_{0.125}Zr_{0.47}Ti_{0.08}Ce_{0.325}O_{1.9375}$ to 2.93 eV for $Y_{0.15}Zr_{0.52}Ti_{0.08}Ce_{0.25}O_{1.925}$. These activation energies tended to be the highest of all of the conductivity processes. There was no trend between activation energy and composition. The factors that affect this activation energy could be more complex.

In 5% H_2/ Argon, $Y_{0.20}Zr_{0.57}Ti_{0.13}Ce_{0.10}O_{1.90}$ showed lower bulk and electrochemical activation energies than in air. The lower bulk activation implies higher oxide ion mobility, due to more oxygen vacancies and less formula oxygen. The lower electrochemical activation energy could be due to less oxygen in the lattice or an effect due to H_2.

Conductivity

For comparing between the different materials investigated, the conductivities at 900°C were shown in Table 4.35 and Figures 4.44-4.53, where gb indicates the grain boundary conductivity and elec indicates the electrochemical processes.

Table 4.35: Conductivities at 900°C

	σ_{900} (bulk)/ Scm^{-1}	σ_{900} (gb)/ Scm^{-1}	σ_{900} (elec)/ Scm^{-1}
$Y_{0.20}Zr_{0.62}Ti_{0.13}Ce_{0.05}O_{1.90}$	$4.23*10^{-3}$		$9.24*10^{-2}$
$Y_{0.20}Zr_{0.57}Ti_{0.13}Ce_{0.10}O_{1.90}$	$3.81*10^{-3}$	$2.17*10^{-2}$	1.51
$Y_{0.15}Zr_{0.52}Ti_{0.08}Ce_{0.25}O_{1.925}$	$5.60*10^{-3}$	$5.41*10^{-3}$	1.12
$Y_{0.15}Zr_{0.52}Ti_{0.13}Ce_{0.20}O_{1.925}$	$3.00*10^{-3}$		$3.64*10^{-2}$
$Y_{0.125}Zr_{0.52}Ti_{0.13}Ce_{0.225}O_{1.9375}$	$2.61*10^{-3}$		$2.89*10^{-2}$
$Y_{0.15}Zr_{0.57}Ti_{0.03}Ce_{0.25}O_{1.925}$	$6.09*10^{-3}$	$1.99*10^{-1}$	$8.18*10^{-2}$
$Y_{0.15}Zr_{0.62}Ti_{0.08}Ce_{0.15}O_{1.925}$	$6.68*10^{-3}$	$2.38*10^{-1}$	3.65
$Y_{0.15}Zr_{0.57}Ti_{0.08}Ce_{0.20}O_{1.925}$	$6.70*10^{-3}$	$7.53*10^{-2}$	$5.77*10^{-2}$
$Y_{0.20}Zr_{0.62}Ti_{0.08}Ce_{0.10}O_{1.90}$	$7.83*10^{-3}$	$3.58*10^{-2}$	$1.38*10^{-1}$
$Y_{0.15}Zr_{0.62}Ti_{0.03}Ce_{0.20}O_{1.925}$	$7.91*10^{-3}$	$6.06*10^{-2}$	$2.47*10^{-2}$
$Y_{0.10}Zr_{0.62}Ti_{0.03}Ce_{0.25}O_{1.95}$	$9.95*10^{-3}$	$1.01*10^{-1}$	$1.13*10^{-1}$
$Y_{0.125}Zr_{0.47}Ti_{0.08}Ce_{0.325}O_{1.9375}$	$4.76*10^{-3}$		$2.44*10^{-2}$
$Y_{0.20}Zr_{0.52}Ti_{0.03}Ce_{0.25}O_{1.90}$	$7.01*10^{-3}$	$2.64*10^{-1}$	$1.67*10^{-2}$
$Y_{0.125}Zr_{0.62}Ti_{0.08}Ce_{0.175}O_{1.9375}$	$6.51*10^{-3}$	$8.20*10^{-2}$	$1.82*10^{-2}$
$Y_{0.20}Zr_{0.52}Ti_{0.08}Ce_{0.20}O_{1.90}$	$5.11*10^{-3}$		$2.38*10^{-2}$
$Y_{0.20}Zr_{0.57}Ti_{0.08}Ce_{0.15}O_{1.90}$	$5.23*10^{-3}$		$3.84*10^{-2}$

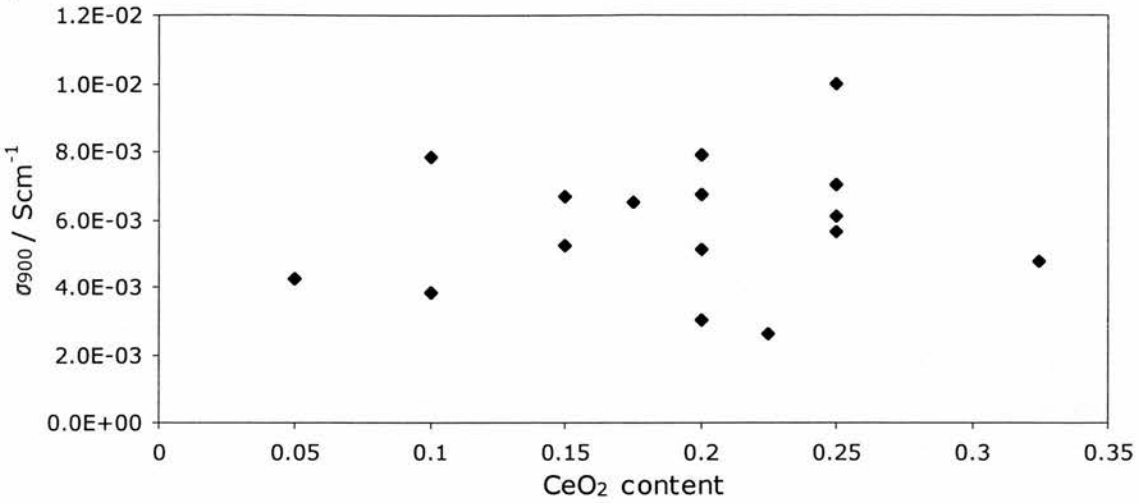

Figure 4.44: Bulk conductivity at 900°C vs. CeO_2 content

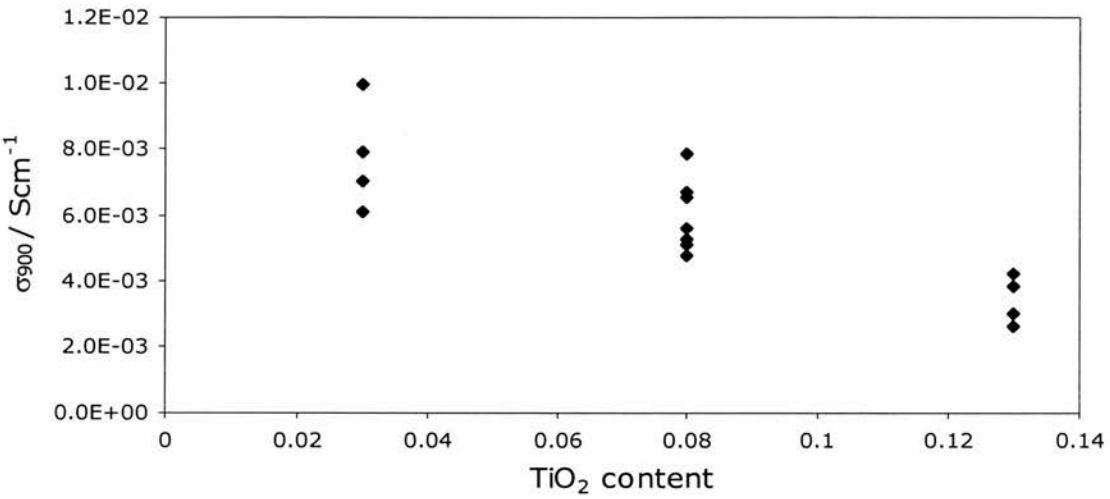

Figure 4.45: Bulk conductivity at 900°C vs. TiO_2 content

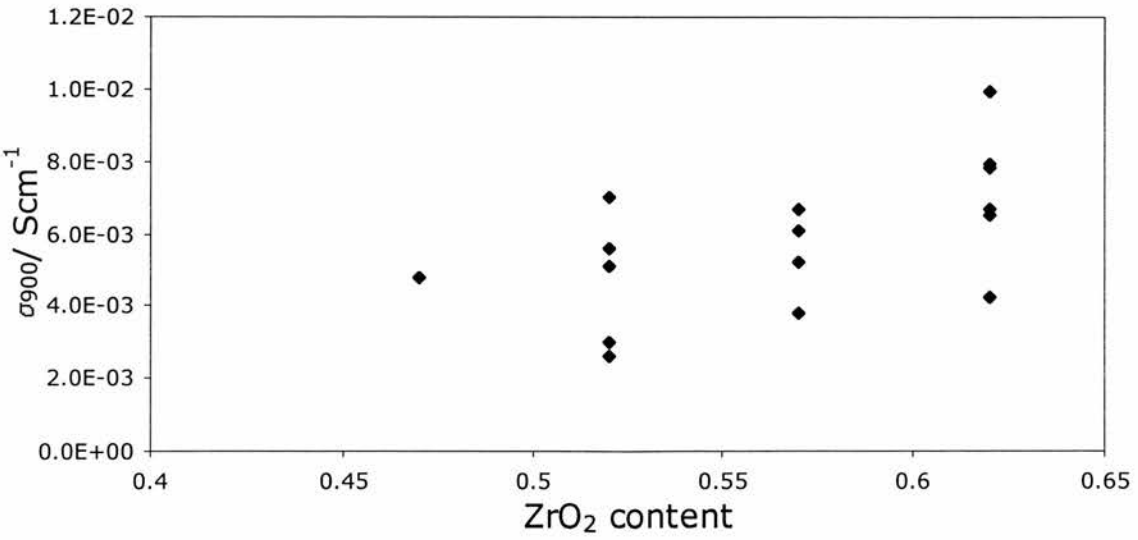

Figure 4.46: Bulk conductivity at 900°C vs. ZrO_2 content

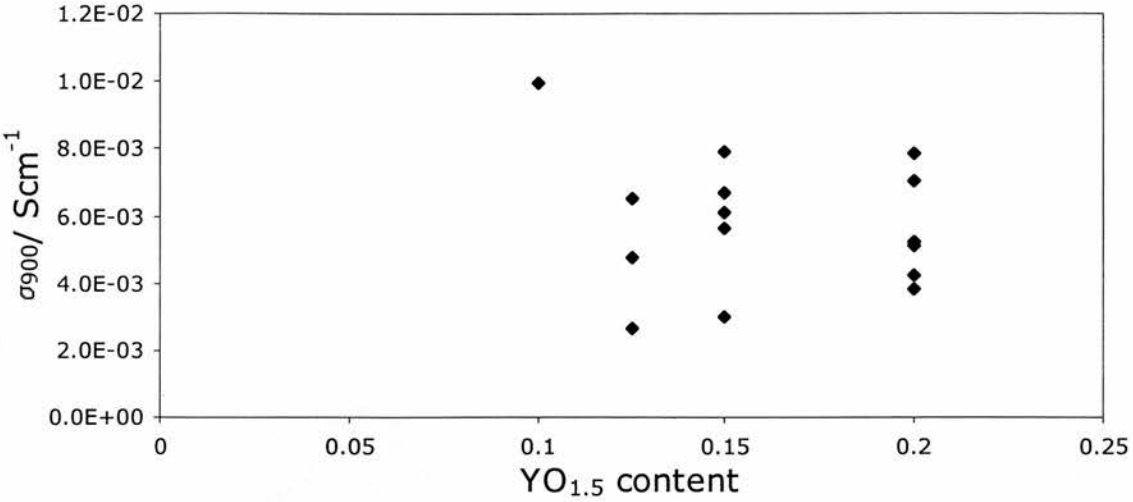

Figure 4.47: Bulk conductivity at 900°C vs. Y_2O_3 content

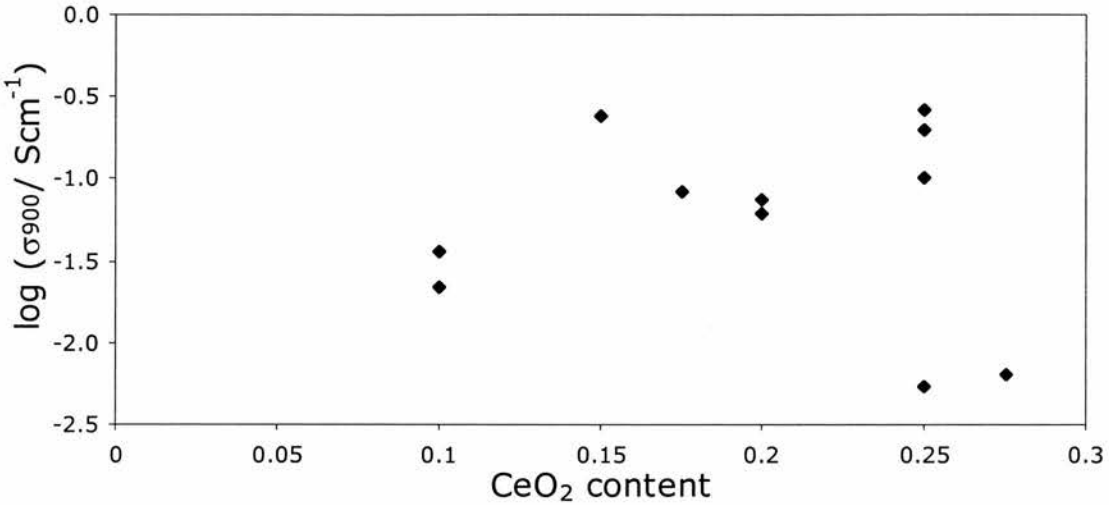

Figure 4.48: Grain boundary conductivity at 900°C vs. CeO_2 content

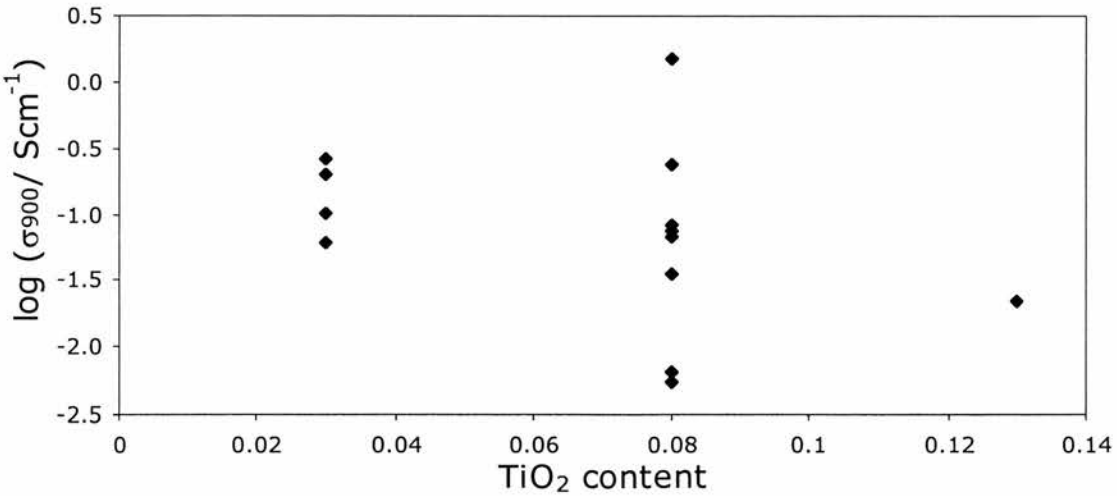

Figure 4.49: Grain boundary conductivity at 900°C vs. TiO_2 content

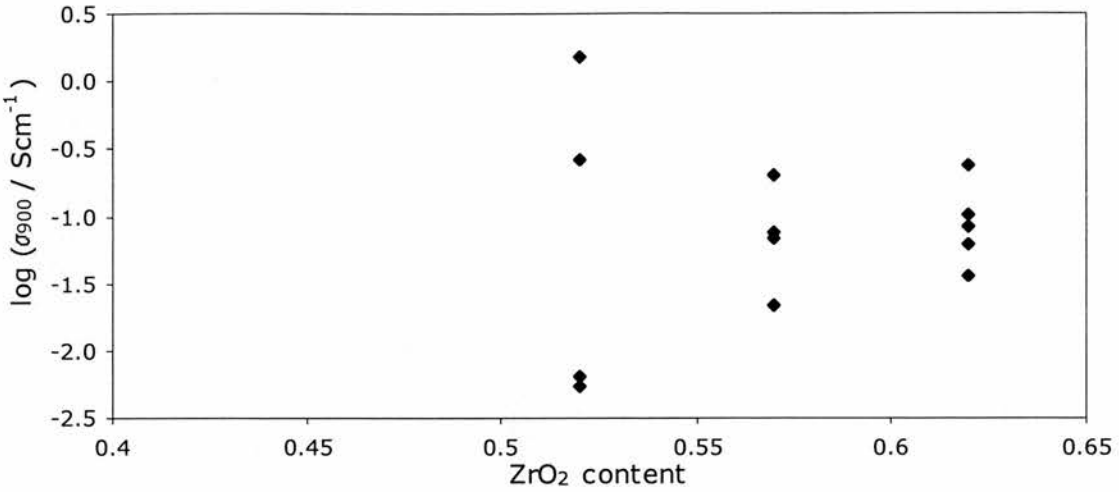

Figure 4.50: Grain boundary conductivity at 900°C vs. ZrO_2 content

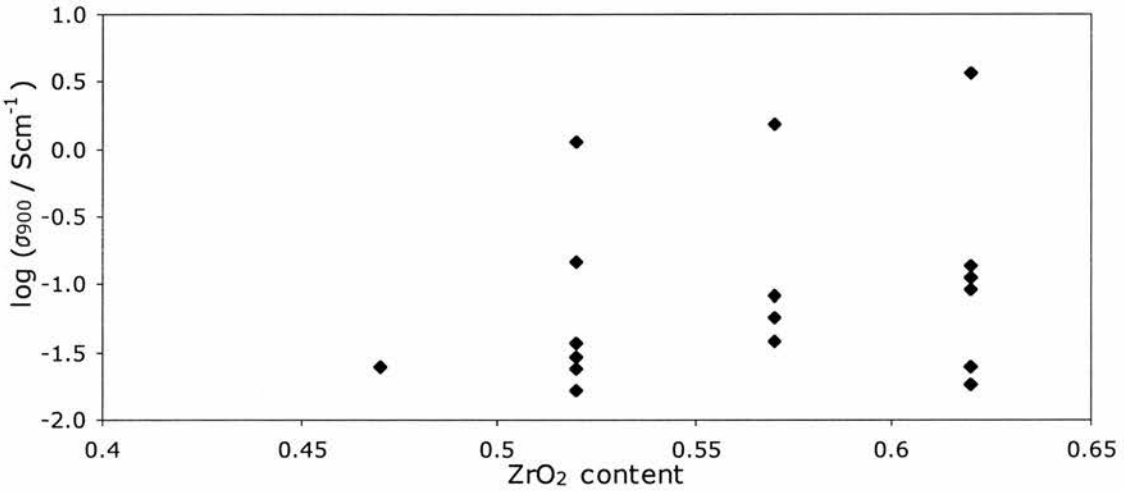

Figure 4.51: Electrochemical processes conductivity at 900°C vs. ZrO_2 content

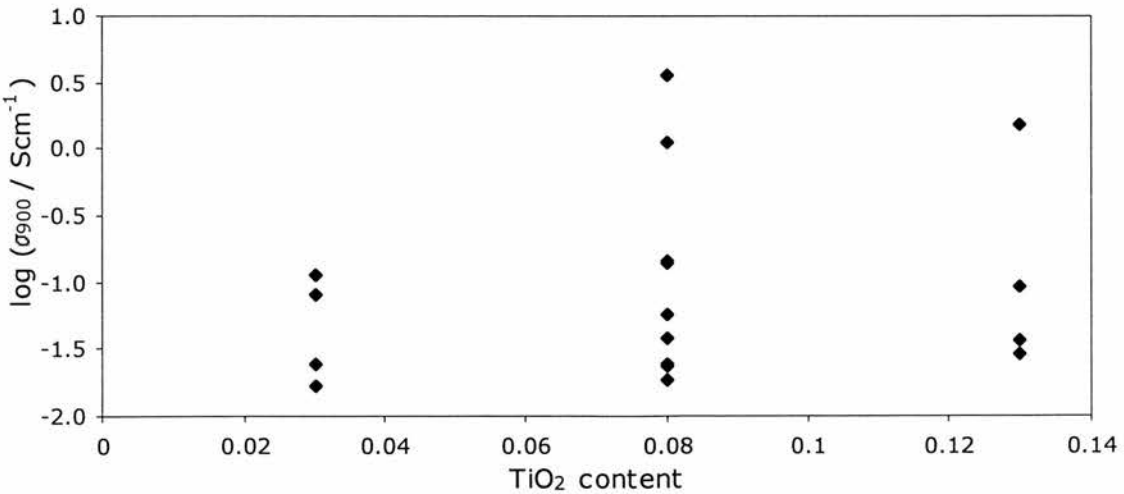

Figure 4.52: Electrochemical processes conductivity at 900°C vs. TiO_2 content

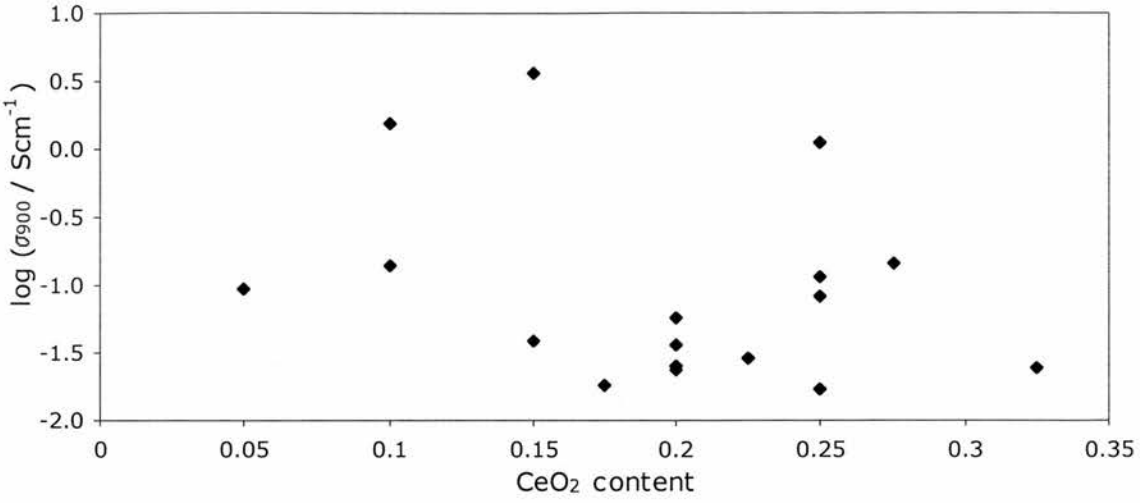

Figure 4.53: Electrochemical processes conductivity at 900°C vs. CeO_2 content

In terms of conductivity, bulk conductivities were within the same order of magnitude, ranging from $2.61*10^{-3}$ Scm^{-1} for $Y_{0.125}Zr_{0.52}Ti_{0.13}Ce_{0.225}O_{1.9375}$ to $9.95*10^{-3}$ Scm^{-1} for $Y_{0.10}Zr_{0.62}Ti_{0.03}Ce_{0.25}O_{1.95}$. In terms of trends of σ with component concentration, σ increased with increasing ZrO_2 content and decreasing TiO_2 content. Finally, pre-exponential factor A ranged from $3.30*10^5$ to $1.36*10^6$ $Scm^{-1}K$, implying that the concentration of charge carriers did not alter significantly.

One explanation for why σ_i decreases with increasing TiO_2 content is that the local bonding environment of Ti^{4+} to oxide ions/ oxygen vacancies was different to that of 8-coordinate environment of the Y^{3+} and Zr^{4+} cations [4.2]. The Ti cations tended to be in distorted sites, perhaps in a 5-coordinate environment [4.3, 4.4]. Alternatively, oxygen vacancies and large Y^{3+} cations help the small Ti cations into a 6-coordinate environment that is more suitable [4.5, 4.6]. Oxide ions and oxygen vacancies associated to Ti may be less mobile than those associated to Y, Zr or Ce cations. This would reduce the oxide ion conductivity of YZTC materials with high Ti content.

In general, the grain boundary conductivity was greater than bulk conductivity, with a wider spread of values, ranging from $5.41*10^{-3}$ Scm^{-1} for $Y_{0.15}Zr_{0.52}Ti_{0.08}Ce_{0.25}O_{1.925}$ to 0.264 Scm^{-1} for $Y_{0.20}Zr_{0.52}Ti_{0.03}Ce_{0.25}O_{1.90}$. The level of σ for grain boundary was usually 10-38 times as high as for the bulk. This conductivity increases with increasing CeO_2 or ZrO_2 content and decreasing TiO_2 content.

Most of the time, the electrochemical processes yielded the highest conductivities, ranging from $1.67*10^{-2}$ Scm^{-1} for $Y_{0.20}Zr_{0.52}Ti_{0.03}Ce_{0.25}O_{1.90}$ to 3.65 Scm^{-1} for $Y_{0.15}Zr_{0.62}Ti_{0.08}Ce_{0.15}O_{1.925}$. σ increases with increasing Y_2O_3 and ZrO_2 content and decreasing CeO_2 content.

4.3.2: DC Conductivity Measurements

These measurements on the dependence of conductivity with pO_2 suggest that the nature of conductivity changes with increasing CeO_2 content. Firstly, the pO_2 range of the ionic domain narrows with increasing CeO_2 content. For $Y_{0.20}Zr_{0.57}Ti_{0.13}Ce_{0.10}O_{1.90}$, the ionic domain was present down to 10^{-16} atm but for $Y_{0.15}Zr_{0.57}Ti_{0.03}Ce_{0.25}O_{1.925}$, it was down to only 10^{-11} atm. This means that the onset of electronic contribution moves to higher pO_2 with increasing CeO_2 content.

With 15+ mol% CeO_2, in the mixed ionic/ electronic conductivity region, there is an irreversible n-type contribution down to a maximum between 10^{-15} and 10^{-18} atm on reduction. A small n-type contribution observed on oxidation for $Y_{0.15}Zr_{0.57}Ti_{0.13}Ce_{0.15}O_{1.925}$, but not for the compositions containing 25 mol% CeO_2. At lower pO_2 levels, total conductivity decreases with decreasing pO_2, as a combination of falling ionic and electronic contributions. It is likely that this may be due to an order/ disorder phenomenon, where there is ordering of defects on reduction down to a level such as 80% Ce reduction. On oxidation, there is a hysteresis, as the ordering is still present until maybe 90% or all of the Ce is reoxidised. This is shown as a broad event at low pO_2 and a sharper peak at high pO_2.

For the n-type electronic conductivity regions, it appears that the maximum σ_e increased with increasing CeO_2 content, as shown in Table 4.36.

Table 4.36: n-type electronic conductivity maxima.

Formula	σ_e max/ Scm^{-1}
$Y_{0.20}Zr_{0.57}Ti_{0.13}Ce_{0.10}O_{1.90}$	$8.85*10^{-3}$
$Y_{0.15}Zr_{0.57}Ti_{0.13}Ce_{0.15}O_{1.925}$	$6.07*10^{-3}$
$Y_{0.15}Zr_{0.52}Ti_{0.08}Ce_{0.25}O_{1.925}$	$2.17*10^{-2}$
$Y_{0.15}Zr_{0.57}Ti_{0.03}Ce_{0.15}O_{1.925}$	$2.61*10^{-2}$

The n-type conductivity at low pO_2 is due to reduction of Ce, with electrons hopping between Ce^{3+} and Ce^{4+} ions. As the pO_2 decreases and more Ce is reduced, the conductivity maximum observed in the plots could be where half of the Ce^{4+} is reduced to Ce^{3+}. Then, as even more Ce is reduced, the majority of the Ce is Ce^{3+}, leading to less Ce^{4+} ions for electrons

to hop to. This would cause electronic conductivity to decrease with decreasing pO_2. This could explain to an extent why conductivity rises to a maximum and falls with decreasing pO_2 but lack of coincidence of different data sets indicate that this is not the case.

In comparison, the $(Y_2O_3)_{0.08}(ZrO_2)_{1-x}(CeO_2)_x$ system shows similar conductivity/ pO_2 behaviour at low pO_2 to these measurements [4.7]. These plots showed the ionic domain, followed by n-type contribution that reaches a maximum, followed by conductivity falling as pO_2 decreases. The suggestion is that as the pO_2 decreases to the point where total conductivity is at a maximum, ionic conductivity (σ_i) and electron mobility (μ_{el}) start to decrease at similar pO_2 levels, implying that their behaviour is connected in some way.

In terms of σ_i decreasing at low pO_2, there are additional oxygen vacancies formed due to Ce reduction and these vacancies may associate to form clusters. While the total vacancy concentration increases, the concentration of free oxygen vacancies drops due to defect association, causing the ionic conductivity drop. The decreasing electronic conductivity was due a decrease in the concentration of hopping/ charge carriers and an accompanying decrease in electron mobility [4.7].

The suggestions for the behaviour of conductivity in this CeO_2-ZrO_2-Y_2O_3 system could well be true for these measurements, as the YZTC materials could be thought of as similar materials with a small amount of TiO_2 added. This does not address the issue of the order/ disorder phenomenon, however.

4.3.3: Comparison with YZT

Previous studies on the conductivity of YZT ($Y_{0.20}Zr_{0.62}Ti_{0.18}O_{1.90}$) were done at 930°C, with a plot of σ vs. pO_2 shown in Figure 4.54 [4.5]

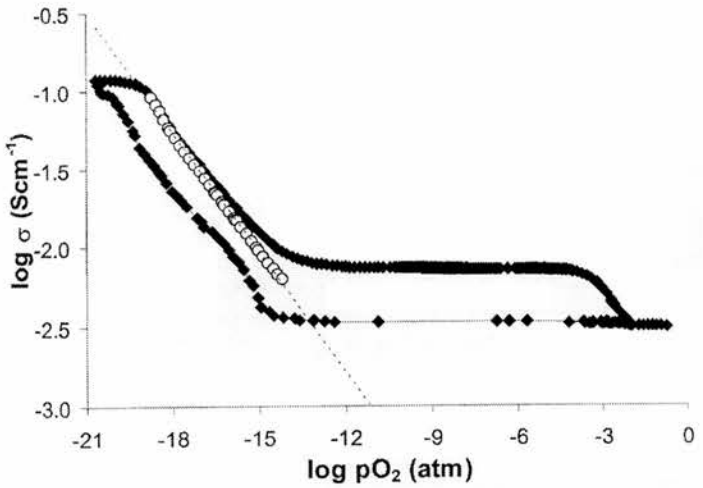

Figure 4.54: σ/ pO_2 dependence of $Y_{0.20}Zr_{0.62}Ti_{0.18}O_{1.90}$ [4.5]

The ionic conductivity of YZT was $8*10^{-3}$ Scm^{-1} and the electronic conductivity showed a $pO_2^{-1/4}$ dependence, reaching a maximum of 0.18 Scm^{-1} at a pO_2 of 10^{-19} atm.

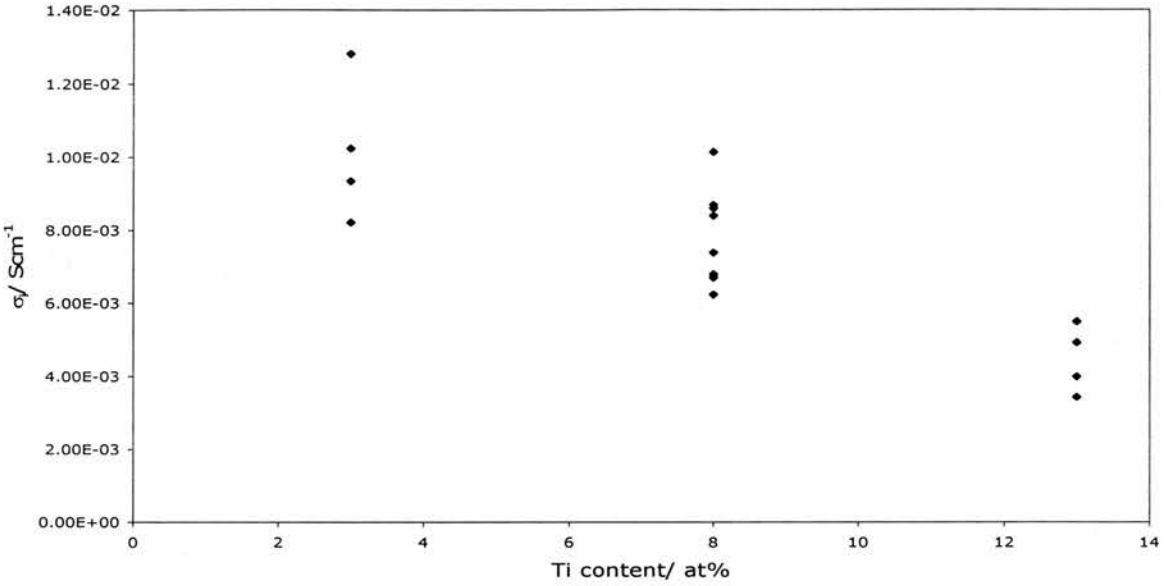

Figure 4.55: Comparison of Ionic conductivities at 930°C

In Figure 4.55, the ionic conductivities measured for YZTC compositions were extrapolated to 930°C, to compare with the value obtained for YZT, as shown in the dotted line at $8*10^{-3}$ Scm^{-1}. Extrapolated conductivities ranged from $3.42*10^{-3}$ to $1.28*10^{-2}$ Scm^{-1} at this temperature. Half of the compositions investigated showed higher ionic conductivity than YZT, with low Ti and high Zr content. The highest conductivity ($1.28*10^{-2}$ Scm^{-1}) was from $Y_{0.10}Zr_{0.62}Ti_{0.03}Ce_{0.25}O_{1.95}$, ~60% higher than that of YZT. Thus, it is possible for YZTC materials to have higher ionic conductivity than YZT.

From DC conductivity measurements, electronic conductivities of the YZTC materials were much less than the 0.18 Scm^{-1} of YZT. The highest level was ~$2.6*10^{-2}$ Scm^{-1} for $Y_{0.15}Zr_{0.57}Ti_{0.03}Ce_{0.25}O_{1.925}$, when the pO_2 was being reduced. It is most likely that the electronic conductivity behaviour of YZT becomes more complicated when CeO_2 is added.

4.4: Conclusions

The conclusions about the conductivity of the YZTC system were as follows:

At 900°C, the ionic (bulk) conductivities in static air were very similar to each other, ranging from 2.61 to $9.95*10^{-3}$ Scm^{-1}. $Y_{0.10}Zr_{0.62}Ti_{0.03}Ce_{0.25}O_{1.95}$ exhibited the highest conductivity. Ionic conductivity increased with increasing ZrO_2 content and decreasing TiO_2 content.

Grain boundary conductivity was more variable between $5.41*10^{-3}$ - 0.264 Scm^{-1}, increasing with increasing CeO_2 content and decreasing TiO_2 content. Low frequency electrochemical conductivity ranged from $1.67*10^{-2}$ to 3.65 Scm^{-1} and tended to increase with increasing Y_2O_3 and ZrO_2 content but decreases with increasing CeO_2 content. When reduced in 5% H_2/ Argon, ionic conductivity was higher and activation energy was lower than in static air. This is likely to be due to additional electronic conductivity.

Activation energies were 1.12-1.24 eV for bulk, 1.04-1.55 eV for grain boundary and 1.64-2.93 eV for electrochemical processes. There were no prominent trends between activation energy and composition. The similar levels of bulk conductivity and activation energy could be due to the compositions being in the concentrated defect regime. Also, at 930°C, it was possible for YZTC compositions to exhibit ionic conductivities greater than for $Y_{0.20}Zr_{0.62}Ti_{0.18}O_{1.90}$ in static air, especially with high Zr content, low Ti content, medium to high Ce content and even with low Y content.

In terms of conductivity/ pO_2 dependence, the materials showed a slight conductivity rise between $0.2\text{-}10^{-4}$ atm, due to a slight temperature rise. The 'ionic domain' was present down to between 10^{-11}-10^{-16} atm, with increasing CeO_2 content moving the onset of electronic conductivity to higher pO_2.

At low pO_2, the electronic conductivity behaviour becomes more complex with increasing Ce content. For 10 mol% CeO_2 content, n-type conductivity was observed on oxidation and reduction. With higher CeO_2 content, n-type conductivity reaches a maximum between 10^{-18} and 10^{-15} atm on reduction then falls with pO_2 decreasing further. On oxidation, there is n-type conductivity for 15 mol% CeO_2 but with higher CeO_2 content, there is only conductivity increasing with increasing pO_2. The σ_e maximum increases from $8.9*10^{-3}$ Scm^{-1} to $2.6*10^{-2}$ Scm^{-1} and the corresponding pO_2 level increases with increasing CeO_2 content.

n-type conductivity is due to electrons hopping between Ce^{3+} and Ce^{4+}. The decreasing of conductivity with decreasing pO_2 behaviour is due to two factors. Firstly, electronic conductivity decreases due to decreasing charge carrier concentration and electron mobility caused by the increasing extent of Ce^{4+} reduction. The second is that ionic conductivity decreases due to the formation of additional oxygen vacancies and association of these vacancies due to clusters. This leads to less free oxygen vacancies and a corresponding drop in oxide ion conductivity [4.7]. These effects become more prominent with higher CeO_2 content, as more formula oxygen is lost on reduction and more oxygen vacancies are formed in charge compensation.

References:

[4.1]: J.C. Ruiz-Morales, P. Núnez, R. Buchanan, J.T.S. Irvine, *Journal of The Electrochemical Society*, 2003, **150**, A1030-A1036

[4.2]: F. Capel, M.A. Bañares, C. Moure, P. Durán, *Materials Letters*, 1999, **38**, 331-335

[4.3]: F. Capel, PhD Thesis, Compultense University of Madrid, 1998

[4.4]: E. Zschech, P.N. Kontouros, G. Petzow, P. Behrens, A. Lessmann, R. Frahm, J. Am. Ceram. Soc., 1993, **1**, 197-201

[4.5]: A.J. Feighery, PhD Thesis, University of St. Andrews, 1998

[4.6]: P. Li, I-W. Chen, *Denki Kagaku*, 1993, **64**, 690

[4.7]: C.H. Lee, G.M. Choi, Solid State Ionics, 2000, **135**, 653-661

Chapter 5: Further Densification

Contents

5: Attempted densification of YZTC

5.1: Background

In order to consider the performance of a YZTC material as a potential SOFC electrolyte, one requirement is that the material is made fully dense (>95% of theoretical density). In the previous sections, the maximum density of pellets that was achieved was ~93% of theoretical density at 1,400°C.

So, one idea is to consider the use of a sintering aid, doped into the YZTC materials in a very small concentration, to facilitate the sintering of YZTC pellets to full density and at temperatures of <1,400°C. In the case of ceria-based materials, nominally, the firing temperature for full densification is 1,300°C – 1,600°C [5.1-5.3]. Apparently, these firing temperatures leads to microstructures that have poor mechanical stability, due to large grain sizes of 1-50 μm [5.4]. If the use of sintering aids can reduce the sintering temperature, this will lead to fully dense ceria-based electrolytes that are more resilient, as the grain growth and grain size is reduced [5.5]. Sintering aids that have been used for this have been transition metal oxides such as MnO_2, Fe_2O_3, CuO and Co_3O_4 [5.4-5.6].

The first sintering aid that was tried was Co_3O_4, as it has been used to sinter nanosized gadolinia-doped ceria ($Gd_xCe_{1-x}O_{2-x/2}$) to >98% of theoretical density at <1,000°C [5.4-5.5]. Co_3O_4 was added to the Gd-doped ceria at concentrations of up to 5 mol% Co_3O_4. It was found by dilatometry studies that $Gd_{0.20}Ce_{0.80}O_{1.90}$ doped with 1+ mol% Co_3O_4 sintered to 98% of theoretical density at <1,000°C. The rate of shrinkage of pellets was at a maximum with the addition of 2 mol% Co_3O_4 and adding more Co_3O_4 had no further effect on this rate. Also, the sintering behaviour was virtually unaffected by Co_3O_4 additions of <1 mol%.

The principle behind the reduced temperature sintering due to the presence of Co_3O_4 doping is that at ~900°C, the Co_3O_4 melts and decomposes to CoO, where the densification of the ceria-based material is due to liquid phase sintering. The sintering temperatures of 900-1,000°C would indicate that the Co_3O_4 decomposition is very important in the reduced-temperature sintering process.

Kleinlogel & Gauckler used nanosized $Gd_{0.20}Ce_{0.80}O_{1.90}$ powder for their sintering experiments, where the average particle size was 20 nm [5.5]. When Co_3O_4 was doped into $Gd_{0.10}Ce_{0.90}O_{1.95}$, the Co_3O_4-doped powder was sieved through a 38μm mesh [5.4]. In all of these experiments, the unfired pellets had densities of 50-60% of theoretical density and the starting 'green density' could also be an important factor in the densification process.

Other studies involved the use of Fe_2O_3 as a sintering aid, as other studies have shown that MnO_2 and Fe_2O_3 was more suitable for $Gd_xCe_{1-x}O_{2-x/2}$ powders with particle sizes of >100 nm. MnO_2 was not as suitable, however, due to the presence of deleterious grain boundary conductivity [5.7].

Sintering measurements were carried out on $Gd_{0.20}Ce_{0.80}O_{1.90}$ doped with Fe_2O_3. With up to 0.5 at% Fe, sintering was improved. T_{max} (temperature of maximum sintering rate) decreased with increasing Fe content for up to 0.5 at% Fe from 1,516°C (no Fe content) to 1,345°C (0.5 at% Fe). Adding more than 0.5 at% Fe had no further effect. Thus, the sintering temperature can lowered by >150°C with Fe_2O_3 addition.

5.2: Attempted densification using Co_3O_4

Attempts to prepare Co_3O_4-doped pellets involved adding up to 4 mol% Co_3O_4 to the YZTC material. The amount of Co_3O_4 required for this was calculated as the amount required by the equation $(YZTC)_{100-x}(Co_3O_4)_x$, where x was the desired Co_3O_4 concentration in mol%.

When preparing the Co_3O_4-doped pellets, an appropriate amount of $Co(NO_3)_2.6H_2O$ was mixed and ground up with the YZTC powder and placed in a crucible for calcination. This involved decomposition of $Co(NO_3)_2.6H_2O$ to CoO by holding at 180-200°C for up to 30 minutes, then the powder mix was heated up to 650°C and held for up to 1 hour, to remove water and oxidise CoO to Co_3O_4.

Next, the powder mix was ground up again and uniaxially dry-pressed at ~148-222 MPa for 2 minutes into 13mm diameter pellets. Green densities of the pellets were not measured, as there was a risk of this damaging the pellets. Pellets were 2-9mm in thickness and were fired at up to 1,000°C for up to 16 hours. Four different compositions were investigated, to determine if the process was affected by composition. The results were shown in Table 5.1.

Table 5.1: Results of firing Co_3O_4-doped YZTC pellets.

YZTC Formula	Co_3O_4/ mol%	Rel. Density/ %	Firing Conditions
$Y_{0.20}Zr_{0.57}Ti_{0.08}Ce_{0.15}O_{1.90}$	2	61.4	975°C, 3 hrs
$Y_{0.15}Zr_{0.57}Ti_{0.13}Ce_{0.15}O_{1.925}$	2	66.7	1,000°C, 16 hrs
$Y_{0.15}Zr_{0.57}Ti_{0.13}Ce_{0.15}O_{1.925}$	2	66.3	1,000°C, 16 hrs
$Y_{0.15}Zr_{0.57}Ti_{0.13}Ce_{0.15}O_{1.925}$	2	79.6	1,200°C, 16 hrs after 2 hrs ball-milling
$Y_{0.15}Zr_{0.57}Ti_{0.13}Ce_{0.15}O_{1.925}$	4	90.5	1,200°C, 16 hrs after 2 hrs ball-milling
$Y_{0.20}Zr_{0.62}Ti_{0.13}Ce_{0.05}O_{1.90}$	4	62.5	1,100°C, 3.5 hrs
$Y_{0.15}Zr_{0.62}Ti_{0.13}Ce_{0.10}O_{1.925}$	4	63.5	1,000°C, 8 hrs

There was mixed success in using Co_3O_4 as a sintering aid. One problem was that the particle sizes were probably too large. Alternatively, 1,000°C may have been too low a firing temperature. Also, some of these pellets were not physically stable and broke up easily. Despite most of the fired pellets being 61.4-63.5% dense, there was one success. One material containing 4 mol% Co_3O_4, fired at 1,200°C was 90.5% dense, as opposed to the normal firing temperature of 1,400°C required to achieve 90% density.

5.3: Attempted densification using Fe_2O_3

These experiments investigated the effect of using Fe_2O_3 as a sintering aid for YZTC materials. Fe_2O_3 is believed to be more suitable for powders that have larger particle sizes than those required for effective low temperature sintering with Co_3O_4. This involved preliminary qualitative sintering experiments on YZTC 30 ($Y_{0.125}Zr_{0.57}Ti_{0.08}Ce_{0.225}O_{1.9375}$) and quantitative experiments on sintering YZTC 3 ($Y_{0.20}Zr_{0.57}Ti_{0.13}Ce_{0.10}O_{1.90}$) in a dilatometer. The difference between these compositions is in sintering temperatures (~1,425°C for YZTC 30 and ~1,500°C for YZTC 3).

Qualitative

Attempts to prepare Fe_2O_3-doped pellets involved adding up to 1 mol% Fe_2O_3 to the YZTC material. Preparing the Fe_2O_3-doped pellets involved an appropriate amount of Fe_2O_3 mixed and ground up with the YZTC powder. Next, the powder mix was ground up again and uniaxially dry-pressed at ~148-296 MPa for 2 minutes into 13mm diameter pellets. Green densities of the pellets were not measured, as there was a risk of this damaging the pellets. Pellets were fired at up for up to 16 hours at temperatures in the range 1,300 – 1,425°C. The results were shown in Table 5.2.

Table 5.2: Results of firing Fe_2O_3-doped YZTC pellets.

Fe_2O_3/ mol%	Rel. Density/ %	Firing Conditions
0	78.2	1,375°C, 22 hours
0	82.2	1,400°C, 16 hours
0.25	81.1	1,300°C, 12 hours
0.25	81.9	1,350°C, 16 hours
0.25	81.7	1,400°C, 12 hours
0.5	83.9	1,350°C, 16 hours
0.5	83.9	1,400°C, 12 hours
1	82.4	1,350°C, 14 hours
1	77.6	1,375°C, 6 hours
1	81.9	1,400°C, 12 hours
1	81.4	1,425°C, 14 hours
0.5	87.8	1,375°C, 8 hours after 45 mins ball-milling
1	86.1	1,375°C, 8 hours after 45 mins ball-milling

From Table 5.2, it appears that the addition of Fe_2O_3 had a slight effect on the sintering of the YZTC material, especially in conjunction with ball-milling. The highest density yielded was 87.8% with 0.5 mol% Fe_2O_3 added and ball-milling of the powder (83.9% without ball-milling and 0.25 mol% Fe_2O_3). There was no clear trends to indicate the effects of Fe_2O_3 doping into the YZTC. Trends may come to light in the quantitative measurements.

Quantitative

There were six pellets of YZTC 3/ Fe_2O_3 powder mixes containing 0.38 – 2.50 mol% Fe_2O_3 (0.75 – 5 at% Fe) and one pellet of YZTC 3 itself for comparison. The powders were ball-milled for 2-3 hours in acetone, pressed uniaxially into pellets using a 13 mm press die and up to 296 MPa pressure for 2 minutes. To ensure that the 'green' pellets were in a form that was stable and would not break up when handled or inserted into the dilatometer, they were heated for 12-24 hours at 1,000°C to 'pre-sinter'. The resultant pellets were up to 16 mm in length after 'pre-sintering' at 1,000°C.

Samples were heated in air flowing at 50cm^3 min^{-1} at 5°C min^{-1} from 25°C to 900°C, holding isothermally for 2 hours at 900°C, followed by heating at 5°C min^{-1} to 1,475°C, cooling down at 5°C min^{-1}. Before each sample run, 'blank' runs were carried out under these conditions using alumina cylinders of similar length to that of the samples. These acted as 'dummy' background runs in conditions similar to those used in the actual experiments. One precaution that was taken during these experiments was that platinum foil was wrapped around the bottom of the crucible and one of the circular faces of the spacer disk that 'sandwich' the sample pellets. This was to prevent potential contamination of the instrument parts through reaction with the sample.

a) YZTC 3 (No Fe_2O_3 present)

The first experiment was carried out on YZTC3 itself without any Fe_2O_3 present, to act as a 'control' experiment to base the effects of Fe_2O_3 additions on. The sample length was 15.816 mm and the experiment profile was shown in Figure 5.1. For more information about the behaviour of the sintering process, the rate of shrinkage with temperature ($\frac{dL/L_o}{dT}$ in units of K^{-1}) was plotted against temperature and shown in Figure 5.2.

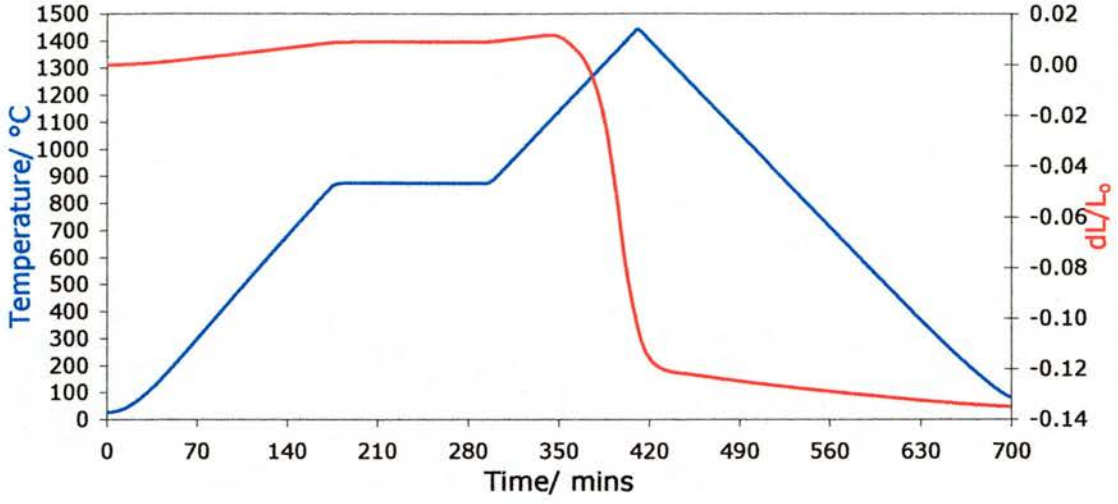

Figure 5.1: Profile of YZTC 3 sintering experiment

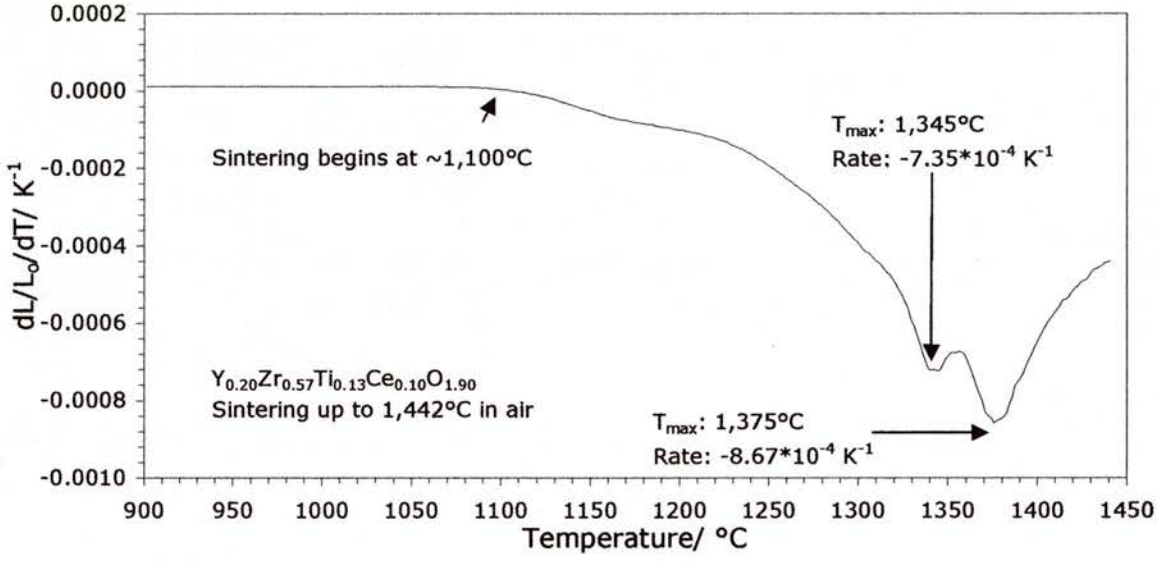

Figure 5.2: Rate of sintering of YZTC 3

From Figure 5.1, the sample expanded 1.17% up to 1,100°C was due to normal thermal expansion of the material. Then, at ~1,100°C, a large shrinkage step began, which was due to the pellet sintering. The sample shrunk 11.37% up to 1,442°C, shrinking further on cooling and total shrinkage was 13.49%. After the experiment finished, the pellet thickness decreased 13.03% to 13.756 mm. Figure 5.2 showed two maximum shrinkage rates observed in the sintering. The first was at 1,345°C and the second at 1,375°C. At temperatures above 1,375°C, the shrinkage rate started slowing down until the end of heating at 1,442°C.
The fired pellet was 79.8% dense. Thus, the pellet had not sintered to full density. This was not surprising, as the synthesis temperature for this material is between 1,475 and 1,500°C.

b) YZTC3/ Fe_2O_3 composition A

The second sample contained YZTC3 and Fe_2O_3 in the ratio of 99.13: 0.87 mol%. The sample length was 15.138 mm and the profile of the experiment is shown in Figure 5.3. Figure 5.4 shows the rate of shrinkage with temperature from 900 °C onwards.

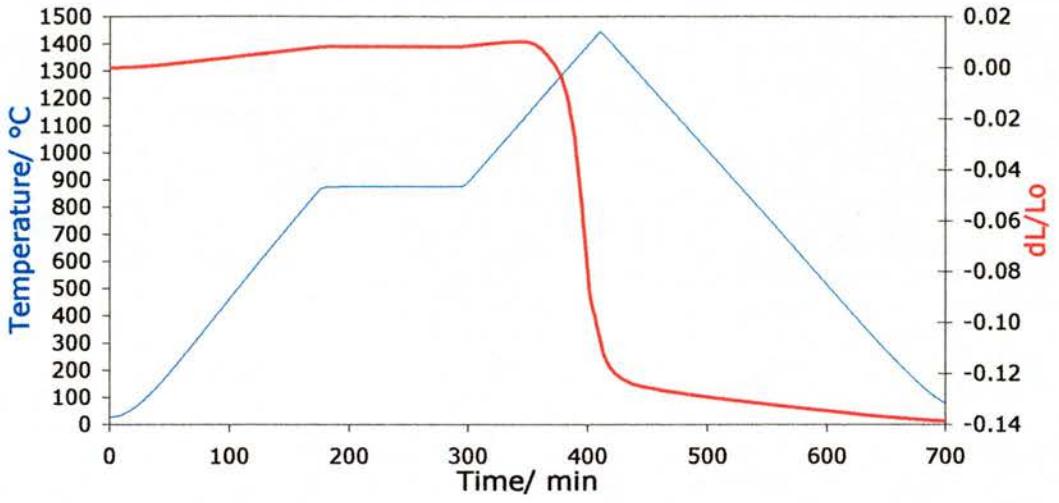

Figure 5.3: Profile of sintering experiment

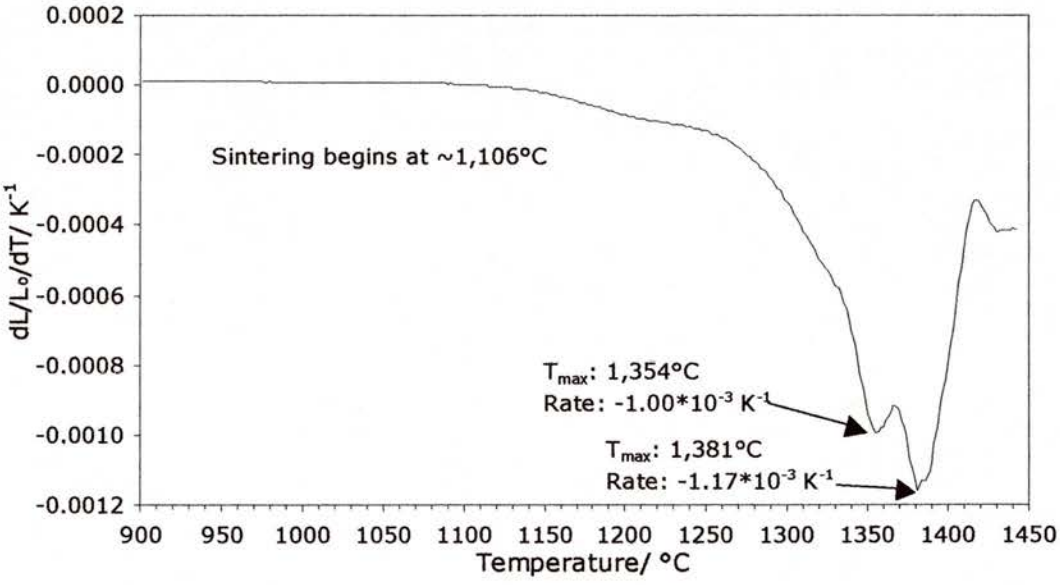

Figure 5.4: Rate of sintering with temperature

This measurement showed similar behaviour to that of the 'control' sample. Sample shrinkage was higher at 11.60% up to 1,442°C and 13.85% in total. After the experiment finished, sample thickness shrunk 13.22% to 13.137 mm. Figure 5.4 showed the two maximum shrinkage rates observed in the previous experiment, although the rates were higher and the temperature maxima occurred at 1,354 and 1,381°C. Between 1,417 and 1,442°C, there was some uncertain behaviour, where the sample shrunk slightly more, then the rate

settled down. After firing, the pellet was 78.6% dense. Compared to the original YZTC3, the addition of a small amount of Fe_2O_3 had a small effect. Firstly, the temperature maxima during sintering were shifted 6-9°C higher and the shrinkage rates were 36% higher than for the undoped material.

c) YZTC3/ Fe_2O_3 composition B

The third sample contained YZTC3 and Fe_2O_3 in the ratio of 98.75: 1.25 mol%. The sample length was 15.227 mm and the profile of the experiment is shown in Figure 5.5. Figure 5.6 shows the rate of shrinkage with temperature from 900 to 1,442°C.

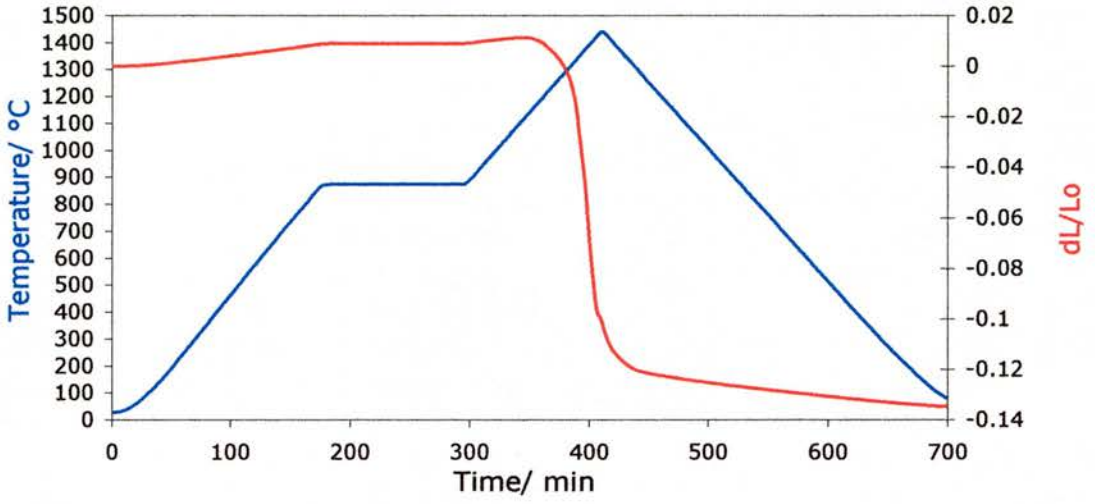

Figure 5.6: Rate of sintering with temperature

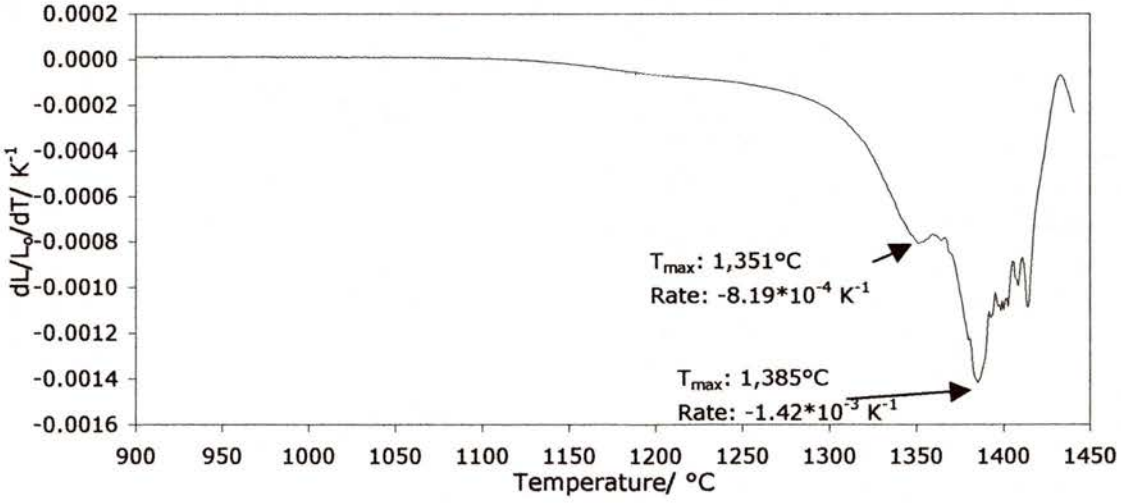

Figure 5.5: Profile of sintering experiment

This measurement showed similar behaviour to that of the 'control' sample. Sample shrinkage was 10.02% up to 1,442°C and 13.46% in total. After the experiment finished, sample thickness decreased 12.93% to 13.258 mm. Figure 5.6 showed the two maximum

shrinkage rates observed in the previous experiment and the temperature maxima occurred at 1,351 and 1,385°C. After firing, the pellet was 74.4% dense. Compared to the original YZTC3, the temperature maxima during sintering were shifted 6-10°C higher and shrinkage rates were 11% higher for the first maximum and at the second maximum, 64% higher than for the undoped material. Figure 5.6 suggests an increased extent of sintering, as the shrinkage rate almost reached zero at 1,433°C.

d) YZTC3/ Fe_2O_3 composition C

The fourth sample contained YZTC3 and Fe_2O_3 in the ratio of 98.41: 1.59 mol%. The sample length was 11.929 mm and the experiment profile is shown in Figure 5.7. Figure 5.8 shows the rate of shrinkage with temperature from 900 to 1,442°C.

In this measurement, sample shrinkage was 18.53% up to 1,442°C and 20.17% in total. After the experiment finished, sample thickness decreased 19.67% to 9.583 mm. Figure 5.8 showed the two maximum shrinkage rates observed in the previous experiment and the temperature maxima occurred at 1,357 and 1,389°C. After firing, the pellet was 87.3% dense. Compared to the original YZTC3, the temperature maxima during sintering were shifted 12-14°C higher and shrinkage rates were almost twice as fast as those for the undoped material. Figure 5.8 suggests an increased extent of sintering, as the shrinkage rate decreased more considerably by the end of heating.

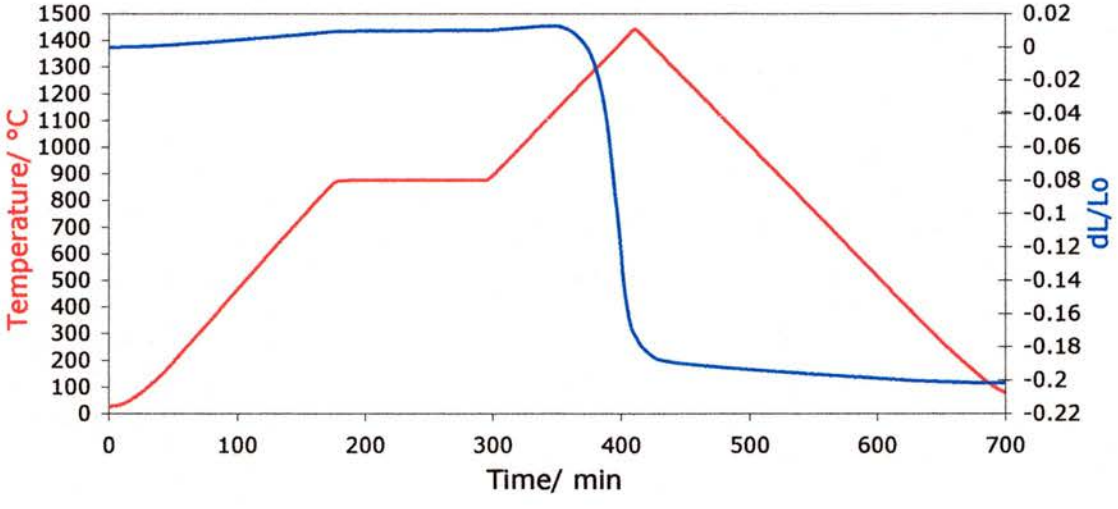

Figure 5.7: Profile of sintering experiment

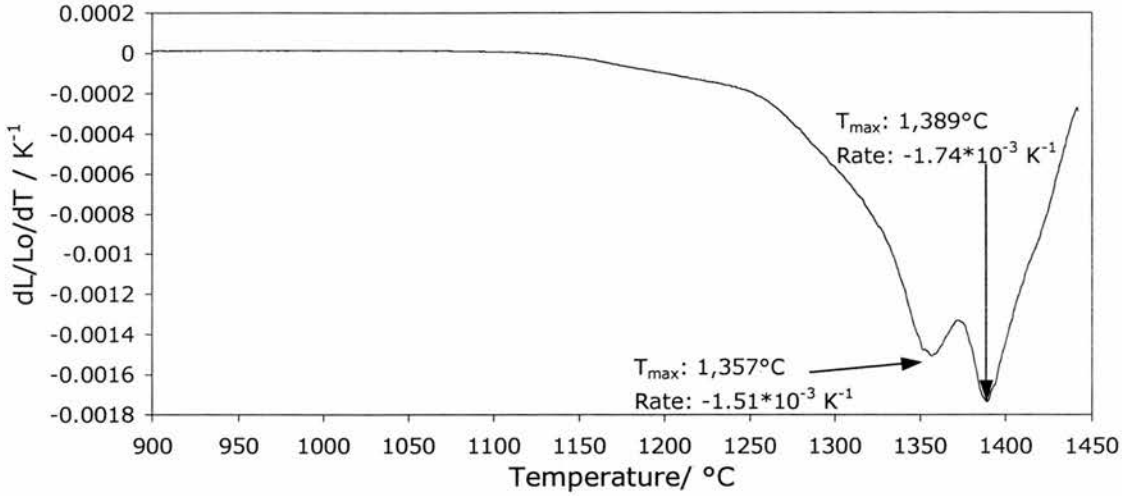

Figure 5.8: Rate of sintering with temperature

e) YZTC3/ Fe_2O_3 composition D

This sample contained YZTC3 and Fe_2O_3 in the ratio of 98.02: 1.98 mol%. The sample length was 12.363 mm and the experiment profile is shown in Figure 5.9. Figure 5.10 shows the rate of shrinkage with temperature from 900 to 1,442°C.

In this experiment, sample shrinkage was 16.36% up to 1,442°C and 18.02% in total. After the experiment finished, sample thickness decreased 17.50% to 10.200 mm. Figure 5.10 showed the two maximum shrinkage rates observed in the previous experiment and the temperature maxima occurred at 1,353 and 1,387°C. After firing, the pellet was 85.0% dense. Compared to the original YZTC3, the temperature maxima during sintering were shifted 8-12°C higher and shrinkage rates were 95% higher for the first maximum and 72% higher for the second maximum. Figure 5.10 suggests an increased extent of sintering, as the shrinkage rate decreased more considerably by the end of heating.

Compared to the composition containing 1.59 mol% Fe_2O_3, the temperature maxima were shifted lower by 2-4°C. The maximum rate at ~1,350°C was 5.3% lower but at ~1,380°C, it was 14% lower. The sample density after firing was also lower and the sample shrinkage after firing was only 16.6%, in contrast to almost 20% for the previous sample.

This indicates that the trend of increasing sintering rates and shrinkage with increasing Fe_2O_3 content only goes so far. It appears that the sintering and densification effects reach a maximum with 1.59 mol% Fe_2O_3 present and in going above this, these effects diminish with increasing Fe_2O_3 content.

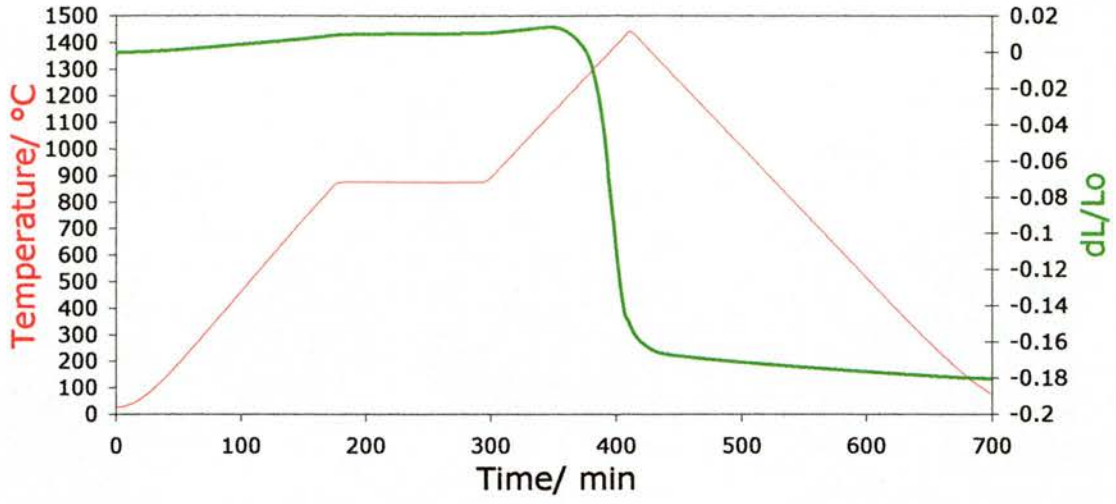

Figure 5.9: Profile of sintering experiment

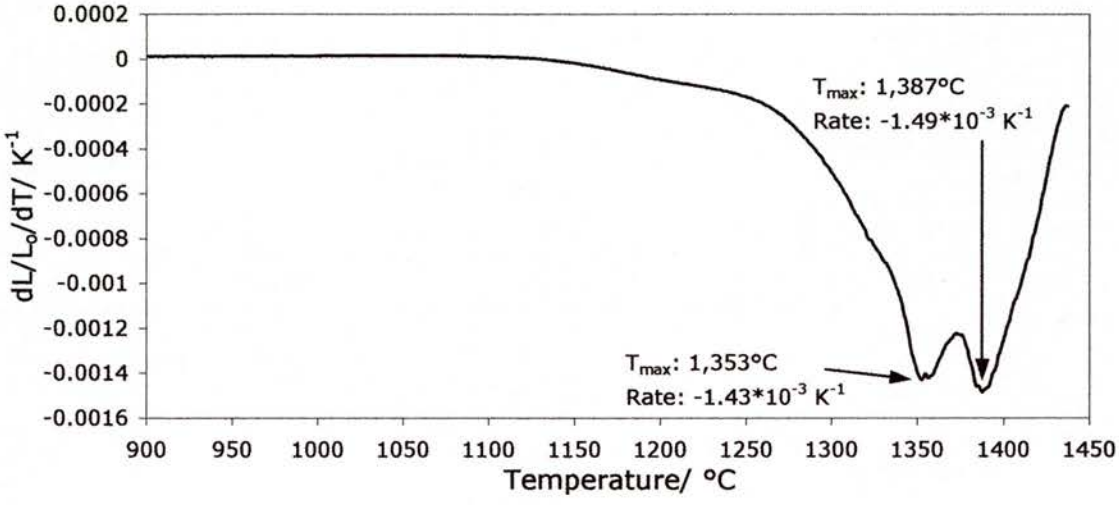

Figure 5.10: Rate of sintering with temperature

f) YZTC3/ Fe_2O_3 composition E

This sample contained YZTC3 and Fe_2O_3 in the ratio of 97.50: 2.50 mol%. The sample length was 14.170 mm and the profile of the experiment is shown in Figure 5.11. Figure 5.12 shows the rate of shrinkage with temperature from 900 to 1,442°C.

In this experiment, sample shrinkage was 8.45% up to 1,442°C and 11.28% in total. After the experiment finished, sample thickness decreased 11.35% to 12.562 mm. Figure 5.10 shows slightly different behaviour to previous measurements. There was a plateau between 1,320 and 1,340°C and there is a maximum at 1,382°C. This corresponds to what was the second maximum seen before. After firing, the pellet was 79.1% dense. Compared to the original YZTC3, the first maximum was replaced by a plateau and the second maximum during sintering was shifted 7°C higher and shrinkage rate was 49% higher for this maximum.

Compared to the previous sample, the events were shifted to lower temperature. The maximum rate at ~1,350°C was replaced by a plateau but at ~1,380°C, the rate was 13% lower. Also, the sample was less dense after firing and the sample shrinkage after firing was 11.4%, in contrast to ~17%.

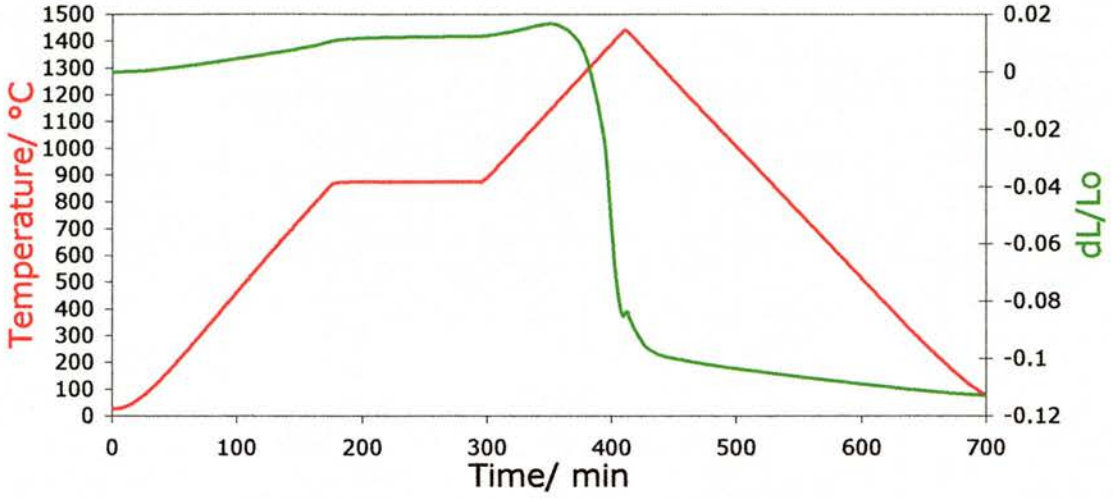

Figure 5.11: Profile of sintering experiment

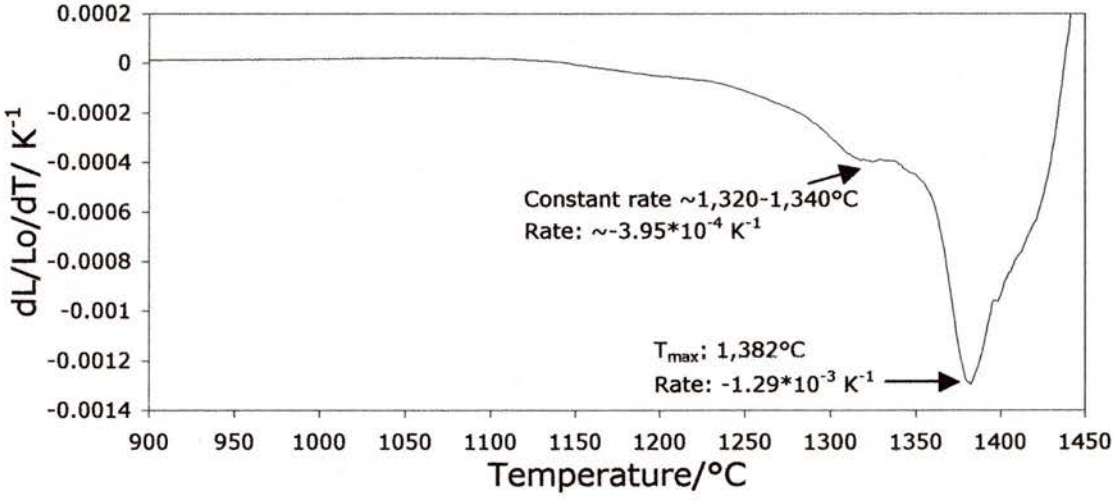

Figure 5.12: Rate of sintering with temperature

Comparisons

The addition of Fe_2O_3 to the YZTC material had some effects on sintering behaviour, as shown in Table 5.3 and Figures 5.13-5.14.

Table 5.3: Rate maxima observed in YZTC/ Fe_2O_3 sintering experiments

Fe_2O_3/ mol%	0	0.87	1.25	1.59	1.98	2.50
T_{max} 1/ °C	1,345	1,354	1,351	1,357	1,353	Plateau 1,320-1,340
T_{max} 2/ °C	1,375	1,381	1,385	1,389	1,387	1,382
Rate 1/ 10^{-4} K^{-1}	-7.35	-10.0	-8.19	-15.1	-14.3	-3.95
Rate 2/ 10^{-4} K^{-1}	-8.67	-11.7	-14.2	-17.4	-14.9	-12.90
Shrinkage/ %	13.49	13.85	13.46	20.17	18.02	11.28

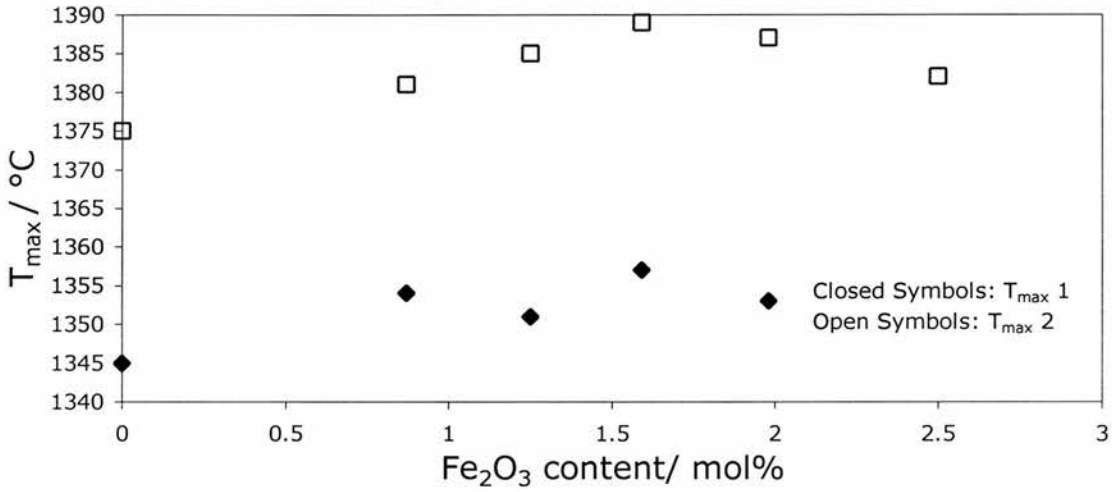

Figure 5.13: Plots of T_{max} against Fe_2O_3 content

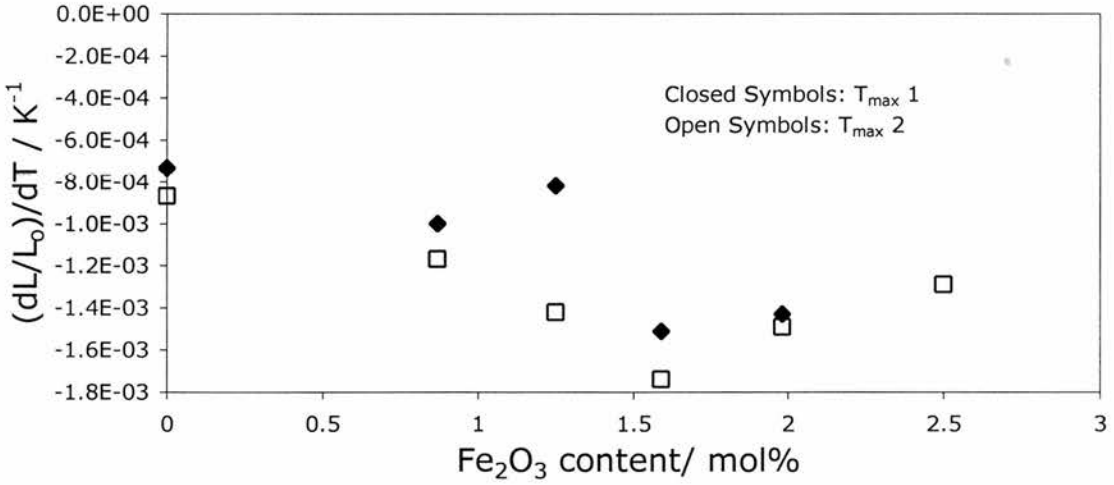

Figure 5.14: Plots of maximum sintering rates against Fe_2O_3 content

It appears from these sintering experiments that the addition of Fe_2O_3 improves sinterability of the YZTC material. There is a strange combination of effects that is caused by doping. Initially, the shrinkage rates and extent of shrinkage increase with increasing Fe_2O_3

content. In contrast, the rate maxima move to slightly higher temperatures (normally associated with reduced sinterability). With 1.59 mol% Fe_2O_3, the maximum sintering rates were twice that of the undoped YZTC, although the temperatures of the maxima were shifted up 12-14°C. With more than 1.59 mol% Fe_2O_3 present, the sintering rates and shrinkage reduce and the maxima move to lower temperatures with increasing Fe_2O_3 content.

The highest sample density achieved was 87.3% for the composition containing 1.59 mol% Fe_2O_3, as opposed to 79.8% for the YZTC itself. Also, samples shrunk in length by 11.3-20.2%. There is a sign that other processes could happen with ≥2.5 mol% Fe_2O_3, as the first peak in the rate/ temperature plot was replaced by a plateau between 1,320-1,340°.

Overall, it appears that the sinterability of the YZTC increased initially with increasing Fe_2O_3 content, reaching a maximum with 1.59 mol% Fe_2O_3 present. While T_{max} moved to increasing temperature with increasing Fe_2O_3 content, the effect of this on sinterability was more than countered by increasing sintering rates that were up to double that of the undoped YZTC. The shrinkage rate/temperature curves showed that the sintering process was more complete with Fe_2O_3 added.

The sintering process involved in the Fe_2O_3-doped YZTC was not the same as the liquid-phase process that occurs with Co_3O_4 doping at ~900-1,000°C [5.5]. It is likely that an alternative sintering mechanism is involved, as Fe_2O_3 is less volatile, melting at ~1,593°C. The effect could be due to a plastic phase deformation or other means that accelerated sintering rates but increased sintering temperatures slightly.

5.4: Conclusions

Doping YZTC with Co_3O_4 had limited success, due to the particle sizes of the powders being too high for the liquid-phase sintering effect to be of use. The best result obtained was 90.5% density for $Y_{0.15}Zr_{0.57}Ti_{0.13}Ce_{0.15}O_{1.925}$/ 2 mol% Co_3O_4, fired at 1,200°C. Fe_2O_3 additions do improve the sinterability overall up to a maximum content of 1.59 mol%.

There are two competing effects. The first is T_{max} increasing by up to 14°C, usually causing less sinterability and the second is an increasing sintering rate up to double that of the YZTC on its own. The overall extent of sintering is due to the second effect being more dominant than the first, as if the Fe_2O_3-YZTC compositions were much more reactive at slightly higher temperatures. The effects were reversed when Fe_2O_3 content was >1.59 mol%.

References:

[5.1]: I. Riess, D. Braunshtein, D.S. Tannhauser, *Journal of the American Ceramic Society*, 1981, **64** [8], 479

[5.2]: P. Duran, C. Moure, J.R. Jurado, *J. Mater. Sci*, 1994, **29** [7], 1940

[5.3]: H. Yahiro, Y. Eguchi, K. Eguchi, H. Aria, *J. Appl. Electrochem*, 1988, **18** [4], 527

[5.4]: G.S. Lewis, A. Atkinson, B.C.H. Steele, *Proceedings of the 4th European Solid Oxide Fuel Cell Forum*, 2000, 773-782

[5.5]: C. Kleinlogel, L.J. Gauckler, *Solid State Ionics*, 2000, 135, 567-573

[5.6]: C. Kleinlogel, L.J. Gauckler, *Proceedings of the 6th International Symposium on Solid Oxide Fuel Cells*, The Electrochemical Society, Pennington, 1999, 225

[5.7]: Z. Tianshu, PhD Thesis, Nanyang Technological University, 2002

Chapter 6: Conclusions

Contents

6: Conclusions

6.1: Overall Summary

For materials in the Y_2O_3-ZrO_2-TiO_2-CeO_2 system, the following conclusions were found:

After firing at 1,400-1,500°C, most compositions investigated had cubic structures, with unit cell edges ranging from 5.111 for $Y_{0.20}Zr_{0.62}Ti_{0.18}O_{1.90}$ to 5.228 Å for $Y_{0.15}Zr_{0.52}Ti_{0.03}Ce_{0.30}O_{1.925}$. The unit cell edge increased with increasing CeO_2 content and decreasing TiO_2 content. In terms of phase formation, it was found that single-phase cubic structures were more difficult to attain with increasing TiO_2 content, requiring increasing Y_2O_3 content to stabilise the phase. All compositions containing 3 mol% TiO_2 were single-phase cubic. For compositions containing 18 mol% TiO_2, single-phase cubic structures could only be attained with 11 mol% Y_2O_3.

Reduction studies indicated that in 5% H_2/ Argon at 900-1,000°C, almost all of the Ce is reduced. In argon, up to 17% of the Ce is reduced in fully oxidised materials. Firing at 1,400-1,500°C in air appeared to be more reducing, however. Materials turned light grey in argon, then dark brown/ black in 5% H_2/ Argon. The effect reduction had on structure was that the unit cell edge decreased slightly in argon by up to 0.0075Å, relative to materials 'as-fired', then rising in 5% H_2/ Argon by up to 0.0533Å, increasing with CeO_2 content.

The thermal expansion coefficient, α ranged from $10.25 - 11.68*10^{-6}$ K^{-1} in oxygen. α increased with increasing CeO_2 content and decreasing TiO_2 content. Argon caused a slight variation in α of up to $\pm 0.37*10^{-6}$ K^{-1}. In 5% H_2/ Argon, α was $0.32 - 0.98*10^{-6}$ K^{-1} lower than α in oxygen and α decreased with increasing CeO_2 content.

At 900°C, the ionic (bulk) conductivities in static air were very similar to each other, ranging from 2.61 to $9.95*10^{-3}$ Scm^{-1}. $Y_{0.10}Zr_{0.62}Ti_{0.03}Ce_{0.25}O_{1.95}$ exhibited the highest conductivity. Ionic conductivity increased with increasing ZrO_2 content and decreasing TiO_2 content. Grain boundary conductivity varied between $5.41*10^{-3}$ - 0.264 Scm^{-1}, increasing with increasing CeO_2 content and decreasing TiO_2 content. Low frequency electrochemical conductivity ranged from $1.67*10^{-2}$ to 3.65 Scm^{-1}, increasing with increasing Y_2O_3 and ZrO_2 content but decreasing with increasing CeO_2 content. When reduced in 5% H_2/ Argon, ionic conductivity was higher and activation energy was lower than in static air, due to an electronic contribution to conductivity.

Activation energies were 1.12-1.24 eV for bulk, 1.04-1.55 eV for grain boundary and 1.64-2.93 eV for electrochemical processes. The similar levels of bulk conductivity and

activation energy suggested the presence of a concentrated defect regime. Also, at 930°C, some YZTC compositions exhibited ionic conductivities greater than for $Y_{0.20}Zr_{0.62}Ti_{0.18}O_{1.90}$ in static air, especially with high Zr content, low Ti content, medium to high Ce content and even with low Y content.

In terms of conductivity/ pO_2 dependence, the materials showed a slight conductivity rise between 0.2-10^{-4} atm, due to a slight temperature rise. The 'ionic domain' was present down to between 10^{-11}-10^{-16} atm, with increasing CeO_2 content moving the onset of electronic conductivity to higher pO_2.

At low pO_2, the electronic conductivity behaviour becomes more complex with increasing Ce content. For 10 mol% CeO_2 content, n-type conductivity was observed on oxidation and reduction. With higher CeO_2 content, n-type conductivity reaches a maximum between 10^{-18} and 10^{-15} atm on reduction then falls with pO_2 decreasing further. On oxidation, there is n-type conductivity for 15 mol% CeO_2 but with higher CeO_2 content, there is only conductivity increasing with increasing pO_2, which shows a hysteresis effect due to defect ordering. The σ_e maximum increases from $8.9*10^{-3}$ Scm^{-1} to $2.6*10^{-2}$ Scm^{-1} and the corresponding pO_2 level increases with increasing CeO_2 content.

n-type conductivity is due to electron hopping between Ce^{3+} and Ce^{4+}. The decrease of conductivity with decreasing pO_2 behaviour is due to the electronic contribution decreasing due to decreasing charge carrier concentration and electron mobility as more Ce^{4+} is reduced. Also, the ionic contribution decreases due to the formation of oxygen vacancy clusters, leading to less free oxygen vacancies. This becomes more prominent with higher CeO_2 content, as more formula oxygen is lost on reduction and more oxygen vacancies are formed in charge compensation.

Doping YZTC with Co_3O_4 had limited success, where the best result obtained was 90.5% density for $Y_{0.15}Zr_{0.57}Ti_{0.13}Ce_{0.15}O_{1.925}$/ 2 mol% Co_3O_4, fired at 1,200°C. Fe_2O_3 additions do improve the sinterability overall up to a maximum content of 1.59 mol%. There are two effects. The first is T_{max} (temperature of maximum shrinkage rate) increasing by up to 14°C and the second is an increasing sintering rate up to double that of the YZTC on its own. The second effect is more important, as if the Fe_2O_3-YZTC compositions were more reactive at slightly higher temperatures. The effects were reversed when Fe_2O_3 content was >1.59 mol%.

6.2: Fuel Cell Testing

As a final experiment, a fuel cell test was performed. This was an electrochemical test of the material $Y_{0.125}Zr_{0.47}Ti_{0.13}Ce_{0.275}O_{1.9375}$, to assess its suitability as a SOFC electrolyte under fuel cell conditions. This composition was chosen due to the ceramic quality of the pellet rather than its electrical performance. The electrolyte was a pellet that was 92% dense, 2.0 cm in diameter and 1.3 mm thick. The electrodes were two symmetrical porous Pt layers in the form of circles 1.3 cm in diameter, which were fired at 875°C. Electrochemical measurements involved cyclic voltammograms taken at 800, 850 and 900°C, respectively at a voltage ramp rate of 5 mVs^{-1}. The atmospheres used were air as oxidant and 'wet' 5% H_2/ Argon as fuel. The V/I curves from these measurements are shown in Figures 6.1-6.3.

Important parameters are V_{obs}, the observed potential, measured from the experiments, shown in blue. V_{exp} is the expected potential, calculated as V_{exp}=IR+E, where IR is the measured current multiplied by the expected resistance derived from AC Impedance measurements. E is the Nernst potential at the temperature of interest, based on a 3% H_2O-4.85% H_2-92.15% Ar fuel gas mixture. This is shown in red. Also, the ionic transport number t_i was calculated as V_{obs}/V_{exp} at zero current.

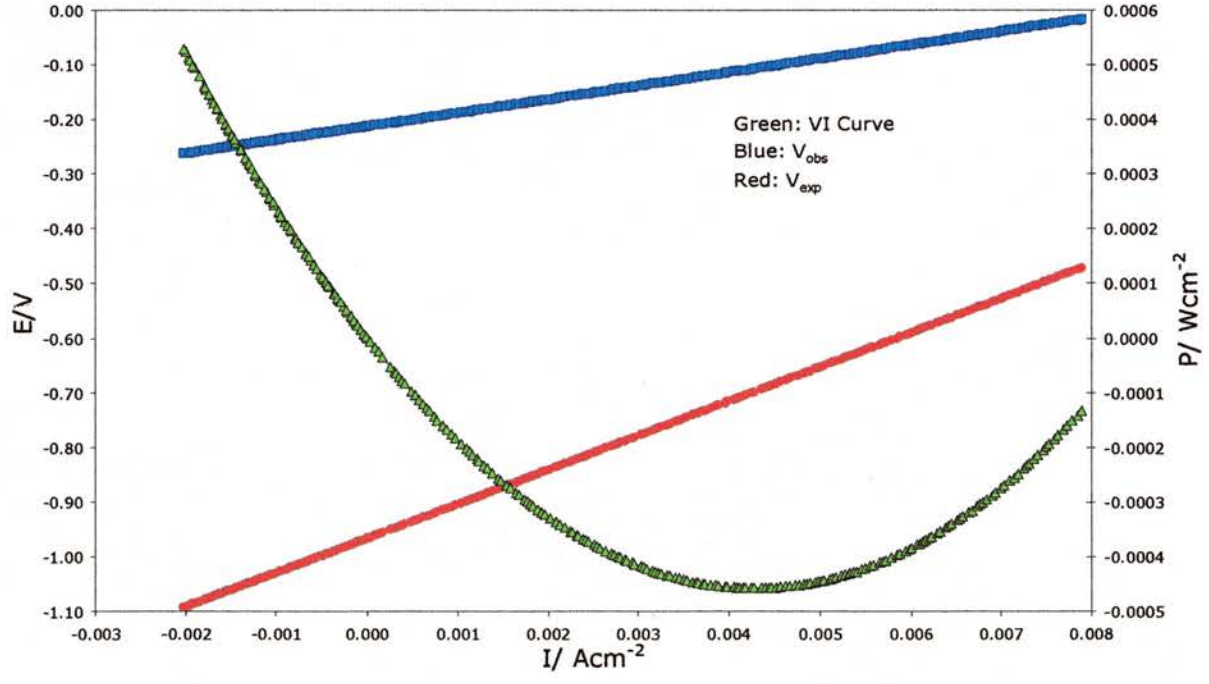

Figure 6.1: V/I curve measured at 800°C

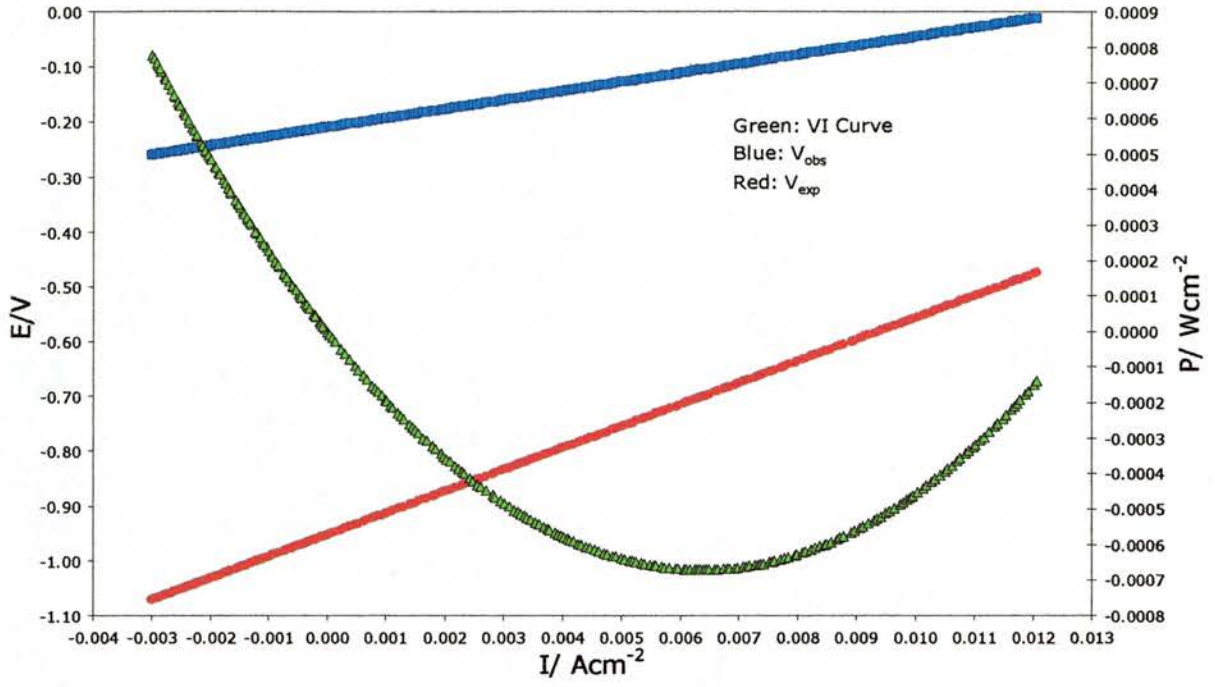

Figure 6.2: V/I curve measured at 850°C

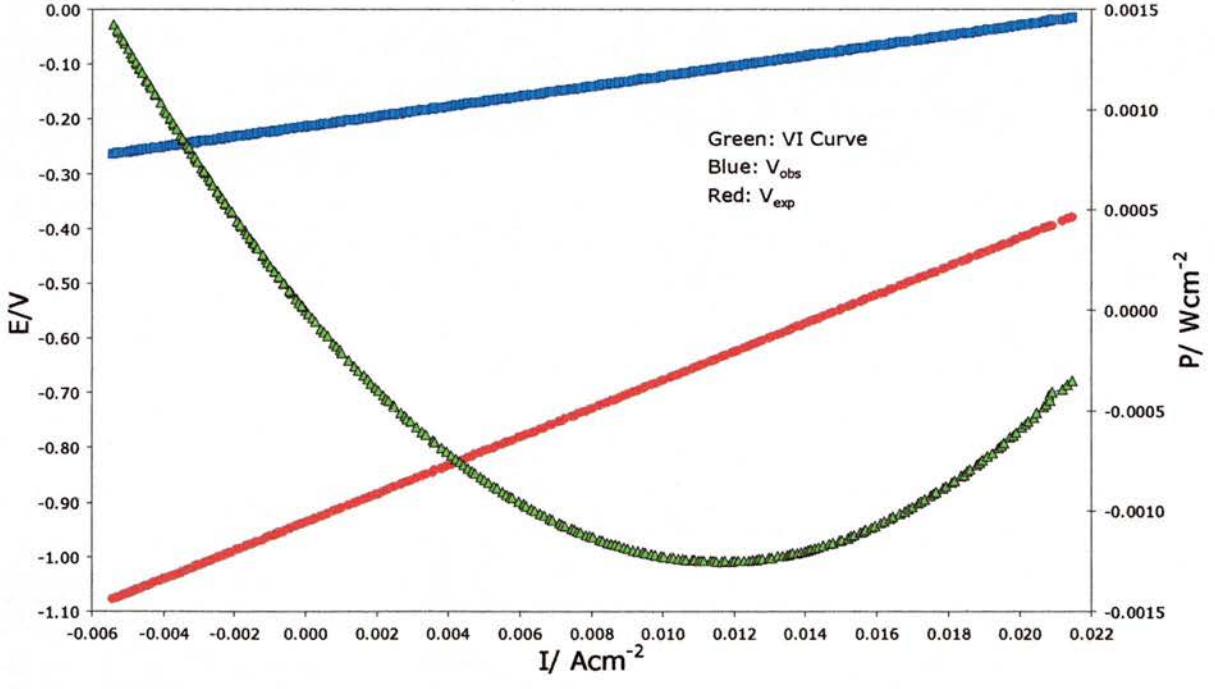

Figure 6.3: V/I curve measured at 900°C

Table 6.1 shows a comparison of the levels of ohmic resistance from the measurements (derived from the slopes of V_{obs}), predicted levels of ohmic resistance derived from the slopes of V_{exp} and ionic transport number t_i.

Table 6.1: Results from V/I curve measurements

Temperature/ °C	R_{ohmic}/ Ω	Predicted R_{ohmic}/ Ω	t_i
800	24.77	62.71	0.2200
850	16.41	39.52	0.2204
900	9.23	25.96	0.2288

Ohmic resistances from the V/I curves were lower than those predicted by the AC impedance measurements, implying that conductivity was higher, as a mixed ionic/ electronic conductivity. At all temperatures, t_i was constant at around 0.22, implying that the ionic contribution to conductivity was 22%. The electronic contribution is dominant, comprising 78% of the conductivity. This is in line with the behaviour of conductivity at low pO_2 observed in Chapter 4.

As pO_2 decreases, the electronic contribution becomes more and more dominant, as shown in Figure 6.4, which is a plot of electronic transport number vs log pO_2 for $Y_{0.20}Zr_{0.57}Ti_{0.13}Ce_{0.10}O_{1.90}$ taken as an example of how this material would behave. The transport number is calculated as the electronic contribution (σ_e) divided by total conductivity (σ). Between 10^{-22} and 10^{-23} atm, at the maximum, the electronic contribution accounts for almost 85% of conductivity.

For this material, the electronic transport at the fuel side is the main limiting factor, leading to the potential drop and under load, σ_e may increase. If the pellet was ~130 μm thick, this may have yielded a respectable current of ~100 $mAcm^{-1}$ but at a low voltage. The electronic contribution is the main obstacle in this case. Hence, due to the potential drop on one side, these materials would not be suitable for use as a SOFC electrolyte, which requires purely ionic conductivity.

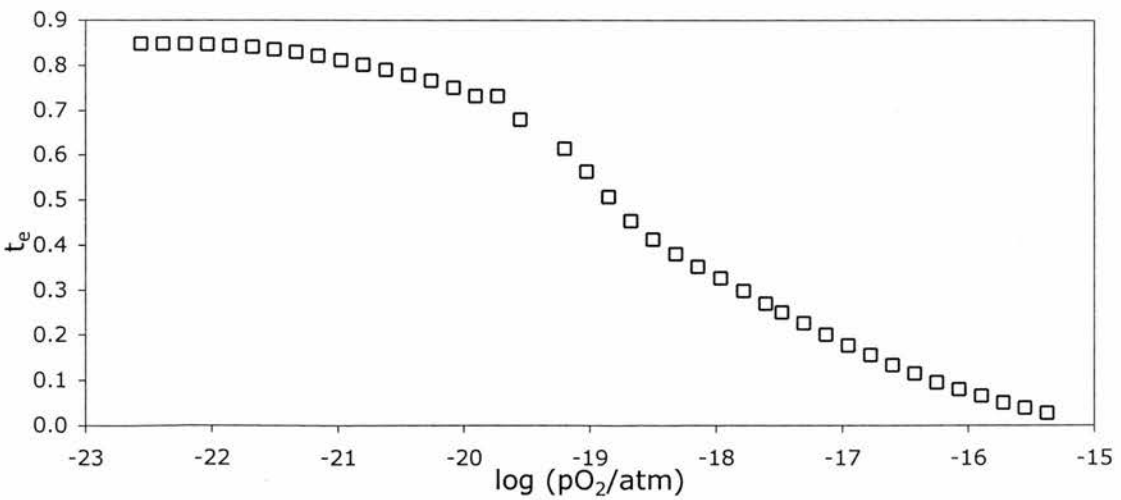

Figure 6.4: Plot of electronic transport number t_e vs. log pO_2 for $Y_{0.20}Zr_{0.57}Ti_{0.13}Ce_{0.10}O_{1.90}$